Technical Report Documentation Page

1. Report No. FHWA/TX-11/0-5220-2	2. Government Accession No.	3. Recipient's Catalog No.
4. Title and Subtitle Investigation of Stormwater Quality Improvements Utilizing Permeable Friction Course (PFC)		5. Report Date September 2010 6. Performing Organization Code
7. Author(s) Bradley J. Eck, Ph.D., P.E., J. Brandon Klenzendorf, Ph.D., Randall J. Charbeneau, Ph.D., P.E., Michael E. Barrett, Ph.D., P.E.		8. Performing Organization Report No. 0-5220-2
9. Performing Organization Name and Address Center for Transportation Research The University of Texas at Austin 1616 Guadalupe, Suite 4.202 Austin, TX 78701		10. Work Unit No. (TRAIS) 11. Contract or Grant No. 0-5220
12. Sponsoring Agency Name and Address Texas Department of Transportation Research and Technology Implementation Office P.O. Box 5080 Austin, TX 78763-5080		13. Type of Report and Period Covered Technical Report September 2006 through August 2010 14. Sponsoring Agency Code
15. Supplementary Notes Project performed in cooperation with the Texas Department of Transportation and the Federal Highway Administration.		
16. Abstract This report describes research into the water quality and hydraulics of the Permeable Friction Course (PFC). Water quality monitoring of 3 locations in the Austin area indicates up to a 90 percent reduction in pollutant discharges from PFC compared to conventional pavement. This reduction is the result of accumulation of pollutants within the pavement and the reduction in pollutants washed off of vehicles during storm events. The project also developed a methodology for measuring permeability of the pavement *in situ*. The required overcoming several instances where conventional assumptions in permeability measurements were violated. In particular, flow through the pavement at the heads evaluated was nonlinear and not consistent with Darcy's law. One dimensional steady state and two dimensional dynamic models of flow in PFC were developed. The latter model is capable of predicting surface and subsurface flow from highways of various geometries.		
17. Key Words Permeable Friction Course, Stormwater quality, Hydraulic modeling, Permeability measurement	18. Distribution Statement No restrictions. This document is available to the public through the National Technical Information Service, Springfield, Virginia 22161; www.ntis.gov.	

19. Security Classif. (of report) Unclassified	20. Security Classif. (of this page) Unclassified	21. No. of pages 318	22. Price

Form DOT F 1700.7 (8-72) Reproduction of completed page authorized

Investigation of Stormwater Quality Improvements Utilizing Permeable Friction Course (PFC)

Bradley J. Eck, Ph.D.
J. Brandon Klenzendorf, Ph.D.
Randall J. Charbeneau, Ph.D.
Michael E. Barrett, Ph.D.

CTR Technical Report:	0-5220-2
Report Date:	September 3, 2010
Project:	0-5220
Project Title:	Investigation of Stormwater Quality Improvements Utilizing Permeable Pavement and/or the Porous Friction Course (PFC)
Sponsoring Agency:	Texas Department of Transportation
Performing Agency:	Center for Transportation Research at The University of Texas at Austin

Project performed in cooperation with the Texas Department of Transportation and the Federal Highway Administration.

Center for Transportation Research
The University of Texas at Austin
1616 Guadalupe, Suite 4.202
Austin, TX 78701

www.utexas.edu/research/ctr

Disclaimers

Author's Disclaimer: The contents of this report reflect the views of the authors, who are responsible for the facts and the accuracy of the data presented herein. The contents do not necessarily reflect the official view or policies of the Federal Highway Administration or the Texas Department of Transportation (TxDOT). This report does not constitute a standard, specification, or regulation.

Patent Disclaimer: There was no invention or discovery conceived or first actually reduced to practice in the course of or under this contract, including any art, method, process, machine manufacture, design or composition of matter, or any new useful improvement thereof, or any variety of plant, which is or may be patentable under the patent laws of the United States of America or any foreign country.

Engineering Disclaimer

NOT INTENDED FOR CONSTRUCTION, BIDDING, OR PERMIT PURPOSES.

Project Engineer: Michael Barrett, Ph.D., P.E.
Professional Engineer License State and Number: Texas No. 82582
P. E. Designation: 82582

Acknowledgments

We would like to acknowledge the contributions of many former students who contributed to the success of this project. These include Christina E. Stanard, M.S., Remi Candaele, M.S., and Patrick Fraiser, M.S. In addition, we would like to recognize J. Gary Lantrip, P.E., Project Director (TxDOT) for his unwavering support, which made this project possible and ensured its success.

Table of Contents

List of Tables

List of Figures

Chapter 1. Introduction

1.1 Background and Motivation

A Permeable Friction Course (PFC) consists of a layer of porous asphalt approximately 50 mm thick placed as an overlay on top of an existing conventional concrete or asphalt surface. Rain that falls on the friction course drains through the porous layer to the original impervious road surface at which point the water drains along the boundary between the pavement types until the runoff emerges at the edge of the pavement.

Porous asphalt overlays are used increasingly by state transportation agencies, including those in Georgia, Texas, California, Arizona, and Utah, to improve drivability in wet weather conditions and to reduce noise from highway traffic. TxDOT began extensive use of PFC in about 2004. PFC use has increased from about 6.3% of asphalt pavements in 2007 to approximately 8.1% in 2010. Total use of PFC in Texas in 2009 was 354,133 tons, and 232,777 tons have been applied in 2010 through June 7th. Acknowledged benefits include:

- Reduced splash and spray
- Better visibility
- Better traction
- Reduced hydroplaning
- Less noise

The study described in this report was motivated by environmental, hydraulic, and economic factors described in the following subsections. A final subsection describes a recent national report on the use of PFCs.

1.1.1 Environmental Motivation

Concern about the environmental impacts of highway runoff has led regulatory agencies to require its treatment prior to discharge using structural Best Management Practices (BMPs). The most common of these BMPs include wet ponds, detention ponds, and sedimentation/filtration basins. These structures have a very high cost/mile compared to other components of highway design, particularly when additional right-of-way must be acquired. Maintenance is also a labor-intensive expense for such items as vegetation management, structural repair and the replacement of filtration media. Often times these structures cease to drain effectively or have ponded areas that breed mosquitoes. Several installations require removal of floatable litter and unsightly debris. These maintenance activities will increase in frequency and cumulative cost as new installations come online. Consequently, there is a need to identify cost-effective alternatives for stormwater treatment, which might include the use of permeable friction courses.

PFC might be expected to reduce the generation of pollutants, retain a portion of generated pollutants within the porous matrix, and impede the transport of pollutants to the edge of the pavement. The porous structure of PFC also may act as a filter of the stormwater. Runoff enters the pores in the overlay surface and is diverted towards the shoulder by the underlying conventional pavement. Pollutants in the runoff can be filtered out as the water flows through the

pores, especially suspended solids and other pollutants associated with particles. Pollutants may become attached to the PFC matrix by straining, collision, and other processes. Material that accumulates in the pore spaces of PFC is difficult to transport and may be trapped permanently. On the surface of a conventionally paved road, splashing created by tires moving through standing water easily can transport even larger particulate matter rapidly to the edge of pavement. However, water velocities within the pore spaces of the PFC are low and likely could only transport the smallest material.

1.1.2 Hydraulic Motivation

In order for PFC to provide both the water quality and safety benefits it is important that sufficient porosity and hydraulic conductivity be maintained for essentially the life of the pavement. Once the pores in the PFC become plugged, then runoff will begin flowing on the surface of the pavement and all the benefits, both in terms of safety and water quality, will be lost.

The loss of porosity within the pavement structure can occur more quickly if the PFC is not correctly installed to achieve the expected 20% porosity and associated permeability. TxDOT currently lacks a sound, scientifically based method to assess whether contractors have achieved the desired properties in the overlay. The current test consists of an empirical method that measures the time required to drain an arbitrary volume of water. To use this data to calculate permeability, one must assume saturated porous media flow in a single direction and well defined boundary conditions. The current TxDOT test does not achieve saturated flow and generates flow in all directions. Consequently, another objective of this research is to develop a standardized test for determining PFC hydraulic properties that can be used at the job site to assess contractor performance.

Another concern about the current use of PFC is the lack of definitive design guidance related to hydraulic constraints. This is an important issue since the runoff should travel for the entire distance across the paved way without surfacing in the outer lanes. This is mostly likely to occur on a multi-lane highway with low cross slope, and in curves and super-elevation transitions with long drainage paths. Although fluid flow within PFC is porous media flow, the pore scale and structure may result in flow characterization that lies outside of the usual range of Darcy's law; conditions under which inertial forces become important. However, the general framework of groundwater hydraulics provides an appropriate basis for quantitative analysis of stormwater flow within PFC (Charbeneau, 2000).

A goal of this research effort will be to determine representative values for the hydraulic conductivity and develop tools for analysis of drainage flows within PFC to determine appropriate hydraulic constraints for the use and installation of PFC. This understanding of flow in PFC will support an additional potential safety application. In very wide multi-lane freeways, sheet flow depth on conventional pavements may become excessive in the outer lanes during intense rainfall events. If PFC can be used in these situations a portion (if not all) of the runoff can move within the pore structure, either reducing or eliminating the problem of excessive water depths on the surface of the roadway. A recent TxDOT-sponsored research effort has investigated pavement drainage for superelevation transitions and PFC could perhaps be used to reduce ponding of runoff on the pavement in these situations.

1.1.3 Economic Motivation

A final consideration in this research is the relative cost of PFC versus other paving options. The cost of PFC is normally considered to be somewhat higher than that of conventional hot mix asphalt. This comparison might be misleading if the PFC surfaced roadway would not have to include the structural BMPs now constructed for conventional highways in the Edwards Aquifer recharge zone and other areas of the state. Consequently, an additional need is a valid cost comparison that includes all elements of the highway project including design life, structural controls (and their maintenance), right-of-way requirements, and alternate paving materials.

1.1.4 NCHRP Report 640

During the conduct of this research, the National Cooperative Highway Research Program (NCHRP) issued Report 640 entitled "Construction and Maintenance Practices for Permeable Friction Courses" (NCHRP, 2009). The report signifies the growing popularity and importance PFC layers for highways in the USA. Several of the future research needs listed in the report are addressed in part by this report:

- Field work to document how water flows within a PFC layer
- Methods for selecting the minimum PFC thickness
- Consideration for water sheets on the PFC surface
- Methods to determine the permeability of PFC layers

1.2 Research Tasks

The scope of work for this project divided the research questions posed above into six unique tasks. A brief description of each task is given below.

Task 1: State of the Practice

This task consists of two elements: a literature review and a survey of other DOTs. The literature review will document the various types of permeable pavements that are now in use internationally. The review will focus on the properties of these pavements, water quantity and quality benefits, maintenance practices, and any identified constraints for their use. The objective of the DOT survey is to catalogue the practices of other DOTs related to the installation and management of porous pavements in general and PFC in particular.

Task 2: Stormwater Monitoring

The quality of highway runoff from a site on Loop 360 in Austin has been monitored since March 2004. A PFC overlay was applied at this site in the summer of 2004 and monitoring resumed in the fall of 2004. Continued monitoring of the site is valuable as a complete record of runoff quality is available since the overlay was first applied. This data will fully document the water quality improvements and whether the observed improvement in water quality will persist for the life of the pavement. In addition, an attempt will be made to identify one or more additional sites for monitoring to confirm the initial results seen at the Loop 360 site.

One shortcoming of the current monitoring site is that it has not been possible to assess the effects of PFC on the volume, rate, and timing of runoff from this type of pavement. The main constraint is that the catchment area to the small edge of pavement sampler is not well

defined. This monitoring effort will install additional equipment to capture the runoff hydrograph from the PFC highway and collect flow weighted composite samples.

Although current regulations for stormwater treatment focus only on the reduction of suspended solids (TSS) in runoff, the proposed sampling effort will analyze for a suite of standard constituents. The results may be useful for meeting treatment requirements in areas other than the Edwards Aquifer, such as for 401 Certifications or complying with Total Daily Maximum Loads (TMDLs).

Task 3: Evaluate the Hydraulic Properties

There are a number of sites in the Austin area and statewide where PFC has been installed. Core samples will be taken at a variety of these sites that represent differences in time since installation, traffic density, vehicle mix, adjacent land use, soils, and other factors. These cores may be taken from the shoulder as well as the active traffic lanes and will be analyzed using appropriate hydraulic tests to determine porosity and hydraulic conductivity.

Task 4: Develop Model to Predict Flow in PFC

The objective of this task is to develop a model that predicts flow in the pore spaces of PFC. This is an important component of the project since it will allow designers to determine whether roadway geometry (width, slope, curves, and superelevation transitions) support the use of PFC without the runoff surfacing in the active traffic lanes.

The model will treat the overlay as a thin unconfined aquifer. In addition, a determination will be made of whether the flow is likely to lie outside of the usual range of Darcy's law and whether conditions under which inertial forces become important are present. This model will also be used to predict flow after the pavement becomes partially clogged.

Task 5: Develop Field Testing Protocol

An important objective of this study is to improve on the test currently used to confirm that a PFC installation was done in such a way as to maximize the water quality and hydraulic performance. The new test is based on sealing of an impermeable circular ring (large washer) to the pavement surface with a vertical cylinder (standpipe) attached at the inner radius of the ring. The test device can accommodate constant head or falling head tests. Developing theory to interpret test results from such a device is a key element of this work. Measurement results are expected to be directly relevant to calculations important for field application of PFC.

Task 6: Whole-Life Cost Comparison

The whole-life cost of a practice includes replacement and maintenance as well as design and construction. Costs for future maintenance and replacement are included in the whole-life cost by determining their present value. In this comparison three systems will be compared. Systems one and two are a conventional hot mix asphalt (HMA) pavement used in conjunction with a structural BMP (such as a sand filter or vegetated filter strip) for stormwater treatment, while the third is PFC alone.

1.3 Report Organization

This report is organized into eight chapters. Chapter 1 gives introductory material and Chapter 8 provides conclusions from the research. The interior chapters correspond to the research tasks given above as shown in Table 1.1. The report contains a considerable amount of

supporting material in the form of tables, figures, and equations. Tables and figures are numbered by chapter and sequence. Equation numbering is consistent within each chapter. Raw data generated from this research is provided in appendices.

Table 1.1: Correspondence between research tasks in scope of work and report chapters

Research Task	**Report Chapter**
Task 1: State of the Practice	N/A Documentation for Task 1 was published as TxDOT Report 0-5220-1 in December 2007.
Task 2: Stormwater Monitoring	Chapter 2
Task 3: Evaluation of Hydraulic Properties	Chapter 3
Task 4: Model to Predict Flow in PFC	Chapter 4 and Chapter 5
Task 5: Field Testing Protocol	Chapter 6
Task 6: Whole-Life Cost Comparison	Chapter 7

Chapter 2. Water Quality Monitoring

2.1 Introduction

This chapter summarizes the results of Task 2: Stormwater Monitoring. PFC is an innovative paving material that is applied as a sacrificial layer on top of conventional pavement. PFC allows water to drain through the overlay rather than on the surface of the roadway. During rain events, water seeps into the porous layer and flows to the side of the road by gravity. By removing water from the road surface, PFC improves safety by reducing splashing and hydroplaning. In addition to safety benefits, PFC has also been shown to reduce concentrations of pollutants commonly observed in highway runoff.

A study in the Netherlands compared runoff water quality from porous overlays and conventional pavement surfaces (Berbee et al., 1999). Lower concentrations of pollutants were observed in runoff sampled from the porous asphalt than from impervious asphalt for many of the constituents monitored. Specifically, total suspended solids (TSS) concentrations were 91% lower, total Kjeldahl nitrogen (TKN) 84% lower, chemical oxygen demand (COD) 88% lower, and total copper (Cu), lead (Pb), and zinc (Zn) ranged from 67-92% lower than in runoff from the conventional asphalt pavement.

Researchers in France have also studied the effects of different types of pavement on the quality of highway runoff (Pagotto et al., 2000). Their research site was a section of a highway where conventional pavement was replaced with porous asphalt. Monitoring before and after the replacement showed that mean TSS levels dropped from 46 mg/L to 8.7 mg/L, an 81% reduction. Concentrations of total metals also decreased: Pb by 78%, cadmium (Cd) by 69%, Zn by 66% and Cu by 35%. Some dissolved metals (Zn and Cd) declined by about 60%.

This chapter presents results of research into water quality aspects of PFC conducted at The University of Texas at Austin. The water quality of runoff from PFC was measured at three locations near Austin, Texas. Taken together, the datasets represent one of the largest PFC monitoring programs in the USA.

2.2 Materials and Methods

2.2.1 Site Descriptions

There are three sites where water quality data were collected during the course of this study. Two of the sites are found on Loop 360 near RR 2222 in Austin, TX. The third site is located on RR 620 near Cornerwood Drive in Round Rock, TX. Satellite images of the three sites are found in Figure 2-1 and Figure 2-2. Loop 360 is overlain with PFC from Lake Austin to US 183 except at traffic signals and bridges. RR 620 is paved with PFC from IH 35 to the intersection at Cornerwood Dr. The 2005 average annual daily traffic (AADT), as estimated by TxDOT, for Loop 360 between Spicewood Springs Road and RM 2222 was 48,000. The AADT for RR 620 between Wyoming Springs Dr. and FM 734 was 32,000 (CAMPO, 2007).

Site 1 is located on the shoulder of southbound Loop 360. Water quality was monitored since March 2004 prior to the installation of PFC in October 2004. Passive samplers were used to monitor stormwater runoff until the system was replaced with an active sampler in December 2006.

Site 2 is located 0.3 miles south of Site 1 on the shoulder of the northbound lane near Lakewood Drive. The passive samplers are located about 200 feet apart, one each for PFC and

conventional pavement. TxDOT feared that the deceleration and acceleration that occurs at intersections would lead to rapid deterioration of PFC and concluded that conventional asphalt would remain at the locations of traffic lights. The proximity of the two samplers allowed for pair samplings to occur where conditions (rainfall depth, storm intensity, traffic counts, etc.) could be assumed homogenous.

Figure 2-1: Satellite Images of Sites 1 and 2 (Google Maps, 2009)

Figure 2-2: Satellite Images of Site 3 Passive Samplers (Google Maps, 2009)

Site 3 is located on either side of Cornerwood Drive on the southbound shoulder of RR 620. The two passive samplers are located about 450 feet apart. Candaele et al. (2008) determined that the hydraulic conductivity and effective porosity of PFC at RR 620 is much lower than that at Loop 360. The goal of adding this third research site was to observe the differences in water quality for a pavement that does not drain as rapidly. The hypothesis was that as the permeability of PFC decreased the water quality would approach that of conventional pavement.

2.2.2 Site 1 Setup

Stormwater runoff quality was monitored at Site 1 on Loop 360 during the period from February 2004 through October 2009. GKY FirstFlush Samplers were originally installed to collect the runoff at this site. Because these passive samplers can only accommodate 5L of runoff, the containers can fill before the end of large storm events, resulting in a sample that is front-weighted. A picture of the edge of pavement sampler is presented in Figure 2-3. A rain gauge also was installed at the site to provide storm totals of rainfall.

In October 2004, TxDOT implemented a PFC overlay project on this section of Loop 360. The overlay was applied on top of the existing conventional asphalt according to TxDOT specifications (TxDOT, 2004). The overlay is visible in Figure 2-3 and the coarse nature of this paving material is evident in this photograph. The lighter gray asphalt at the edge of pavement is the conventional surface below the PFC. Runoff sampling at the site was discontinued during the overlay installation and resumed upon completion of the overlay project.

New instrumentation was installed at the site in November 2006. A collection system 60 feet (18.3 m) long was installed along the edge of pavement and the runoff was routed to an H-flume where runoff rates were recorded and flow weighted water quality samples were collected using an automatic sampler. Consequently, at this site there has now been collection of runoff samples since the initial installation of the PFC nearly 5 years ago.

Figure 2-3 Photograph of installed sampler at edge of pavement.

The stormwater collection system was constructed to act like a gutter on the shoulder of the road (Figure 2-4). It is made up of six 10 foot sections of 4 inch diameter PVC pipe that are connected with rubber joints. A quarter circle of the cross section was cut laterally along the pipe to create an entrance for water runoff. Plastic flashing was used to allow runoff to enter the PVC pipe. The flashing has a 1" overhang that is placed within the opening in the PVC pipe. Flashing was secured to the pavement using silicone. The pipe runs along the edge of the pavement until it makes a 90 degree turn and runs underground in a completely closed PVC pipe. The underground pipe runs for about 20 feet before emptying into an H-flume.

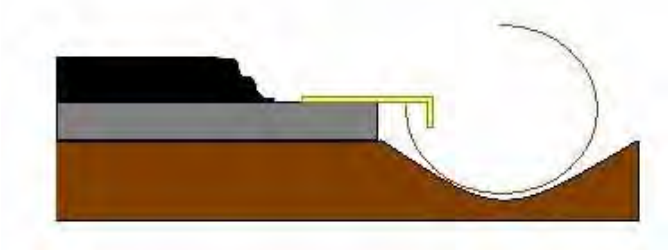

Figure 2-4: Cross section of collection system

An ISCO 4230 Bubbler Flow Meter monitors the depth of water runoff in the H-flume approach and calculates the corresponding flow rate. Just downstream of the bubble flow meter the runoff flows into a container where samples can be drawn using an ISCO 3700 Portable Sampler. The samples are pumped through a Teflon coated suction line into a 10L Nalgene bottle.

A secure storage box is located onsite to house the sampling equipment and bubble flow meter. It is powered by a 12-volt marine battery that is charged by a solar panel. An ISCO 674 Rain Gauge is located onsite and is connected to the flow meter. The rain gage is a tipping bucket that measures rainfall in 0.01 inch increments. Rainfall data is sent to the flow meter every 5 minutes. Photographs of the Loop 360 site are found in Figure 2-5 and Figure 2-6. For more detailed information regarding the design, installation, and programming of the active sampler refer to Stanard et al. (2008).

Figure 2-5: Loop 360 sampling site

Figure 2-6: Flume and Sampling Box at Loop 360

2.2.3 Site 2 Setup

Two GKY First Flush samplers were installed in February 2007. The first flush samplers have five holes in the top of the lid to allow runoff to flow into the containers. Inside each

sampler is a 5 L plastic container that can be easily removed. Once the containers are full, buoyant plastic flaps seal the holes.

The locations for the samplers were chosen so that neither would be affected by the close proximity of the transition from PFC to conventional pavement. The samplers were installed by digging a hole on the edge of the pavement, filling it with concrete, and insuring that the boxes were level so that water would be collected by gravity. Silicone was used to create a level transition from the pavement to the boxes and to fill any holes that might divert water from the box. Photographs of the passive samplers at Site 2 are found in Figure 2-7.

2.2.4 Site 3 Setup

Site 3 passive samplers were installed in January 2009 on the shoulder of RR 620. Setup is very similar to that of Site 2. Locations for samplers were based on the closest combination of paired sampling as well as ease of access. Both boxes are located adjacent to parking lots. Photos of the RR 620 site are found in Figure 2-8.

Figure 2-7: Passive Samplers at Loop 360, PFC (Left) and Conventional Pavement (Right)

Figure 2-8: Passive Samplers at RR 620, PFC (Left) and Conventional Pavement (Right)

2.2.5 Sampling Procedure

Prior to rain events the sites were prepared for sampling. For the active sampler on Loop 360, a battery powered leaf blower was used to clean the PVC pipes and flume of debris. The sampling box was wiped clean and a new 10L Nalgene bottle was placed in the storage box. The sampler was programmed to begin sampling at the start of runoff. The rain gauge was checked for clogging and all tubing was checked for proper connections. For the passive samplers, roadside debris was cleared and the boxes were cleaned of any dirt and any residual water was removed. Clean sampling boxes were placed in the samplers and lids were tightened to secure a level surface for water to enter the boxes.

2.2.6 Analytical Procedures

After the storms, all the sampling containers were removed and secured with a lid. The samples were taken to the Lower Colorado River Authority (LCRA) lab in Austin for analysis. The samples were delivered to the LCRA lab as soon as possible. If the lab was closed post-sampling, the samples were stored in a cold room at 4°C and delivered as soon as the lab was open.

Table 2-1 contains the parameters and methods used by the LCRA lab for analyzing the samples. The Practical Quantification Limit represents the minimal limit at which concentrations can be accurately quantified. Concentrations less than these amounts are said to be “Not Detected” (ND).

T-tests were performed (non-paired at Site 1 and paired at Sites 2 and 3) to determine whether statistically significant changes in concentration had occurred. Changes were determined to be significant when the p-value was less than 0.05.

Table 2.1: Parameters and Methods for Analysis

Parameter	Units	Method	Practical Quantification Limit
Total Suspended Solids	mg/L	E160.2	1.0
Total Kjeldahl Nitrogen (TKN)	mg/L	E351.2	0.40
Nitrate and Nitrite as N (NO_3^+/NO_2)	mg/L	E353.2	0.04
Total Phosphate as P	mg/L	E365.4	0.02
Dissolved Phosphate as P	mg/L	E365.4	0.02
Chemical Oxygen Demand (COD)	mg/L	E4104.4	70
Total Copper (Cu)	µg/L	E200.8	2.00
Dissolved Copper	µg/L	E200.8	1.02
Total Lead (Pb)	µg/L	E200.8	1.00
Dissolved Lead	µg/L	E200.8	1.02
Total Zinc (Zn)	µg/L	E200.8	5.00
Dissolved Zinc	µg/L	E200.8	4.08

2.3 Results and Discussion

2.3.1 Site 1 Results

At Site 1, five samples of runoff were collected from the conventional pavement and 47 samples of runoff were collected after the PFC overlay. The data indicate that the runoff generated from the PFC surface has consistently lower concentrations of particles and particle associated pollutants than that from the traditional asphalt surface. This difference in water quality also was noted upon visual inspection of the runoff samples collected at the edge of pavement.

The EMCs measured during the sampled storm events at the original site before and after installation of the PFC are shown in Table 2.2. Concentrations of TSS, total phosphorus, and total lead, copper, and zinc are significantly lower in runoff generated from the PFC surface than in runoff generated from the conventional asphalt surface. A negative sign on the removal efficiency indicated that an increase in concentration of dissolved copper was observed; however, it is not known why this occurred. The concentrations of nitrate/nitrite, dissolved copper and zinc, and total and dissolved phosphorus did not exhibit a significant difference between the two road surfaces. These data indicate that the PFC has little to no effect upon the concentrations of dissolved constituents in the stormwater runoff.

Table 2.2: Comparison of Conventional Asphalt and PFC for Site 1

Constituent	Conventional Asphalt	PFC	Reduction %	p-values
TSS (mg/L)	117.8	8.8	92	0.016
TKN (mg/L)	1.13	1.00	11	0.796
NO_3^+/NO_2 (mg/L)	0.43	0.39	9	0.875
Total P (mg/L)	0.13	0.07	48	0.047
Dissolved P (mg/L)	0.06	0.03	24	0.483
COD (mg/L)	64	61.05	4	0.863
Total Copper (µg/L))	26.84	13.48	50	0.010
Dissolved Copper (µg/L)	5.94	10.54	-77	0.045
Total Lead (µg/L)	12.57	1.12	91	0.025
Dissolved Lead (µg/L)	< 1.0	< 1.0	NA	NA
Total Zinc (µg/L)	167.4	29.27	83	0.002
Dissolved Zinc (µg/L)	47.06	22.02	53	0.139

During the first four storms after installation of the overlay, EMCs of TKN and COD were also less than that in runoff from the conventional pavement, which agrees with the findings of previous research (Berbee et al., 1999). After the fourth storm, concentrations increased abruptly and returned to levels observed from the conventional pavement. This change corresponds to the time when the roadside shoulder was mowed. This maintenance activity distributed a substantial amount of cut grass, leaves, and other organic matter on the PFC where it may have become lodged in the pavement pores resulting in the observed increase in concentration.

After more than 5 years of monitoring, no significant correlation between discharge concentrations at the edge of pavement and time since installation or cumulative rainfall volume has been observed. As an example, Figure 2-9 presents the concentrations of total suspended solids for each of the monitored events at the original site, while Figure 2-10 presents a similar graph for total zinc.

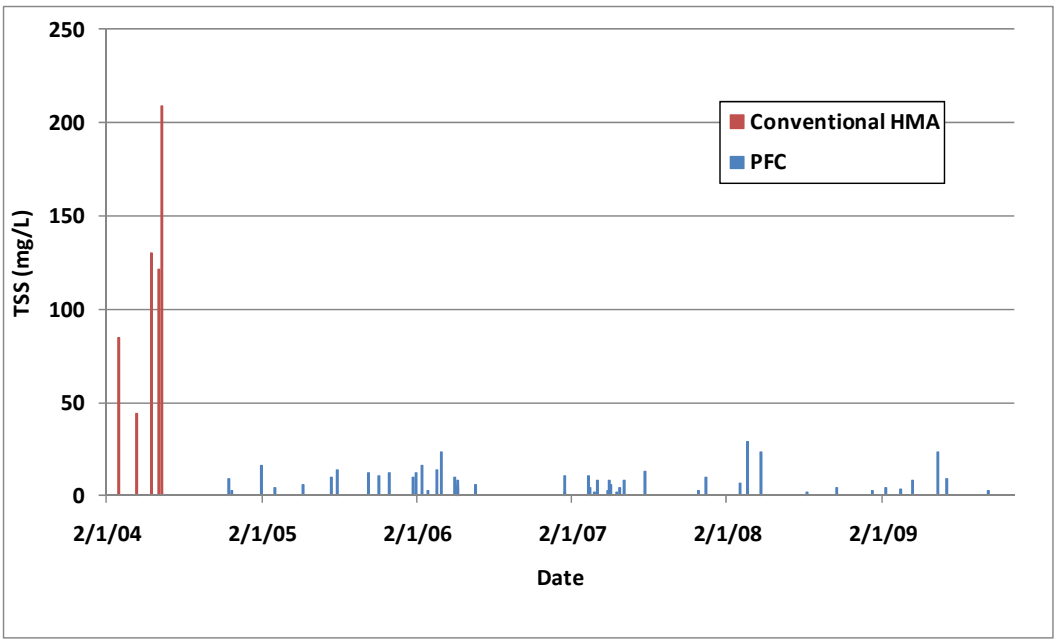

Figure 2-9: TSS concentrations over time

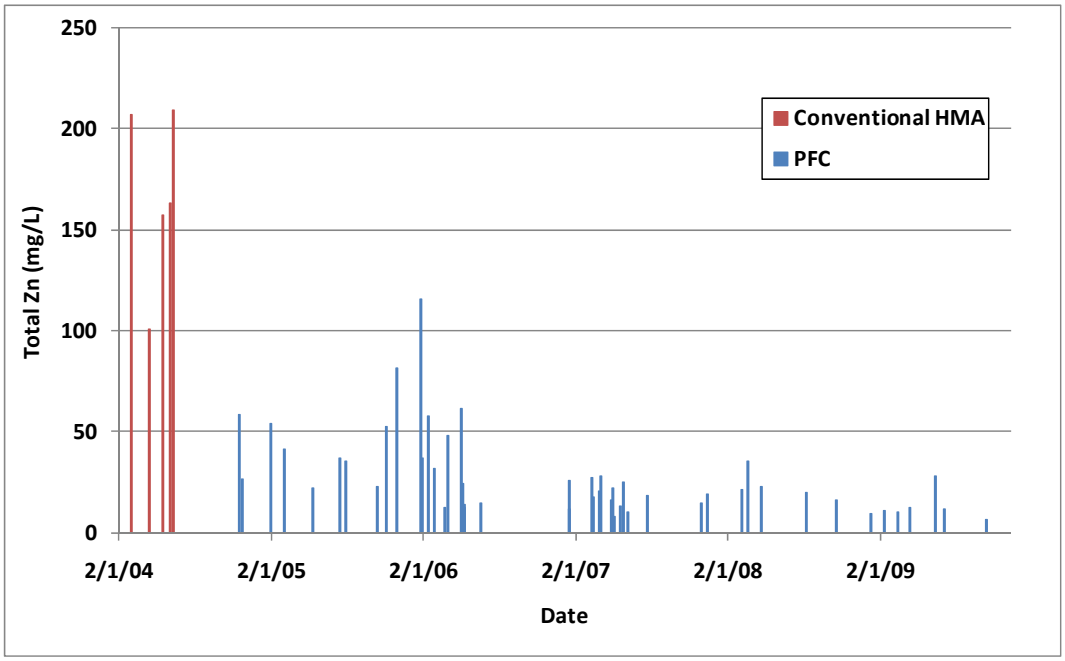

Figure 2-10: Total Zinc concentrations over time

2.3.2 Site 2 Results

A total of 15 storms were monitored at Site 2 with paired samplers. Mean concentrations for runoff at Site 2 are presented in Table 2.3 along with the p-value from a paired t-test to determine whether observed differences in concentration are significant. Performance overall is very similar to Site 1, with significant concentration reductions for TSS, total P, and total metals.

Also similar to Site 1 is the small increase in dissolved copper concentrations. Figure 2-11 presents the paired TSS concentrations from this site, which highlights the very consistent reduction in TSS observed during the study.

2.3.3 Site 3 Results

Eight paired samples were collected at Site 3 on RR 620 during 2009 and average runoff concentrations are reported in Table 2.4, along with the p-value from a paired t-test. Despite the lower porosity and permeability at this site, the average pollutant reduction is similar to that observed at the two sites on Loop 360. Statistically significant reductions are observed for TSS, TKN, total P, COD, and total metals, which is more constituents than exhibited significant reductions at the other two sites. In general, the runoff concentrations from the conventional pavement are substantially higher than those observed on Loop 360. Figure 2-12 presents a comparison of TSS concentrations observed for individual events at Site 3. It is very apparent from this figure that the reductions are both substantial and very consistent.

Table 2.3: Constituent EMCs for Conventional Asphalt and PFC at Site 2

Constituent	Conventional Asphalt	PFC	Reduction %	p-value
TSS (mg/L)	148	18	88	<0.000
TKN (mg/L)	1.10	0.92	16	0.116
NO_3/NO_2 (mg/L)	0.17	0.25	-52	0.123
Total P (mg/L)	0.15	0.05	63	0.006
Dissolved P (mg/L)	0.03	0.03	21	0.144
COD (mg/L)	75	60	20	0.109
Total Copper (µg/L)	30	13	57	<0.000
Dissolved Copper (µg/L)	6.3	9.0	-44	0.015
Total Lead (µg/L)	11	1.3	88	<0.000
Dissolved Lead (µg/L)	<1.0	<1.0	NA	NA
Total Zinc (µg/L)	130	21	84	<0.000
Dissolved Zinc (µg/L)	18	11	40	0.043

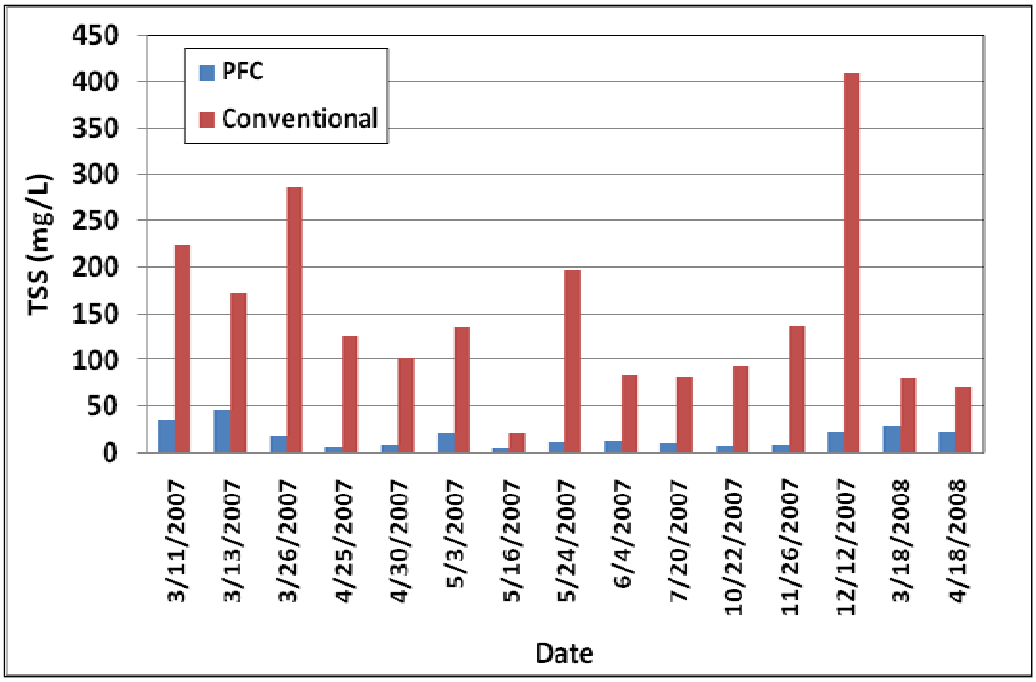

Figure 2-11 TSS Concentrations at Site 2

Table 2.4: Comparison of Runoff Concentrations at Site 3

Constituent	HMA	PFC	Reduction %	p-value
TSS (mg/L)	222	14.8	93	0.014
TKN (mg/L)	2.11	0.69	67	0.024
NO_3^+/NO_2 (mg/L)	0.35	0.26	25	0.621
Total P (mg/L)	0.22	0.05	77	0.007
Dissolved P (mg/L)	0.04	0.02	37	0.283
COD (mg/L)	121	38	68	0.018
Total Copper (µg/L)	24	9.1	63	0.005
Dissolved Copper (µg/L)	7.73	5.90	24	0.580
Total Lead (µg/L)	19.6	1.3	93	0.001
Dissolved Lead (µg/L)	<1.0	<1.0	NA	NA
Total Zinc (µg/L)	173	24	86	<0.000
Dissolved Zinc (µg/L)	21.4	12	44	0.332

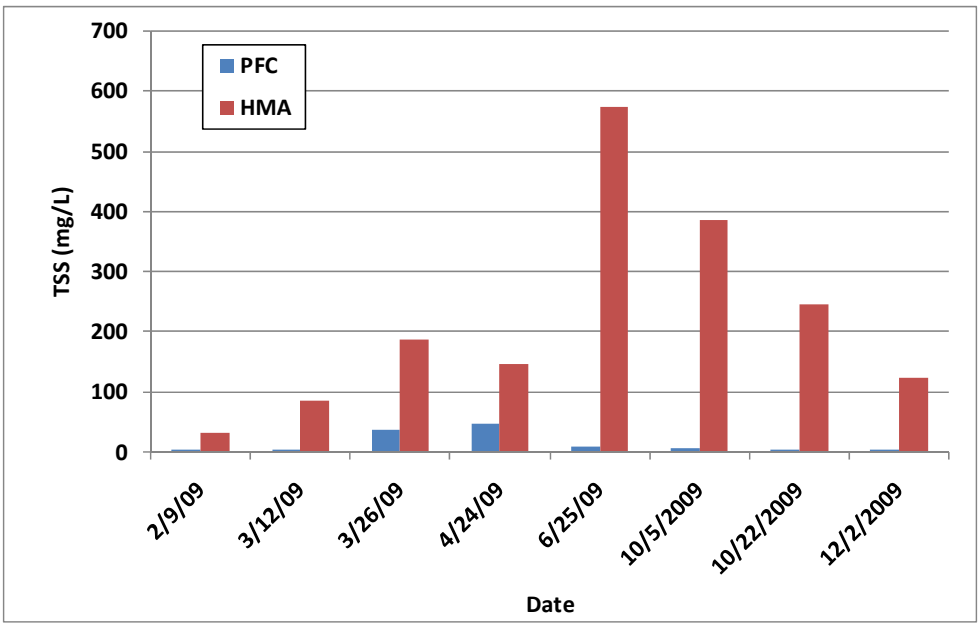

Figure 2-12 TSS Concentrations Observed at Site 3

2.3.4 Combined TSS Results

In this study, the constituent of primary interest in highway runoff is TSS both because it is commonly regulated and because it generally corresponds to levels of other particle-bound constituents. Grouping data by location (Site 1-3) and pavement type (PFC or hot mix asphalt (HMA)) yields six bins. Box and whisker plots were prepared for each bin (Figure 2-13). In the plots, the median is shown as a heavy line and the middle half of the data (interquartile range) is boxed. Whiskers extend to last observation within 1.5 interquartile ranges from the end of the box; points outside this range are plotted. The data show that the median TSS concentration in runoff is lower for PFC than from HMA. The variability in TSS concentrations—as measured by the interquartile range—is in every case smaller for PFC. This finding, that runoff from PFC has lower and more consistent levels of TSS, demonstrates that American installations of PFC provide water quality improvement similar to European installations.

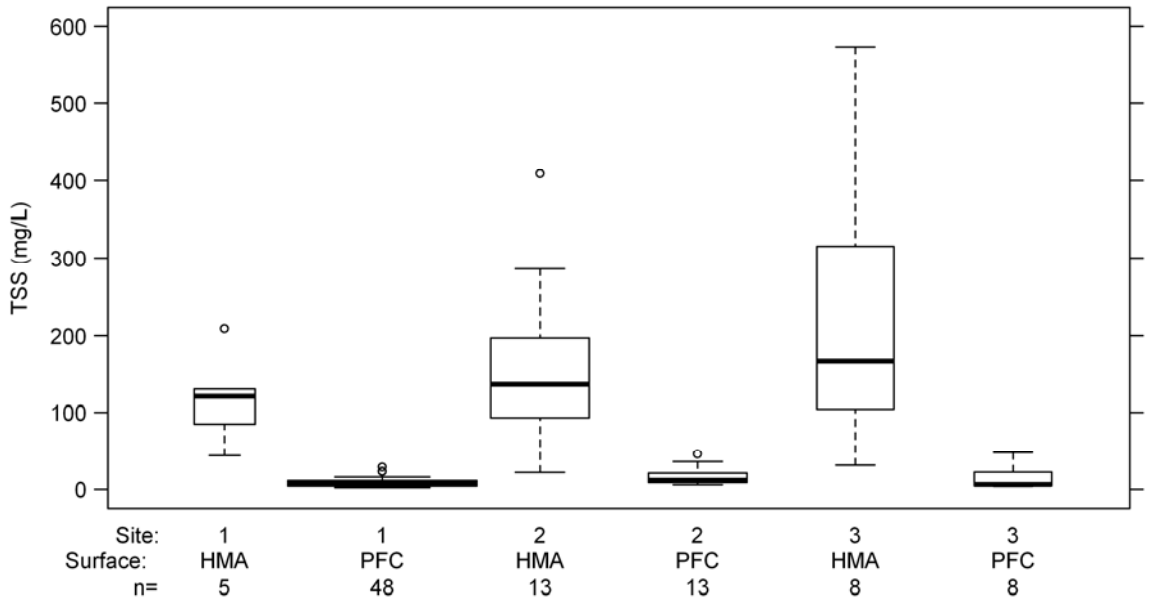

Figure 2-13: Box and whisker plots of TSS concentrations by monitoring location and pavement surface.

Note: Whiskers extend to the last observation within 1.5 times the interquartile range; box widths are proportional to the square root of the number of observations.

An important question in the application of PFC with respect to stormwater quality is how performance changes over time. One unique feature of the dataset presented in this paper is that the PFC in North Carolina is approximately five years older than that in Texas. Plotting TSS against pavement age therefore gives a picture of the lifespan of a PFC layer (Figure 2-14) The very high value observed at NC2 occurred directly after a major snowstorm when salt and sand were applied to the road. Correlation tests of TSS with PFC age using Kendall's tau were conducted for each monitoring site and for the all the PFC measurements together. The overall Kendall's tau correlation coefficient was -0.079 with p=0.35, showing no significant correlation. This finding, runoff concentrations are consistent through the life of a PFC, suggests that in many cases replacing PFC at the end of its structural life is sufficient to provide continuously better runoff water quality.

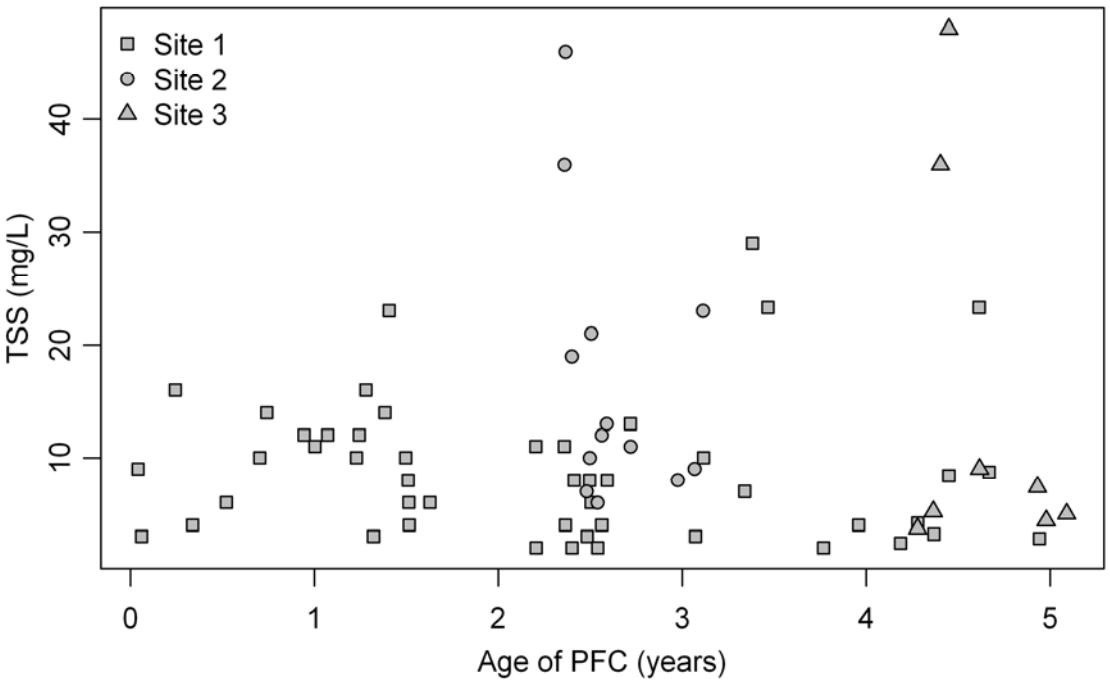

Figure 2-14: TSS concentrations for PFC roadways as a function of pavement age

The finding that PFC provides removal of particle associated contaminants suggests that the porous structure of PFC traps particles during the runoff process. It is also possible that the absence of water on the roadway—due to the drainage properties of PFC—causes fewer contaminants to be washed from passing vehicles. If PFC truly traps particles, then it would be expected to clog over time and its porosity would decrease. Porosity of the Texas monitoring sites have been measured from core samples and found to be decreasing faster than would be accounted for by TSS removal from stormwater.

Collectively, the TSS results suggest that differences in concentrations between the pavements are due to differences in how the pavements deal with particles. Particle size distribution analysis was used to further investigate the influence of particle processes on the water quality of runoff from PFC. As an example, particle size distributions from TX2 on July 1, 2009 (Figure 2-15) show that particles in the size range 3-60µm are primarily responsible for higher TSS levels in runoff from conventional pavement.

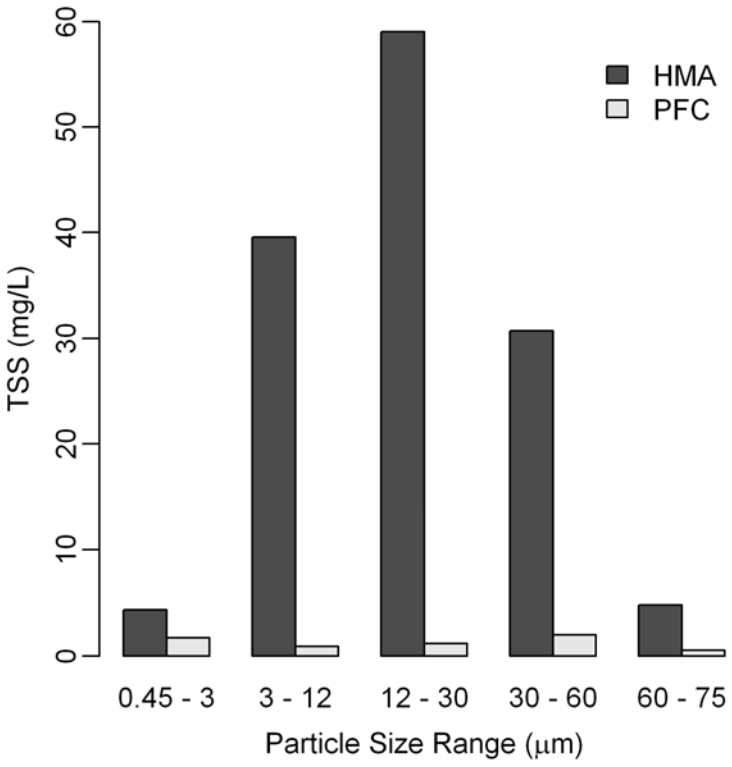

Figure 2-15: Example particle size distributions for PFC and conventional pavement from Site 2 on July 1, 2009

2.4 Conclusions

Porous asphalt overlays are proving to be a versatile material for highway pavements. The ability to provide safer driving conditions in wet weather by eliminating the splash and spray effect and the prevention of hydroplaning promise many safety benefits. The added benefit of improved water quality is becoming better understood.

Site 1 at Loop 360 has been monitored for over 5 years, including 6 months prior to the installation of PFC. The runoff from conventional pavement and PFC were compared. The results show a drastic improvement due to the installation of PFC. TSS concentrations were reduced by 92% while total metal concentrations (zinc, lead, and copper) were reduced between 50-91%. A common concern of PFC is the lifespan of the water quality benefits; however, the results do not indicate any trends toward a decline in water quality.

Site 2 provided the opportunity to collect samples from both PFC and conventional pavement from the same storm events. The water quality performance is similar to Site 1, with TSS concentrations being reduced by 88%. Comparable reductions were also observed for phosphorus and total metals.

Site 3 provided insight into the water quality of runoff from a location where lab and field tests indicate a lower hydraulic conductivity. The results also showed a significant reduction in TSS (93%) and total metal concentrations (63–93%). Interestingly, while the runoff from conventional pavement was more polluted than Site 2, the runoff from PFC remained relatively unchanged between the two sites. If decrease in hydraulic conductivity is to be an indicator of

failure, Site 3 has yet to approach such a threshold. Further monitoring of hydraulic conductivity as well as water quality should be conducted in order to observe failure.

From these results it is evident that the runoff generated from a PFC surface is of better quality than that from the traditional asphalt surface. Many regulatory agencies in the US require an 80 percent reduction in the amount of TSS discharged from new developments. The TSS removal observed during this project easily exceeds this threshold; consequently, this type of overlay has now been approved by the Texas Commission on Environmental Quality as a Best Management Practice (BMP) for highways in lieu of ponds, filters, or other structures commonly constructed to treat stormwater runoff.

A critical component in the assessment of the water quality benefits of PFC is whether the pollutant reduction observed in this study will persist over the life of the pavement. As particles and particle associated pollutants accumulate within the pore structure it seems likely that more runoff will travel on the surface of the pavement resulting in concentrations that might not be significantly different from those observed in runoff from conventional asphalt pavements. In addition, clogging of the pores in the pavement will likely reduce the other benefits associated with PFC (spray and noise reduction). Pavement cleaning machines could be used to remove accumulated pollutants and prolong the water quality benefits. Consequently, an evaluation of potential maintenance practices is recommended.

Chapter 3. Hydraulic Properties

3.1 Introduction

3.1.1 Background and Motivation

Urbanization and the development of land result in the natural land cover being replaced by impervious surfaces. Roadways, parking lots, sidewalks, and buildings are among the typical structures that result in impervious surfaces and prevent rainfall from naturally infiltrating into the ground and recharging groundwater supplies. The effects of urbanization on the hydrologic processes of an area include, but are not limited to, increased peak flows and increased flow velocities during rainfall events. This can result in stream erosion and increased likelihood of flooding. The use of porous pavement is one technique for mitigating these effects.

Field et al. (1982) provide an overview of the advantages and disadvantages of using a completely porous pavement system. Completely porous pavement systems consist of a porous asphalt or porous concrete surface course as well as a porous reservoir base course and subgrade. The goal of porous pavement is to drain all the rainfall runoff into the reservoir base course and then allow the water to slowly infiltrate into the surrounding natural soil. This reduces the peak runoff flow rate and improves the water quality by removing pollutants from the road surface through filtering of sediment particles and the pollutants associated with sediment. In addition, porous pavement removes runoff from the surface, which helps to improve driver safety. Less surface runoff reduces the potential for hydroplaning and reduces splash and spray from vehicles, which allows for better visibility. However, there have been concerns with respect to the structural integrity of a completely porous pavement system. In the use of traditional impervious roadways, the subgrade is designed for a specified compaction strength and to remain free of water in order to maintain adequate structural strength. With the use of completely porous pavements, water is allowed to infiltrate into the subgrade. This suggests that the structural strength of the roadway may be adversely impacted during rainfall events.

In an effort to avoid the structural concerns of completely porous pavement systems, a different approach is needed. Recently, many state departments of transportation have begun using only a porous surface course in order to take advantage of the driver safety benefits. A porous asphalt surface course serves as a sacrificial overlay in that it is expected to degrade and be replaced more frequently than conventional pavements with a typical design life of roughly 10 years (TRB, 2009). Void space in the porous asphalt is created by removing the fine aggregate from traditional asphalt mixes and increasing the volume of asphalt binder. The lack of fines results in a porous matrix of large angular aggregate, on the order of 1.0 cm (0.4 in) in diameter, held together by asphalt binder. A porous surface course consists of a porous asphalt layer up to 50 mm (2 in) thick with roughly 20% effective porosity on top of a conventional impervious hot mix asphalt concrete (HMAC) or Portland cement concrete roadway surface. Conventional roadway surfaces typically have a porosity of less than 5%. During a rainfall event, the water enters the pore space of the surface course and is removed from the surface. Water then flows laterally along the underlying impervious asphalt layer to the roadway shoulder. The water resurfaces at the shoulder where it flows into a ditch or drainage swale running parallel to the road. Figure 3-1 shows a schematic view of a typical porous surface course overlay.

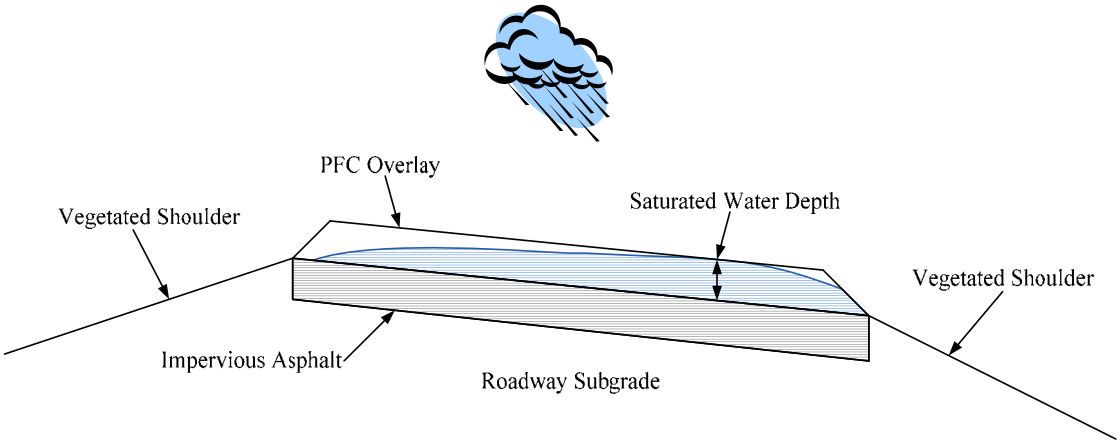

Figure 3-1: Porous surface course overlay schematic

In order to take full advantage of the benefits of PFC, we must gain a better understanding of the hydraulic characteristics of the porous asphalt. A review of previous research conducted on PFC documented in the literature is provided in Section 3.2. The hydraulic characteristics of PFC are influenced by its porosity and hydraulic conductivity. It is expected that these two hydraulic characteristics are positively correlated. These parameters are, in general, not constant in space or time. The porosity and hydraulic conductivity of a PFC layer can change along the length and width of the roadway, but in general, we will assume homogeneous characteristics of these parameters. Furthermore, over time the pore space in the PFC can become clogged with sediment resulting in a decrease in porosity, and ultimately an expected decrease in hydraulic conductivity. Therefore, these parameters are not constant in time. Accurate measurement of these hydraulic characteristics is necessary to ensure adequate drainage of surface runoff and maintain the benefits of PFC. Related research is currently being conducted on the water quality improvements from a section of PFC compared to conventional HMAC. The smaller concentration in suspended solids observed in runoff from the PFC surface when compared to a conventional HMAC surface suggest that sediment is trapped in the pore space of the PFC over time. This is expected to result in a decrease in hydraulic conductivity and porosity over time. Being able to measure the in-situ hydraulic conductivity of a PFC layer at any given time is necessary to determine whether too much clogging has occurred and if the drainage benefits will persist for the next rainfall event. Creating a well defined methodology for the accurate measurement of the hydraulic characteristics of PFC both in the laboratory and in the field is one objective of the TxDOT research study that will be addressed in this chapter. A second objective is the development of a numerical model to predict flow within PFC. The majority of this objective is addressed in the work of Eck (2010). However, the present work will address numerical modeling of the nonlinear flow characteristics that have been observed to occur during hydraulic conductivity testing.

3.1.2 Research Objectives

This research study defines a methodology for measuring the hydraulic conductivity and porosity of a PFC overlay. PFC core specimens can be extracted from the roadway surface and analyzed in the laboratory to determine hydraulic conductivity and porosity. In addition, a field test can be used to determine the in-situ hydraulic conductivity of the PFC overlay. Hydraulic data collected over the past four years is analyzed to determine the changes in porosity and

hydraulic conductivity at three different roadways around Austin, Texas (TX). Obtaining accurate measurements of the hydraulic characteristics and analyzing the change in these characteristics over time gives necessary information as to how the water quality and driver safety benefits of PFC will persist through time, and when maintenance or replacement of the PFC layer is needed. In addition, numerical modeling of the nonlinear flow regime observed in PFC during testing provides a better understanding of how these effects impact the flow of water through PFC. The objectives of this research can be divided into four major categories: evaluate hydraulic properties of PFC in the laboratory, evaluate hydraulic conductivity of PFC in the field, develop a numerical model of the nonlinear head distribution through a PFC core specimen, and analyze the change in hydraulic properties of PFC over time and at different locations.

3.1.2.1 Evaluate Hydraulic Properties in the Laboratory

The first objective, addressed in Section 3.3, is to evaluate both the hydraulic conductivity and porosity of PFC core specimens. This is accomplished through laboratory testing on the PFC core specimens using a series of constant head tests to determine the hydraulic conductivity, and a submerged unit weight method to determine the porosity. PFC core specimens were extracted from three roadways near Austin, TX (Loop 360, FM 1431, and RR 620) over the past four years (March 2007, February 2008, February 2009, and February 2010). Core specimens were not collected at FM 1431 in 2010 due to recent realignment of the roadway and abandonment of the previous coring location. A methodology for determination of the hydraulic conductivity for two-dimensional flow is described, and data collected from each core specimen is reported. Understanding of the hydraulic properties in a controlled laboratory setting is useful with respect to modeling of flow through the PFC layer for design purposes, such as the required thickness of PFC necessary to avoid surface runoff.

3.1.2.2 Evaluate Hydraulic Conductivity in the Field

Determination of hydraulic conductivity in the lab can be time consuming and may disturb the core specimen during the extraction process. Therefore, a quick, accurate field method for determination of hydraulic conductivity is necessary. This field test must be non-destructive so that the hydraulic properties of the PFC can be easily measured throughout the life cycle of the overlay. The field test will provide information on the extent of clogging that has occurred, as well as whether or not the benefits of PFC are likely to persist in the near future. Current field testing conducted by TxDOT is not sufficient to determine the hydraulic conductivity of the PFC overlay as mentioned in Section 2.3.2 and described in detail in Section 4.1. The second objective, addressed in Section 3.4, describes the test methodology and a new test apparatus developed at CRWR for determination of in-situ hydraulic conductivity using a falling head test. This allows for quick measurement of hydraulic conductivity using the principles established during lab testing for nonlinear flow. This information will help to determine the rate at which clogging occurs since the test can easily be conducted in the field at regular intervals.

3.1.2.3 Numerical Modeling of Hydraulic Characteristics

The third objective of this research, addressed in Section 3.5, is to develop a finite difference numerical model to analyze the nonlinear flow characteristics through PFC. During both lab and field testing, a nonlinear flow relationship exists between the flow rate and change in head for two-dimensional flow conditions. Therefore, the typical linear Darcy flow that occurs

in most porous media is not sufficient to describe flow through PFC under testing conditions. This objective will determine the difference between the typical linear approximations to flow in porous media compared to the nonlinear flow observed in PFC cores. This is of particular interest due to the two-dimensional flow in PFC that has not been analyzed in detail in the past. The initial concern with nonlinear flow is to model the flow conditions that occur during the laboratory core tests used to determine hydraulic conductivity. The results of the numerical model will relate the measureable flow characteristics in the lab and field to the theoretical flow characteristics, which cannot be directly measured in two-dimensional flow, thereby determining a true hydraulic conductivity.

3.1.2.4 Analyze Hydraulic Properties based on Location and Time

Over time the hydraulic conductivity and porosity are expected to decrease due to the entrapment of sediment in the PFC pore space. The final objective, addressed in Section 3.6, will analyze the laboratory results and determine any statistical differences in the hydraulic properties of the PFC core specimens over time and from each roadway location. This information, together with water quality data collected at a PFC site, will help to determine when water quality benefits are no longer persistent based on changes in hydraulic conductivity. The experimentally obtained coefficients used to describe the nonlinear flow through PFC will be compared to empirical equations presented in the literature. This will help determine which previous work, if any, applies to flow through PFC. Finally, analysis of the amount of trapped sediment in a PFC core specimen will help to determine if the improved water quality benefits are a result of filtering of the stormwater runoff or simply a decrease in source pollutants from the surface of vehicles due to decreased splash/spray.

3.1.3 Chapter Organization

This section describes the details of various testing protocols together with the data collected to date. The details of the numerical modeling techniques are presented as well. Section 3.2 provides a review of related literature pertaining to previous research conducted on PFC, and a summary of flow equations through porous media describing both the linear and nonlinear flow relationships. Section 3.3 provides the details of the laboratory testing conducted on PFC core specimens both for porosity and hydraulic conductivity measurements. Section 3.4 provides the details of the field testing conducted on the PFC overlay for measurement of in-situ hydraulic conductivity. Section 3.5 provides the details of the numerical modeling of nonlinear flow through porous media and describes the relationships between the measureable and theoretical coefficients needed to characterize the nonlinear flow properties. Section 3.6 presents statistical analysis of the porosity and hydraulic conductivity data to determine any changes in hydraulic properties based on time and location. In addition, the hydraulic characteristics are compared to empirical equations in the literature. Finally, an estimate for the volume of sediment removed from the stormwater runoff and trapped within the PFC overlay is presented. Section 3.7 provides a summary of the research study and conclusions to each of the research objectives.

3.2 Literature Review

A review of previous literature conducted on applicable porous media flow is summarized here. This will cover the typical linear Darcy flow through porous media at low velocity. Next, nonlinear flow at higher velocities is reviewed together with different models with which to characterize nonlinear flow. This includes theoretical development of nonlinear

flow, estimation of nonlinear model coefficients, and experimental results for parallel and converging boundaries. Literature pertaining specifically to PFC is also reviewed. This includes the solution of steady state flow equations that model PFC flow as an unconfined aquifer, previous research results on methods for determination of hydraulic conductivity in porous asphalt, and additional literature pertaining to the water quality benefits of PFC. Finally, a short review of other issues addressed in this research is provided as well as how this research will expand the current literature.

3.2.1 Linear Flow through Porous Media

Flow through porous media is typically characterized by the linear Darcy's law (Darcy, 1856). This is a well known law used in the field of groundwater, hydrogeology, engineering, and other fields of hydraulics. Virtually any textbook on these subjects will discuss Darcy's law (see for example Bear, 1972; Muskat, 1982; Fetter, 1994; and Charbeneau, 2000; among others). Darcy's law defines a linear relationship between flow rate and hydraulic gradient as given in Equation (3.1).

$$Q = -KIA \tag{3.1}$$

In Equation (3.1), Q is the volumetric flow rate with units [L^3/T], K is the hydraulic conductivity [L/T], I is the hydraulic gradient [L/L], and A is the cross-sectional area of flow [L^2], where [L] represents units of length and [T] represents time. The negative sign is necessary because water flows from high hydraulic head to low hydraulic head, which is in the negative direction of the hydraulic gradient. The hydraulic conductivity is a measure of the ease with which a fluid flows through the porous medium.

Darcy's law is applicable to flow through most natural porous media systems. However, in general, it is only applicable for laminar flow and/or low velocity flow. The velocity can be found by first looking at the specific discharge, q:

$$q = \frac{Q}{A} = -KI \tag{3.2}$$

In Equation (3.2), q is the specific discharge or Darcy velocity [L/T], which is simply the volumetric flow rate per unit area. The actual fluid velocity through the porous media is greater than the specific discharge. This is due to the fact that the entire area is not available for flow due to the presence of solid material. Therefore, the average fluid velocity can be approximated using the effective porosity, n_e, of the porous media:

$$v = \frac{q}{n_e} \tag{3.3}$$

In Equation (3.3), v is the average fluid velocity [L/T] and n_e is the effective porosity of the porous media. The value of n_e is always less than unity, and for typical PFC overlays the effective porosity is approximately 0.2 or 20%.

The hydraulic gradient, I, is the change in hydraulic head with respect to each direction. Therefore, Darcy's law is actually a vector equation for multiple directions of flow. The

hydraulic head is related to the elevation head, pressure head, and velocity head of the fluid. In most cases, the velocity head is relatively small and assumed to be equal to zero:

$$h = z + \frac{p}{\rho g} \tag{3.4}$$

Equation (3.4) defines the hydraulic head h [L] as the summation of the elevation head z [L] and pressure head, where p is the fluid pressure [M/L/T^2], ρ is the fluid density [M/L^3], g is the gravitational acceleration constant [L/T^2], where [M] represents units of mass. The hydraulic gradient is equal to the spatial change in hydraulic head. In Cartesian coordinates this is represented as:

$$I_x = \frac{\partial h}{\partial x},\ I_y = \frac{\partial h}{\partial y}, \text{ and } I_z = \frac{\partial h}{\partial z} \tag{3.5}$$

Equation (3.5) gives the hydraulic gradient in the x-, y-, and z-directions. Similarly, the hydraulic gradient can be given in two-dimensional cylindrical coordinates as:

$$I_r = \frac{\partial h}{\partial r} \text{ and } I_z = \frac{\partial h}{\partial z} \tag{3.6}$$

Where r is the radial direction and z is the vertical direction. The third dimension in cylindrical coordinates is the θ-direction. However, for the purposes of this research study, there is no flow in the θ-direction.

The hydraulic conductivity K represents the ease with which water flows through the porous media and depends on both the fluid properties and porous media properties. The intrinsic permeability, given the symbol k, depends solely on the porous media properties and is related to the hydraulic conductivity as follows:

$$K = \frac{\rho g}{\mu} k \tag{3.7}$$

In Equation (3.7), μ is the fluid dynamic (absolute) viscosity [M/L/T] and k is the intrinsic permeability of the porous medium [L^2]. If k is known for a given porous medium, then the hydraulic conductivity can be calculated for any fluid properties. However, for this research study, we are only concerned with water as the fluid, so use of the intrinsic permeability is not necessary during testing. The intrinsic permeability can be estimated based on properties of the porous media such as porosity or grain size through various empirical equations. The following equation for k is calculated for the mean grain diameter d_{50} (Charbeneau, 2000):

$$k = \frac{{d_{50}}^2}{360} \tag{3.8}$$

In general, k can be represented by some appropriate length squared, divided by an empirically determined constant (Bear, 1972).

Since Darcy's law is actually a vector equation, the hydraulic conductivity is a tensor quantity for each direction. Therefore, in an anisotropic case, K will have a different value for each direction. However, for the purposes of this research, it is assumed that the hydraulic conductivity of PFC is isotropic, which results in K being a constant in space with only one value.

Finally, it should be noted that although the hydraulic conductivity is a constant when Darcy's law is applicable, the hydraulic conductivity represents the relationship between specific discharge and hydraulic gradient as the specific discharge approaches zero. This means that the hydraulic conductivity is the slope of the relationship between specific discharge and hydraulic gradient at zero. This is an important distinction necessary for nonlinear flow. We shall refer to the hydraulic conductivity as the specific discharge approaches zero as the "true hydraulic conductivity." In nonlinear flow, we can consider an "effective hydraulic conductivity," which is not a constant and changes as a function of the hydraulic gradient. This concept will be introduced in Section 3.5.

3.2.2 Nonlinear Flow through Porous Media

The phenomenon of a nonlinear flow regime has been observed in numerous porous media experiments in the past. A clear understanding as to the cause of deviation from the linear Darcy's law has not been fully achieved. The causes of nonlinear flow have been debated in the literature and will be discussed here briefly. However, before the causes of nonlinear flow are discussed, two models used to characterize the nonlinear flow relationship are described, in addition to the transition between linear and nonlinear flow.

3.2.2.1 Forchheimer Equation

One of the most common equations used to characterize nonlinear flow is the Forchheimer equation (c.f. Reynolds, 1900; Forchheimer, 1901; Bear, 1972; and Charbeneau, 2000). Numerous attempts have been made to derive the Forchheimer equation and a discussion of these efforts is provided in Section 2.2.5. The Forchheimer equation relates the hydraulic gradient as a nonlinear function of specific discharge:

$$I = aq + bq^2 \tag{3.9}$$

In Equation (3.9), I is the hydraulic gradient and q is the specific discharge as defined above; the negative sign has been omitted for simplicity, but it is understood that the direction of flow is opposite the direction of increasing head. a [T/L] is the linear Forchheimer coefficient and b [T^2/L^2] is the nonlinear Forchheimer coefficient.

In the case of linear Darcy flow, $b = 0$ and $a = 1/K$. Therefore, at small specific discharge or low velocity, the q^2 term will be negligible and Darcy's law will be a good approximation to the Forchheimer equation. In this case, the hydraulic conductivity is equal to $1/a$, which is the slope of the nonlinear relationship as the specific discharge approaches zero. This agrees with our definition of "true hydraulic conductivity" given in Section 2.1. Interestingly, in the original writings of Darcy (1856), previous work cited by de Prony uses a very similar form of the Forchheimer equation to describe pipe flow. Although this equation was not applied to nonlinear flow in porous media, it is important to note its use prior to its application in porous media flow by Forchheimer.

The Forchheimer equation can also be represented in the following transformed form:

$$I = \frac{q}{K}\left(1 + \frac{q}{n}\right) \tag{3.10}$$

Equation (3.10) gives the Forchheimer equation as a function of the hydraulic conductivity K and transformed nonlinear Forchheimer coefficient n [L/T], where n is related to the previously described Forchheimer coefficients using the following relation:

$$n = \frac{a}{b} \tag{3.11}$$

This form of the Forchheimer equation is useful because if the value of n is known, then the ratio q/n can be compared to a value of one to determine if the nonlinear effects are significant for a given specific discharge.

In most cases in the literature, the Forchheimer equation is applied only to one-dimensional flow. However, in general it is applicable in multiple dimensions as a vector equation. The quadratic term creates some difficulty in representing the Forchheimer equation as a vector equation. Therefore, many researchers (Giorgi, 1997; Ewing et al., 1999; Moutsopoulos and Tsihrintzis, 2005; among others) have proposed the following representation of the vector Forchheimer equation in Cartesian coordinates:

$$\vec{I} = a\vec{q} + b|q|\vec{q} \tag{3.12}$$

In this case, the quadratic term is simply the magnitude of the specific discharge vector times the directional specific discharge vector. This allows both a and b to be tensor quantities for the anisotropic case. Wang et al. (1999) investigate numerical simulations of a model porous medium for the Forchheimer equation in three-dimensional Cartesian coordinates. They found that the tensor for both the linear and nonlinear coefficients can be represented as a diagonal matrix with two of the three values being the same magnitude. Therefore, they were only able to simulate two-dimensional anisotropic conditions. For the assumption of isotropic conditions, both a and b are constant scalars. In cylindrical coordinates, the vector Forchheimer equation is more complex and will be discussed in Section 3.5 as used for the purposes of this research study.

The Forchheimer equation can also be expressed based on a pressure gradient instead of a hydraulic gradient. The pressure is related to the hydraulic head by $p = \rho g h$. Taking the gradient of the pressure term and relating it to the Forchheimer equation gives the following one-dimensional Forchheimer equation based on pressure:

$$-\frac{dp}{dx} = \frac{\mu q}{k} + b^* \rho q^2 \tag{3.13}$$

In Equation (3.13), b^* has dimensions [1/L] and the Forchheimer coefficients can be related to the Forchheimer equation based on hydraulic gradient as follows:

$$a = \frac{\mu}{\rho g k} = \frac{1}{K} \text{ and } b = \frac{b^*}{g} \tag{3.14}$$

This form of the Forchheimer equation is useful when measuring the fluid pressure and also for determining the transition to nonlinear flow, as described in Section 2.2.3. The linear Forchheimer coefficient, *a*, depends on both the properties of the porous media as well as the properties of the fluid. As expected, this is similar to the properties known to influence the hydraulic conductivity. The nonlinear Forchheimer coefficient, *b*, depends only on the properties of the porous medium. It is related to the inertial forces that depend on the pore geometry of the porous medium.

3.2.2.2 Izbash Equation

The Izbash equation is another common equation used to describe the nonlinear flow relationship for high velocity (Izbash, 1931; Bordier and Zimmer, 2000). Also known as the power law, the Izbash equation is an empirical equation for which no formal derivation has been provided. The Izbash equation is as follows:

$$q = KI^m \tag{3.15}$$

In Equation (3.15), the specific discharge is represented as a power function of the hydraulic gradient with power *m*. For low velocity laminar flow, Darcy's law applies and *m* = 1.0. For fully turbulent flow *m* = 0.5. In most nonlinear flow cases, *m* has a value between 1.0 and 0.5. Clearly, if the Izbash equation is solved for the hydraulic gradient in the turbulent flow case, the hydraulic gradient is related to the specific discharge squared, as in the Forchheimer equation. Use of the Izbash equation is not directly considered in this research study. However, several previous research studies use this equation instead of the Forchheimer equation.

Although the Izbash equation can be shown to fit experimental data for nonlinear flow quite well, there is no theoretical derivation of the Izbash equation from first principles (i.e. conservation of mass and momentum). Therefore, the use of the Izbash equation is not an ideal situation. Furthermore, the Izbash equation assumes nonlinear flow for all values of specific discharge. As the specific discharge approaches zero, the Forchheimer equation approaches the linear Darcy's law relationship better than the Izbash equation. For these reasons, the Forchheimer equation is used in this research study.

3.2.2.3 Transition to Nonlinear Flow

The nonlinear flow relationship occurs for high velocity flows, but the transition to this nonlinear flow relationship is not well defined. Nonlinear flow occurs as a result of increased inertial forces, which are negligible for linear laminar flow conditions. Laminar flow may exist in many of the flow conduits of the porous media even if the overall flow is nonlinear. Therefore, nonlinear flow is not necessarily a result of fluid turbulence in the porous media but simply an increase in inertial effects that can no longer be neglected. Many researchers have attempted to provide a guideline as to when the onset of nonlinear flow occurs based on characteristics of the flow. The most common transition point is based on the value of the Reynolds number.

$$\mathrm{Re} = \frac{\rho q d}{\mu} \tag{3.16}$$

Equation (3.16) defines the Reynolds number Re as a function of the specific discharge, the fluid properties, and a characteristic length dimension, *d*. The Reynolds number is a nondimensional number that relates the ratio of microscopic inertial forces to viscous forces. In pipe flow, the Reynolds number can be used to determine the transition between laminar and turbulent flow based on the pipe diameter. However, in porous media flow, there is no uniform length dimension for which to characterize the flow due to the multiple flow paths, particle size distribution, etc. associated with the porous medium.

A common choice for the length dimension is to use some representative grain diameter size. The diameter of the grains in porous media is related to the size of the flow channels between the grains. Therefore, the mean grain diameter, d_{50}, is expected to represent the average flow channel diameter and will be used in this research study. In addition, a smaller grain size, d_{10}, is sometimes used and represents the smallest 10% of particle diameters. The reasoning behind this choice is that the smallest flow channels will govern the flow through the porous media. This suggests that the smallest flow channels will be the ones that restrict the overall flow through the media. Collins (1961) suggests the use of $d = (k/n_e)^{1/2}$, where k is the intrinsic permeability [L^2] and n_e is the porosity. Ward (1964) suggests the use of $d = k^{1/2}$. Therefore, there are many possibilities for the length dimension to be used in determining the Reynolds number. The most common length dimension is to use d_{50} due to the ease with which it can be determined.

It is expected that in coarse grained media, linear flow conditions will exist for a Reynolds number less than some value between 1 and 10, when the Reynolds number is calculated based on the mean grain diameter, d_{50} (Bear, 1972). Laminar flow typically still exists until Re = 100 or larger, but a nonlinear flow relationship occurs prior to the onset of turbulence. This nonlinear relationship results either due to the flow properties or the material properties. The flow properties that produce nonlinear flow are a large specific discharge or hydraulic gradient. The material properties that create nonlinear flow are a large porosity or hydraulic conductivity (Sen, 1990). More specifically, the nonlinear relationship arises due to either large microscopic inertial forces or microscopic interfacial drag (viscous) forces (Hassanizadeh and Gray, 1987).

The use of the Reynolds number as an indicator for the presence of inertial effects, which result in nonlinear flow, has been debated in the literature. The reasoning behind this debate is that the Reynolds number represents microscopic flow conditions. It can be shown that even when microscopic inertial effects are significant, the macroscopic flow can remain linear, as in Darcy's law, for certain flow conditions. Therefore, Ruth and Ma (1992) suggest the use of a specific Reynolds number that they call the Forchheimer number. The length dimension in the Forchheimer number is equal to $b^* k_0$.

$$Fo = \frac{\rho q b^* k_0}{\mu} \tag{3.17}$$

In Equation (3.17), *Fo* is the Forchheimer number that is essentially a specific value of the Reynolds number. k_0 is the intrinsic permeability [L^2] as the specific discharge approaches zero. Ruth and Ma (1992) suggest that the intrinsic permeability is velocity dependant and the

Forchheimer number can be used to determine if the nonlinear effects are negligible. When the Forchheimer number becomes experimentally significant with respect to a value of one, the nonlinear flow effects can no longer be ignored. The Forchheimer equation based on pressure as represented by Equation (3.13) can be written in terms of the Forchheimer number as:

$$-\frac{dp}{dx} = \frac{\mu}{k}(1 + Fo)q \tag{3.18}$$

From this representation of the Forchheimer equation, it can be seen that when the Forchheimer number becomes significant with respect to a value of one, nonlinear flow conditions will exist. Zeng and Grigg (2006) suggest a critical Forchheimer number for which the nonlinear effects become significant. They define the nonlinear effect, *E*, as the ratio of the pressure gradient consumed in overcoming liquid-solid interactions to the total pressure gradient as:

$$E = \frac{b^* \rho q^2}{-dp/dx} = \frac{Fo}{1 + Fo} \tag{3.19}$$

Equation (3.19) relates the Forchheimer number to the nonlinear effects, *E*. *E* can be associated with the error of ignoring the nonlinear effects. Therefore, Zeng and Grigg (2006) show that if ten percent error is an acceptable limit of the nonlinear effects, the corresponding critical Forchheimer number would be *Fo* = 0.11. The use of the Forchheimer number, as opposed to the typical Reynolds number, provides a better estimate of when nonlinear effects become significant but requires knowledge of the material properties of the porous media.

3.2.2.4 Estimation of Forchheimer Coefficients

Many researchers have attempted to estimate the two Forchheimer coefficients from either a theoretical standpoint or a purely empirical development from experimental data. Sidiropoulou et al. (2007) provide a review of multiple empirical equations in the literature for estimating the Forchheimer coefficients, *a* and *b*. In addition, Li and Engler (2001) provide a literature review of empirical correlations for estimating the nonlinear Forchheimer coefficient only. A complete summary of all the equations will not be provided here. In Section 6.5 the numerical results obtained from this study will be compared with several empirical equations for estimating the Forchheimer coefficients. At this point, the empirical equations will be presented and briefly discussed. The typical factors used in many of these empirical equations are the fluid properties, porosity of the porous medium, and particle diameter of the porous medium. The majority of these empirical equations are based on laboratory experiments. Kelkar (2000) estimates the nonlinear coefficient for observations in the field and determined that the nonlinear coefficient is significantly greater when measured in the field compared to lab measurements. This claim is based on gas flow to a well and does not agree with the experimental data obtained in this research study and presented in Section 5.5.

There are several important empirical equations that will be discussed here due to their common reference in the literature. Ergun (1952) was among the first researchers to thoroughly investigate nonlinear flow effects through porous media. He claims the linear term of the Forchheimer equation represents viscous energy losses and the nonlinear term represents kinetic

energy losses. Ergun expanded on the Kozeny-Carman equation and developed the following equations for the two Forchheimer coefficients:

$$a = \frac{150\mu(1-n_e)^2}{\rho g n_e^{\ 3} D_p^{\ 2}} \tag{3.20}$$

$$b = \frac{1.75(1-n_e)}{g n_e^{\ 3} D_p} \tag{3.21}$$

where D_p is the diameter of the particles that make up the porous media. From these relationships, Ergun also derived two friction factors representing the relative viscous energy losses and kinetic energy losses, with respect to the total pressure drop for the flow, as a function of Reynolds number.

Ward (1964) conducted a dimensional analysis for nonlinear flow and determined the following empirical Forchheimer coefficients:

$$a = \frac{360\mu}{\rho g D_p^{\ 2}} \tag{3.22}$$

$$b = \frac{10.44}{g D_p} \tag{3.23}$$

Ward uses the square root of intrinsic permeability as a length scale, where the intrinsic permeability is given in Equation (3.8). This length scale is used to define the Reynolds number:

$$\mathrm{Re}_k = \frac{\rho q \sqrt{k}}{\mu} \tag{3.24}$$

The symbol Re_k in Equation (3.24) means the Reynolds number is determined from the intrinsic permeability. Similar to Ergun, Ward determined a dimensionless friction factor as a function of Reynolds number for the porous media. The general friction factor is given as:

$$f_k = \frac{1}{\mathrm{Re}_k} + c_w \tag{3.25}$$

In Equation (3.25), f_k is the friction factor, and c_w is a constant that is a function of the porous media. For the porous media Ward conducted experiments on, he found $c_w = 0.550$. Ward also showed that at low values of Re_k where Darcy's law applies, $c_w = 0.0$ resulting in a linear relationship between f_k and Re_k on a log-log plot. As Re_k increases at the onset of nonlinear flow, a transition occurs and the full Equation (3.25) applies. Finally, at large Re_k, the friction factor is a constant equal to c_w. This type of graph is similar to the common Moody diagram for friction losses in pipe flow. Many subsequent research studies have referenced the work of Ergun and Ward and expanded on these models.

3.2.2.5 Causes of Nonlinear Flow

Darcy's law describes the specific discharge as a linear function of the hydraulic gradient given in Equation (3.2). This equation is only applicable for laminar flow at low velocities. Initially, it was thought that the onset of turbulent flow within the flow channels of a porous medium caused a deviation from Darcy's law. However, Hassanizadeh and Gray (1987) point out that deviations from Darcy's law are not caused by turbulence, as experimental data have shown nonlinear flow to occur for a Reynolds number near 10. Turbulence does not occur until the Reynolds number approaches a value of 300, suggesting that turbulence does not exist at the onset of nonlinear flow. Ergun (1952) states that pressure losses (or hydraulic head losses) are caused by kinetic energy losses and viscous energy losses. In linear flow, the kinetic energy losses are negligible and Darcy's law is applicable for low velocity where laminar flow typically occurs. Ward (1964) pointed out that there is no sharp division between laminar, transition, and turbulent flows in porous media due to the varying sizes of the flow channels. If turbulent flow occurs in some parts of the media, laminar flow may still exist in other parts of the porous media. In general, deviations from Darcy's law are typically attributed to increased microscopic inertial forces.

When investigating the causes of nonlinear flow, it is important to differentiate between the microscopic flow conditions and the macroscopic flow conditions. This distinction has been the focus of many developments in the literature that have attempted to derive the Forchheimer equation starting from the Navier-Stokes equations for conservation of momentum. Irmay (1958) was among the first to attempt a derivation of the Forchheimer equation from the Navier-Stokes equations for a model of spheres representing a homogeneous isotropic porous medium. Hassanizadeh and Gray (1987) suggest there are three possible mechanisms that cause nonlinear flow: turbulence, microscopic inertial forces, and increased microscopic drag or viscous forces. As previously mentioned, they rule out turbulence based on the value of the Reynolds number. By using an averaging technique on the Navier-Stokes equations, they conclude that the growth of microscopic viscous forces, or drag forces, on the pore walls at high velocity give rise to the nonlinear effects observed at the macroscopic scale. Ruth and Ma (1992) investigate the momentum equation at the microscopic scale and use an averaging theorem to obtain a macroscopic equation. They suggest that "as the Reynolds number is increased, inertial effects lead to secondary flow patterns" that cause circulation as the fluid flows past a particle. This secondary flow pattern is then dissipated due to viscosity. Ruth and Ma (1992) suggest that this viscous dissipation leads to a nonlinear increase in the pressure drop observed on the macroscopic scale and is a function of the Reynolds number. Ma and Ruth (1993) expand on the previous work and show that the microscopic inertial forces lead to a distorted velocity and pressure field, which results in the onset of nonlinear flow effects. They go on to suggest that at high Reynolds number, both the inertial forces and viscous forces contribute equally to balancing the pressure gradient of the fluid.

Various other methods at deriving the Forchheimer equation have been attempted aside from averaging the Navier-Stokes equations. Giorgi (1997) attempts to derive the Forchheimer equation using the method of matched asymptotic expansions. The Forchheimer equation is constructed by using a permeability tensor, which is a function of the fluid velocity and retaining the first two terms of the expansion, thereby deriving the quadratic term in the Forchheimer equation. Thauvin and Mohanty (1998) created a numerical model of a porous media network that allowed them to change various properties of the media such as porosity, tortuosity, pore size, pore throat radius, etc. and determine how those changes impact the Forchheimer

coefficients. They then used regression to develop empirical equations useful for predicting the Forchheimer coefficients and compared those values with other equations in the literature. One finding of Thauvin and Mohanty (1998) relevant to PFC is the relationships they found for a decrease in pore size. As PFC becomes clogged with sediment it is expected that the pore size is decreasing. Thauvin and Mohanty (1998) showed that a decrease in pore size results in a decrease in porosity and permeability, and an increase in the nonlinear Forchheimer coefficient. Chen et al. (2001) use a homogenization method to derive the Forchheimer equation. In summary, the Forchheimer equation has been derived using various approaches, methods, and taking advantage of a range of approximations. There still appears to be a debate as to the actual causes of the deviation from Darcy's law, but it is generally believed that increased inertial forces result in nonlinear flow. Finally, in general, there is very little literature available that derives the Izbash equation for modeling nonlinear flow from a theoretical standpoint. Therefore, the Forchheimer equation is preferred over the Izbash equation as a better representation of nonlinear flow.

3.2.2.6 Nonlinear Flow Solution in a Confined Aquifer

For this research study, many of the flow equations are presented in cylindrical coordinates to match the experimental laboratory setup. The majority of the literature describing nonlinear flow in a radial direction is related to groundwater wells in confined aquifers. Bear (1979) gives a steady state solution for Forchheimer flow in a confined aquifer around a discharge well. The solution gives the head profile at any radial distance r from the well. The radius of the well is R_w and the thickness of the aquifer is a constant t_a:

$$h(R_w) - h(r) = a\frac{Q}{2\pi t_a}\ln\left(\frac{r}{R_w}\right) + b\left(\frac{Q}{2\pi t_a}\right)^2\left(\frac{1}{R_w} - \frac{1}{r}\right) \qquad (3.26)$$

Therefore, the purely radial condition of Forchheimer flow in a confined aquifer has been solved, but no literature is available on a combination of radial and vertical Forchheimer flow or for an unconfined aquifer.

The previous derivation of the radial Forchheimer flow assumes steady state conditions. This assumption is not always applicable, resulting in the need for a transient solution. A transient solution has been developed for Darcy radial flow in a confined aquifer as described by the Theis equation (Theis, 1935). This equation relates the drawdown (change in head) to the Theis well function, which is a function of time. The Theis equation describes the development of the drawdown cone that results due to pumping as a function of time and radial distance for a linear flow relationship.

For nonlinear flow, an exact analytic solution for transient Forchheimer flow does not currently exist. However, some approximate transient solutions have been attempted by Sen (1988), Wu (2002), and Mathias et al. (2008) for radial Forchheimer flow to a well in a confined aquifer. Sen (1988) developed a transient solution similar to the Theis equation for linear flow applied to a well with a zero radius. A similarity solution was found through the use of the Boltzmann transformation, which results in a Bernoulli differential equation. However, it should be noted that Camacho-V. and Vasquez-C. (1992) suggest this transformation only applies to the linear flow case and is not valid for the nonlinear flow case. Sen (1992) replied to this comment and suggests that the transformation is valid but depends on the nonlinear Forchheimer coefficient. In either case, the solution by Sen (1988) consists of a modified well function that

changes with time and with the nonlinear Forchheimer coefficient, *b*. For $b = 0$, the modified well function becomes the Theis well function for linear Darcy flow. It was shown that the drawdown for nonlinear flow increases more rapidly during a certain time interval when compared to the linear flow drawdown. When compared to the linear flow case, near the well location, the drawdown is always smaller for nonlinear flow, but farther away from the well, the drawdown is greater for nonlinear flow (Sen, 1987). Sen (1990) expanded on this original model and applied it to a well with a finite radius.

Wu (2002) uses the Warren-Root model, which treats fracture and matrix flow interactions using a double-porosity concept. Mathias et al. (2008) present a set of approximate solutions that include a large time approximation derived from matched asymptotic expansions, a Laplace transform approximation for significant well-bore storage in turbulent flow, and a simple heuristic function for when the flow is very turbulent and the well radius is infinitesimally small. These approximations are then compared to equivalent finite difference solutions. The developments are useful in comparing the nonlinear transient flow conditions to the linear transient flow conditions. However, they only exist for the radial flow conditions observed in a confined aquifer.

3.2.2.7 Nonlinear Flow Investigation of Converging Boundaries

The experimental laboratory test setup used in this research study involves two-dimensional radial flow. Therefore, the flow paths will be diverging as flow exits the core specimen in the radial direction. Although there is no literature on two-dimensional diverging flows experiencing nonlinear flow conditions, there have been experimental tests in the past for flows with converging boundary conditions. Thiruvengadam and Pradip Kumar (1997) conducted experimental tests on a coarse grain porous media in a test setup with converging boundaries. They determined an exponential expression for the hydraulic gradient under radial flow conditions. The experimental tests, when corrected for porosity and wall effects, matched the theoretical equation for the hydraulic gradient suggesting that the flow can be modeled as radial flow. Venkataraman and Rama Mohan Rao (2000) expanded on the work by Thiruvengadam and Pradip Kumar (1997), and compared nonlinear flow in parallel boundaries to flow in converging boundaries. They mention that in the case of parallel flow, the hydraulic gradient is the same in the direction of flow. However, for converging boundaries, the cross-sectional area decreases in the direction of flow, resulting in a change in velocity, and a subsequent change in hydraulic gradient with the flow. It is typically assumed that the linear Forchheimer coefficient, *a*, is constant for both parallel boundaries and converging boundaries. However, it is possible that the nonlinear Forchheimer coefficient, *b*, changes for flows with converging boundaries. Therefore, Venkataraman and Rama Mohan Rao (2000) conducted experimental tests with porous media flow in converging boundaries using the empirical equations developed by Ward (1964) to determine the Forchheimer coefficients. They derived an altered Forchheimer equation for converging boundaries and determined two convergence factors that are useful for converting *a* and *b* for converging flow to the corresponding *a* and *b* for parallel flow. They determined that both the linear and nonlinear Forchheimer coefficients are, in fact, constants for converging flow when the convergence factor is used. Furthermore, they developed a graph of friction factor (determined empirically from Ward, 1964) versus Reynolds number for the Forchheimer equation, which resembles the typical Moody diagram used for pipe flow (c.f. Hwang and Houghtalen, 1996). This graph uses Equations (3.24) and (3.25) determined by Ward (1964). Figure 3-1 shows the results of their experiments for various porous materials with converging boundaries once the Forchheimer coefficients were converted

back to those for parallel boundaries. Both Ergun (1952) and Ward (1964) developed a similar graph as shown in Figure 3-2 for a single porous media experiencing parallel flow.

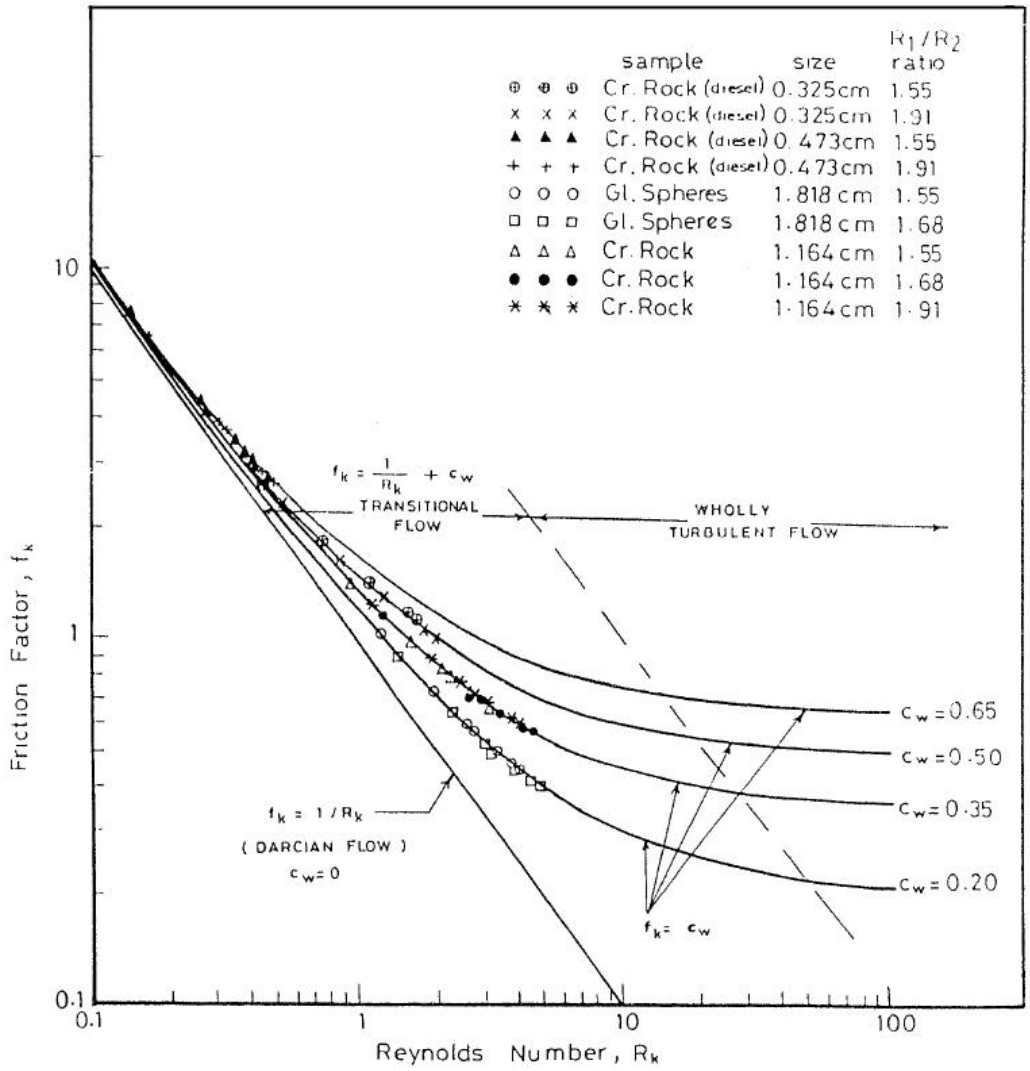

Figure 3-2: Relationship between friction factor and Reynolds number for nonlinear parallel flow

(Source: Venkataraman and Rama Mohan Rao, 2000)

A similar relationship for the friction factor versus Reynolds number was previously presented by Venkataraman and Rama Mohan Rao (1998) for nonlinear flow conditions modeled with the Forchheimer equation. In this work, they analyzed experimental data presented in the literature for parallel flow and used the empirical relationships developed by Ward (1964). Reddy and Rama Mohan Rao (2006) continued the work on nonlinear flow with converging boundaries using a slightly different experimental setup. They suggest that the Forchheimer coefficients vary not only along the direction of flow, but also in the radial direction due to convergence. This contradicts the previous findings and Srivastava (2009) provides a discussion on this issue. Srivastava shows that the Forchheimer coefficients do not change because Reddy and Rama Mohan Rao (2006) are using an average hydraulic gradient. Furthermore, if the

Forchheimer coefficients do change with the flow, then it would be expected that the hydraulic conductivity of a homogeneous isotropic porous medium changes if the flow is converging or diverging. Therefore, it can be shown that the Forchheimer coefficients are constant for both parallel and converging/diverging flows. This is an important aspect of the current research study since we will be investigating a diverging flow condition.

Goggin et al. (1988) developed a minipermeameter that uses air flow to determine the permeability of rock materials. The device essentially measures the pressure change as gas leaves a standpipe sealed on the rock surface. Flow is assumed to be a combination of vertical and diverging radial flow, which is similar to the flow conditions used in this research, as described in Section 3.3 Three. However, the no flow boundary conditions in this research study are not present in the analysis of the minipermeameter. Goggin et al. claim to have solved the Forchheimer equation for this two-dimensional flow problem, but they provide no details of the methods with which the equation is solved. As will be shown in Section 3.5, the solution of the Forchheimer equation in two-dimensions can be problematic and requires special consideration to solve. The problem setup proposed by Goggin et al. (1988) appears to be the most similar solution to what is considered in this research study. However, as mentioned, no information is provided on how this solution was obtained.

3.2.3 Permeable Friction Course Review

Previous research in the literature has been specifically conducted on PFC. These studies describe the analytic solutions of water depth profiles within a PFC layer, methodology for measuring hydraulic conductivity, and water quality improvements. An overview of additional benefits of porous pavements is provided briefly in Section 3.1. These benefits include reduced splash/spray during rainfall events, improved traction, reduced chance of hydroplaning, improved stormwater runoff quality, and noise reduction. A recent report by the Transportation Research Board (TRB, 2009) provides an overview of construction and maintenance practices of PFC as well as the driver safety and environmental benefits of the use of PFC.

3.2.3.1 Water Depth Solutions

There have been several studies that have modeled flow through PFC under constant rainfall intensity in order to determine the water depth profile within the PFC. These studies have assumed linear flow utilizing Darcy's law and have only addressed one-dimensional flow at steady state. Essentially, the PFC layer can be modeled as an unconfined aquifer on a sloping impervious surface. It is assumed that there are small slopes in the water surface such that the Dupuit-Forchheimer assumptions apply. The Dupuit-Forchheimer assumptions state that the head in the unconfined aquifer is independent of the water depth such that only horizontal flow occurs. In addition, the assumption is made that the discharge is proportional to the slope of the water surface elevation (Charbeneau, 2000). The result of applying the Dupuit-Forchheimer assumptions is to convert the governing partial differential equation for flow to a first order nonlinear ordinary differential equation.

Jackson and Ragan (1974) were among the first to model flow through an entirely porous pavement. They developed numerical solutions to the Dupuit-Forchheimer assumptions that lead to the Boussinesq equation assuming Darcy flow conditions. The use of Darcy's law is only applicable when resistive forces dominate over inertial forces. Jackson and Ragan used an explicit central difference scheme (CDS) finite difference model to solve the Boussinesq equation for a pavement with zero slope in order to determine the effect of underdrain spacing on

discharge rates. Yates et al. (1985a) develop an analytic solution for flow down a sloping unconfined aquifer under constant rainfall intensity. The Dupuit-Forchheimer assumptions are applied resulting in a second order nonlinear differential equation. The authors investigate a solution to this equation for two possible cases of boundary conditions. The first case is for a known downstream head and flux boundary, and the second is both a known downstream and upstream head boundary. They also determine the location of a groundwater drainage divide if it exists. Yates et al. (1985b) adds to the previous work by using a finite difference scheme to solve the governing nonlinear differential equation and then making additional assumptions to linearize the governing equation and comparing the results. Loaiciga (2005) solves essentially the same problem as Yates et al. for flow down an unconfined sloping aquifer. However, after applying the Dupuit-Forchheimer assumptions, Loaiciga uses a transformed variable to linearize the equations.

Ranieri (2002) was the first researcher to model water depths specifically within PFC. He developed a runoff model to determine the required PFC thickness necessary to contain the entire runoff within the pore space based on the roadway geometry, rainfall intensity, and PFC hydraulic conductivity. Ranieri starts with the Boussinesq equation and investigates two forms of the solution that essentially correspond to subcritical and supercritical flow conditions, as defined based on the magnitude of the rainfall intensity, hydraulic conductivity, and roadways slope. The theoretical model is validated with a laboratory experiment that simulated rainfall on PFC and measured the water depth within the pore space. Ranieri recognized that the flow regime within the PFC layer is nonlinear, and therefore introduced a factor that is multiplied by the hydraulic conductivity to account for nonlinear flow. The introduction of the factor follows the Lindquist-Kovacs theory that defines multiple flow regimes between laminar and turbulent flow conditions (Kovacs, 1981). The original Lindquist-Kovacs theory multiples the hydraulic conductivity by a factor that is a function of the Reynolds number. The Reynolds number for flow within a PFC layer changes along the flow path due to the continuous addition of water from the rainfall. Therefore, instead of altering the factor along the length of the flow path, Ranieri suggests the use of an empirical factor that depends on the rainfall rate, roadway inclination, and hydraulic conductivity. Ranieri (2007) expands on the earlier work and provides some minor corrections to the original model. A correction is made for the case when the upstream boundary condition is not impervious. In addition, it was recognized that in certain cases there exists a drainage divide within the PFC layer. Finally, the model is solved with a fourth order Runge-Kutta method in order to investigate how changes in roadway slope, rainfall intensity, PFC depth, and other design parameters effect the maximum water depth within the PFC.

Tan et al. (2004) use a commercially available three-dimensional finite element model to determine the effects of various roadway geometries on the drainage performance of PFC for both saturated and unsaturated flow conditions. They consider an anisotropic porous medium and developed design curves to determine the necessary PFC thickness based on longitudinal slope, cross slope, rainfall intensity, and pavement width. Charbeneau and Barrett (2008) provide analytic solutions to the governing equations of flow through PFC. These solutions expand on the previous work by Yates et al. (1985) and Loaiciga (2005) by investigating three ranges of rainfall intensity and a variety of boundary conditions that influence the analytic solutions. In addition, Charbeneau and Barrett address the issue of saturated PFC flow with the addition of overland sheet flow, which is not addressed in the previous works, and suggest a method for

determining the spacing of underdrains. Figure 3-3 depicts a typical water depth profile within the PFC layer.

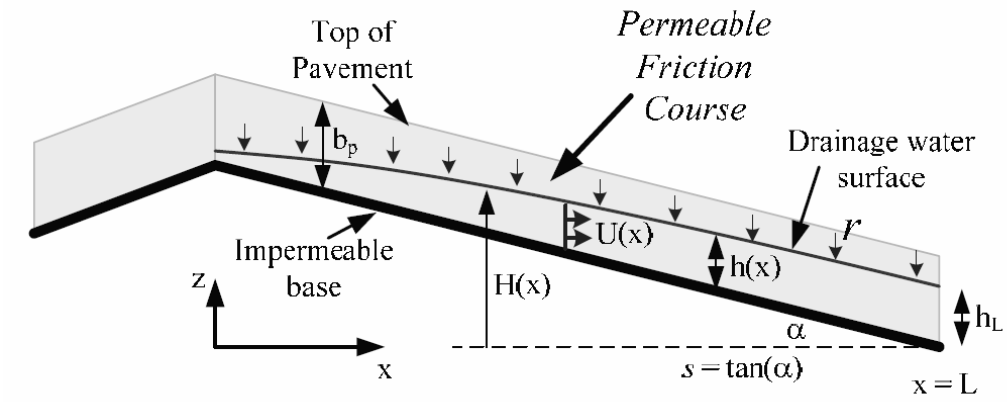

Figure 3-3: Water depth profile in PFC (source: Charbeneau and Barrett, 2008)

Eck et al. (in press) provide a correction to Charbeneau and Barrett (2008) by addressing the criteria for the onset of surface overland sheet flow. In summary, the majority of the work conducted on water depth solutions within PFC are typically for steady state, constant rainfall conditions, with a known hydraulic conductivity assuming Darcy's law applies. Therefore, since the hydraulic conductivity is one of the major influencing factors for these models, accurate measurement of the hydraulic conductivity is needed.

3.2.3.2 Hydraulic Conductivity Measurements

Previous studies have been conducted on methods to measure the hydraulic conductivity of porous asphalt mixes. Tan et al. (1997) describe a falling head test to measure the one-dimensional hydraulic conductivity under a nonlinear flow relationship. They use a pressure transducer to measure the water depth as it falls through a porous asphalt sample formed to fit the test apparatus. The nonlinear flow conditions are modeled from the Izbash equation and a one-dimensional hydraulic conductivity is measured. Fwa et al. (1998) investigate additional materials as well as measure both horizontal and vertical hydraulic conductivity. The resulting hydraulic conductivity in both directions are very similar, suggesting the media they tested is isotropic. Tan et al. (1999) develop an automatic field permeameter utilizing a falling head test to determine the three-dimensional hydraulic conductivity. The three-dimensional hydraulic conductivity is then converted to an effective isotropic hydraulic conductivity using a correction factor based on the wetted zone of the PFC during testing as determined from a commercially available finite element model. However, this finite element model does not account for surface runoff observed during field testing as a result of improper modeling of the underlying impervious boundary. One-dimensional laboratory tests were then conducted in order to determine the anisotropy of the porous asphalt by comparing to the effective isotropic hydraulic conductivity. The anisotropy ratio of horizontal to vertical hydraulic conductivity is reported to range from 1.1 to 2.5 for various porous asphalt mix designs. Fwa et al. (2001a) provide results for in-situ hydraulic conductivity using their automatic field permeameter and found a range in hydraulic conductivity from 0.5 centimeters per second (cm/s) to 4.5 cm/s (0.2 to 1.8 in/s). These studies all utilize the Izbash equation for nonlinear flow and do not directly measure the

hydraulic gradient for three-dimensional flow conditions. In order to solve this problem, they use a finite element model that does not accurately simulate the flow conditions observed due to the lack of surface runoff.

Clogging of the porous asphalt with sediment from stormwater runoff is expected to decrease the hydraulic conductivity over time. Therefore, Fwa et al. (1999) define a test methodology to compare the relative clogging potential of multiple porous media mix designs. Tan et al. (2000) improve on this test procedure and compare the clogging results to the theoretical Giroud model developed for sediment retention and clogging of geotextile fibers. The theoretical model defines the hydraulic conductivity as a function of the mass of sediment trapped for a given thickness of porous media. Tan et al. (2003) compare the experimentally determined decrease in hydraulic conductivity to the theoretical Kozeny-Carmen equation and introduce an empirical constant that can be used to characterize the clogging potential of the porous medium. In order to combine all the work on measurement of hydraulic conductivity and clogging potential of porous asphalt, Fwa et al. (2001b) present a rational method for designing a porous pavement drainage layer. Chai et al. (2004) incorporate this methodology and simulate flow conditions on a porous pavement for both short-term and long-term urban drainage control using a finite element model for both saturated and unsaturated porous media flow.

There are several documented testing devices used in the field to estimate the relative drainage capacity of a porous asphalt surface course. The method described by Tan et al. (2002) provides the best estimate of hydraulic conductivity. However, as previously mentioned, this method uses the Izbash equation and assumes a three-dimensional permeability based on a finite element method, which does not account for surface runoff. This device has a standpipe radius of 7.5 cm (3 in) centered on a base plate with a radius of 25 cm (9.8 in). In addition, several other devices are currently being used to estimate drainage capacity but do not give any indication of the actual hydraulic conductivity that is necessary for modeling flow through PFC. Isenring et al. (1990) describe a field test developed by the Institute for Transportation, Traffic, Highway and Railway Engineering (IVT) of the Switzerland Institute of Technology called the IVT permeameter. The IVT permeameter is essentially a vertical pipe which is placed on the porous asphalt surface and sealed with putty at the base. A falling head test is conducted and the drainage capacity is expressed as the time needed to drain 2.27 liters (L) of water through the PFC. A similar test procedure described in TxDOT (2004a) is used in the State of Texas. The drainage capacity is reported as the time to drain 5.1 L of water. Van Heystraeten and Moraux (1990) investigate porous asphalt in Belgium and show an outflow meter used to measure in-situ drainage capacity. Although they give little information on this device, it appears to work as a double-ring infiltrometer. Finally, in the State of California, drainage capacity is determined by creating a circular trough in the surface of the porous asphalt and expressing drainage capacity as the time needed for water to flow out of the trough (see Caltrans, 2004). Although there are a variety of testing procedures currently being used, none of these give an actual estimate of the hydraulic conductivity of the porous asphalt. These methods are best suited during construction when the porous asphalt is being compacted. After each pass of the compaction vehicle, the falling head test can be easily conducted. Once the drainage capacity reaches a specified level, compaction of the layer is complete and construction of the PFC layer is finished. Although useful during the construction process, these methods provide no useful information for modeling of flow through PFC for design or maintenance purposes.

3.2.4 Hydraulic Characteristics of Conventional Pavements

A quick review of literature on conventional impervious pavements is useful to get an idea of the relative magnitude of values for hydraulic characteristics of various pavements types. Masad et al. (1999) investigate methods for determining the porosity of conventional impervious asphalt mix designs. Multiple porosity measurement methods were used, including the specific gravity (submerged unit weight) method, optical image analysis method, and x-ray tomography analysis method. All three methods compared favorably. Porosity measurements on PFC core specimens reported in this section will use both the submerged unit weight method and image analysis method. Masad et al. (1999) report a range of porosity in conventional asphalt from 1.5% to 11% depending on the amount of compaction, with most samples having a porosity of less than 3%. Similarly, Krishnan and Rao (2001) report porosity values of 2-3% for conventional asphalts. Therefore, porosity values in PFC are significantly larger than for conventional asphalt.

Comparing values of hydraulic conductivity between conventional asphalt and PFC is also useful. The assumption is made that the underlying conventional pavement surface is impervious when modeling flow through PFC. Masad et al. (2004) report an average hydraulic conductivity of up to 5×10^{-3} cm/s (2×10^{-3} in/s). Tarefder et al. (2005) provide a range of hydraulic conductivity values for different conventional asphalt mix designs. Most values are on the order of 10^{-5} cm/s (4×10^{-6} in/s) Hassan et al. (2008) report hydraulic conductivity values for conventional hot mix asphalt on the order of 10^{-6} cm/s (4×10^{-7} in/s). Finally, Wiles and Sharp (2008) investigate what they call the secondary permeability of impervious cover. This refers to the hydraulic conductivity of cracks, fractures, and construction joints in conventional pavements. They report a range of hydraulic conductivity values from 10^{-3} cm/s to 10^{-6} cm/s (4×10^{-7} to 4×10^{-7} in/s). Therefore, the hydraulic conductivity of conventional pavements can range over several orders of magnitude. However, the hydraulic conductivity of PFC will be shown to be on the order of 1 cm/s (0.4 in/s) on average, with a minimum hydraulic conductivity of 0.02 cm/s (0.0079 in/s). Since the average value is multiple orders of magnitude greater than for conventional pavements, the assumption of a completely impervious underlying boundary is sufficient for the purposes of this research study.

3.2.5 Contribution of Research Study

The research study and results described in this section will help to expand the current understanding and measurement of the hydraulic properties of PFC. This will be accomplished by the development of both a laboratory and field hydraulic conductivity measurement tests. Current methods for measurement of PFC hydraulic conductivity are well defined only for one-dimensional flow. In order to measure the in-situ hydraulic conductivity, a two-dimensional flow test in cylindrical coordinates must be conducted due to the relatively small thickness of the PFC layer (roughly 50 mm). Previous work avoided this complication by attempting to numerically model the flow conditions. However, the results of this model do not accurately represent the flow conditions which occur during a field test.

The use of a two-dimensional measurement test creates additional complications in that the flow paths are diverging. Therefore, the hydraulic gradient and specific discharge of the flow cannot be directly measured for use in the Forchheimer equation. Previous work avoided this problem by calculating an average hydraulic gradient. This research study will instead apply a modified Forchheimer equation for the overall flow conditions in which the hydraulic gradient and specific discharge do not need to be measured. This model is described in Section 3.3.2. The

use of the modified Forchheimer equation allows for accurate measurement of the hydraulic characteristics describing the two-dimensional flow through PFC.

In order to properly relate the modified Forchheimer coefficients for the overall flow conditions to the true Forchheimer coefficients, the use of a numerical model is needed. This research study has developed a finite difference numerical model from which a relationship between the modified Forchheimer coefficients and true coefficients is simulated based on the geometry of the test setup. Using this information, we are able to determine the actual hydraulic conductivity of the PFC layer. Previous research has attempted to make approximations when calculating the hydraulic conductivity for two-dimensional flow.

Finally, four years worth of data for the hydraulic properties of PFC have been collected at three different roadways around Austin, TX. Statistical analyses of these data will determine whether the porosity and hydraulic conductivity have changed over time and between each roadway location. Comparison of these potential changes with stormwater quality monitoring data being collected at two of the roadway locations will help to determine when a reduction in hydraulic conductivity will adversely impact the water quality benefits of PFC. This will provide a guideline for when maintenance/cleaning of the PFC layer is required, or possibly when replacement of the PFC layer is needed. Currently, no scientific guidelines exist that demonstrate how to properly maintain a PFC layer.

3.3 Laboratory Experimentation

In order to properly measure the PFC hydraulic conductivity and gain a better understanding of the nonlinear flow properties of PFC, laboratory experimental tests must be conducted. This is accomplished through a series of constant head permeability tests. This section describes the extraction process of PFC core specimens which have been tested, and the laboratory methodology for determining core specimen porosity and Forchheimer coefficients.

3.3.1 PFC Core Specimen Extraction

3.3.1.1 Coring Process

Laboratory experiments to determine porosity and hydraulic conductivity were conducted on PFC core specimens taken from three roadways around Austin, TX. PFC core specimens can be extracted by saw-cutting the road surface. A typical core specimen consists of the approximately 50 mm thick layer of PFC on the surface together with the underlying thicker impermeable HMAC. Prior to any testing, the layer of HMAC must be removed from the PFC layer. The coring process was organized by Gary Lantrip of TxDOT. Two TxDOT crash trucks were utilized to divert traffic from the travel lane in which the coring was taking place. This helped to avoid traffic accidents and protect the workers during the coring process. Additional details on the coring process are provided by Candaele (2008).

The cylindrical core specimens are extracted by a drill press attached to a truck. The drill press is operated by a subcontractor and is shown in Figure 3-4. During the coring process and removal of the HMAC layer, water is continuously applied to the saw blades in order to reduce any increases in temperature due to cutting friction. Therefore, temperature effects on the asphalt binder material are not expected to be significant. However, the addition of water may have an impact on the transport of fine particles created by the cutting process as well as the fine particles previously trapped in the void space of the PFC. Fine particles can either be washed out of the void space with the water, or can be drawn into the void space due to capillary forces. Visual

inspection of the core specimens show that fine particles are washed out of the PFC during the coring processes. This suggests the core specimen has been disturbed and may create error between the core specimens and the in-situ PFC layer. Such disturbances cannot be avoided but are expected to be minor.

Figure 3-4: Drill press used for core extraction

In March 2007, a total of nine 15.2 cm (6 in) diameter cores were extracted from north Loop 360, east FM 1431, and north RR 620. Porosity and hydraulic conductivity tests were conducted by Candaele (2008). In February 2008, twelve 20.3 cm (8 in) diameter PFC core specimens were extracted near the same sites. The change in core diameter was done to determine whether the core size had a significant effect on the resulting porosity or hydraulic conductivity measurements. In February 2009, an additional twelve 20.3 cm (8 in) diameter cores were extracted. However, for this extraction, cores were taken from south RR 620 roughly 1.6 km away from the previous extraction site. The change in extraction site was made in order to take core specimens near a new stormwater quality monitoring site that had been recently installed. Finally, in February 2010, an additional nine 15.2 cm (5 in) diameter cores were extracted. Six core specimens were taken from Loop 360 and three cores were taken from south RR 620. No cores were extracted from FM 1431 due to the recent realignment of the road and abandonment of the previous coring location. Figure 3-5 shows a typical 20.3 cm (8 in) diameter PFC core specimen immediately after extraction.

Figure 3-5: Extracted PFC core with porous layer and impermeable base

3.3.1.2 Loop 360 Site

The PFC overlay on Loop 360 was installed in October 2004. The average annual daily traffic count for the year 2005 was 48,000 vehicles per day (CAMPO, 2009). The coring location at Loop 360 is on the northbound lane, north of the intersection with Lakewood Drive. Three cores were extracted from the travel lane in 2007. In 2008, 2009, and 2010, three cores were extracted from the travel lane and an additional three cores were extracted from the roadway shoulder. All cores were extracted just north of the bridge over Bull Creek. Figure 3-6 shows the relative location of the core extraction site, which has a latitude of 30° 22' 22" North (N) and longitude of 97° 47' 03" West (W). There are two stormwater quality monitoring sites near this location. Stanard (2008) and Frasier (2009) discuss the water quality results obtained at this location.

Figure 3-6: Loop 360 core extraction site (courtesy: Google Earth)

3.3.1.3 FM 1431 Site

The PFC overlay on FM 1431 was installed in February 2004. The average annual daily traffic count for the year 2005 was 18,200 vehicles per day (CAMPO, 2009). The coring location on FM 1431 is on the eastbound lane just east of the intersection with Hur Industrial Boulevard. Three cores were extracted from the travel lane in each of the three study years at this site (2007, 2008, and 2009). As previously mentioned, no cores were extracted in 2010 due to realignment of the roadway and abandonment of the previous coring location. There is no roadway shoulder at this location. Figure 3-7 shows the relative location of the core extraction site, which has a latitude of 30° 31’ 00” N and longitude of 97° 52’ 20” W. The realignment of the roadway under construction can be seen in this figure.

Figure 3-7: FM 1431 core extraction site (courtesy: Google Earth)

3.3.1.4 RR 620 Site

The PFC overlay on RR 620 was installed in June 2004. The average annual daily traffic count for the year 2005 was 32,000 vehicles per day (CAMPO, 2009). There are two coring locations on RR 620. The first location is for the cores extracted in 2007 and 2008, on the northbound travel lane just north of the intersection with O'Connor Drive. Figure 3-8 shows the relative location of the first coring site, which has a latitude of 30° 30' 06" N and longitude of 97° 43' 12" W. The second location is for the cores extracted in 2009 and 2010. A new stormwater monitoring site was installed near Cornerwood Drive; therefore, the cores were extracted near this site to gain information on the PFC layer at that location. The second site is roughly 1.6 km south of the first site, and is located just north of the intersection with Cornerwood Drive in the southbound travel lane. Figure 3-9 shows the relative location of the second coring site, which has a latitude of 30° 29' 18" N and longitude of 97° 43' 48" W.

Figure 3-8: First RR 620 core extraction site (courtesy: Google Earth)

Figure 3-9: Second RR 620 core extraction site (courtesy: Google Earth)

3.3.1.5 Core Specimen Naming System

The cores are distinguished from one another by a three character naming system. The first character in the core name corresponds to the site, or roadway, from which the core was extracted. Site 1 corresponds to Loop 360, site 2 is FM 1431, and site 3 is RR 620. The second character refers to the core location along that site. For each site, the core locations are relatively close to each other, and each site had three core locations. For the cores extracted in March 2007, the core locations are given capital letters (A, B, or C); for the cores extracted in February 2008, the core locations are given numbers (1, 2, or 3); for the cores extracted in February 2009, the core locations are given Roman numerals (i, ii, or iii); and for the cores extracted in February 2010, the core locations are given lower case letters (a, b, or c). Finally, the third character in the core name refers to whether that core was extracted from the travel lane (T) or shoulder (S). Only Loop 360 (site 1) has a large enough shoulder from which to extract cores, and only the 2008, 2009, and 2010 cores were taken from both the travel lane and the shoulder. For example, core 2-A-T is a core from FM 1431 (site 2), the first core location (A) which was from the travel lane (T). Since the core location is a letter (A), this is a core extracted in 2007. Core 1-2-S is from Loop 360 (site 1), the second core location (2), from the shoulder (S). Since the core location is a number (2), this is a core extracted in 2008. Core 3-iii-T is from RR 620 (site 3), the third core location (iii), from the travel lane (T). Since the core location is a Roman numeral (iii), this is a core extracted in 2009. Finally, core 1-a-T is from Loop 360 (site 1), the first core location (a), from the travel lane (T) in the year 2010.

3.3.2 Porosity Measurements

Porosity measurements were conducted at the TxDOT Asphalt Laboratory in Cedar Park, TX. Preparation included cutting the impermeable HMAC base material from the bottom of the core specimen so that the entire core consists of only PFC material. Therefore, the thickness of the core may be slightly less than the actual PFC thickness in-situ. Candaele (2008) determined the porosity for the 2007 cores using a submerged unit weight water displacement method (Regimand and James, 2004) and a destructive image analysis method. Both methods gave very similar results. In the image analysis method, fluorescent epoxy is injected into the pore space of the specimen. The epoxy is allowed to harden and the core is sliced vertically. Each slice is scanned, and computer software is used to count the number of pixels representing the epoxy and the number of pixels representing the PFC aggregate. With these two values, the porosity can be determined. This method is a destructive method and does not allow for further testing on the core specimens. Therefore, the submerged unit weight method is preferred as it is non-destructive. Candaele (2008) gives additional details on each of these methods.

Due to the favorable agreement between porosity values obtained from each method for the first set of cores, only the submerged unit weight method was used for the subsequent core specimens. There are several steps necessary to determine the porosity from the submerged unit weight method. Once the impermeable base is removed from the specimen, the PFC core is vacuum sealed in a plastic bag as shown in Figure 3-10.

Figure 3–10: PFC core vacuum sealed in plastic bag for porosity measurement

The submerged weight of the vacuum sealed core specimen is measured, and then the core is removed from the bag and the submerged weight of only the core is measured. Finally, the core is allowed to oven dry overnight and the dry weight of the core is measured. With these three measurements, the total volume of the core and volume of the solids be calculated using the following equations:

$$V_t = \frac{W_b + W_s - W_{sub,total}}{\rho} - V_b \tag{3.27}$$

$$V_s = \frac{W_s - W_{sub,solid}}{\rho} \tag{3.28}$$

In Equations (3.27) and (3.28), V_t is the total volume of the core (solid volume plus void volume), V_s is the volume of the solids in the specimen, W_b is the weight of the plastic bag, V_b is the volume of the plastic bag, W_s is the oven dry weight of the solids, $W_{sub,total}$ is the submerged weight of the core vacuum sealed in the bag, $W_{sub,solid}$ is the submerged weight of only the core specimen, and ρ is the density of water. The effective porosity can then be calculated as:

$$n_e = \frac{V_t - V_s}{V_t} \tag{3.29}$$

Table 3.1 through 3.4 give the porosity measurements of the PFC core specimens for each of the past four years. In addition, the radius of the core, R_c, and the thickness of the core specimen, b_c, are included. Section 3.6 provides a statistical analysis of these data to determine the changes in porosity both in time and at different locations.

Table 3.1: Porosity of 2007 core specimens (source: Candaele, 2008)

Core ID	Porosity, n_e (%)	R_c (cm)	b_c (cm)
1-A-T	22.78	7.51	4.45
1-B-T	21.64	7.54	3.74
1-C-T	20.36[a]	N/A	N/A
2-A-T	23.17	7.52	3.56
2-B-T	20.51	7.52	4.08
2-C-T	20.98[a]	N/A	N/A
3-A-T	20.30[a]	N/A	N/A
3-B-T	19.44	7.54	4.02
3-C-T	19.55	7.54	3.95

[a] Porosity determined from destructive image analysis method.

Table 3.2: Porosity of 2008 core specimens

Core ID	Porosity, n_e (%)	R_c (cm)	b_c (cm)
1-1-T	22.97	10.92	4.66
1-1-S	21.68	10.96	3.99
1-2-T	22.77	10.97	4.81
1-2-S	20.28	10.91	3.75
1-3-T	18.54	10.95	4.08
1-3-S	21.52	10.92	3.50
2-1-T	15.77	10.93	3.25
2-2-T	16.62	10.89	3.53
2-3-T	16.18	10.90	3.05
3-1-T	12.38	10.91	3.41
3-2-T	12.82	10.88	2.79
3-3-T	14.50	10.93	3.54

Table 3.3: Porosity of 2009 core specimens

Core ID	Porosity, n_e (%)	R_c (cm)	b_c (cm)
1-i-T	17.00	10.92	4.24
1-i-S	20.49	10.92	3.47
1-ii-T	18.14	10.92	4.34
1-ii-S	19.20	10.92	3.18
1-iii-T	18.78	10.97	4.51
1-iii-S	19.74	10.92	3.27
2-i-T	15.57	10.93	3.24
2-ii-T	16.23	10.90	3.39
2-iii-T	15.90	10.93	3.44
3-i-T	12.96	10.93	3.68
3-ii-T	13.45	10.91	3.86
3-iii-T	17.96	10.92	3.76

Table 3.4: Porosity of 2010 core specimens

Core ID	Porosity, n_e (%)	R_c (cm)	b_c (cm)
1-a-T	18.25	7.616	4.709
1-a-S	20.96	7.603	3.825
1-b-T	22.67	7.639	4.599
1-b-S	19.95	7.511	3.980
1-c-T	16.60	7.521	4.860
1-c-S	19.69	7.522	3.870
3-a-T	13.34	7.507	4.214
3-b-T	13.60	7.512	4.109
3-c-T	13.95	7.533	4.190

3.3.3 Laboratory Measurements

3.3.3.1 Laboratory Setup and Constant Head Test Procedure

Measurement of the hydraulic conductivity of the PFC core specimens is problematic for two reasons: the two-dimensional flow paths which occur in PFC and the nonlinear flow regime

observed during testing. In most typical hydraulic conductivity measurements of porous media, the flow path is only in one dimension (vertical or horizontal), and the flow regime is typically linear such that Darcy's law applies. In the laboratory, a series of constant head tests are conducted to determine the hydraulic conductivity of each core specimen. The test apparatus and test procedure used to measure the hydraulic conductivity were developed for this research study and are described in detail by Candaele (2008). A preliminary method for determining the hydraulic conductivity is provided by Charbeneau et al. (in press). However, the methodology presented does not fully incorporate the nonlinear flow effects. A brief overview of the experimental setup is provided here. A constant head is established from a constant flow rate produced by a peristaltic pump to an inflow standpipe centered on the PFC core specimen. The standpipe has a radius of R_s = 1.878 cm (0.739 in) for this setup. Water flows downward vertically at the inflow area and turns to exit the core radially at the circumference of the core. This creates a two-dimensional flow pattern in cylindrical coordinates. The reason for this unique flow setup is to mimic the flow conditions for the field test described in Section 3.4

The testing procedure consists of placing a PFC core specimen between two pliable rubber membranes, each roughly one cm (0.4 in) thick. Holes have been drilled into the membranes, where appropriate, to allow for an inflow boundary on the top surface at the location of a standpipe, and to allow for the measurement of hydraulic head at various radial distances from the center of the core both on the top surface and bottom surface of the core specimen. The rubber membranes and PFC core specimen are then placed between two metal plates which are tightened with threaded rods to compress the rubber membranes. This compression is applied to allow the membranes to enter the surface void space of the PFC core and create a no flow boundary on the upper and lower surfaces of the core. Similarly, the metal plates have appropriate holes drilled in them to allow water to enter the PFC core through a standpipe attached to the top plate, and tubes are attached to the radial hydraulic head measurement positions and connected to a slanted manometer board. The core, rubber membranes, and metal plates are placed in a Plexiglas tank and submerged in water. Figure 3-11 shows the experimental setup during testing and Figure 3-12 provides a schematic view of the setup with several important dimensions. R_c is the radius of the core specimen, b_c is the thickness of the core specimen, and h_s is the head in the standpipe measured from the constant water level in the tank. Therefore, h_s is actually the change in head throughout the core.

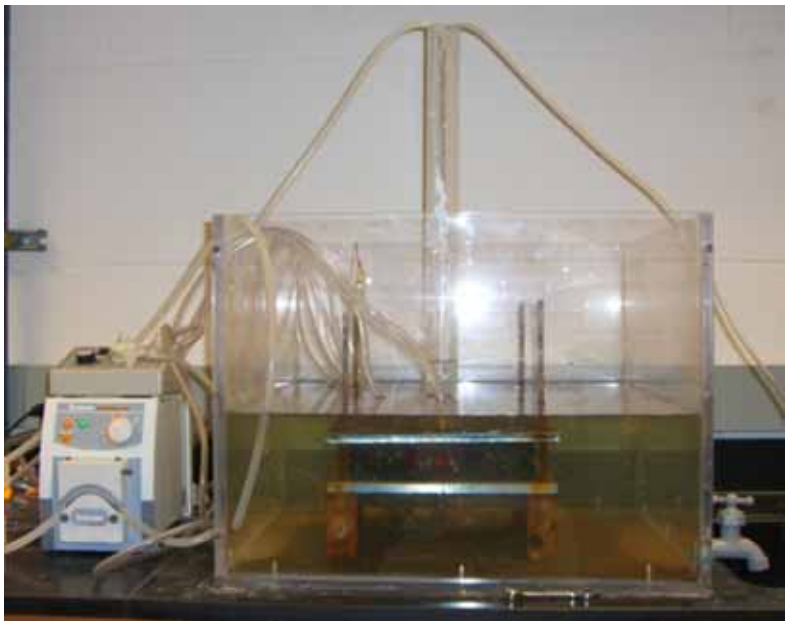

Figure 3-11: Laboratory experimental setup

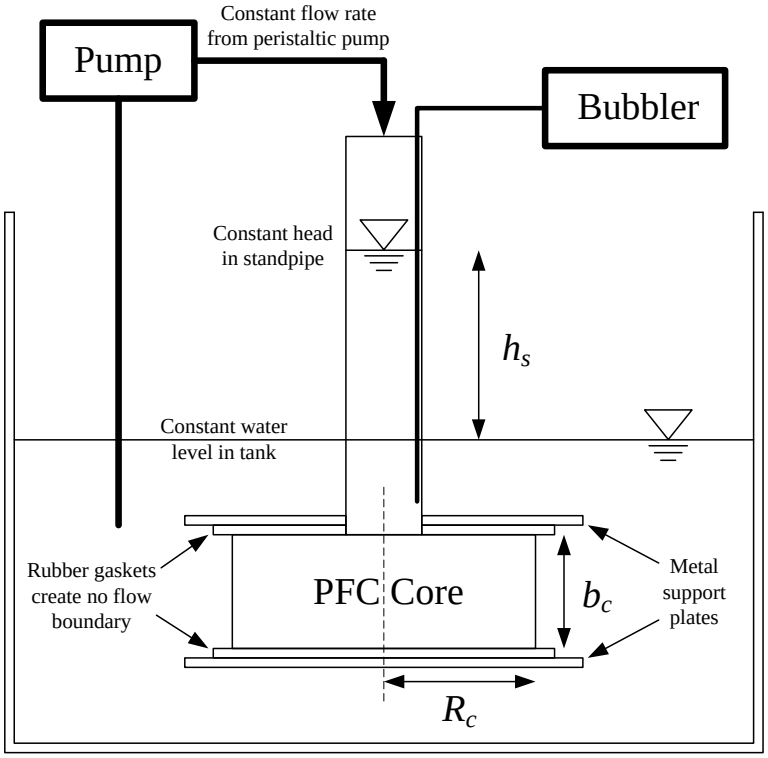

Figure 3-12: Schematic of laboratory setup

Prior to testing, water is flushed through the core specimen in order to remove any air bubbles that may be present. The core is allowed to sit submerged overnight so that any additional air may leave the pore space. This will ideally create a saturated core specimen, which

simplifies the mathematical equations derived below. In addition, the tubes on the manometer board must be flushed out to remove any air bubbles, which can only be accomplished by flushing the air bubbles into the core specimen. Therefore, the ability to create a completely saturated core specimen can be difficult.

Hydraulic conductivity testing consists of taking two measurements: volumetric flow rate and water depth in the standpipe. A constant flow rate is provided by one of two peristaltic pumps. The first pump (VWR mini-pump variable flow) is a low flow pump and can produce flow rates from 1.0 to 8.0 cm^3/s (0.061 to 0.49 in^3/s). The second pump (Heidolph pumpdrive 5106) can produce higher flow rates and has a range of flow from 2.0 to 40.0 cm^3/s (0.12 to 2.4 in^3/s). The volumetric flow rate is measured with a stopwatch and graduated cylinder. The water depth in the standpipe is measured with an ISCO bubble flow meter (model #4230) shown in Figure 3-13. Prior to testing, the bubbler is set to a value of zero for the water depth in the tank. This establishes the hydraulic head on the outflow boundary as the datum.

Figure 3-13: ISCO bubbler used to measure standpipe head

Prior to starting the pump and creating an inflow, the head at each radial position is measured on the slanted manometer board shown in Figure 3-14. This establishes the zero head elevation for each radial head position as well as the zero elevation at the standpipe. The peristaltic pump is turned on at a desired flow rate and steady state conditions are achieved. Typically, steady state is achieved in 15 minutes, but for PFC core specimens that appear to be considerably clogged with sediment, steady state can take considerably longer. Steady state is achieved when the reading on the ISCO bubbler does not change after roughly 10 minutes. At steady state, the bubble reading gives the head in the standpipe, and the manometer board gives the head reading at various radial positions on the top and bottom surface of the core specimen.

The flow rate is then determined with a stopwatch and graduated cylinder. Both the head values and flow rate are measured twice and the average of the two is taken as the head and flow rate value for that test. This procedure completes one test and is repeated for a different flow rate until a curve of head in the standpipe as a function of flow rate is created.

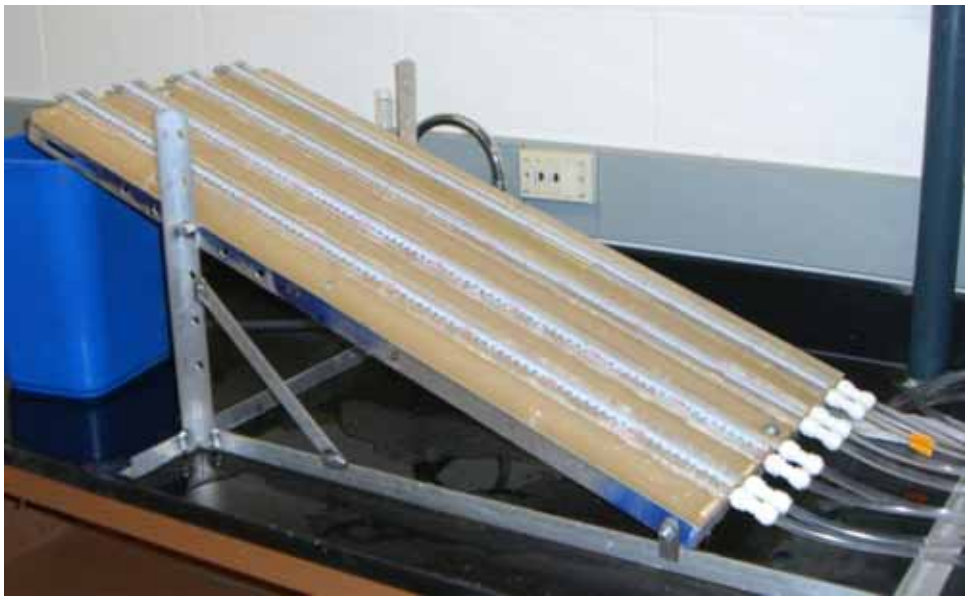

Figure 3-14: Slanted manometer board for radial head measurements

3.3.3.2 Modified Forchheimer Equation

The data collected for a series of constant head tests gives the head in the standpipe as a function of flow rate. The data show that this relationship is nonlinear. Therefore, Darcy's law is not applicable and the use of the Forchheimer equation is required. However, the original Forchheimer equation relates the hydraulic gradient as a function of specific discharge. Neither the hydraulic gradient nor specific discharge can be measured precisely for this experimental setup due to the fact that the flow is two-dimensional and the streamlines within the core specimen are diverging. The use of a Forchheimer-type equation is necessary to analyze the data. Equation (3.30) gives the empirical modified Forchheimer equation used for the purposes of this research:

$$h_s = \alpha Q + \beta Q^2 \qquad (3.30)$$

where h_s is the head on the standpipe, Q is the volumetric flow rate, and α [T/L^2] and β [T^2/L^5] are the modified Forchheimer coefficients. The modified Forchheimer equation replaces the hydraulic gradient in the original Forchheimer equation with the head in the standpipe, which is actually the change in head through the core specimen since the datum is taken as the head on the outflow boundary. The specific discharge in the original Forchheimer equation is replaced with the volumetric flow rate in the modified Forchheimer equation. These two changes result in a change to the two Forchheimer coefficients. The modified Forchheimer equation defines the nonlinear relationship for the global conditions of the core.

The volumetric flow rate is related to the specific discharge through $Q = Aq$. Q can be measured, but the area for flow changes as water moves through the core specimen. The inflow

value of A is the area of the standpipe, πR_s^2. The outflow value of A is the circumference of the core times the thickness, $2\pi R_c b_c$. Therefore, A is not constant as flow passes through the core. Similarly, the hydraulic gradient for the overall core specimen is equal to the change in head, h_s, divided by the length over which this change occurs. However, the flow path length is also not constant for flow through the core. The shortest possible flow path length is $R_c - R_s$, which occurs at the upper no flow boundary. The longest flow length is $R_c + b_c$, which occurs at the lower no flow boundary. Since the flow path length and area are not known, these variables have been lumped into the modified Forchheimer coefficients. As will be shown in Section 3.5, the original Forchheimer coefficients can be related to the modified Forchheimer coefficients through the results of numerical simulations. Therefore, the modified Forchheimer equation is an empirical equation for the overall global conditions of the core specimen.

The use of Equation (3.30) to model the nonlinear flow through a PFC core specimen is useful and provides a good method for determining the modified Forchheimer coefficients. However, it is also useful to rearrange the modified Forchheimer Equation (3.30) to the following transformed form:

$$\frac{h_s}{R_c} = \frac{Q}{\xi}\left(1 + \frac{Q}{\eta}\right) \tag{3.31}$$

The transformed modified Forchheimer equation represented in Equation (3.31) is useful because hRsR/RRcR represents an average hydraulic gradient through the core. Although this is not the actual hydraulic gradient, it does serve to nondimensionalize the equation. Furthermore, representing the nonlinear term as shown suggests that the value of Q/η can be compared to the value of one in order to determine whether the nonlinear effects are significant. The two transformed modified Forchheimer coefficients of Equation (3.31), ξ and η, can be compared to the two coefficients of Equation (3.30), α and β, through the following relationships:

$$\xi = \frac{R_c}{\alpha} \tag{3.32}$$

$$\eta = \frac{\alpha}{\beta} \tag{3.33}$$

In Equations (3.32) and (3.33), ξ has units of [L^3/T] and can be calculated from the core radius and the linear modified Forchheimer coefficient α through Equation (3.32). η also has units of [L^3/T] and is related to both the modified Forchheimer coefficients, α and β, through Equation (3.33). As discussed below, the use of Equation (3.30) as the modified Forchheimer equation is desirable for determination of the two coefficients from the experimental data. Once the two coefficients are determined, the use of Equation (3.31) as the transformed modified Forchheimer equation is desirable due to its nondimensional form, the units of ξ and η are the same as the flow rate, and the magnitude of Q/η can be compared to a value of one to determine the relative magnitude of the nonlinear effect.

The modified Forchheimer coefficients (α and β) can be determined experimentally from a series of constant head tests. Figure 3-15 shows a typical graph of h_s as a function of Q with the model fit for the modified Forchheimer Equation (3.30).

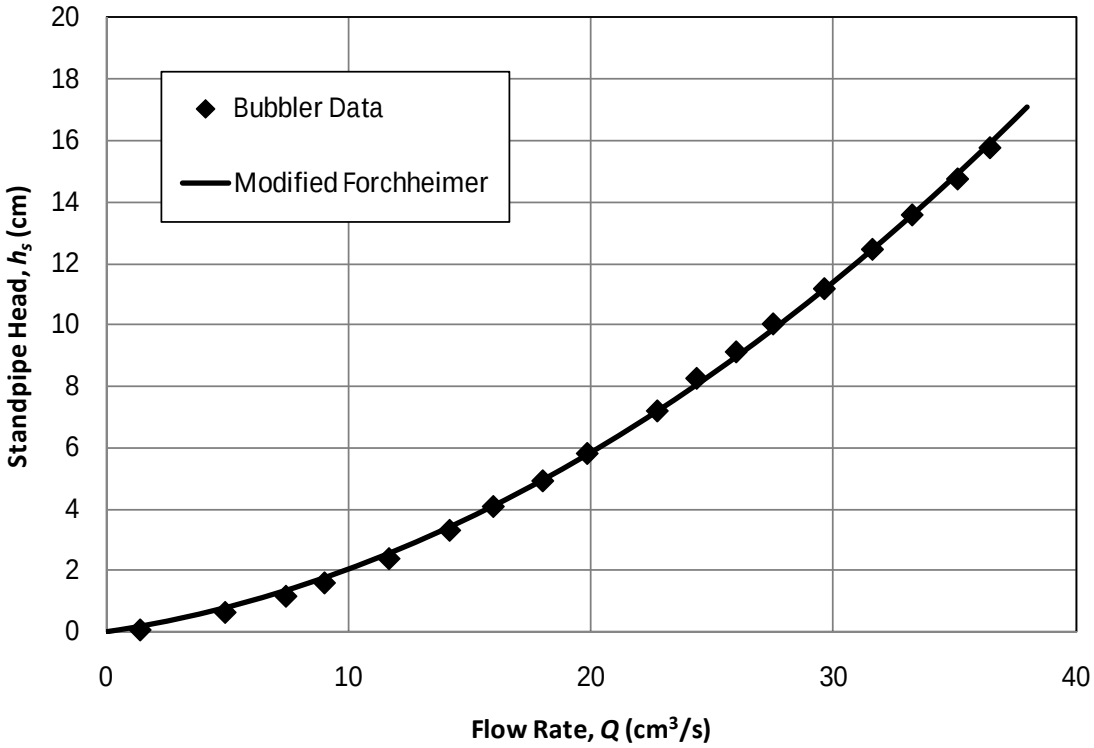

Figure 3-15: Typical constant head data (Core 1-2-S)

The modified Forchheimer coefficients are determined by minimizing the standard error between the measured standpipe head data, h_{sd}, and the modeled standpipe head, h_{sm}, determined from the modified Forchheimer Equation (3.30). The standard error can be calculated as:

$$S.E. = \sqrt{\frac{1}{N}\sum_{i=1}^{N}\left(h_{sd} - h_{sm}\right)_i^2} \tag{3.34}$$

In Equation (3.34), *S.E.* is the standard error between the data and the modified Forchheimer equation for N observed data points. The standard error is minimized by simultaneously changing the value of α and β so that the model results closely match the observed data. This is accomplished using the Solver tool in Microsoft Excel. The use of Equation (3.30) as opposed to Equation (3.31) for calculating the standard error is due to the form of the equations. If Equation (3.31) is used, the Solver tool will minimize the standard error by simply increasing the value of η to be so large such that the nonlinear term is negligible. Therefore, Equation (3.30) is the most useful for determining the modified Forchheimer coefficients from the experimental data.

Although we can experimentally determine the modified Forchheimer coefficients (α and β or ξ and η), this gives us no indication of the values of the original Forchheimer coefficients (a and b or K and n) without further investigation. In order to address this issue and determine the true hydraulic conductivity, we must conduct numerical simulations of flow through the PFC core specimen as described in Section 3.5. For now, we will simply report the values of the

modified Forchheimer coefficients and determined the hydraulic conductivity once the numerical model has been explained and results have been presented.

3.3.3.3 Falling Head Lab Test Procedure

Although a series of constant head tests is the preferred method for determining the modified Forchheimer coefficients, a falling head test can also be conducted in the laboratory. Comparison of the falling head test to the constant head test results is useful for determining whether the same nonlinear curve can be measured from both methods. This is a necessary concern as the field test for measuring in-situ hydraulic conductivity is based on the falling head principle.

In order to conduct the falling head test in the lab, the same test setup for the constant head tests is used with the core specimen submerged in water and compressed between the two rubber membranes. The water level in the tank is drained so that the surface of the water is near the top surface of the PFC core specimen. Therefore, this essentially means the top of the PFC surface is taken as the head datum. During a falling head test, the source head h_s varies with time. Assuming nonlinear flow conditions, the head-discharge relationship using the modified Forchheimer Equation (3.30) may be inverted to give Q as a function of h_s. Combined with the continuity equation for the water level in a standpipe with radius R_s one finds:

$$-\pi R_s^{\,2}\frac{dh_s}{dt} = Q = \frac{\alpha}{2\beta}\left[\sqrt{1+\frac{4\beta h_s}{\alpha^2}}-1\right] \tag{3.35}$$

Equation (3.35) may be integrated to give the time for the standpipe head to decrease from the initial level $h_s(0)$ to an arbitrary level $h_s(t)$ as follows:

$$\frac{t}{\pi R_s^{\,2}\alpha} = \sqrt{1+\frac{4\beta h_s(0)}{\alpha^2}}-\sqrt{1+\frac{4\beta h_s(t)}{\alpha^2}}+\ln\left(\frac{\sqrt{1+4\beta h_s(0)/\alpha^2}-1}{\sqrt{1+4\beta h_s(t)/\alpha^2}-1}\right) \tag{3.36}$$

With Equation (3.36), three readings of time-depth pairs $[t, h_s(t)] = [0, h_s(0)]$, $[t_1, h_s(t_1)]$, and $[t_2, h_s(t_2)]$ are sufficient to determine the two unknown coefficients α and β, where the third time-depth measurement is used for an initial condition.

The constant head test, while more time-consuming, allows one to better define the entire head-discharge curve, and thus obtain a more reliable estimate of the hydraulic conductivity. That notwithstanding, the variation between the constant head and falling head tests is much less than the natural variation expected at field sites and among laboratory core specimens as described in Section 3.4.2. Both the constant head and falling head test methodologies provide useful and reproducible information on the hydraulic characteristics of PFC.

3.3.3.4 Establishment of No Flow Boundaries

One possible concern with this experimental test setup is whether the rubber membranes are actually creating a no flow boundary on the surface of the PFC core by simply compressing the core. When the core specimens are extracted, the specimen contains the PFC layer together with the underlying impervious asphalt. Prior to the porosity measurements, the impervious asphalt layer is removed. In order to test whether the rubber membranes are creating a no flow boundary, one of the remaining impervious asphalt layer specimens was placed in the test setup

and compressed in an identical way as the PFC cores. A falling head test was conducted on the impervious core to determine if there is a significant amount of flow due to the presence of the rubber membranes. A period of roughly 24 hours was allowed to pass with water in the standpipe, and the water level dropped only by a couple of centimeters within that time. Therefore, it can be assumed that any flow that may occur due to the rubber membranes is negligible compared to the much larger flow rates through the PFC pore space. Furthermore, this test shows that simply compressing the core specimen with the arm strength of a typical engineering graduate student is sufficient to create the required no flow boundary, and no special tools are needed to compress the core under a greater load.

3.3.4 Lab Test Results

3.3.4.1 Constant Head Lab Results

The PFC core specimens extracted from the three different roadways in the years 2007, 2008, and 2009 were all tested in the laboratory using the series of constant head tests described in Section 3.3.1. From these tests, the modified Forchheimer coefficients were determined by minimizing the standard error between the constant head data and the modified Forchheimer Equation (3.30). Tables 3.5 through 3.7 gives the modified Forchheimer coefficients and resulting standard error for each of the core specimens tested.

Table 3.5: Modified Forchheimer coefficients of 2007 core specimen (source: Candaele, 2008)

Core ID	α (s/cm^2)	β (s^2/cm^5)	ξ (cm^3/s)	η (cm^3/s)	*S.E.* (cm)
1-A-T	0.7016	0.0143	10.74	49.07	0.5860
1-B-T	0.0477	0.0028	158.06	16.98	0.1253
2-A-T	0.1883	0.0093	39.98	20.26	0.2118
2-B-T	0.4035	0.0154	18.63	26.18	0.3604
3-B-T	0.2965	0.0390	25.45	7.61	0.4659
3-C-T	0.2860	0.0141	26.52	20.28	0.3330

Table 3.6: Modified Forchheimer coefficients of 2008 core specimens

Core ID	α (s/cm^2)	β (s^2/cm^5)	ξ (cm^3/s)	η (cm^3/s)	*S.E.* (cm)
1-1-T	0.1520	0.0092	71.88	16.51	0.3578
1-1-S	0.0551	0.0052	198.93	10.53	0.0459
1-2-T	0.1454	0.0115	75.42	12.64	0.1188
1-2-S	0.1172	0.0088	93.11	13.36	0.1226
1-3-T	0.0916	0.0066	119.57	13.97	0.1039
1-3-S	0.0735	0.0050	148.70	14.73	0.0405

Core ID	α (s/cm^2)	β (s^2/cm^5)	ξ (cm^3/s)	η (cm^3/s)	*S.E.* (cm)
2-1-T	0.2892	0.0188	37.80	15.39	0.3171
2-2-T	0.1392	0.0103	78.25	13.56	0.1175
2-3-T	0.2985	0.0187	36.54	15.92	0.2313
3-1-T	2.4007	0.2887	4.55	8.31	0.7898
3-2-T	3.0288	0.7882	3.59	3.84	0.1884
3-3-T	0.5850	0.0699	18.69	8.37	0.5957

Table 3.7: Modified Forchheimer coefficients of 2009 core specimens

Core ID	α (s/cm^2)	β (s^2/cm^5)	ξ (cm^3/s)	η (cm^3/s)	*S.E.* (cm)
1-i-T	0.0686	0.0082	159.21	8.35	0.0807
1-i-S	0.0468	0.0039	233.50	11.96	0.0527
1-ii-T	0.2245	0.0151	48.62	14.89	0.3434
1-ii-S	0.0655	0.0074	166.53	8.89	0.1528
1-iii-T	0.0924	0.0053	118.77	17.45	0.0634
1-iii-S	0.1434	0.0141	76.17	10.21	0.1731
2-i-T	0.7067	0.204	15.46	34.58	1.3659
2-ii-T	0.3092	0.0097	35.26	31.78	0.3686
2-iii-T	0.1356	0.0090	80.58	15.08	0.1174
3-i-T	1.2954	0.1283	8.44	10.10	0.9058
3-ii-T	0.7192	0.0539	15.17	13.35	0.5381
3-iii-T	0.5424	0.0761	20.13	7.13	0.4604

As previously mentioned, these values give no indication of the hydraulic conductivity without further numerical modeling. However, it is interesting to note some general trends. One would expect that the linear modified Forchheimer coefficient would be related to the hydraulic conductivity. A large hydraulic conductivity is expected to occur for small values of α and large values of ξ. The data suggest that in general, the Loop 360 cores have a larger hydraulic conductivity than the cores from FM 1431 and RR 620. Further investigation of these relationships is provided in Section 3.6.

The nonlinear modified Forchheimer coefficient, particularly the η coefficient, can be used to determine when nonlinear flow effects are significant. As previously mentioned, if the value Q/η is large compared to a value of one, then the nonlinear flow effects cannot be ignored. Therefore, the larger the value of η, the more likely that Q/η will be small and nonlinear flow effects will be negligible. In general, the value of η is on the order of 10 cm^3/s (0.61 in^3/s),

meaning that if the flow rate approaches a value of 10 cm^3/s (0.61 in^3/s), the nonlinear flow effects will become significant. It is interesting to note from Figure 3-15 that for flow rates less than roughly 10 cm^3/s (0.61 in^3/s), the experimental data could be fairly closely approximated with a linear relationship.

In addition to determining the modified Forchheimer coefficients by minimizing the standard error, we can also conduct a multiple linear regression on the model in order to obtain the two coefficients. The resulting values of α and β are the same for both methods, but the regression provides additional information that is worth noting. The p-values for each coefficient are very small, suggesting that the model is statistically significant. The regression results also provide 95% confidence intervals for both coefficients to give an indication of the precision of each coefficient. For the linear coefficient, the 95% confidence interval is roughly plus/minus 10% of the actual value. For the nonlinear coefficient, the 95% confidence interval is roughly 5% of the actual value. The relatively small confidence intervals, together with the small p-values, suggest this is an appropriate model to use in order to represent the experimental data.

3.3.4.2 Falling Head Lab Results

Several of the 2008 and 2009 core specimens were also tested in the laboratory using the falling head approach. The falling head test was conducted simply for verification that both methods would produce similar results. In general, it was assumed that the series of constant head tests will produce more reliable results.

The same core specimen (1-2-S) shown in Figure 3-15 was also tested using the falling head approach. The initial, intermediate, and final head values are as follows: $h_s(0)$ = 40.6 cm (16.0 in), $h_s(t_1)$ = 20.3 cm (8.0 in), and $h_s(t_2)$ = 2.54 cm (1 in). The average of three sets of time measurements are taken with results (plus/minus one standard deviation): t_1 = 4.04 ± 0.10 sec and t_2 = 11.41 ± 0.21 sec. Using the mean time values in Equation (3.36), one finds α = 0.153 s/cm^2 (0.987 s/in^2) and β = 0.00675 s^2/cm^5(0.714 s^2/in^5). Similarly, α and β can be determined using the plus/minus one standard deviation to determine the variability in the falling head results. Figure 3-16 shows the curve of h_s versus Q for the averaged falling head test as well as its uncertainty from plus/minus one standard deviation together with the constant head test results. Good agreement exists between the constant head and falling head tests, suggesting that both methods are acceptable for determining the modified Forchheimer coefficients.

Table 3.8 provides the modified Forchheimer coefficients for the select cores tested using the falling head approach. In addition, the percent difference (*P.D.*) of the modified Forchheimer coefficients from the falling head test when compared to the constant head tests is provided in order to give an indication of the error that may be involved with the falling head test.

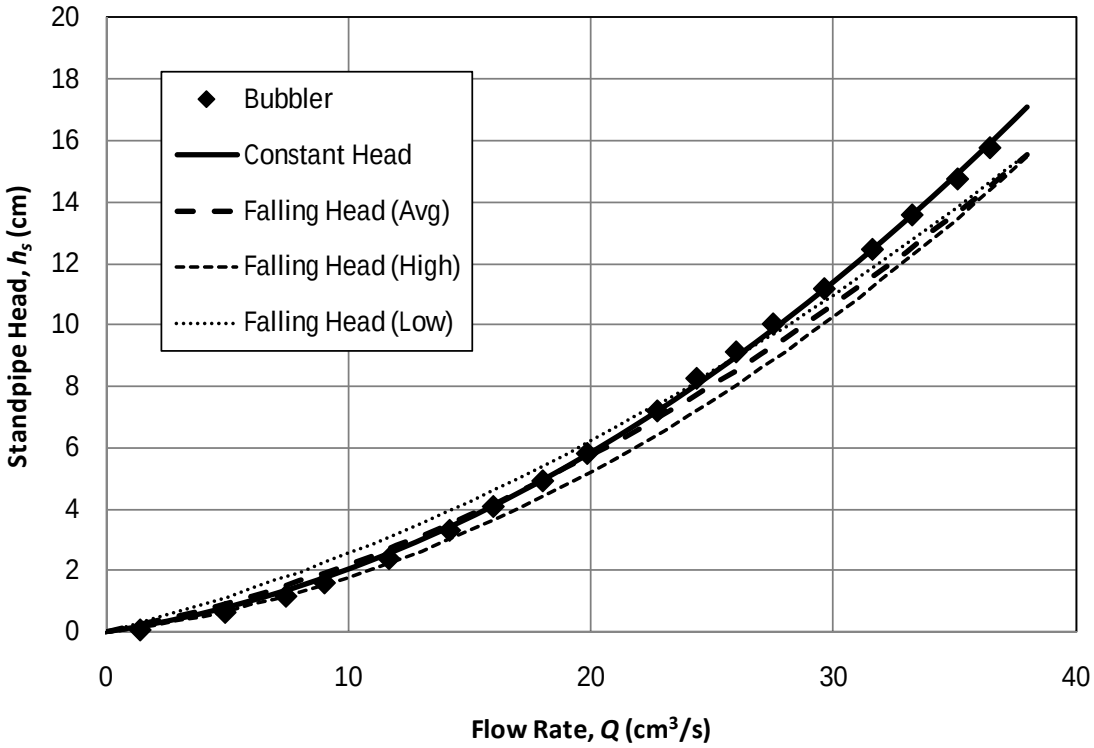

Figure 3-16: Falling head test results (Core 1-2-S)

Table 3.8: Modified Forchheimer coefficients for falling head tests on 2008 and 2009 core specimens

Core ID	α (s/cm^2)	β (s^2/cm^5)	ξ (cm^3/s)	η (cm^3/s)	*P.D.* in α	*P.D.* in β
1-1-S	0.1505	0.0050	72.50	30.35	-173.2	5.2
1-2-T	0.1480	0.0135	74.13	10.94	-1.7	-17.6
1-2-S	0.1188	0.0110	91.86	10.84	-1.4	-25.0
2-1-T	0.4161	0.0516	26.27	8.06	-43.9	-174.6
2-i-T	0.4057	0.0405	26.94	10.01	42.6	-98.2
2-iii-T	0.1873	0.0064	58.33	29.38	-38.1	29.1
3-i-T	0.9443	0.1799	11.57	5.25	27.1	-40.3
3-ii-T	0.5112	0.0715	21.34	7.15	28.9	-32.8
3-iii-T	0.5413	0.0836	20.17	6.47	0.2	-9.9

The same general trends observed in the constant head tests are seen here as well. Furthermore, there can be some large differences between the constant head and falling head tests. Many of the falling head tests are within acceptable levels of error when compared to the

constant head tests, but there are several cases where the percent difference is very large. For this reason, the series of constant head tests is preferred in the laboratory.

In addition, all of the 2010 core specimens were tested only using the falling head approach. Although the constant head test method is the preferred method for determining the modified Forchheimer coefficients of a core specimen, the 2010 cores were not tested using the constant head method due to time constraints. Table 3.9 provides the modified Forchheimer coefficients for the 2010 core specimens using the falling head approach.

Table 3.9: Modified Forchheimer coefficients for falling head tests on 2010 core specimens

Core ID	α (s/cm^2)	β (s^2/cm^5)	ξ (cm^3/s)	η (cm^3/s)
1-a-T	0.2997	0.0576	25.41	5.20
1-a-S	0.0868	0.0038	87.54	22.86
1-b-T	0.0524	0.0049	145.88	10.78
1-b-S	0.0750	0.0030	100.13	25.09
1-c-T	0.1804	0.0176	41.69	10.23
1-c-S	0.0737	0.0022	102.02	33.13
3-a-T	0.5464	0.1627	13.74	3.36
3-b-T	5.7616	3.0130	1.30	1.91
3-c-T	1.2329	0.6265	6.11	1.97

The linear modified Forchheimer coefficients for Loop 360 core specimens are greater than those from RR 620, again suggesting a greater hydraulic conductivity on Loop 360. Furthermore, in general, the nonlinear coefficient η is smaller for RR 620. All core specimens have a significant nonlinear effect, but the cores from RR 620 are significant at smaller flow rates due to the smaller η coefficients.

3.4 Field Experimentation

In order to properly measure the in-situ hydraulic conductivity of PFC, field experimental tests must be conducted. This is accomplished through a falling head permeability test. In-situ hydraulic conductivity measurements are necessary to properly determine the extent of clogging the PFC layer has experienced. As the PFC layer becomes clogged over time, it is expected that the porosity and hydraulic conductivity will decrease and drainage benefits of the PFC will be lost. Therefore, a well defined field test is necessary to determine whether the drainage benefits of PFC will persist in the future. This section describes a new field test apparatus developed specifically for this research study as well as the test procedure for determining the in-situ modified Forchheimer coefficients.

3.4.1 Need for Improved Field Test

A field test method in the State of Texas currently exists for measuring the drainage capacity of PFC, and is described in detail by TxDOT (2004a). The current TxDOT method measures the time it takes to drain 27.9 cm (11 in) of water from a 15.2 cm (6 in) diameter pipe into the PFC layer. Plumbers putty is used to seal the interface between the pipe and the PFC surface. The current TxDOT test apparatus is shown in Figure 3-17. Although this test is useful for determining adequate compaction of the PFC layer between passes of the compaction vehicle during the construction process, it gives no indication of the hydraulic conductivity of the PFC layer. TxDOT provides a guideline of 20 sec as the minimum drainage capacity for newly constructed PFC layers. Based on the dimensions of the TxDOT test apparatus, a drainage time of 20 sec corresponds to an average minimum flow rate of 255 cm^3/s (15.6 in^3/s).

Although the current TxDOT method can be used to compare the relative drainage capacity of a PFC layer, it cannot provide the actual hydraulic conductivity. One of the major reasons this is not possible is because as the water flows out of the pipe and into the PFC, the water immediately resurfaces after it moves out from under the plumber's putty. This results in very little actual porous media flow during the test, and so there is not adequate information from which to determine the hydraulic conductivity. Other traditional permeameters, such as a double-ring infiltrometer, typically assume vertical flow paths into the porous media. Although these devices work well for natural soils, they are not effective for PFC due to the impervious boundary roughly 5 cm (2 in) or less from the surface. Because of the presence of this boundary, the method for determining the hydraulic conductivity from traditional permeameters is no longer valid. Therefore, there is a need for a new test apparatus from which to measure the hydraulic conductivity of PFC that accounts for two specific flow features, namely forcing water to flow through the PFC layer and accounting for the underlying impervious boundary near the surface.

Figure 3-17: Current TxDOT PFC drainage capacity test

A new field test apparatus developed at CRWR has been designed and constructed specifically for this research study that forces water to flow through the PFC layer; analysis of the results take into account the underlying impervious boundary. The new field test apparatus is shown in Figure 3-18. This apparatus consists of a solid metal base plate of radius R_c = 22.9 cm (9.02in). A standpipe is centered on the plate with a radius R_s = 5.1 cm (2 in). A layer of vacuum grease (Dow Corning high vacuum grease) is placed on the bottom side of the base plate and is allowed to enter the surface void space of the PFC in order to create a no flow boundary along the surface of the plate. This helps to eliminate any flow that may occur between the PFC surface and the base plate surface. Water flows vertically into the PFC layer from the standpipe and turns to flow radially away from the standpipe and out from under the base plate. As water flows out from under the base plate, surface runoff tends to occur. This test apparatus mimics the boundary conditions imposed on the core specimens in the laboratory and can therefore be analyzed in the same way.

Figure 3-18: CRWR field test apparatus

3.4.2 Field Measurements

3.4.2.1 Falling Head Test Procedure

The results of the laboratory experiments are used to determine the modified Forchheimer coefficients for a PFC core specimen. Although the laboratory method is effective in determining these coefficients, it is not ideal due to the destructive nature of the coring process and time restraints associated with conducting a series of constant head tests. Therefore, a need exists for a nondestructive field test in which the modified Forchheimer coefficients can be easily measured in-situ. This can be accomplished with a falling head test in the field, as opposed to a series of constant head tests in the lab. A falling head test in the field is necessary due to the large flow rates and large volume of water required for constant head field tests. The falling head test is conducted using the new CRWR test apparatus described above. As mentioned in Section 3.3.3.3, during a single falling head test, three time-depth measurements are taken. These three measurements are used to determine the two modified Forchheimer coefficients, with the third measurement used for the initial condition. The use of Equation (3.36) in Section 3.3.3.3 is used to determine the two modified Forchheimer coefficients and is repeated here for convenience.

$$\frac{t}{\pi R_s^{\,2}\alpha} = \sqrt{1+\frac{4\beta h_s(0)}{\alpha^2}} - \sqrt{1+\frac{4\beta h_s(t)}{\alpha^2}} + \ln\left(\frac{\sqrt{1+4\beta h_s(0)/\alpha^2}-1}{\sqrt{1+4\beta h_s(t)/\alpha^2}-1}\right) \quad (3.37)$$

A similar test procedure as described in Section 3.3.3 is used in the field. Charbeneau et al. (in press) also describe the test methodology needed to conduct the field test. The following outlines the necessary materials needed to conduct the field test as well as a step-by-step procedure to properly obtain the required measurements.

The following materials are needed to conduct the falling head field test:

- *Proposed CRWR field test apparatus*: used to channel water into the PFC surface and create radial flow without surface runoff; the standpipe should be graduated in divisions of 0.3 cm (0.1in) (see Figure 4.2).
- *Stopwatch*: used to record the time for water to drain in divisions of 0.01 sec; must have a split function to record an intermediate time during the test.
- *Vacuum grease*: used to seal the PFC surface under the base plate of the test apparatus; Dow Corning silicon high vacuum grease works well, and typically 200 to 230 mL (one and a half tubes) is sufficient to cover the base plate surface during dry conditions.
- *Water*: roughly 45 L of water is sufficient to conduct one falling head test.

The following steps represent the CRWR test procedure for determining the in-situ modified Forchheimer coefficients:

1) Select an area of the existing PFC surface to test. Remove any debris on the surface and choose a sufficiently flat area so that the base plate of the test apparatus can sit flat on the roadway surface and create a good seal with the PFC.
2) Place roughly 200 to 230 mL of vacuum grease on the underneath side of the base plate. Spread the vacuum grease by hand to create a uniform distribution.
3) Place the test apparatus onto the PFC pavement surface. Use enough force (typically standing on the base plate is sufficient) to create a water-tight seal between the base plate and the pavement surface such that the vacuum grease enters the surface voids of the PFC.
4) Flush an initial volume of water though the test apparatus to saturate the pore space. Typically about 19 L of water is necessary for sufficient saturation.
5) Fill the test apparatus with water to the top of the standpipe.
6) Start the timing device when the water level reaches the marking of 36.6 cm (14.4 in) on the standpipe. This corresponds to a water depth of 40.4 cm (15.9 in) above the PFC surface.
7) Use the split function on the timing device when the water level reaches the marking of 18.3 cm (7.2 in) on the standpipe. This corresponds to a water depth of 22.1 cm (8.7 in) above the PFC surface.

8) Stop the timing device when the water level reaches the marking of 0.0 cm (0.0 in) on the standpipe. This corresponds to a water level of 3.8 cm (1.5 in) above the PFC surface.

9) Record the three time-depth measurements.

10) Repeat steps 5 through 9 until a total of three falling head tests are completed. Average the three time measurements to get the average time-depth measurement necessary to calculate the modified Forchheimer coefficients using Equation (3.37).

An additional concern with the field test is the existing moisture content of the roadway itself, particularly after recent rainfall events. It is assumed that the pore space in the PFC layer is saturated for testing conditions. This suggests that if there was a recent rainfall event and the PFC layer had not fully dried then the assumption of saturated conditions would be more likely. However, experience has shown that when the PFC surface is moist, the vacuum grease does not create a good bond with the PFC surface. After rainfall events, there is a possibility that the testing apparatus may float during the test due to the poor bond. Therefore, a larger amount of vacuum grease may be needed in order to create the upper no flow boundary, and standing on the device during testing is recommended to avoid the possibility of floating. The test can be conducted properly after rainfall events, but additional care is needed in order to ensure that the upper no flow boundary is created. When the test is completed and the test apparatus is moved, the vacuum grease should cause the apparatus to stick to the PFC surface. If the apparatus did not stick to the surface when removed, then more vacuum grease should be added and the test procedure should be repeated.

3.4.2.2 Investigation of Saturated Pore Space

One of the assumptions in the theoretical development of the test process is that the pore space must be completely saturated. Due to the slope of the roadway in the field, water is constantly flowing down gradient toward the roadway shoulder by gravity. This suggests that the pore space may not be entirely saturated despite the initial volume of water allowed to drain through the test apparatus prior to testing. In the event that the pore space is not completely saturated, the hydraulic conductivity measurement would most likely result in an artificially high hydraulic conductivity. This increase in hydraulic conductivity is a result of some of the water acting to fill the pore space of the PFC.

An initial volume of 19 L of water is allowed to flow into the PFC layer prior to testing in order to saturate the pore space. In order to determine whether saturated conditions are actually achieved by the initial drainage prior to conducting the falling head test, a diffuser was built that allows water to drip into the PFC layer upslope from the test location. The diffuser consists of a 1.5 meter (m) long piece of PVC pipe attached to a 189 L water supply tank. The diffuser and water supply tank are shown in Figure 3-19 and Figure 3-20, respectively. The diffuser has nine 0.64 cm (0.25 in) diameter holes drilled through the PVC, and are spaced 15.2 cm (6 in) apart and allow water to drip out. The flow rate from the diffuser can be controlled by a valve attached upstream of the diffuser. Prior to using the diffuser, an initial falling head test is conducted using the test procedure described above. Then 75.7 L (20 gal) of water is dripped into the PFC over a time of 15 minutes. With this volume of water in the pore space, it appears that the pores have become completely saturated. A second falling head test is conducted resulting in the same modified Forchheimer coefficients within the experimental error, verifying that saturated

conditions are achieved with only the initial drainage volume of 19 L. This confirms our assumption of saturated conditions.

Figure 3-19: Testing prior to using diffuser upslope

Figure 3-20: 189 L water supply tank

3.4.2.3 Comparison with Constant Head Field Test

Although a falling head test is preferred in the field, a limited number of constant head tests were measured in the field as well. A falling head test serves to theoretically represent an infinite number of constant head tests. In order to determine whether a series of constant head

tests is equivalent to a falling head test, several constant head tests were attempted in the field. The conduction of these tests requires a large amount of water due to the ease of flow through the PFC as well as the time required to reach steady state conditions. The head is measured as a constant in the standpipe, and the flow rate is measured with a stopwatch and graduated bucket. In addition, it is difficult to obtain precise measurements due to the large flow rates needed. Figure 3-21 shows a constant head field test with water flowing by gravity from the water supply tank, which must be continuously refilled with water from smaller buckets during the test in order to maintain a constant water level in the tank. The constant water level in the tank is necessary to obtain a constant flow rate.

Figure 3-21: Constant head field test

Four constant head tests were conducted in the field, followed by one falling head test. The results are shown in Figure 3-22. The modified Forchheimer coefficients can be determined by fitting a curve to the four constant head tests by minimizing the standard error similar to the method used for the laboratory constant head data. There is good consistency between the constant head and falling head data, though more constant head measurements are necessary, especially at small discharge values, in order to better estimate the linear modified Forchheimer coefficient α. The similar shape between the constant head and falling head test results suggest that the falling head test serves as a good comparison to a series of constant head tests. However, the difference between the two curves can be attributed to the uncertainty associated with each of the constant head tests. The large flow rates needed to conduct a constant head test in the field make it difficult to obtain a constant flow rate and accurately measure that rate. In addition, obtaining steady state conditions are not guaranteed in the field. Furthermore, the large flow rates

sustained during the constant head test may have flushed particles out of the flow paths in the PFC pore space, which will alter the Forchheimer coefficients.

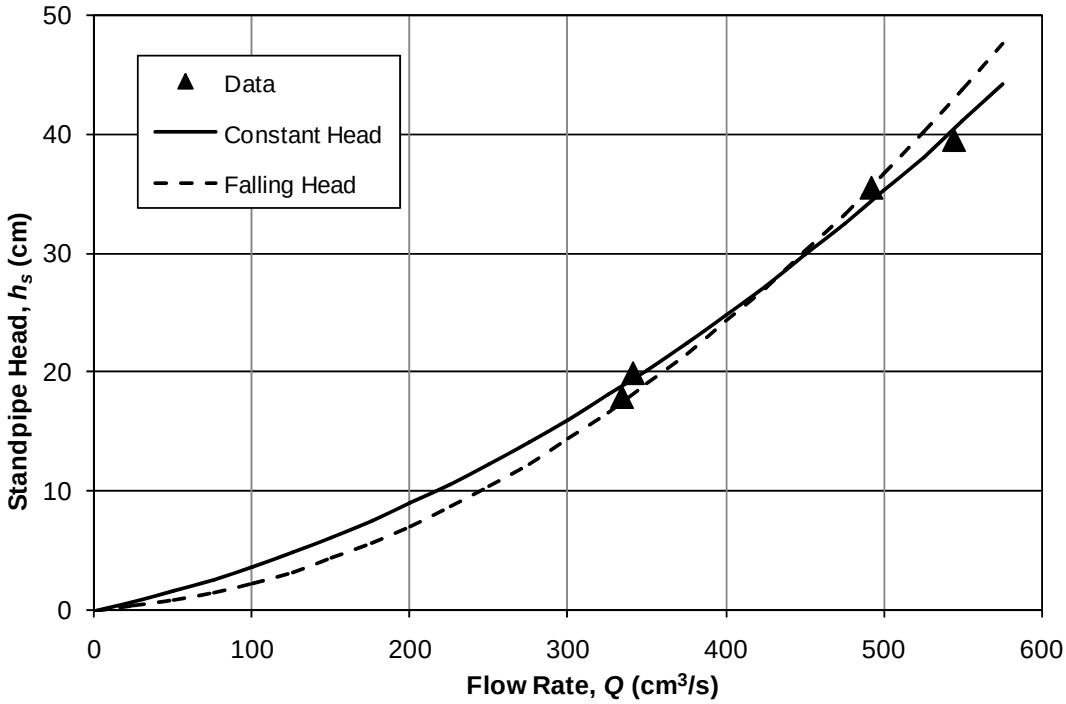

Figure 3-22: Comparison between constant and falling head field tests

3.4.2.4 Effect of Roadway Slope

The final assumption that was investigated in this research study is the impact of gravity on the flow conditions due to the effect of the roadway slope. The longitudinal slope and cross slope of the roadway surface create a constant conveyance of water through the PFC overlay due to gravity alone. Therefore, gravity may have an effect on the field conditions, which would most likely result in an artificially high hydraulic conductivity measurement. This is because water will be transported through the porous media by the established head in the standpipe as well as by gravity. Since gravity is not included in any of the falling head equations, the transport of water by gravity would be attributed to the head difference, resulting in a high hydraulic conductivity estimate.

This is addressed by considering the following equation for the change in head through the test apparatus, i.e. the change in head from the inflow area to the outflow area:

$$h_s(\theta) = h_s + sR_c\cos(\theta) \tag{3.38}$$

In Equation (3.38), $\theta = 0$ corresponds to the downslope direction and s is the slope of the roadway; h_s is the change in head as before, but now corresponds specifically for a flat surface, i.e. $\theta = \pi/2$. Now, if we assume each flow path leading from the standpipe is independent, then the incremental discharge in the θ-direction can be given as:

$$\delta Q(\theta) = \frac{\alpha}{2\beta}\left[\sqrt{1+\frac{4\beta(h_s + sR_c\cos(\theta))}{\alpha^2}} - 1\right]\delta\theta \qquad (3.39)$$

Equation (3.39) gives the incremental discharge $\delta Q(\theta)$ as a function of the change in head. The total discharge from the standpipe can be found by integrating Equation (4.3) as follows:

$$Q(h_s, s) = \frac{1}{\pi}\int_0^{\pi}\frac{\alpha}{2\beta}\left[\sqrt{1+\frac{4\beta(h_s + sR_c\cos(\theta))}{\alpha^2}} - 1\right]d\theta \qquad (3.40)$$

Equation (3.40) can be solved numerically with a simple finite difference code. Of primary interest is the impact of the roadway slope for the smallest head value measured during testing. At the end of the falling head test, the final time measurement is taken for a value of h_s = 3.8 cm (1.5 in.), and it should be expected that gravity will have the largest impact on the flow rate for this change in head. Table 4.1 calculates the flow rate from Equation (3.40) for multiple values of the roadway slope and then determines the percent error produced by the roadway slope when compared to zero slope. The modified Forchheimer coefficients used are α = 0.0204 s/cm^2 (0.132 s/in^2) and β = 1.57×10^{-4} s^2/cm^5(0.0166 s^2/in^5), as determined from a falling head test conducted on Loop 360.

As can be seen in Table 3.10, the effect of the roadway slope is less than one percent error for slopes less than 6%. On the roadways for which the field test has been conducted, the roadway slope is roughly 4%, which will result in a percent error of roughly half a percent. Therefore, it can be assumed that the roadway slope has very little impact on the falling head test results, and Equation (3.37) can be used without any modification to calculate the modified Forchheimer coefficients.

Table 3.10: Numerical results for effect of roadway slope

Slope, *s* (cm/cm)	***Q* (cm^3/s)**	**Percent Error (%)**
0.00	104.00	0.00
0.02	103.89	0.11
0.04	103.56	0.43
0.06	102.98	0.98
0.08	102.16	1.78

3.4.2.5 Establishment of No Flow Boundary

The two main assumptions made in analyzing the falling head test are saturated pore space and the upper and lower no flow boundary conditions. The assumption of saturated pore space is addressed in Section 3.4.2.2. The lower no flow boundary is assumed to be created due to the underlying impervious pavement surface and cannot be verified through testing. However,

there is no reason to believe that the lower no flow boundary is not established. Therefore, the main concern is whether the upper no flow boundary is properly established between the PFC surface and the metal base plate. Vacuum grease is used to create this no flow surface. As mentioned in Section 3.4.2.1, the vacuum grease will cause the metal base plate to stick to the surface if properly used. In this event, it is assumed that a good bond was obtained during testing and the no flow boundary was subsequently created. In order to confirm the creation of a no flow boundary, the test apparatus was used on conventional impervious asphalt and impervious concrete surfaces. The same test procedure outlined above was used on these two surfaces in order to determine whether there was significant flow between the impervious surfaces and the metal base plate. The falling head test was conducted and on the concrete surface, the total drainage time was nearly 11 minutes; on the asphalt surface, the total drainage time was nearly 30 minutes. Therefore, although this does not create a perfect no flow boundary, the flow is small enough that it can be considered negligible. When compared to the longest drainage time observed in the field on PFC, this drainage accounts for less than 5% error. Furthermore, this test helped to confirm that roughly 200 to 230 mL of vacuum grease is sufficient to create the no flow boundary under dry testing conditions.

3.4.3 Field Test Results

3.4.3.1 TxDOT Field Test Results

The current TxDOT field test described in Section 4.1 does not give any indication of the hydraulic conductivity of the PFC, but instead reports the drainage time for the falling head test. TxDOT guidance suggests that the typical drainage time is normally less than 20 sec for newly constructed PFC mixtures. Several TxDOT falling head tests have been conducted in the field during the core extraction process, and the TxDOT results are reported in Table 3.11.

Table 3.11: TxDOT field test results

Roadway	Location	Date	Drainage Time (sec)
Loop 360	Shoulder	6-29-08	17.84
Loop 360	Shoulder	6-29-08	19.81
Loop 360	Shoulder	2-2-09	14.28
Loop 360	Travel Lane	2-2-09	16.45
Loop 360	Shoulder	2-5-10	12.62
Loop 360	Travel Lane	2-5-10	19.82
FM 1431	Travel Lane	2-2-09	112.61
RR 620	Travel Lane	2-2-09	69.73
RR 620	Travel Lane	2-5-10	44.98

The results from the TxDOT field test suggest that Loop 360 has retained relatively good drainage capacity throughout its life. None of the drainage times exceed 20 sec for all Loop 360 tests. However, for both FM 1431 and RR 620, drainage times were significantly greater than the 20 sec guideline, suggesting that these two roadways have experienced significant clogging. Although this test provides information on the drainage capacity of the PFC, it does not indicate

whether the drainage capacity is sufficient for providing proper drainage benefits. The minimum average flow rate which is considered acceptable under the TxDOT procedure is 255 cm^3/s (15.6 in^3/s). This average flow rate will be compared to average flow rates determined from the CRWR test procedure in the following section.

3.4.3.2 CRWR Field Test Results

In order to better measure the in-situ hydraulic conductivity of PFC, the new CRWR field test described in Section 3.4.2.1 can be used to determine the modified Forchheimer coefficients, which give an indication of the hydraulic conductivity as described in Section 3.5. Table 3.12 provides the results of the CRWR field falling head test. The middle and final times are reported with plus/minus one standard deviation together with the resulting modified Forchheimer coefficients calculated using Equation (3.37).

Table 3.12: CRWR field test results

Roadway	Location	Date	t_1 (sec)	t_2 (sec)	α (s/cm^2)	β (s^2/cm^5)
Loop 360	Shoulder	6-29-08	3.92±0.14	11.12±0.22	0.0204	1.57×10^{-4}
Loop 360	Shoulder	6-29-08	4.28±0.13	12.36±0.30	0.0254	1.81×10^{-4}
Loop 360	Shoulder	9-25-08	4.07±0.18	11.75±0.16	0.0238	1.65×10^{-4}
Loop 360	Shoulder	9-25-08	4.17±0.19	11.90±0.41	0.0216	1.80×10^{-4}
Loop 360	Shoulder	11-9-08	3.88±0.15	10.63±0.01	0.0093	1.84×10^{-4}
Loop 360	Shoulder	11-23-08	3.27±0.00	9.05±0.05	0.0100	1.26×10^{-4}
Loop 360	Shoulder	2-2-09	4.46±0.14	12.88±0.21	0.0262	1.97×10^{-4}
Loop 360	Travel Lane	2-2-09	4.30±0.22	12.17±0.46	0.0197	2.00×10^{-4}
Loop 360	Shoulder	2-5-10	3.97±0.11	11.33±0.14	0.0206	1.64×10^{-4}
Loop 360	Travel Lane	2-5-10	3.47±0.19	10.11±0.16	0.0223	1.15×10^{-4}
FM 1431	Travel Lane	2-2-09	17.35±1.15	52.16±3.13	0.1430	2.50×10^{-3}
RR 620	Travel Lane	2-2-09	9.17±0.02	25.86±0.40	0.0403	9.17×10^{-4}
RR 620	Travel Lane	2-5-10	10.89±0.30	32.12±0.19	0.0784	1.07×10^{-3}

The results of the new field test also show that FM 1431 and RR 620 are more clogged than Loop 360 due to the longer drainage times. In addition, it appears that the modified nonlinear Forchheimer coefficients are significantly smaller than what was determined from the constant head laboratory tests on the core specimens report in Section 3.3.4.1. This can be attributed to the larger testing apparatus used in the field. The numerical model described in Section 3.5 will show that we expect smaller coefficients as the standpipe and/or core radii increase.

On Loop 360 there are several hydraulic conductivity tests that were conducted with both the TxDOT and CRWR field tests at the same location. A correlation was attempted to relate the two results for these paired tests; however, no relationship could be found between the two tests.

The final drainage time and average flow rate during the test were analyzed for comparison, but again no relationships were found. Therefore, test results from the TxDOT test cannot be used to estimate the results of the CRWR test in order to obtain a value for the hydraulic conductivity.

A final assessment of the field data is to compare the average flow rates obtained from the CRWR test to the minimum recommended flow rate based on the TxDOT guideline of 255 cm^3/s (15.6 in^3/s). As with the TxDOT field test results, both FM 1431 and RR 620 had smaller average flow rates when conducted with the CRWR field test. However, on Loop 360, half of the test results from the CRWR test have average flow rates less than the minimum suggested TxDOT guideline. Therefore, although the TxDOT test showed that the flow rates observed on Loop 360 were greater than the minimum suggested flow rate, the CRWR test shows that half of the flow rates are smaller than the guideline flow rate. The CRWR field tests result in very similar in-situ hydraulic conductivity values, signifying that the TxDOT guideline is not applicable for other testing devices.

3.4.3.3 Sensitivity of Time Measurement

The use of a stopwatch for measuring time during the falling head test in the field is useful as it provides a simple measuring device that is inexpensive and readily available. However, the use of such a device can result in some discrepancy due to possible human error. For this reason, it is recommended that the time measurements from three falling head tests be averaged in order to reduce any human error. To determine the uncertainty which can result from human error, a sensitivity analysis on the time measurements is provided here. Sensitivity is quantified by incrementally increasing or decreasing the actual time measurements observed in the field and determining the resulting change to the modified Forchheimer coefficients calculated from Equation (3.37).

A falling head field test conducted on Loop 360 has the following averaged time-depth measurements with plus/minus one standard deviation: $h_s(t_0)$ = 40.4 cm (16 in), $h_s(t_1)$ = 22.1 cm (8.70 in), $h_s(t_2)$ = 3.8 cm (1.5in), t_0 = 0 sec, t_1 = 3.89 ± 0.14 sec, and t_2 = 11.12 ± 0.22 sec. This results in the following modified Forchheimer coefficients: α = 0.0204 s/cm^2 (0.132 s/in^2) and β = 1.57×10^{-4} s^2/cm^5(0.0166 s^2/in^5). The sensitivity analysis will be conducted by either increasing or decreasing the two time measurements by Δt = 0.1 sec or 0.2 sec and determining the resulting percent change of the modified Forchheimer coefficients when compared to the above reported values.

Figure 3-23 and Figure 3-24 show the sensitivity on the linear and nonlinear modified Forchheimer coefficients, respectively. The four curves correspond to changes to the middle time (t_1), final time (t_2), both times in the same direction (both times increased or decreased), and both times in the opposite direction (middle time increased with final time decreased and vice versa). Clearly small changes in the time measurements can result in large changes to the calculated modified Forchheimer coefficients. The sensitivity to the linear coefficient is greater than that of the nonlinear coefficient, which is unfortunate because it is the linear coefficient that will be used to determine the in-situ hydraulic conductivity. However, the field tests conducted to date have resulted in very reliable and repeatable data when the average of three time measurements is used. Therefore, when conducted properly, the proposed field test is considered reliable. The in-situ hydraulic conductivity data reported in Section 3.5.5.5 show very little variability, suggesting sensitivity in time measurements is not a major source of error.

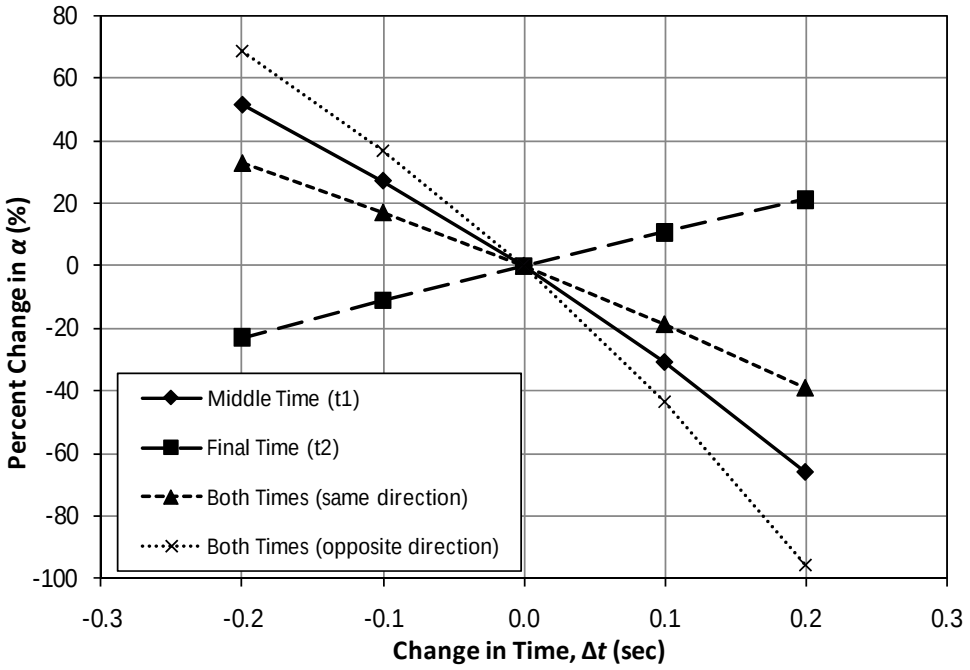

Figure 3-23: Time sensitivity of linear modified Forchheimer coefficient

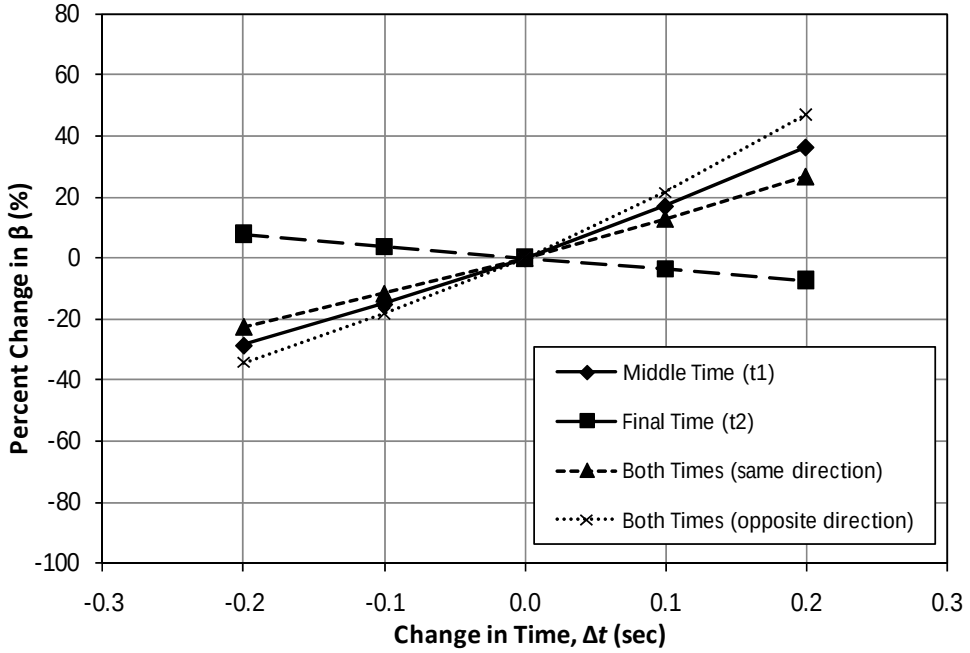

Figure 3-24: Time sensitivity of nonlinear modified Forchheimer coefficient

It should be noted that the above sensitivity analysis was conducted on data obtained from Loop 360, which has the best drainage properties of all three roadways and will therefore have the largest sensitivity to small changes in time. The sensitivity analysis can be conducted on the other roadways with larger drainage times and it can be shown that for FM 1431, for example, the change in modified Forchheimer coefficients is less than ±10% error.

Consequently, the larger the drainage times, the less sensitive the result is to small changes in the time measurements. As shown in Section 3.4.3.2, the larger drainage times tend to have more variability than the shorter times, which suggests that although the time measurements can be very sensitive to small changes in time, in general, we would not expect to see significant errors from our field measurements. This simply provides a method to quantify the possible uncertainty in the measurements.

3.4.3.4 Comparison to Video Results

In an effort to determine how accurate the field test results are at fully defining the falling head test by only reporting three time-depth measurements, a video of the falling head test was recorded. From the video, multiple points can be measured instead of the suggested three points during the test. A graph of head versus time can be accurately determined from the video. This curve can then be compared to the corresponding times calculated from Equation (3.37) for each of the head values using the modified Forchheimer coefficients determined from the average of three falling head tests. The goal is to show that the three time-depth measurements taken during the falling head test are sufficient to fully characterize the results of the falling head test.

Two videos were taken of the falling head test at Loop 360 and RR 620 on February 5, 2010. Prior to taking these videos, the falling head test procedure defined in Section 3.4.2.1 was conducted in order to determine the modified Forchheimer coefficients. Figure 3-25 and Figure 3-26 show the curves of standpipe head versus time for RR 620 and Loop 360, respectively.

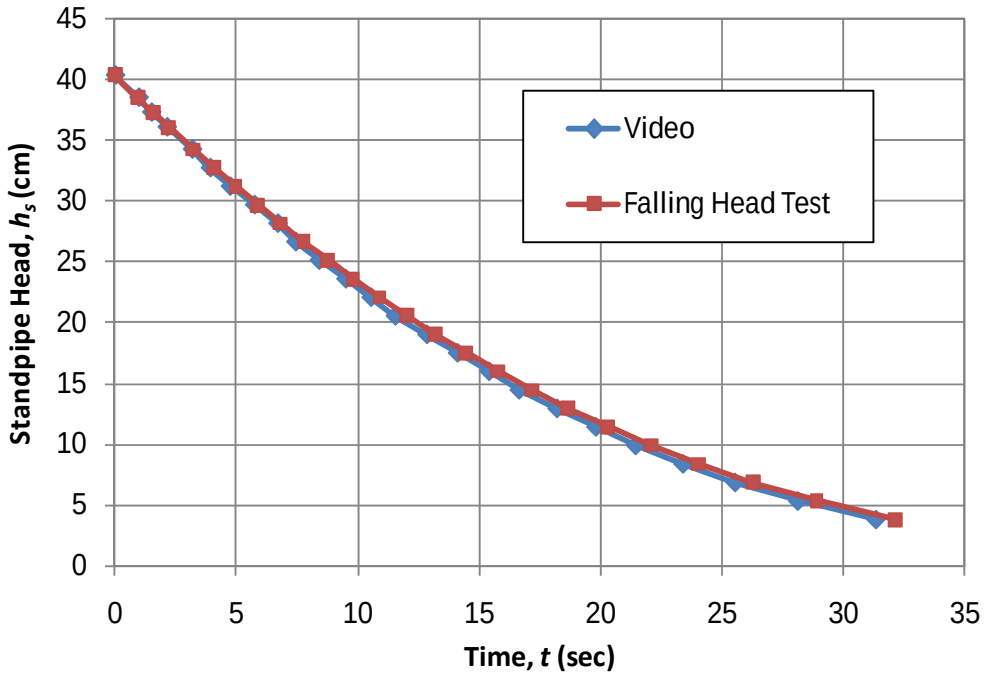

Figure 3-25: Comparison of falling head test to video on RR 620

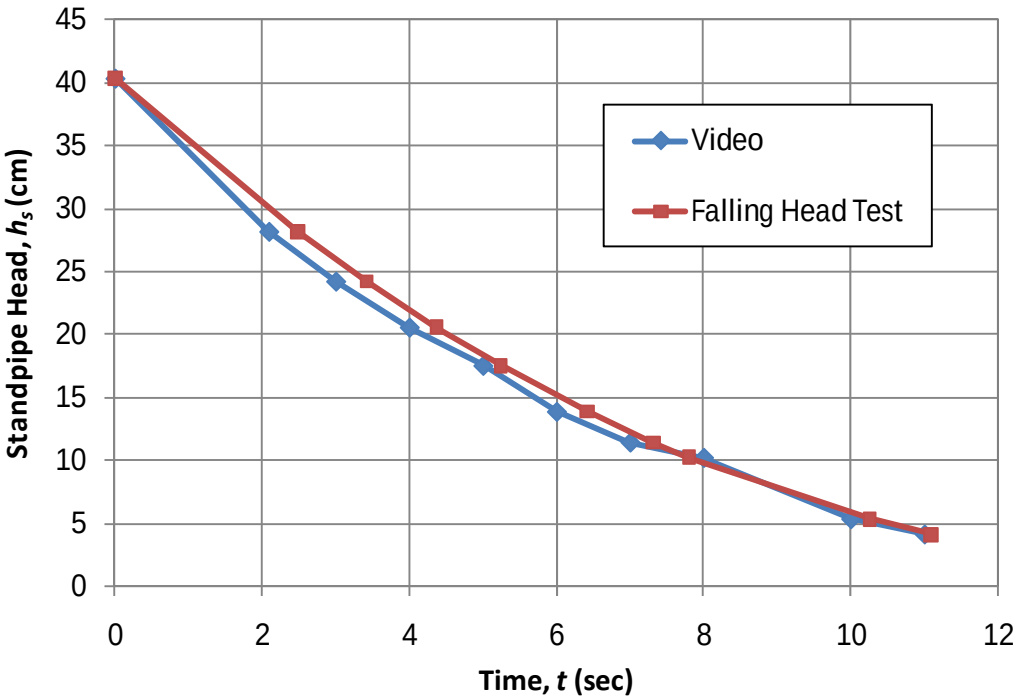

Figure 3-26: Comparison of falling head test to video on Loop 360

The hydraulic conductivity on RR 620 is much lower than Loop 360, resulting in a longer time scale on RR 620 and the head in the standpipe decreasing at a slower rate. Because of this, it was easier to view the change in head on RR 620 from the video. On Loop 360, not only was the standpipe head falling faster, but the video was not zoomed in enough in order to accurately determine the change in time for less than a second. Because of the inability to decipher the change in time for less than a second, the "Video" curve in Figure 3-26 is not smooth. However, both videos produce a curve very similar to what was observed from the falling head test using Equation (3.37). Furthermore, the standard error can be calculated between the two curves in order to quantify the error involved in the falling head test. The standard error corresponds to the difference between the observed time in the video compared to the calculated time from the falling head test. The standard error on RR 620 for this test is 0.43 sec; the standard error on Loop 360 is 0.31 sec. Both tests produce reliable results, and this comparison shows that simply taking three time-depth measurements for the falling head test is sufficient to fully characterize the results of the falling head test.

3.5 Numerical Modeling

3.5.1 Purpose of Numerical Model

Experimental studies have shown that under the large hydraulic gradients imposed during testing conditions, flow through PFC exhibits a nonlinear flow relationship which can be modeled using the Forchheimer equation. However, due to the two-dimensional flow paths observed in both lab tests of PFC core specimens and field tests, the use of a modified Forchheimer equation for the global conditions of the PFC was introduced. Experimental testing will result in determination of the two modified Forchheimer coefficients (α and β or ξ and η),

but give no indication of the original Forchheimer coefficients (a and b or K and n). In order to determine a relationship between the modified and original Forchheimer coefficients, a numerical model is needed. The proposed numerical model solves the continuity equation in two-dimensional cylindrical coordinates using a finite difference scheme.

The purpose of this numerical model is to solve the continuity equation using the original Forchheimer equation for various assumed values of a and b. The result will give the head distribution through a core specimen for a specified value of the head on the standpipe, h_s. With this head distribution, the flow rate Q through the core specimen can be calculated based on the outflow hydraulic gradient. Simulating multiple values of h_s and calculating the corresponding flow rate will create a curve of h_s versus Q. From this curve the values of the modified Forchheimer coefficients can be determined by regression. Therefore, the inputs to the model are the core geometry (R_s, R_c, and b_c), the original Forchheimer coefficients (a and b), and the head on the standpipe (h_s). The output from the model is the flow rate (Q) and ultimately the modified Forchheimer coefficients (α and β) when multiple values of h_s are simulated. Essentially, this numerical model is analogous to the constant head tests conducted in the laboratory. The goal of the model is to relate the original Forchheimer coefficients to the modified Forchheimer coefficients so that we are able to determine the hydraulic conductivity from the modified Forchheimer coefficients. The numerical model was written in FORTRAN using a finite difference scheme.

3.5.2 Modeling of Linear Flow

Prior to modeling the Forchheimer equation we will investigate a simpler case for linear flow through a PFC core specimen using Darcy's law. The modeling of the linear case is beneficial in order to compare to the nonlinear case and therefore determine where the nonlinear effects have the greatest impact on the head distribution through the core, as well as to test whether the nonlinear solution approaches the linear solution for small values of h_s or b. The method shown below is similar in approach to that presented by Charbeneau et al. (in press). However, the nonlinear effects will be fully incorporated by the numerical model developed for the present research study, which is an improvement over the Charbeneau et al. approach.

3.5.2.1 Approximate Analytical Solution

As previously mentioned, the PFC core specimen is cylindrical with a radius of R_c and thickness b_c. The coordinate system can be taken as cylindrical coordinates with the origin centered on the top surface of the core and the vertical z-direction positive downward. The flow during a constant head test has vertical flow from the standpipe with radius R_s centered on the top of the specimen and radial flow along the edges of the core radius R_c. The setup is shown schematically in Figure 3-27. The established head in the standpipe, h_s, is uniform over the source disk $0 \le r \le R_s,\ z = 0$. The constant head along the outflow boundary is taken as the datum, so that $h = 0$ on $r = R_c,\ 0 \le z \le b_c$.

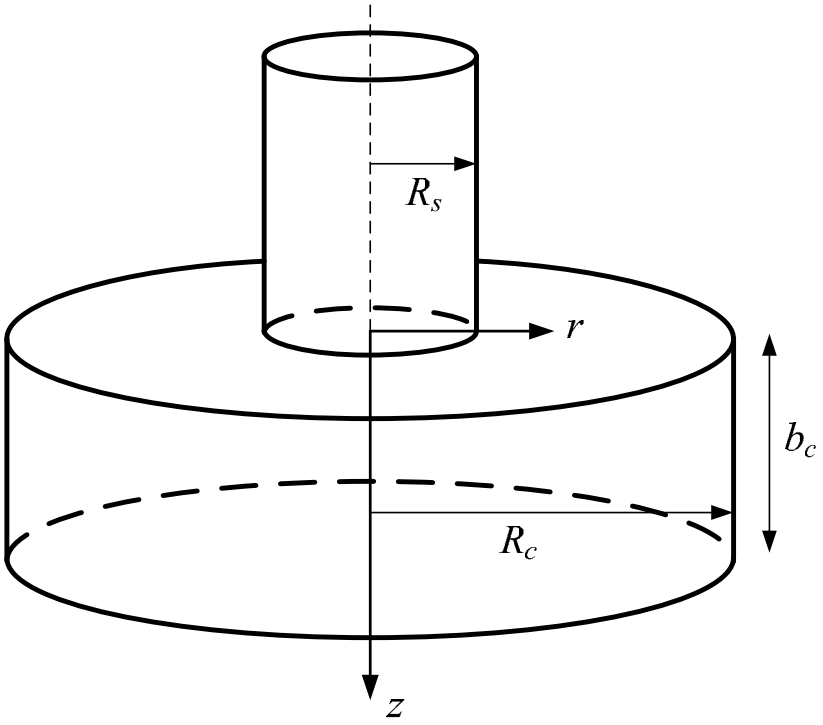

Figure 3-27: Coordinate system and core dimensions

As mentioned in Section 3.2.1, flow through most typical porous media generally follows Darcy's law, so this linear relationship will be examined for the time being as a first approximation to the nonlinear case. Darcy's law as a vector function is given as:

$$\vec{q} = -K\vec{I} \tag{3.41}$$

For the PFC core setup described above, Equation (3.41) can be used in the continuity equation in cylindrical coordinates to determine the governing equation for Darcy flow. In two-dimensional cylindrical coordinates, the continuity equation can be written as:

$$\frac{1}{r}\frac{\partial}{\partial r}\left(r\vec{q}_r\right)+\frac{\partial \vec{q}_z}{\partial z}=0 \tag{3.42}$$

And with the substitution of Darcy's law:

$$\frac{1}{r}\frac{\partial}{\partial r}\left(rK_r\vec{I}_r\right)+\frac{\partial K_z\vec{I}_z}{\partial z}=0 \tag{3.43}$$

The general continuity equation assumes a constant fluid density, as well as no flow in the θ-direction. Assuming an isotropic hydraulic conductivity, $K_r = K_z = K$, and substituting the

change in head for each hydraulic gradient results in the governing two-dimensional continuity equation for an isotropic hydraulic conductivity using Darcy's law:

$$\frac{1}{r}\frac{\partial}{\partial r}\left(r\frac{\partial h}{\partial r}\right)+\frac{\partial^2 h}{\partial z^2}=0 \qquad (3.44)$$

The continuity equation in cylindrical coordinates for linear flow has been solved analytically by Carslaw and Jaeger (1959, pg. 215) through the use of Bessel functions. The Carslaw and Jaeger solution is for an infinite medium and has the following solution:

$$h^*(r,z)=\frac{2}{\pi}h_s\sin^{-1}\left(\frac{2R_s}{\sqrt{(r-R_s)^2+z^2}+\sqrt{(r+R_s)^2+z^2}}\right) \qquad (3.45)$$

In Equation (3.45) the head $h^*(r,z)$ represents the head distribution with boundary conditions that apply to an infinite core (R_c and b_c approach infinity). However, the boundary conditions for the laboratory core specimens used in this research study are finite. Therefore, the applicable boundary conditions for the experimental setup are as follows:

$$h(r,z)=h_s(t) \qquad [0\le r\le R_s;\ z=0] \qquad (3.46)$$

$$\frac{\partial h(r,z)}{\partial z}=0 \qquad [R_s<r\le R_c;\ z=0] \qquad (3.47)$$

$$h(r,z)=0 \qquad [r=R_c;\ 0\le z\le b_c] \qquad (3.48)$$

$$\frac{\partial h(r,z)}{\partial z}=0 \qquad [0\le r\le R_c;\ z=b_c] \qquad (3.49)$$

The first boundary condition, Equation (3.46), states that the head on the source disk is equal to the head in the standpipe, which can change as a function of time. For testing purposes, the head on the standpipe is allowed to reach steady state such that it is a constant with respect to time. Equation (3.47) defines a no flow boundary on the top surface of the core for a radius greater than the radius of the standpipe. Equation (3.48) is the constant head at the outflow boundary, which is taken as the datum and set to a value of zero. Equation (3.49) defines a no flow boundary along the entire bottom surface of the core.

The volumetric flow rate can be determined from the head distribution through the following relation based on a linear flow relationship:

$$Q=-2\pi K_z\int_0^{R_s} r\frac{\partial h(r,0)}{\partial z}\,dr=-2\pi R_c K_r\int_0^{b_c}\frac{\partial h(R_c,z)}{\partial r}\,dz \qquad (3.50)$$

The first part of Equation (3.50) calculates the flow rate that occurs across the inflow boundary, while the second part of the equation is the flow rate across the outflow boundary. The flow rate is not necessarily uniform over either the inflow or outflow boundary, but both equations should result in the same value to maintain continuity when Darcy's law is applicable.

Carslaw and Jaeger (1959) provide the solution to Equation (3.50) using the flow across the inflow boundary as follows:

$$Q = 4Kh_s R_s \tag{3.51}$$

Equation (3.51) has assumed an isotropic porous medium such that K_z is replaced with the generic hydraulic conductivity, K.

In order to determine the flow rate from the outflow boundary in Equation (3.50), a different approach is necessary. The effects of the finite vertical and radial dimensions are approximately addressed through the introduction of a linear shape factor F in Equation (3.51), which is changed to:

$$Q = 4Kh_s R_s F \tag{3.52}$$

Setting Equation (3.52) equal to the second part of Equation (3. 50) shows that the linear shape factor is defined by:

$$F = -\frac{\pi}{2}\frac{R_c}{R_s}\frac{1}{h_s}\int_0^{b_c}\frac{\partial h(R_c, z)}{\partial r}dz \tag{3.53}$$

The practical issue becomes how to evaluate Equation (3.53) while taking into account the finite size of the PFC core specimen. The effects of the finite vertical dimension of the core are approximately addressed using the method of images in order to establish the no flow boundary conditions. However, the addition of each image (or image pair) alters the head both across the inflow and outflow boundaries. Head values are calculated using:

$$h(r, z; N_i) = \frac{2}{\pi}h_s \sum_{j=-N_i}^{N_i} \sin^{-1}\left(\frac{2R_s}{\sqrt{(r-R_s)^2 + (z+2jb_c)^2} + \sqrt{(r+R_s)^2 + (z+2jb_c)^2}}\right) \tag{3.54}$$

In Equation (3.54), $h(r,z;N_i)$ is the approximate solution to the Darcy continuity equation using the method of images, is a function of the r- and z-directions, and also depends on the number of image pairs, N_i. The image $j = 0$ corresponds to the basic solution given by Equation (3.45). The image $j = 1$ corresponds to a source disk located a distance $z = 2b_c$ below the surface ($z = 0$). This image attempts to make the plane $z = b_c$ a no flow boundary according to Equation (3.49); however, it causes an upward gradient across the $z = 0$ surface. The image $j = -1$ attempts to cancel this upward gradient, etc. This image solution satisfies the continuity Equation (3.44), and as the number of images is increased, the no flow boundary conditions are more closely met.

The question remains of how well this approximate solution can satisfy the constant uniform head conditions along the inflow and outflow boundaries.

The effects of the finite radial dimension of the core can be addressed by nondimensionalizing the head distribution $h(r,z;N_i)$ for a unit head difference given the variable $H_u(r,z;N_i)$. This is accomplished by nondimensionalizing with respect to the head difference between the inflow and outflow areas. For the inflow area, the approximate head value can be described as the head at the location of mid-area within the standpipe. This mid-area location occurs at $r = R_s/\sqrt{2}$, $z = 0$. The head at the outflow boundary is given as $\bar{h}_b(r = R_c, b_c; N_i)$:

$$\bar{h}_b(r = R_c, b_c; N_i) = \frac{1}{b_c}\int_0^{b_c} h(R_c, z; N_i)dz \tag{3.55}$$

Therefore, the normalized unit head difference, H_u, can be calculated as:

$$H_u(r, z; N_i) = \frac{h(r, z; N_i) - \bar{h}_b(R_c, b_c; N_i)}{h(R_s/\sqrt{2}, 0; N_i) - \bar{h}_b(R_c, b_c; N_i)} \tag{3.56}$$

This results in a head distribution with a value of one at the standpipe inflow area and a value of zero at the outflow boundary. The contours of the head along the core are shown in Figure 3-28 and Figure 3-29. These figures are normalized to the core radius, R_c, with Figure 3-28 having a vertical dimension of $b_c/R_c = 1$ and Figure 3-29 having $b_c/R_c = 0.5$. The inflow boundary for both figures occurs for $r/R_c < 0.25$, $z/b_c = 0$. The inflow is initially entirely vertical flow. The outflow boundary occurs at $r/R_c = 1$, and is purely radial. Furthermore, the comparison of the two figures shows that for a smaller relative core thickness, the head distribution becomes purely radial at a much faster rate.

The actual head distribution is equal to the head on the standpipe times the unit head distribution:

$$h(r,z;N_i) = h_s H_u(r,z;N_i) \tag{3.57}$$

Because this is a linear problem, the head can be nondimensionalized in this manner and the use of Equation (3.57) is appropriate. This will not be the case for nonlinear flow as shown in Section 5.3.7.

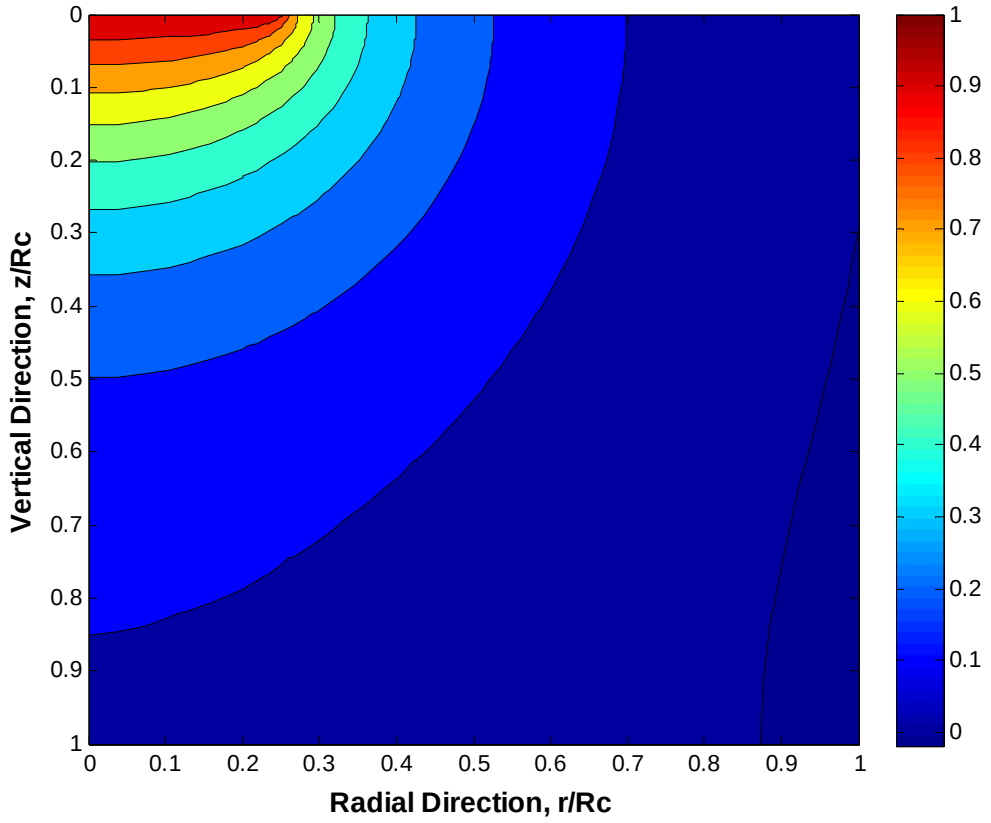

Figure 3-28: Contour plot of normalized unit head distribution for linear flow using method of images analytic solution with R_s/R_c = 0.25 and b_c/R_c = 1

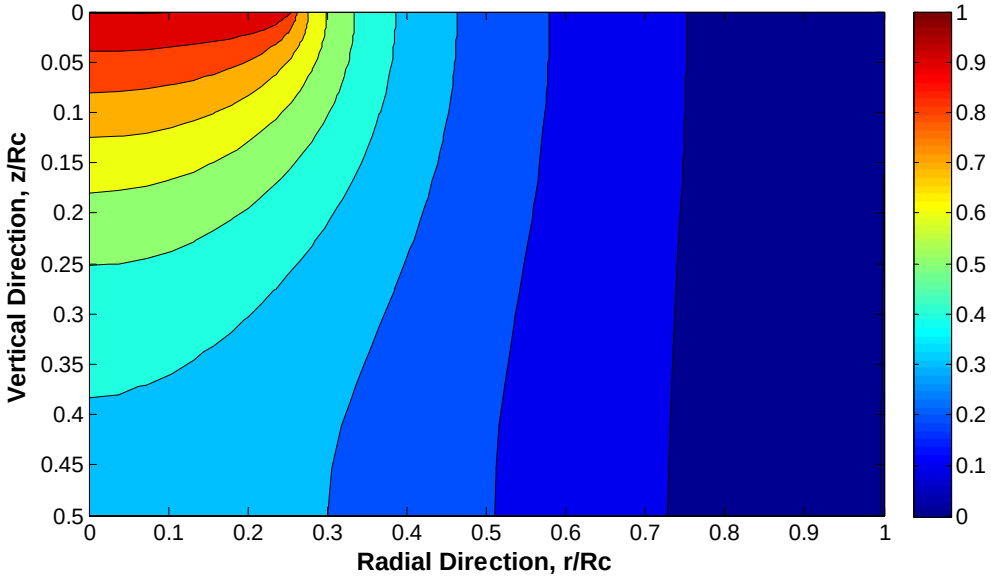

Figure 3-29: Contour plot of normalized unit head distribution for linear flow using method of images analytic solution with R_s/R_c = 0.25 and b_c/R_c = 0.5

The method of images used in the solution shown in Equation (3.54) and the normalized solution in Equation (3.56) is used to create the no flow boundary at the top and bottom of the PFC core. However, this method has an impact on the constant head boundaries at the inflow and outflow areas. For the inflow area, the solution with $N_i = 0$ provides the exact constant head required by the boundary condition in Equation (3.46). As the value of N_i is increased, the head is no longer constant along this inflow boundary. On the other hand, for the outflow area, the solution with $N_i = 0$ does not provide a constant head at the outflow boundary as specified in Equation (3.48). As the value of N_i increases, the head approaches the required constant head at the outflow boundary. To summarize, as the number of images is increased, the solution better approximates the two no flow boundaries and the outflow constant head boundary, yet deviates from the required constant head inflow boundary.

The unit head difference approximate solution is evaluated in Figure 3.30. Figure 3.30(a) shows the calculated radial distribution of head across the inflow boundary for an example with $R_s/R_c = 0.25$ and $b_c/R_c = 0.5$, which is the same head distribution shown in Figure 3-29. The solution without images ($N_i = 0$) exactly satisfies the boundary condition across the inflow surface. Addition of image pairs result in an increase in head at the center of the source area and a corresponding decrease in head near the boundary of the inflow area. However, with just a few images, the overall error is less than one-half percent from the unit value imposed. The use of $r = R_s/\sqrt{2}$ for determining the head on the inflow boundary is the location where $H_u = 1$ in Figure 3-30(a) with the addition of image pairs. Figure 3-30(b) shows the head distribution across the outflow boundary. Addition of source images improves the approximate solution accuracy for a constant head along this boundary, with use of only a few images giving a solution within about 0.1 percent accuracy. The overall solution behavior is shown in Figure 3-30(c) with $N_i = 100$. This figure shows the vertical head distribution at different radial stations from the center of the specimen to the edge. The first two stations are within the source zone such that the head at the upper boundary is unity. The vertical gradient beneath the source region is greater towards the sides of the inflow boundary than in the middle of the inflow boundary. The radial gradient is largest along the upper no flow boundary, but the radial gradient becomes fairly uniform near the outflow boundary. Both vertical and horizontal flow components are important.

The shape factor definition from Equation (3.53) and the approximate image solution from Equation (3.54) show that the linear shape factor is a function of the size of the core (specimen volume) and the radius of the standpipe under linear flow conditions. This may be expressed and calculated through a dimensionless form:

$$F = F\left(\frac{R_s}{R_c}, \frac{b_c}{R_c}\right) \tag{3.58}$$

The shape factor typically has a magnitude near unity for the linear flow conditions. For example, with the geometry used to calculate results shown in Figure 3-30, one can calculate $F(0.25,0.5) = 1.08$. Values for the shape factor F are presented in Table 3.13 for varying R_s/R_c and b_c/R_c. F is designated as a linear shape factor because it is determined from an approximate solution using the method of images of the linear Darcy-type flow equation. The linear shape factor cannot be used once nonlinear flow effects are taken into account.

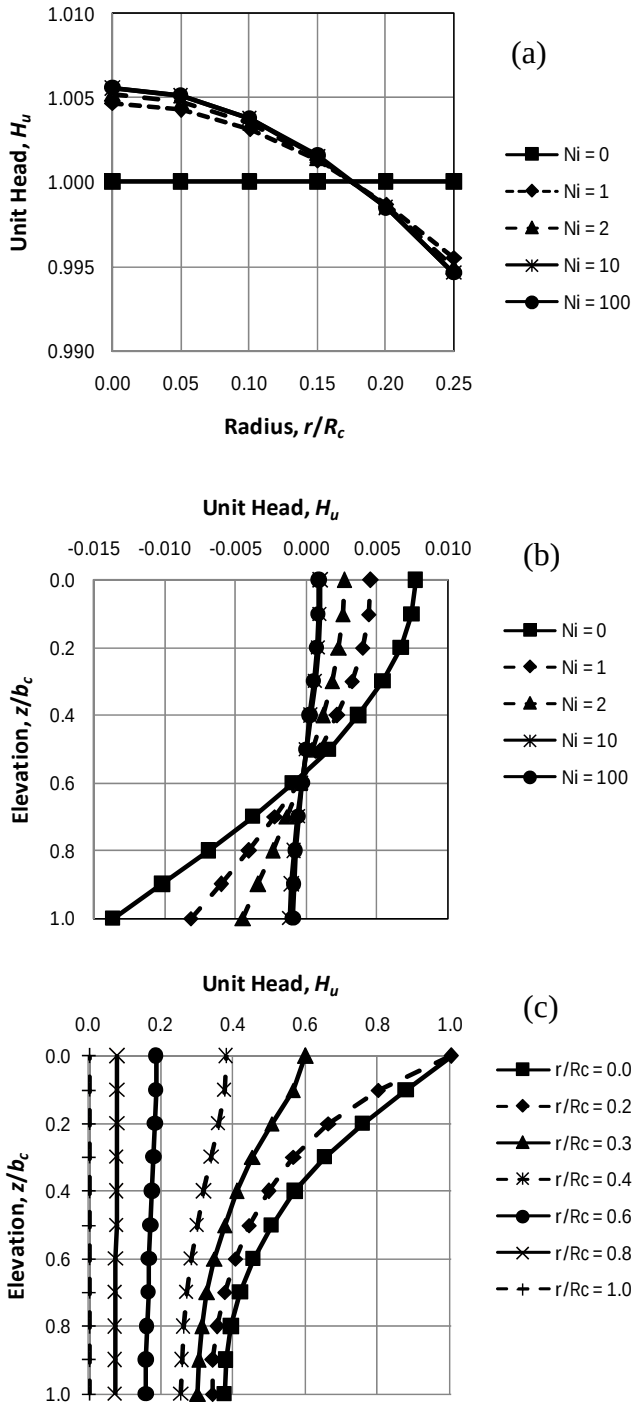

Figure 3-30: Normalized unit head difference solution using method of images: (a) inflow boundary, (b) outflow boundary, (c) overall solution behavior for NRiR = 100

Table 3.13: Linear shape factor values using method of images

R_s/R_c \ b_c/R_c	0.20	0.25	0.30	0.35	0.40	0.45	0.50	0.55	0.60
0.05	0.911	0.956	0.985	1.004	1.017	1.027	1.034	1.039	1.042
0.10	0.826	0.900	0.950	0.985	1.010	1.029	1.042	1.052	1.060
0.15	0.765	0.856	0.922	0.970	1.006	1.032	1.052	1.067	1.079
0.20	0.722	0.824	0.901	0.960	1.005	1.039	1.065	1.084	1.100
0.25	0.693	0.802	0.888	0.955	1.008	1.048	1.080	1.104	1.123
0.30	0.675	0.789	0.882	0.956	1.015	1.062	1.099	1.127	1.150
0.35	0.666	0.784	0.883	0.963	1.028	1.080	1.122	1.155	1.181
0.40	0.664	0.787	0.891	0.977	1.047	1.104	1.150	1.186	1.216
0.45	0.670	0.797	0.906	0.997	1.072	1.134	1.184	1.224	1.256
0.50	0.682	0.814	0.928	1.024	1.104	1.170	1.224	1.268	1.303

If flow through the PFC core specimen experienced linear flow, the hydraulic conductivity could be determined from Equation (3.52) once a relationship between h_s and Q is determined. The use of this equation takes into account flow in two-dimensional cylindrical coordinates as well as the core geometry. However, this solution only applies to linear flow which follows Darcy's law. Therefore, although this is a valid solution, it does not apply to the nonlinear flow relationship observed in PFC. It is useful to provide an analytic solution in order to gain an understanding of how flow moves through the PFC core specimen which can be used to validate the more advanced numerical models which are described below.

3.5.2.2 Overview of Linear Numerical Model

The previous section describes an approximate analytical solution for two-dimensional linear flow through a core specimen using Darcy's law. The solution gives the head distribution throughout the core and the hydraulic conductivity can be calculated based on the relationship between the head on the standpipe h_s and the flow rate Q, as well as the core dimensions. A finite difference numerical model can be used to solve for the head distribution through the core with more precise inflow and outflow boundary conditions. The method of images used in the approximate analytical solution does not accurately meet the inflow and outflow boundary conditions. Therefore, a finite difference solution to the two-dimensional flow can be used to precisely meet these boundary conditions.

The finite difference model solves the same continuity equation given in Equation (3.44) with boundary conditions provided in Equation (3.46) through Equation (3.49). Furthermore, since the flow problem is symmetric about the center of the core, only half of the flow domain needs to be modeled. Symmetry introduces an additional boundary condition:

$$\frac{\partial h(r,z)}{\partial r} = 0 \qquad [r = 0;\ 0 \le z \le b_c] \tag{3.59}$$

Equation (3.59) states that the change in head in the radial direction is zero at the center of the core. Therefore, there is no radial flow across the center of the core. The finite difference model solves the continuity equation together with the five boundary conditions.

The following subsections describe the grid generation used in the finite difference model, the method used to address the singularity at r = 0 in the continuity equation, the

differencing scheme used to approximate the partial differential equation, and finally some results for the linear head distribution through the core specimen.

3.5.2.3 Grid Generation

The numerical model uses a finite difference scheme to solve the partial differential continuity equation in two-dimensional cylindrical coordinates. The finite difference grid used to solve this equation is described in detail in this section. Of particular interest in this finite difference model is to accurately model the core specimen geometry. Therefore, the grid must have nodes located precisely at the locations of the boundary conditions. This forces a node to be created at the center of the core $r = 0$. In addition, the boundary conditions change at the location of the standpipe radius, so a node must exist precisely at $r = R_s$. Finally, the core radius and core thickness also must be modeled correctly. As a result, the domain of the grid extends in the r-direction until $r = R_c$ and in the z-direction until $z = b_c$.

The largest hydraulic gradients are located directly under the standpipe. As the flow moves away from the standpipe, the gradients decrease in the vertical direction due to the no flow boundary. Also, as flow exits the core, the gradients are smaller due to the diverging nature of the flow. Because the highest gradients are located immediately under the standpipe, it is beneficial to refine the grid in this area. This is accomplished in the vertical direction by using an expansion ratio. The expansion ratio in the vertical direction is denoted as r_{ez}, and a vertical expansion ratio of $r_{ez} = 1.1$ is used for this finite difference scheme. This means that the difference between nodes is 10% larger than the previous difference for increasing z.

As previously mentioned, it is necessary to precisely model the radius of the standpipe. Therefore, a node is created at $r = R_s$, in addition to nodes at $r = 0$ and $r = R_c$. The nodes placed between these three points are also spaced with an expansion factor. The number of elements is explicitly stated for $0 \le r \le R_s$ and for $R_s \le r \le R_c$. Instead of using constant spacing in each of these domains, an expansion ratio is used in order to maintain the second order scheme described in Section 3.5.2.5 (Ferziger and Peric, 2002). Two separate expansion ratios are necessary in the radial direction: r_{er1} is the expansion ratio from $r = R_s$ to $r = 0$, and r_{er2} is the expansion ratio from $r = R_s$ to $r = R_c$.

The expansion ratios are calculated based on the initial element size around $r = R_s$. The radial elements on either side of the node at $r = R_s$ have a specified spacing of $\Delta r = 0.15$ cm (0.059 in). Both radial expansion ratios are calculated by this initial spacing and the remaining length of the domain (either R_s or $R_c - R_s$ depending on the direction in question). The initial spacing is given as:

$$\Delta r = \frac{L(1 - r_{er})}{1 - r_{er}^{\,n_i}} \tag{3.60}$$

L in Equation (3.60) is either R_s or $R_c - R_s$ depending on the direction in question, n_i is the number of elements in that direction, and r_{er} is either r_{er1} or r_{er2} depending on the direction. The only unknown in Equation (3.60) is r_{er} and it can be determined from a Newton-Raphson method (c.f. Ferziger and Peric, 2002). The Newton-Raphson method uses the function $f(r_{er})$ and its derivative $f'(r_{er})$ to extend a tangent line at the current guess of r_{er} until it crosses zero, and uses that location as the second guess of r_{er}. The method is repeated until the change in r_{er} values is very small. The function and its derivative used for this root-finding technique are:

$$f(r_{er}) = \frac{1 - r_{er}}{1 - r_{er}^{\,n_i}} - \frac{\Delta r}{L} \tag{3.61}$$

$$\frac{\partial f(r_{er})}{\partial r_{er}} = f'(r_{er}) = -\frac{r_{er}^{\,n_i}(n_i - 1) - r_{er}^{\,n_i - 1} n_i + 1}{\left(r_{er}^{\,n_i} - 1\right)^2} \tag{3.62}$$

The change in r_{er} values is designated as dr_{er} and is equal to:

$$dr_{er} = \frac{-f(r_{er})}{f'(r_{er})} \tag{3.63}$$

The initial guess value of r_{er} used is 1.1. This value can then be used in $f(r_{er})$ and $f'(r_{er})$ to determine dr_{er}, from which the second guess value can be determined. The process is repeated until dr_{er} becomes nearly zero. At this point, the root to Equation (3.60) has been found.

A typical grid generated from this numerical model is shown in Figure 3-31. The domain of this grid is R_c = 10.922 cm (4.3 in) and b_c = 3.468 cm (1.37 in). This is the typical domain of a PFC core specimen and R_s = 1.878 cm (0.739 in), which is the same value used during experimental testing. This grid has 40 elements in the *z*-direction, 10 elements for $r \le R_s$, 30 elements for $R_s \le r \le R_c$, and the following expansion ratios: r_{ez} = 1.1, r_{er1} = 1.049, and r_{er2} = 1.044.

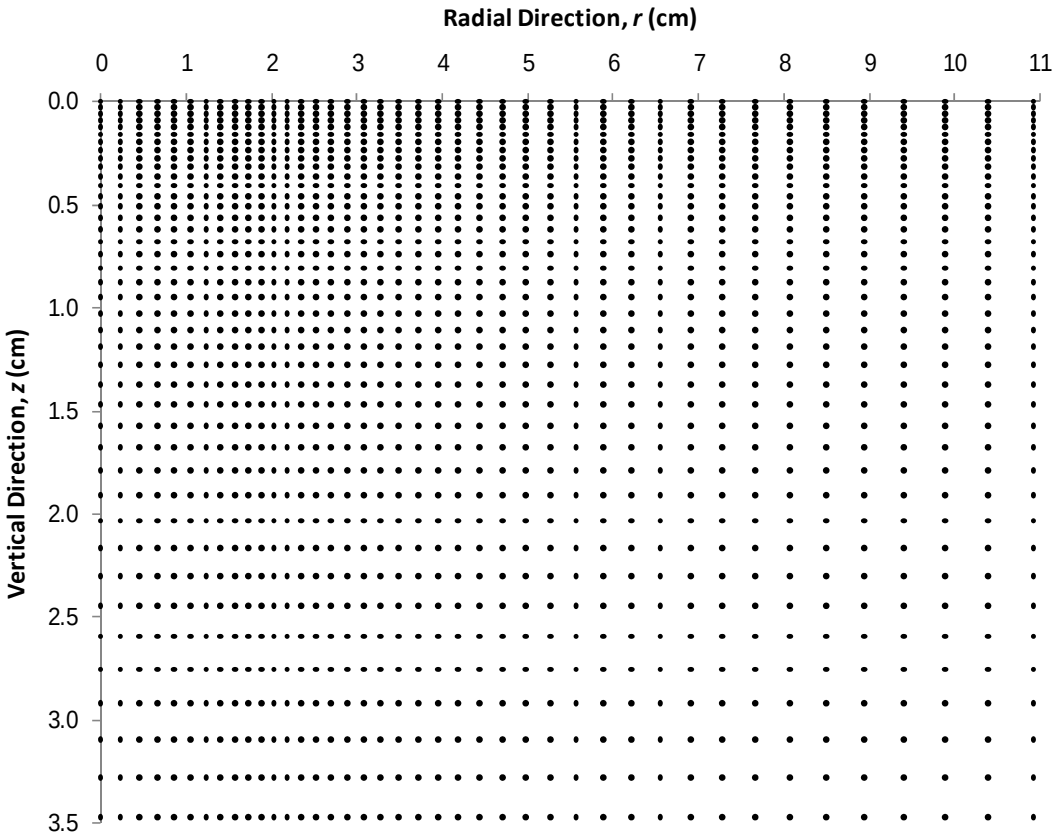

Figure 3-31: Typical grid generation

3.5.2.4 Singularity Removal for Linear Model

The continuity equation in cylindrical coordinates as written in Equation (3.44) has a singularity at $r = 0$. In other words, the equation cannot be solved for $r = 0$ due to the $1/r$ term approaching infinity. Therefore, this singularity must be removed in order to properly model the equation at $r = 0$. In order to accomplish this we can follow a similar procedure outlined by Smith (1965, pg. 44). The continuity equation written in Equation (3.44) can be expanded as follows:

$$\frac{1}{r}\frac{\partial h}{\partial r} + \frac{\partial^2 h}{\partial r^2} + \frac{\partial^2 h}{\partial z^2} = 0 \tag{3.64}$$

The singularity exists in the first term only and results in a value of 0/0 for $r = 0$ due to the symmetry boundary condition in Equation (3.59).

As described by Smith (1965), the first derivative can be expanded using a Maclaurin expansion to obtain:

$$\frac{\partial h(r,z)}{\partial r} = \frac{\partial h(0,z)}{\partial r} + r\frac{\partial^2 h(0,z)}{\partial r^2} + \frac{r^2}{2}\frac{\partial^3 h(0,z)}{\partial r^3} + \ldots \tag{3.65}$$

The first term on the right hand side of Equation (3.65) is equal to zero due to the symmetry boundary condition. If we drop the higher order terms, we can approximate the first derivative as:

$$\frac{\partial h(r,z)}{\partial r} \approx r \frac{\partial^2 h(0,z)}{\partial r^2} \tag{3.66}$$

Putting the above equation into the continuity Equation (3.64) and canceling the r terms gives the following continuity equation for $r = 0$:

$$2\frac{\partial^2 h}{\partial r^2} + \frac{\partial^2 h}{\partial z^2} = 0 \tag{3.67}$$

The use of Equation (3.67) removes the singularity at $r = 0$ and can be used in the finite difference model to determine the head at the center of the core.

3.5.2.5 Linear Model Differencing Scheme

The differencing scheme used to solve the partial differential equation is a second order, five point central difference scheme (CDS). The computational node is shown in Figure 3-32 for node i,j where i represents the radial direction and j represents the vertical direction. Node i,j is located at radial location r_i and vertical location z_j.

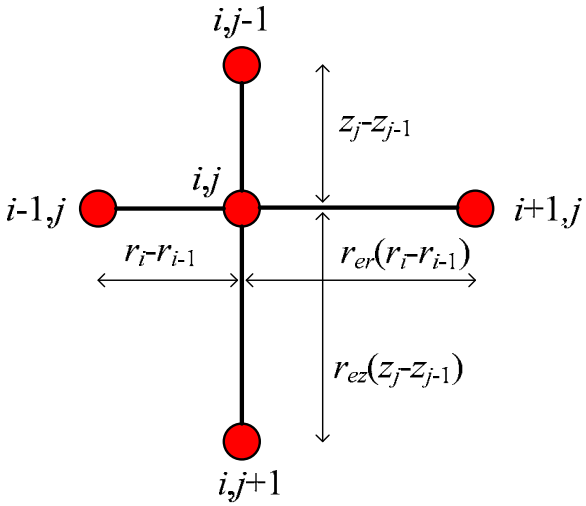

Figure 3-32 Computational node schematic for linear model

The equation being solved for the linear solution is the two-dimensional continuity equation in cylindrical coordinates. However, the Crank-Nicolson method will be used to solve the equation in pseudo-time. This is essentially the time dependent solution, except the hydraulic conductivity has been removed from the equation. Therefore, the equation being solved for the linear solution is:

$$\frac{\partial h}{\partial t} = \frac{1}{r}\frac{\partial h}{\partial r} + \frac{\partial^2 h}{\partial r^2} + \frac{\partial^2 h}{\partial z^2} \tag{3.68}$$

Equation (3.68) can be discretized using the computation node discussed above. The three terms on the right hand side are approximated using the equations presented below with a CDS. Due to the use of an expansion ratio, the approximation depends on the location of the computational node. However, as described by Ferziger and Peric (2002), the CDS with the use of an expansion ratio results in a second order approximation.

$$\left.\frac{1}{r}\frac{\partial h}{\partial r}\right|_{i,j} \approx \frac{1}{r_i}\frac{h_{i+1,j}\left(r_i - r_{i-1}\right)^2 + h_{i,j}\left[\left(r_{i+1} - r_i\right)^2 - \left(r_i - r_{i-1}\right)^2\right] - h_{i-1,j}\left(r_{i+1} - r_i\right)^2}{\left(r_{i+1} - r_{i-1}\right)\left(r_{i+1} - r_i\right)\left(r_i - r_{i-1}\right)} \tag{3.69}$$

$$\left.\frac{\partial^2 h}{\partial r^2}\right|_{i,j} \approx 2\frac{h_{i+1,j}\left(r_i - r_{i-1}\right) - h_{i,j}\left(r_{i+1} - r_{i-1}\right) + h_{i-1,j}\left(r_{i+1} - r_i\right)}{\left(r_{i+1} - r_{i-1}\right)\left(r_{i+1} - r_i\right)\left(r_i - r_{i-1}\right)} \tag{3.70}$$

$$\left.\frac{\partial^2 h}{\partial z^2}\right|_{i,j} \approx 2\frac{h_{i,j+1}\left(z_j - z_{j-1}\right) - h_{i,j}\left(z_{j+1} - z_{j-1}\right) + h_{i,j-1}\left(z_{j+1} - z_j\right)}{\left(z_{j+1} - z_{j-1}\right)\left(z_{j+1} - z_j\right)\left(z_j - z_{j-1}\right)} \tag{3.71}$$

The Crank-Nicolson method is an implicit method used to approximate the time derivative for the head distribution at time level n+1 from the average of the head distributions at time levels n and n+1. The time derivative is approximated as follows:

$$\left.\frac{\partial h}{\partial t}\right|_{i,j} \approx \frac{{h_{i,j}}^{n+1} - {h_{i,j}}^{n}}{\Delta t} \approx \frac{1}{2}\left\{-\right\}^{n+1} + \frac{1}{2}\left\{-\right\}^{n} \tag{3.72}$$

Equation (3.72) is the Crank-Nicolson approximation of the time derivative where the terms in braces {-} refer to the three terms on the right hand side (RHS) approximated using Equations (3.68) through (3.71) at time levels n and n+1. A similar approach is used at the center of the core for $r = 0$. However, instead, the equation being solved is described in Equation (3.67). Only a slight modification is necessary to the discretization scheme in order to solve this equation at the centerline. The initial condition for the head distribution is taken as 10^{-6} throughout the entire core except at the inflow and outflow boundaries.

The result of the Crank-Nicolson method is an implicit system of equations which must be solved as a system of linear equations in matrix form. A penta-diagonal matrix is formed from this system of equations as shown in Figure 3-33 where E, W, P, S, and N are the coefficients associated with the east node, west node, computational node, south node, and north node, respectively. These coefficients can be determined from the approximations of the derivatives in Equations (3.68) through (3.71). The matrix of coefficients is multiplied times the vector of unknown head values at time level n+1. The RHS is a vector of known head values times the corresponding coefficients. The system of equations can be easily solved with a banded LU

decomposition solver. The time step used in this model is Δt = 0.01 sec and the computational time needed to reach steady state conditions is on the order of one minute.

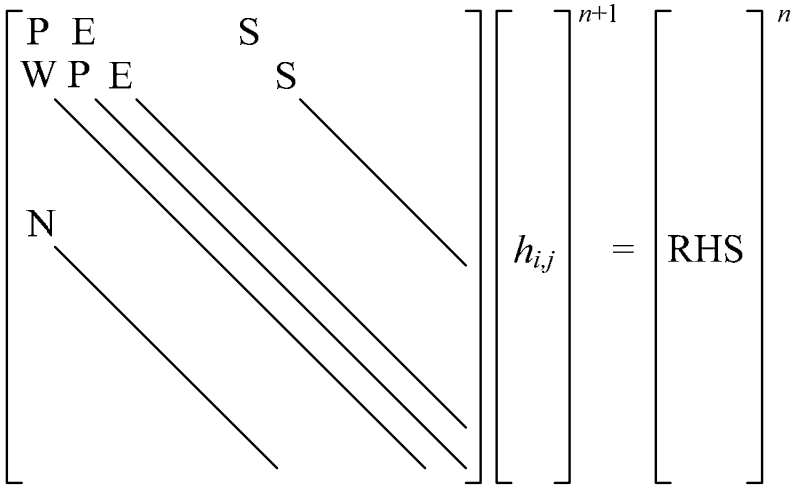

Figure 3-33: System of linear equations

Using the described Crank-Nicolson method, the penta-diagonal matrix has a bandwidth equal to the number of elements in the radial direction. The five coefficients corresponding to the interior node calculations can be determined as:

$$\mathrm{E} = -\frac{\Delta t\left(r_i - r_{i-1}\right)^2 + 2\Delta t r_i\left(r_i - r_{i-1}\right)}{2r_i\left(r_{i+1} - r_{i-1}\right)\left(r_{i+1} - r_i\right)\left(r_i - r_{i-1}\right)} \tag{3.73}$$

$$\mathrm{W} = \frac{\Delta t\left(r_{i+1} - r_i\right)^2 - 2\Delta t r_i\left(r_{i+1} - r_i\right)}{2r_i\left(r_{i+1} - r_{i-1}\right)\left(r_{i+1} - r_i\right)\left(r_i - r_{i-1}\right)} \tag{3.74}$$

$$\mathrm{P} = 1 - \frac{\Delta t\left[\left(r_{i+1} - r_i\right)^2 - \left(r_i - r_{i-1}\right)^2\right] + 2\Delta t r_i\left(r_{i+1} - r_{i-1}\right)}{2r_i\left(r_{i+1} - r_{i-1}\right)\left(r_{i+1} - r_i\right)\left(r_i - r_{i-1}\right)} + \\ + \frac{\Delta t\left(z_{j+1} - z_{j-1}\right)}{\left(z_{j+1} - z_{j-1}\right)\left(z_{j+1} - z_j\right)\left(z_j - z_{j-1}\right)} \tag{3.75}$$

$$\mathrm{S} = -\frac{\Delta t\left(z_j - z_{j-1}\right)}{\left(z_{j+1} - z_{j-1}\right)\left(z_{j+1} - z_j\right)\left(z_j - z_{j-1}\right)} \tag{3.76}$$

$$\mathrm{N} = -\frac{\Delta t\left(z_{j+1} - z_j\right)}{\left(z_{j+1} - z_{j-1}\right)\left(z_{j+1} - z_j\right)\left(z_j - z_{j-1}\right)} \tag{3.77}$$

$$\mathrm{RHS}^{n} = -\mathrm{E}h_{i+1,j}{}^{n} - \mathrm{W}h_{i-1,j}{}^{n} + (2-\mathrm{P})h_{i,j}{}^{n} - \mathrm{S}h_{i,j+1}{}^{n} - \mathrm{N}h_{i,j-1}{}^{n} \tag{3.78}$$

Slight modifications to the above coefficients are needed for the nodes on the boundaries due to the various boundary conditions. It is interesting to note that the above coefficients do not depend on the value of hydraulic conductivity. Furthermore, the head distribution is unchanged for the same nondimensional core geometry (R_s/R_c and b_c/R_c) and a normalized head value. This is useful because it allows for scaling of the head distribution if the core geometry is known. This will not be the case for nonlinear flow, as shown in Section 3.5.3.7.

Steady-state is achieved based on the value of the maximum relative change in head at each node. Therefore, the convergence criterion is determined from the L_∞-norm. The L_∞-norm is given as:

$$L_\infty = \max_{i,j}\left|\frac{h_{i,j}{}^{n+1} - h_{i,j}{}^{n}}{h_{i,j}{}^{n+1}}\right| < \varepsilon \tag{3.79}$$

Convergence is achieved when the L_∞-norm is less than $\varepsilon = 10^{-6}$. The Crank-Nicolson method is unconditionally stable meaning that the selection of Δt will not result in an unstable solution.

As previously mentioned, the input to the model is the core geometry (R_s, R_c, and b_c), the standpipe head (h_s), and the hydraulic conductivity ($1/a$). Once the continuity equation is solved and the head distribution through the core determined, the flow rate can be calculated based on the outflow gradient. The flow rate is found from $Q = qA$, where $q = I/a$ from Darcy's law and $A = 2\pi R_c dz$. The result is the second part of Equation (3.50). The flow rate can be approximated from the head distribution as follows:

$$Q = \frac{2\pi R_c}{a}\sum_{j=1}^{n_z-1}\frac{h_{n_r-1,j} - h_{n_r,j}}{R_c - r_{n_r-1}}\left(\frac{r_{ez}(z_j - z_{j-1}) + z_{j+1} - z_j}{r_{ez}+1}\right) \tag{3.80}$$

Equation (3.80) gives the approximation of the flow rate for all internal nodes. A slight modification to the above equation is needed for the two nodes on the edge of the domain. n_z is the number of elements in the vertical direction and n_r is the number of elements in the radial direction.

3.5.2.6 Linear Numerical Model Results

The linear numerical model using the above described discretization scheme and Crank-Nicolson method can be used to solve for the head distribution through a core specimen with a given core geometry. The grid refinement analysis presented in Section 5.4.1 suggests a domain of 40×40 elements as used here will produce accurate results. Figure 3-34 shows the normalized head distribution for a core with R_s = 2.5 cm (0.98 in), R_c = 10 cm (3.9 in), and b_c = 5 cm (1.97 in). This head distribution is comparable to the method of images solution shown in Figure 3-30.

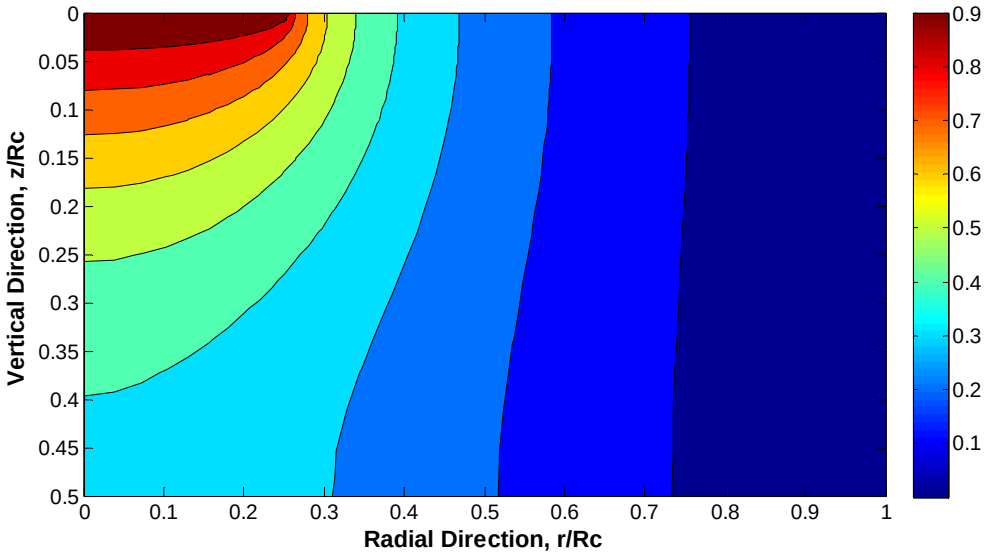

Figure 3-34: Contour plot of normalized unit head distribution for linear flow using Darcy numerical model solution with R_s/R_c = 0.25 and b_c/R_c = 0.5

The boundary conditions, particularly the inflow and outflow known head boundaries, are more accurately represented for the linear numerical model. A comparison between the method of images solution and the linear numerical model solution can be conducted by calculating the difference between the head values at each node. The relative difference, or percent difference, is not desirable for this comparison because the method of images solutions calculates very small head values near the outflow boundary which cause the percent difference values to increase drastically. Therefore, a contour plot of the method of images head minus the linear numerical model head is shown in Figure 3-35. Clearly, the largest difference between the two models is near the location of the standpipe. At this location, the boundary conditions change from a known head boundary to a no flow boundary. For this reason, the grid used is refined near the standpipe location as mentioned in Section 3.5.2.3 using the expansion ratios.

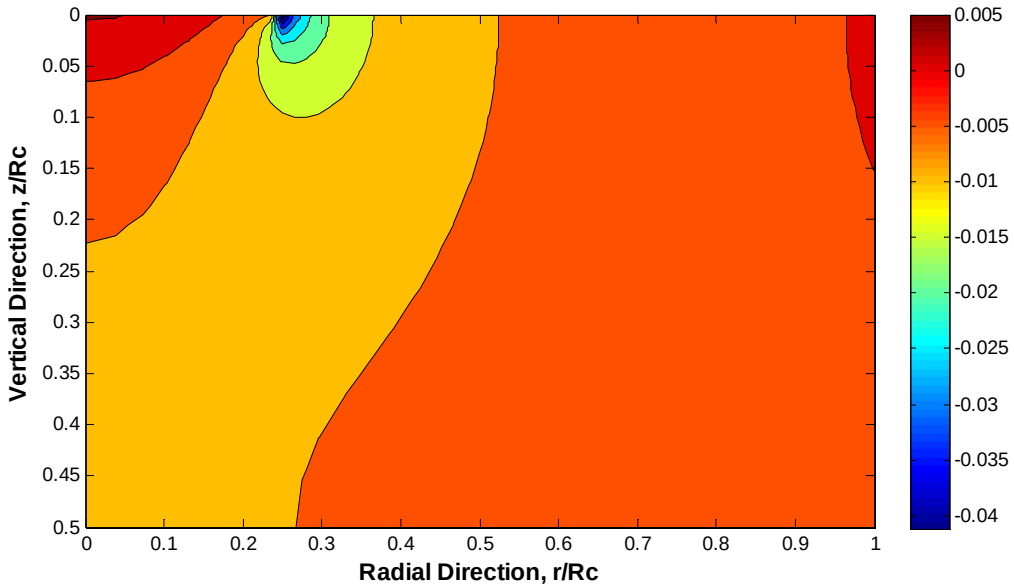

Figure 3-35: Contour plot of head difference between method of images solution and linear numerical model solution with R_s/R_c = 0.25 and b_c/R_c = 0.5

Finally, a comparison of the outflow rates for both the method of images solution and the linear numerical model solution can be compared. The outflow rate can be determined in one of two ways: from the Carslaw and Jaeger equation modified for a finite core geometry using the linear shape factor as described in Equation (3.52), or from the outflow hydraulic gradient as determined from the head distribution assuming purely radial flow as described in Equation (3.80). For the method of images solution, the two outflow rates are approximately the same, to within less than one percent error. The reason for this slight difference is due to the minimal error in the boundary conditions of the method of images solution. For the linear numerical model based on Darcy's law, the two outflow rates are exactly the same. There is a small error between the method of images flow rate and linear numerical model flow rate, again due to the improper boundary conditions of the method of images. Figure 3-36 shows the standpipe head as a function of flow rate for both solutions using a core geometry of R_s = 2.5 cm (0.98 in), R_c = 10 cm (3.9 in), and b_c = 5 cm (1.97 in). Two values of the hydraulic conductivity are specified to determine the flow rates: K = 1 cm/s (0.4 in/s) and K = 0.5 cm/s (0.2 in/s).

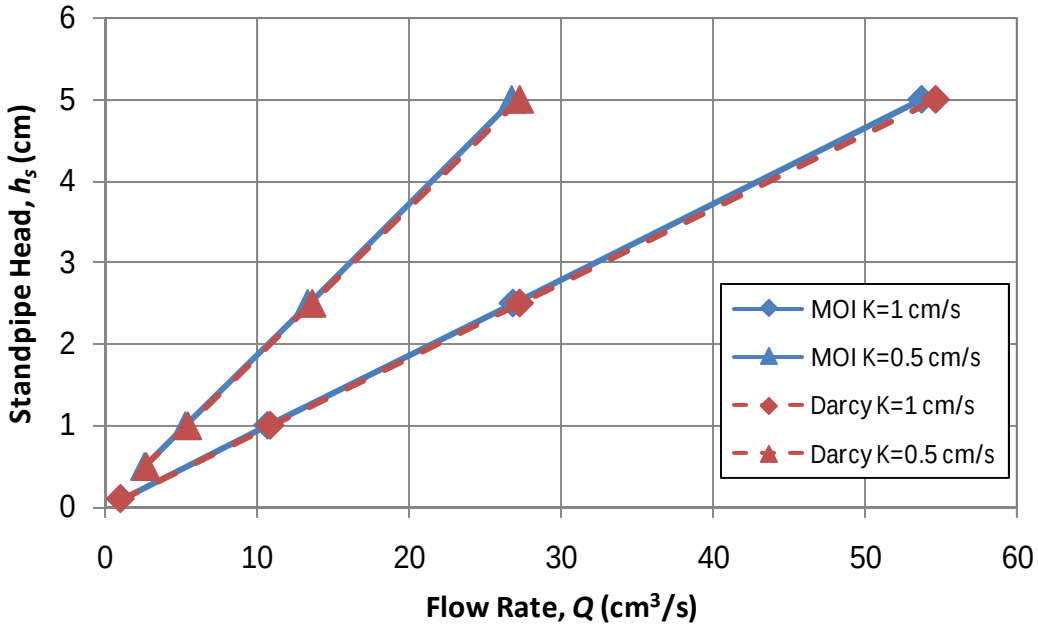

Figure 3-36: Comparison of flow rates determined from method of images and linear numerical model solutions with R_s/R_c = 0.25 and b_c/R_c = 0.5

Clearly, the calculated flow rates for both solutions are approximately the same, meaning our linear numerical model produces the results we would expect. Furthermore, the relationship between the standpipe head and flow rate is linear, also as anticipated. The two hydraulic conductivity values shown in Figure 3-36 also behave as predicted. Specifically, the slopes of the lines are a function of 1/*K*. The line corresponding to K = 0.5 cm/s (0.2 in/s) is exactly twice the slope of the line for K = 1 cm/s (0.4 in/s).

3.5.3 Modeling of Nonlinear Flow

3.5.3.1 Overview of Nonlinear Numerical Model

Section 3.5.2.5 describes the finite difference model that was created to solve the linear flow problem using Darcy's law. Although this model provides information on the general head distribution through the core, it is not applicable for flow through a PFC core. Experimental tests have shown a nonlinear relationship through PFC core specimens which can be modeled with the Forchheimer equation. The objective of the nonlinear numerical model is the same as before: to solve the two-dimensional continuity equation in cylindrical coordinates. However, now instead of using Darcy's law to determine the fluid specific discharge in the continuity Equation (3.42), the Forchheimer equation must be used. The specific discharge as given by the Forchheimer equation is:

$$q = \frac{a}{2b}\left[\sqrt{1+\frac{4b}{a^2}I}-1\right] \tag{3.81}$$

Equation (3.81) is the specific discharge as determined from the nonlinear Forchheimer equation. Similar to the linear case using Darcy's law, the specific discharge is input into the

continuity equation in order to get a partial differential equation in terms of head. As shown in the following subsection, the resulting equation does not have the proper invariance properties to simply substitute Equation (3.81) into the continuity equation and solve. Therefore, a more advanced approach is needed to properly model the continuity equation using the Forchheimer equation.

The nonlinear numerical model has the same domain as the linear model; namely, the radius of the core specimen and the thickness of the PFC layer. Due to symmetry it is only necessary to model half of the core. The same boundary conditions apply in the nonlinear flow case as were used in the linear model. The five boundary conditions are given in Equations (3.46) through (3.49) and the symmetry boundary condition Equation (3.59). The objective of the nonlinear model is to input the core geometry (R_s, R_c, and b_c) for a known standpipe head (h_s) and assumed porous media properties (a and b), and calculate the outflow rate (Q). For multiple values of h_s, a curve of h_s versus Q can be created which will be nonlinear. From this curve the two modified Forchheimer coefficients (α and β) can be determined and compared to laboratory results. With the assumed values of the original Forchheimer coefficients, the values of the modified Forchheimer coefficients can be calculated. This relationship can be used to estimate the original Forchheimer coefficients from the known modified Forchheimer coefficients obtained through experimental testing. Because the finite difference model is based on the original Forchheimer equation, an assumed value of the original Forchheimer coefficients must be made.

The finite difference model used to solve the continuity equation based on the Forchheimer equation requires a grid to approximate the partial differential equation. The same grid generation described in Section 3.5.2.3 for the linear model is used for the nonlinear model as well. As previously mentioned, this grid creates a node at the location of the standpipe in order to properly model the standpipe radius boundary. Expansion ratios are used in all directions in order to have a fine mesh on the upper core surface near the standpipe.

3.5.3.2 Invariance Properties of Forchheimer Equation

The Forchheimer equation does not have the proper invariance properties to be used in two-dimensional cylindrical coordinates without some additional investigation. As mentioned in Section 3.2.2.1 the Forchheimer equation has been used in two-dimensional flow problems, but the quadratic term is typically taken as the magnitude of the specific discharge times its vector. The source of the invariance problems is outlined below, followed by the suggested method for avoiding the problem and the proper approach used in the numerical model.

The Forchheimer equation is given as:

$$I = aq + bq^2 \tag{3.82}$$

from which the specific discharge is given in Equation (3.81). For two-dimensional flow in cylindrical coordinates, there is flow in both the radial and vertical directions. The hydraulic gradient in the radial and vertical directions, respectively, is given as:

$$I_r = aq_r + bq_r^2 \tag{3.83}$$

$$I_z = aq_z + bq_z^2 \tag{3.84}$$

In Equations (3.83) and (3.84), I_r is the radial hydraulic gradient and q_r is the radial specific discharge, and similarly for I_z and q_z. For two-dimensional flow, the local hydraulic gradient is the sum of the squares of the radial and vertical gradients, which can be found using Equations (3.83) and (3.84):

$$I = \sqrt{I_r^{\,2} + I_z^{\,2}} = \sqrt{(aq_r)^2 + 2abq_r^{\,3} + \left(bq_r^{\,2}\right)^2 + (aq_z)^2 + 2abq_z^{\,3} + \left(bq_z^{\,2}\right)^2} \qquad (3.85)$$

Similarly, the local specific discharge is the sum of the squares of the radial and vertical specific discharges. The radial and vertical specific discharges are found using Equation (3.81) with the appropriate direction for q and I. The local specific discharge is:

$$q = \sqrt{q_r^{\,2} + q_z^{\,2}} = \frac{a}{b}\sqrt{1 + \frac{b}{a^2}(I_r + I_z) - 0.5\sqrt{1 + \frac{4bI_r}{a^2}} + 0.5\sqrt{1 + \frac{4bI_z}{a^2}}} \qquad (3.86)$$

If the local hydraulic gradient and local specific discharge given in Equations (3.85) and (3.86) are substituted into the Forchheimer Equation (3.82), an identity is not achieved which illustrates the source of the invariance problem. Therefore, using the specific discharge in Equation (3.81) in the continuity equation is not sufficient because the equation cannot be rotated to another system of coordinates and maintain the same value. This requires further investigation to create another representation of the Forchheimer equation which is rotational.

3.5.3.3 Governing Continuity Equation for Forchheimer Flow

For the linear Darcy's law, the hydraulic conductivity is considered the slope of the linear relationship. For the nonlinear case, the hydraulic conductivity is considered the slope of the nonlinear relationship for a zero specific discharge. As the specific discharge increases, the slope increases as well resulting in the nonlinear relationship. We can consider the slope (which is a function of specific discharge) to be an effective Forchheimer hydraulic conductivity, which is not a constant and is given the symbol K_F. Using this approach, the Forchheimer equation can be rewritten in vector notation as:

$$\vec{q} = K_F \vec{I} \qquad (3.87)$$

where the scalar effective Forchheimer hydraulic conductivity is:

$$K_F = \frac{a}{2bI}\left[\sqrt{1 + \frac{4b}{a^2}I} - 1\right] \qquad (3.88)$$

Equation (3.87) is a rotational vector representation of the Forchheimer equation and can be modeled in any coordinate system. However, for low Reynolds number (small hydraulic gradient), this equation does not approximate Darcy's law. Therefore, we need to find a representation of the Forchheimer specific discharge that represents Darcy's law as the hydraulic gradient approaches zero. This can be accomplished by looking at the ratio of the Forchheimer

specific discharge in Equation (3.81) to the Darcy specific discharge in Equation (5.1), where $K = 1/a$:

$$\frac{q_F}{q_D} = \frac{K_F I}{KI} = \frac{a^2}{2bI}\left[\sqrt{1+\frac{4b}{a^2}I} - 1\right] = \Phi(r,z) \tag{3.89}$$

$\Phi(r,z)$ in Equation (3.89) is a dimensionless quantity called the hydraulic conductivity ratio, and is the ratio of the effective Forchheimer hydraulic conductivity to the true Darcy hydraulic conductivity. The true hydraulic conductivity ($K = 1/a$) is a constant for Darcy flow, but the effective Forchheimer hydraulic conductivity is not constant and depends on the magnitude of the hydraulic gradient. In cylindrical coordinates, the hydraulic gradient depends on both the *r*- and *z*-directions, so that the hydraulic conductivity ratio is a function of both directions.

The Forchheimer specific discharge can now be determined from Equation (3.89) as follows:

$$\vec{q} = K_F \vec{I} = K\Phi\vec{I} \tag{3.90}$$

Equation (3.90) is rotational for any system of coordinates, *K* is a constant that can either be isotropic or anisotropic, and Φ is a scalar which depends on the magnitude of the hydraulic gradient and is a function of both the *r*- and *z*-directions. Using Equation (3.90) in the continuity equation is the proper method to model nonlinear flow in two-dimensions. Additional investigation of the hydraulic conductivity ratio is required to ensure that the Forchheimer equation approaches Darcy's law for low hydraulic gradients and is discussed in the next subsection.

The objective of the nonlinear numerical model is to solve the continuity equation now using Equation (3.90) for the specific discharge. Plugging this into the continuity Equation (3.42) gives:

$$\frac{1}{r}\frac{\partial}{\partial r}\left(rK\Phi I_r\right) + \frac{\partial}{\partial z}\left(K\Phi I_z\right) = 0 \tag{3.91}$$

Since *K* is assumed to be a constant, it can be taken out of the derivatives and dropped out of the equation for the isotropic case. Representing the gradients as the change in head for the corresponding direction, Equation (3.91) can be rewritten as:

$$\Phi\left(\frac{1}{r}\frac{\partial h}{\partial r} + \frac{\partial^2 h}{\partial r^2} + \frac{\partial^2 h}{\partial z^2}\right) + \frac{\partial \Phi}{\partial r}\frac{\partial h}{\partial r} + \frac{\partial \Phi}{\partial z}\frac{\partial h}{\partial z} = 0 \tag{3.92}$$

Equation (3.92) is the governing partial differential equation for the head distribution for two-dimensional Forchheimer flow in cylindrical coordinates. Notice that the term in parentheses is the continuity equation for Darcy flow multiplied by the scalar hydraulic conductivity ratio. However, this term is not equal to zero (as in Darcy flow) because the head distribution does not

match that produced by Darcy flow. The finite difference model will solve Equation (3.92) in order to determine the head distribution through the core.

3.5.3.4 Analysis of Hydraulic Conductivity Ratio

Now that the Forchheimer equation has been rewritten with proper invariance properties, we must determine whether this form of the Forchheimer equation approaches Darcy's law for small hydraulic gradients. This can be accomplished by taking the limit of the hydraulic conductivity ratio as the hydraulic gradient approaches zero. It can be shown that this limit is:

$$\lim_{I\to 0}\Phi = \lim_{I\to 0}\frac{a^2}{2bI}\left[\sqrt{1+\frac{4b}{a^2}I}-1\right]=1 \qquad (3.93)$$

Therefore, the limit of the Forchheimer Equation (3.90) is:

$$\lim_{I\to 0}\vec{q} = \lim_{I\to 0}K\Phi\vec{I} = K\vec{I} \qquad (3.94)$$

This is equivalent to Darcy's law, satisfying the requirement that the Forchheimer equation approaches Darcy's law for small hydraulic gradients.

A graphical approach can be used to show that the hydraulic conductivity ratio approaches a value of one for low hydraulic gradients. Using Equation (3.89) with a = 0.3 s/cm (0.76 s/in) and b = 0.2 s^2/cm^2 (1.29 s^2/in^2) results in Figure 3-37. This shows that for low hydraulic gradient (or low Re), the hydraulic conductivity ratio approaches a value of one, representing Darcy flow.

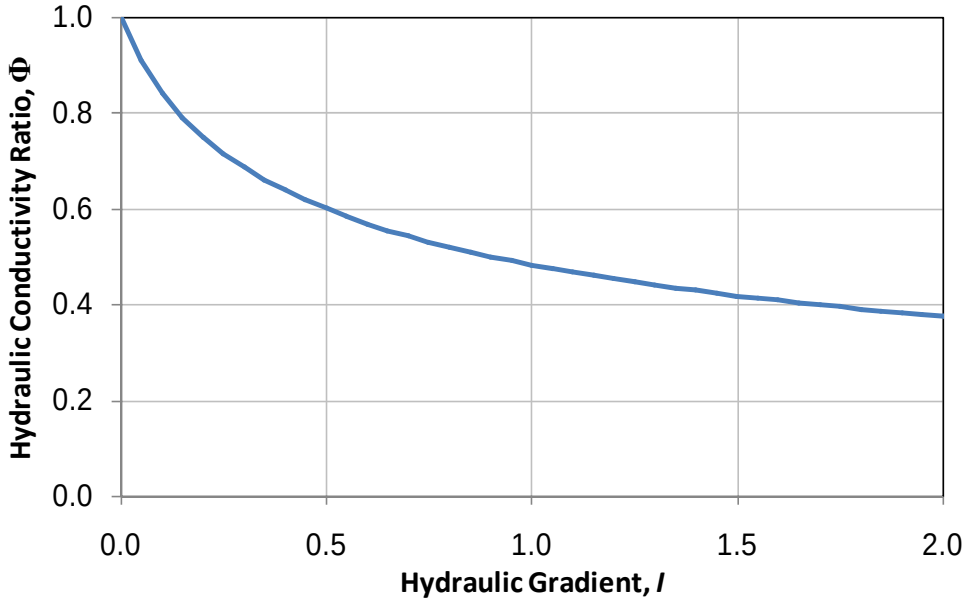

Figure 3-37: Hydraulic conductivity ratio Φ as a function of hydraulic gradient

The hydraulic conductivity ratio is a scalar which is a function of both the *r*- and *z*-directions so that the hydraulic gradient used to calculate Φ is the local gradient given as the sum of the squares of the gradient in both directions. Φ can be found as follows:

$$\Phi(r,z) = \frac{a^2}{2b\sqrt{[I_r(r,z)]^2 + [I_z(r,z)]^2}}\left[\sqrt{1+\frac{4b}{a^2}\sqrt{[I_r(r,z)]^2 + [I_z(r,z)]^2}} - 1\right] \tag{3.95}$$

where I_r and I_z are the partial derivates of the head in the *r*- and *z*-directions, respectively.

3.5.3.5 Singularity Removal for Nonlinear Model

The nonlinear model also has a singularity at $r = 0$ in the governing Equation (3.92). In order to remove the singularity, a similar approach to that used in Section 5.2.4 is needed. The first radial derivative can be approximated as before:

$$\frac{\partial h(r,z)}{\partial r} \approx r\frac{\partial^2 h(0,z)}{\partial r^2} \tag{3.96}$$

Substituting this into Equation (3.92) and recalling that the first radial derivative at $r = 0$ is equal to zero results in the following partial differential equation:

$$\Phi\left(2\frac{\partial^2 h}{\partial r^2} + \frac{\partial^2 h}{\partial z^2}\right) + \frac{\partial \Phi}{\partial z}\frac{\partial h}{\partial z} = 0 \tag{3.97}$$

Equation (3.97) is the governing partial differential equation for nonlinear flow at $r = 0$.

3.5.3.6 Nonlinear Model Differencing Scheme

The differencing scheme used to solve the governing nonlinear partial differential equation is the same as for the linear case: a second-order, five point CDS using the computational node in Figure 3-38. However, due to the addition of the hydraulic conductivity ratio, additional nodes are needed in order to properly determine Φ as it depends on additional nodes to find the hydraulic gradient. The suggested computational node for the nonlinear model is shown in Figure 3-38.

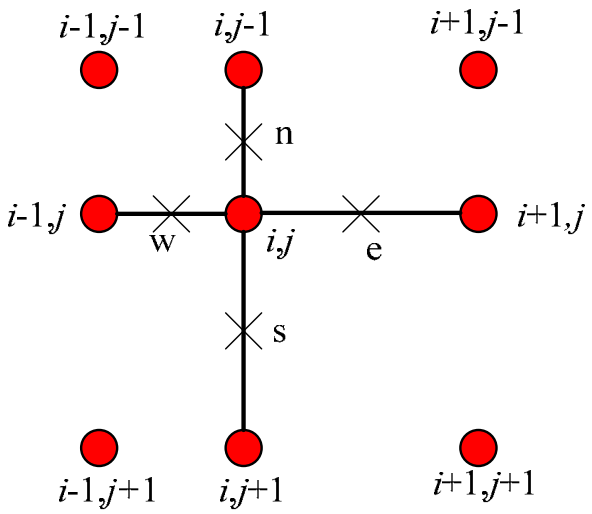

Figure 3-38: Computational node schematic for nonlinear model

The simplest way to model the governing partial differential equation is in the following form:

$$\frac{1}{r}\frac{\partial}{\partial r}\left(r\Phi\frac{\partial h}{\partial r}\right)+\frac{\partial}{\partial z}\left(\Phi\frac{\partial h}{\partial z}\right)=0 \qquad (3.98)$$

The terms in parentheses in Equation (3.98) can be taken as a new variable and the first derivative can be approximated at the half nodes shown in Figure 3-38 and designated as e, w, s, and n. The first derivative is approximated using the same method as before, described by Equation (3.69). However, instead of using $h_{i\text{-}1,j}$ and $h_{i+1,j}$, we will use h_w and h_e, which can be found as the average of $h_{i,j}$ and $h_{i\text{-}1,j}$ or $h_{i+1,j}$. Using the half node method requires an approximation for Φ at each half node location. Since Φ is determined based on the magnitude of the local hydraulic gradient, the four additional nodes are needed. For example, in order to approximate Φ_w, both the radial and vertical hydraulic gradients are needed. The radial hydraulic gradient is determined from $h_{i\text{-}1,j}$ and $h_{i,j}$, while the vertical hydraulic gradient is determined from the average of the two surrounding hydraulic gradients. The first vertical gradient is approximated using $h_{i\text{-}1,j\text{-}1}$, $h_{i\text{-}1,j}$, and $h_{i\text{-}1,j+1}$, and the second vertical gradient is approximated using $h_{i,j\text{-}1}$, $h_{i,j}$, and $h_{i,j+1}$. A similar approach is needed to find the hydraulic conductivity ratio at the other three half nodes.

The solution of the resulting approximation to the partial differential equation is found using the Gauss-Seidel iterative method (c.f. Smith, 1965). Time is not considered for this case due to the nonlinear nature of the problem. Therefore, the Gauss-Seidel iterative method is useful for simply finding the steady state solution. This method uses a known value of the head to calculate a new value of the head for a given node. That new value is then used to update the following node value and the solution is updated across the grid. Of particular interest is the initial guess at the head distribution needed to start the iterative process. For the nonlinear model, the initial guess used is the head distribution obtained from the linear model. Therefore, our initial guess is the solution for Darcy's law presented in Section 3.5.2.6, and is used to iterate upon in order to solve the continuity equation based on the Forchheimer equation. The Gauss-

Seidel method is relatively quick at determining a solution, and the iteration is stopped based on the relative change in head at each node. The same convergence criterion described in Equation (3.79) is used for the nonlinear case. The L_∞-norm is used to determine convergence so that the relative change in head at all nodes is less than $\varepsilon = 10^{-6}$ when a solution is found. Computational time to run the model is on the order of approximately two minutes.

The Gauss-Seidel iterative method updates the current head value at a node of interest based on the surrounding nodes. Due to the numbering scheme used, the updated value (n+1) is calculated based on the updated values for the western and northern nodes, and the previous values (n) for the eastern and southern nodes. This is represented in Equation (3.99) below with the following coefficient values determined from the differencing scheme:

$$h_{i,j}^{\,n+1} = \frac{-1}{\mathrm{P}}\left(\mathrm{E}h_{i+1,j}^{\,n} + \mathrm{W}h_{i-1,j}^{\,n+1} + \mathrm{S}h_{i,j+1}^{\,n} + \mathrm{N}h_{i,j-1}^{\,n+1}\right) \tag{3.99}$$

where

$$\mathrm{E} = \frac{\Phi_\mathrm{e}\left(r_{i+1}+r_i\right)\left(r_i-r_{i-1}\right)^2}{r_i\left(r_{i+1}-r_{i-1}\right)\left(r_{i+1}-r_i\right)^2\left(r_i-r_{i-1}\right)} + \frac{2\Phi_{i,j}\left(r_i-r_{i-1}\right)^2\left[\left(r_{i+1}-r_i\right)^2-\left(r_i-r_{i-1}\right)^2\right]}{\left[\left(r_{i+1}-r_{i-1}\right)\left(r_{i+1}-r_i\right)\left(r_i-r_{i-1}\right)\right]^2} \tag{3.100}$$

$$\mathrm{W} = \frac{\Phi_\mathrm{w}\left(r_{i-1}+r_i\right)\left(r_{i+1}-r_i\right)^2}{r_i\left(r_{i+1}-r_{i-1}\right)\left(r_{i+1}-r_i\right)\left(r_i-r_{i-1}\right)^2} - \frac{2\Phi_{i,j}\left(r_{i+1}-r_i\right)^2\left[\left(r_{i+1}-r_i\right)^2-\left(r_i-r_{i-1}\right)^2\right]}{\left[\left(r_{i+1}-r_{i-1}\right)\left(r_{i+1}-r_i\right)\left(r_i-r_{i-1}\right)\right]^2} \tag{3.101}$$

$$\begin{aligned}\mathrm{P} = {} & \frac{2\Phi_{i,j}\left[\left(z_{j+1}-z_j\right)^2-\left(z_j-z_{j-1}\right)^2\right]^2}{\left[\left(z_{j+1}-z_{j-1}\right)\left(z_{j+1}-z_j\right)\left(z_j-z_{j-1}\right)\right]^2} - \frac{2\Phi_\mathrm{s}\left(z_j-z_{j-1}\right)^3+2\Phi_\mathrm{n}\left(z_{j+1}-z_j\right)^3}{\left(z_{j+1}-z_{j-1}\right)\left(z_{j+1}-z_j\right)^2\left(z_j-z_{j-1}\right)^2} + \\ & + \frac{2\Phi_{i,j}\left[\left(r_{i+1}-r_i\right)^2-\left(r_i-r_{i-1}\right)^2\right]^2}{\left[\left(r_{i+1}-r_{i-1}\right)\left(r_{i+1}-r_i\right)\left(r_i-r_{i-1}\right)\right]^2} + \\ & - \frac{\Phi_\mathrm{e}\left(r_{i+1}+r_i\right)\left(r_i-r_{i-1}\right)^3+\Phi_\mathrm{w}\left(r_{i-1}+r_i\right)\left(r_{i+1}-r_i\right)^3}{r_i\left(r_{i+1}-r_{i-1}\right)\left(r_{i+1}-r_i\right)^2\left(r_i-r_{i-1}\right)^2}\end{aligned} \tag{3.102}$$

$$\mathrm{S} = \frac{2\Phi_\mathrm{s}\left(z_j-z_{j-1}\right)^2}{\left(z_{j+1}-z_{j-1}\right)\left(z_{j+1}-z_j\right)^2\left(z_j-z_{j-1}\right)} + \frac{2\Phi_{i,j}\left(z_j-z_{j-1}\right)^2\left[\left(z_{j+1}-z_j\right)^2-\left(z_j-z_{j-1}\right)^2\right]}{\left[\left(z_{j+1}-z_{j-1}\right)\left(z_{j+1}-z_j\right)\left(z_j-z_{j-1}\right)\right]^2} \tag{3.103}$$

$$\mathrm{N} = \frac{2\Phi_\mathrm{n}\left(z_{j+1}-z_j\right)^2}{\left(z_{j+1}-z_{j-1}\right)\left(z_{j+1}-z_j\right)\left(z_j-z_{j-1}\right)^2} - \frac{2\Phi_{i,j}\left(z_{j+1}-z_j\right)^2\left[\left(z_{j+1}-z_j\right)^2-\left(z_j-z_{j-1}\right)^2\right]}{\left[\left(z_{j+1}-z_{j-1}\right)\left(z_{j+1}-z_j\right)\left(z_j-z_{j-1}\right)\right]^2} \tag{3.104}$$

When solving the system of equations using the Gauss-Seidel iterative method, the hydraulic conductivity ratio Φ remains at the previous iterative value. Therefore, Φ is not updated as the calculations proceed through the grid. The reason for lagging the calculation of Φ is that it depends on the hydraulic gradient at a point. So on one side of the computational node,

the head value will be updated, but on the other side, the head will not be updated. Therefore, this would give an incorrect value of Φ since it depends on both values of the head. The lagging behind for Φ does not appear to produce any additional error or result in a significant increase in computational time.

It is interesting to note that the Forchheimer coefficients are included in the Φ term as shown in Equation (3.95). The nondimensional ratio b/a^2 is needed to calculate Φ, so the head distribution should be the same for a constant core geometry and any combination of b and a such that the b/a^2 ratio remains constant. Therefore, although the head distribution cannot be normalized for a unit head as in the linear case, the head distribution is a function of only one nondimensional parameter: b/a^2.

As before, the input to the model is the core geometry (R_s, R_c, and b_c), the standpipe head (h_s), and the original Forchheimer coefficients (a and b). Once the continuity equation is solved and the nonlinear head distribution through the core is determined, the flow rate can be calculated based on the outflow gradient. The flow rate is found from $Q = qA$, where $A = 2\pi R_c dz$ and q is found from the Forchheimer equation given in Equation (3.81). The outflow rate can be approximated from the head distribution for all internal nodes as follows:

$$Q = \frac{\pi R_c a}{b} \sum_{j=1}^{n_z-1} \left[\sqrt{1 + \frac{4b}{a^2} \frac{h_{n_r-1,j} - h_{n_r,j}}{R_c - r_{n_r-1}}} - 1 \right] \left(\frac{r_{ez}\left(z_j - z_{j-1}\right) + z_{j+1} - z_j}{r_{ez} + 1} \right) \quad (3.105)$$

Equation (3.105) gives the approximation of the flow rate for all internal nodes. A slight modification to the above equation is needed for the two nodes on the edge of the domain. n_z is the number of elements in the vertical direction and n_r is the number of elements in the radial direction.

3.5.3.7 Nonlinear Numerical Model Results

The nonlinear numerical model using the above described discretization scheme and Gauss-Seidel iterative method can be used to solve for the head distribution through a core specimen with a given core geometry. The grid refinement analysis presented in Section 3.5.4.1 suggests a domain of 40×40 elements as used here will produce accurate results. Figure 3-39 shows the unit head distribution for a core with R_s = 2.5 cm (0.98 in), R_c = 10 cm (3.9 in), b_c = 5 cm (1.97 in), a = 1 s/cm (2.54 s/in), and b = 10 s^2/cm^2(64.5 s^2/in^2). This head distribution is comparable to the linear numerical model solution shown in Figure 3-34. It should be noted that although this figure is presented with the vertical and radial directions normalized to the core radius, the nonlinear solution does not scale in this way. As shown below, the nonlinear head distribution cannot be normalized. The following figures are presented in this way solely for comparison purposes to the linear numerical model results.

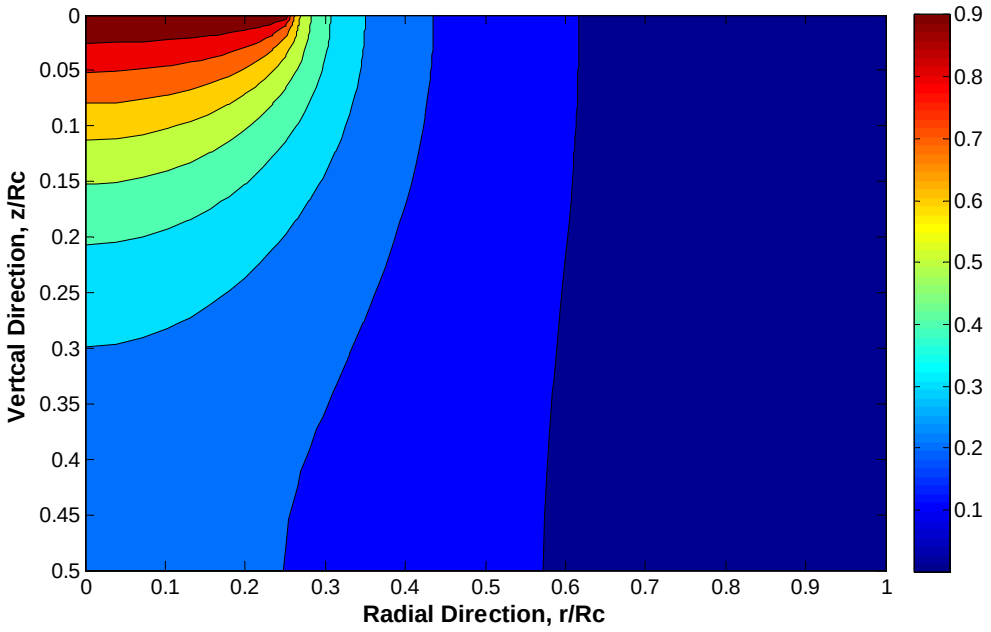

Figure 3-39: Contour plot of unit head distribution for nonlinear flow using Forchheimer numerical model solution with R_s/R_c = 0.25 and b_c/R_c = 0.5

A comparison between the linear numerical model and nonlinear numerical model solutions can be conducted by calculating the percent difference between the head values at each node. A contour plot of the linear numerical model head minus the nonlinear numerical model head divided by the linear head is shown in Figure 3-40 expressed as a percent. The largest percent difference between the two models is near the outflow boundary. At this location, the head values are very nearly zero. The general trend in percent difference follows the contour plot for the head distribution, with the exception of zero percent difference at the known outflow boundary. For this core geometry, the nonlinear head distribution can be up to 45% lower than the linear head distribution.

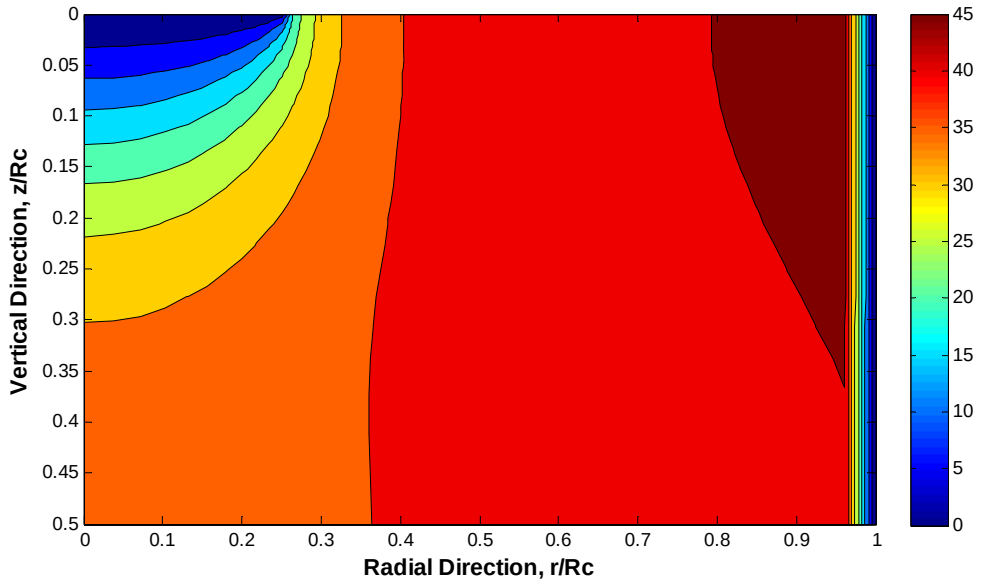

Figure 3-40: Contour plot of percent difference between unit head distribution for linear and nonlinear numerical model solutions with R_s/R_c = 0.25 and b_c/R_c = 0.5

The outflow rate can be determined for both the linear and nonlinear numerical models from Equations (3.80) and (3.105), respectively. A graph of the two models shows that the nonlinear flow rate approaches the linear flow rate as the flow rate decreases. This characteristic is discussed in more detail in the next section. Figure 3-41 shows how the nonlinear flow rate approaches the linear flow rate for the above core geometry with a = 1 s/cm and b = 1 s^2/cm^2. The nonlinear numerical model results show that the relationship between h_s and Q can be fully defined using the quadratic modified Forchheimer equation.

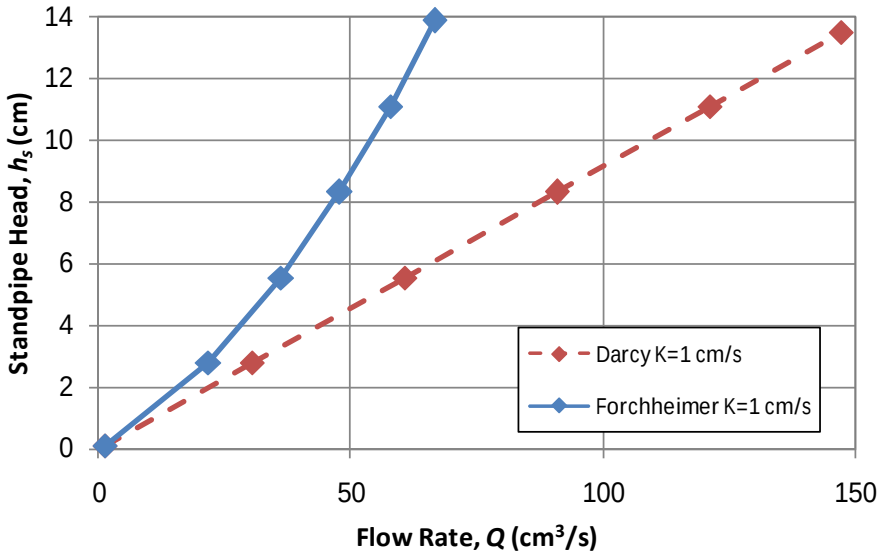

Figure 3-41: Comparison of flow rates determined from linear and nonlinear numerical model solutions with R_s/R_c = 0.25 and b_c/R_c = 0.5

In addition to comparing the nonlinear flow rate to the linear flow rate for the same hydraulic conductivity, it is also interesting to compare two nonlinear flow rates with the same hydraulic conductivity but different nonlinear terms. Figure 3-42 shows the same core geometry as in Figure 3-41, but now the nonlinear term has been changed from b = 1 s^2/cm^2 to 10 s^2/cm^2. As expected, the greater nonlinear term results in more curvature in the flow rate relationship. Furthermore, the modified linear Forchheimer coefficient α is the same for both curves because a is the same.

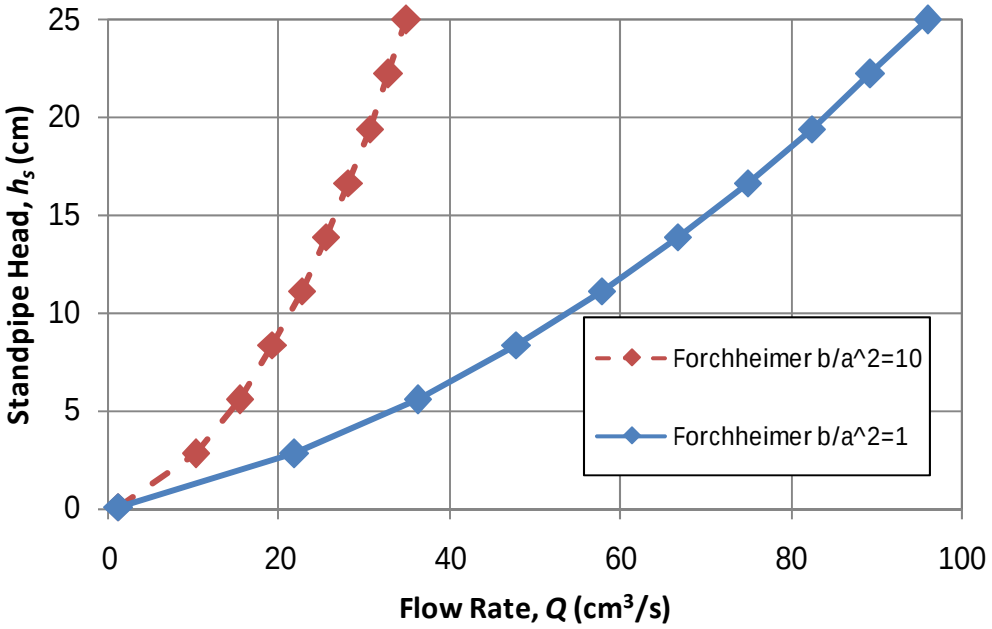

Figure 3-42: Comparison of flow rates determined from nonlinear numerical model solutions with R_s/R_c = 0.25, b_c/R_c = 0.5, a = 1 s/cm, and b = 1 or 10 s^2/cm^2

As previously mentioned, the nonlinear numerical model cannot be represented in a nondimensional way, meaning the head distribution is not the same for a normalized unit head and normalized vertical and radial dimensions. To illustrate this point, we can graph the head distribution along the radial direction for a constant vertical coordinate for various values of h_s. Figure 3-43 shows the head distribution along the top and bottom surfaces of a PFC core with R_s = 2.5 cm, R_c = 10 cm, b_c = 5 cm, a = 1 s/cm, and b = 10 s^2/cm^2. The head distribution is normalized to the standpipe head. As seen in the figure, the head distributions do not collapse to a single line as in the linear case. For this reason, the nonlinear flow case cannot be nondimensionalized with respect to the standpipe head.

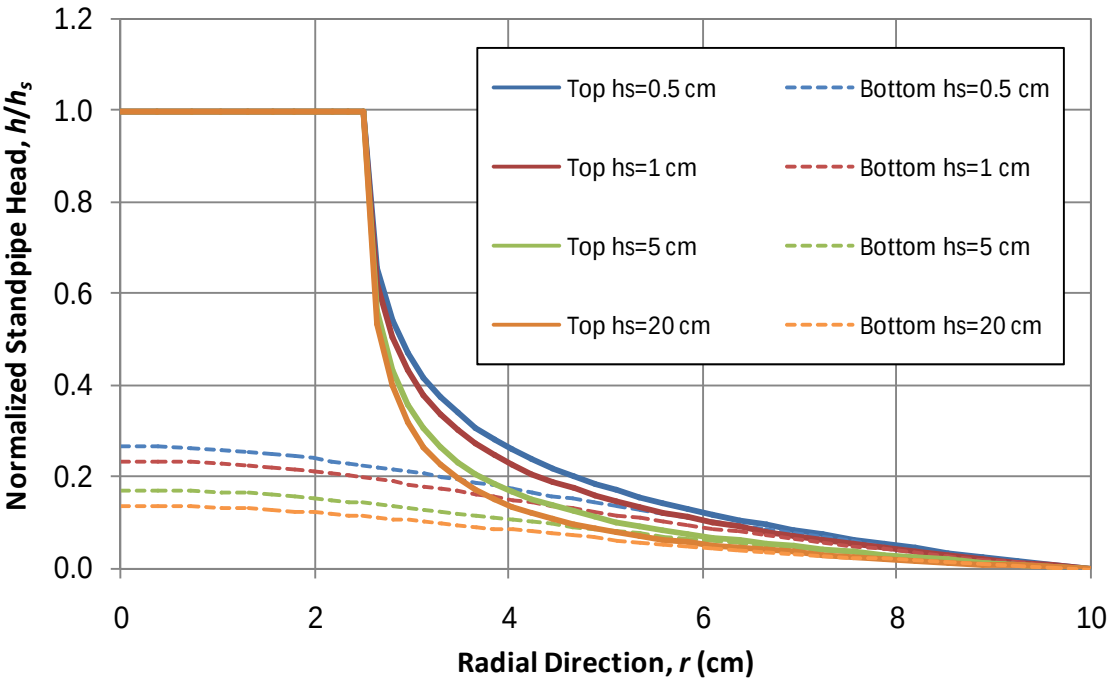

Figure 3-43: Lack of nondimensionalization for nonlinear numerical model

The final result to investigate is the value of the hydraulic conductivity ratio Φ, determined from the nonlinear numerical model. Φ can be calculated at each node once the nonlinear head distribution is determined. A typical distribution of the hydraulic conductivity ratio is shown in Figure 3-44, with R_s = 2.5 cm, R_c = 10 cm, b_c = 5 cm, a = 1 s/cm, b = 10 s^2/cm^2, and h_s = 1 cm.

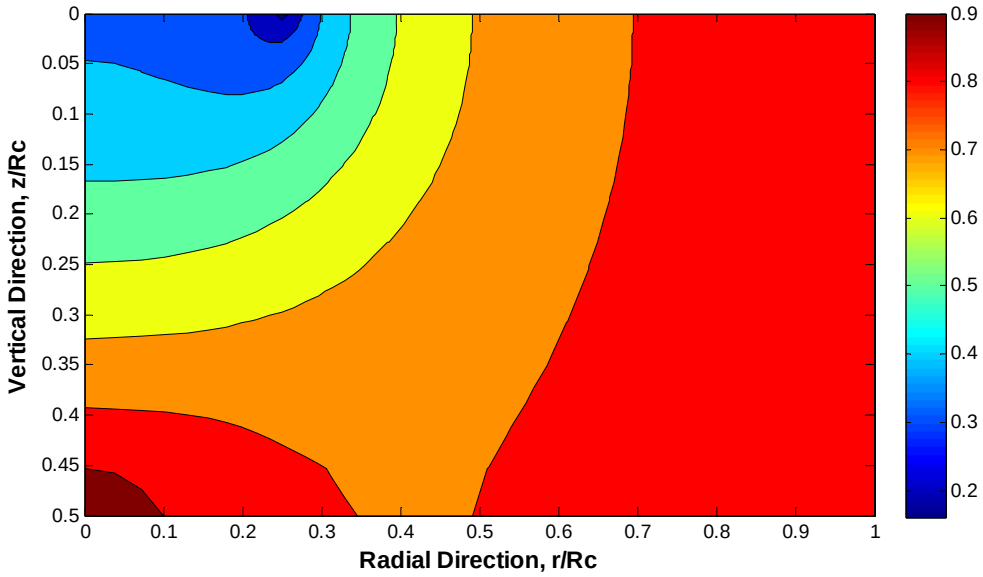

Figure 3-44: Distribution of hydraulic conductivity ratio Φ

The smaller values of Φ correspond to where the nonlinear effect is greatest. As Φ approaches a value of one, it is expected that the nonlinear hydraulic conductivity approaches the true value of the hydraulic conductivity (for the linear case). Therefore, we can see that Φ is smallest near the location of the standpipe and under the inflow boundary, and generally typically increases towards the outflow boundary. This result is expected because as the flow reaches the outflow boundary, the specific discharge is decreasing and the Forchheimer equation is approaching Darcy's law. The largest value of Φ actually occurs at the center of the core on the lower boundary. At this location, there is both a no flow boundary in the radial direction (due to symmetry) and a no flow boundary in the vertical direction. Because of this, we expect to see virtually no flow and the Forchheimer equation should be approximately equal to Darcy's law. This distribution gives an idea of where, within the core, the nonlinear effects are dominant. It should be noted that this distribution of Φ is for h_s = 1 cm. As h_s increases, the distribution of Φ will have a similar shape, but the values will decrease, meaning the nonlinear effects are more dominant and cover more of the domain.

3.5.4 Model Characteristics

3.5.4.1 Grid Refinement

The goal of the numerical model used in this research study is primarily to determine the outflow rate for a given core geometry, original Forchheimer coefficients, and standpipe head. Therefore, grid refinement is based on a comparison of outflow rate as the number of elements in the grid increases. Because the grid is based on an expansion ratio, it is difficult to compare head values at various locations within the core specimen since the nodes are not calculated at the same radial and vertical positions as the number of elements increases. For this reason, an overall model result, in this case outflow rate, is used for grid refinement purposes. Figure 3-45 shows the grid refinement results.

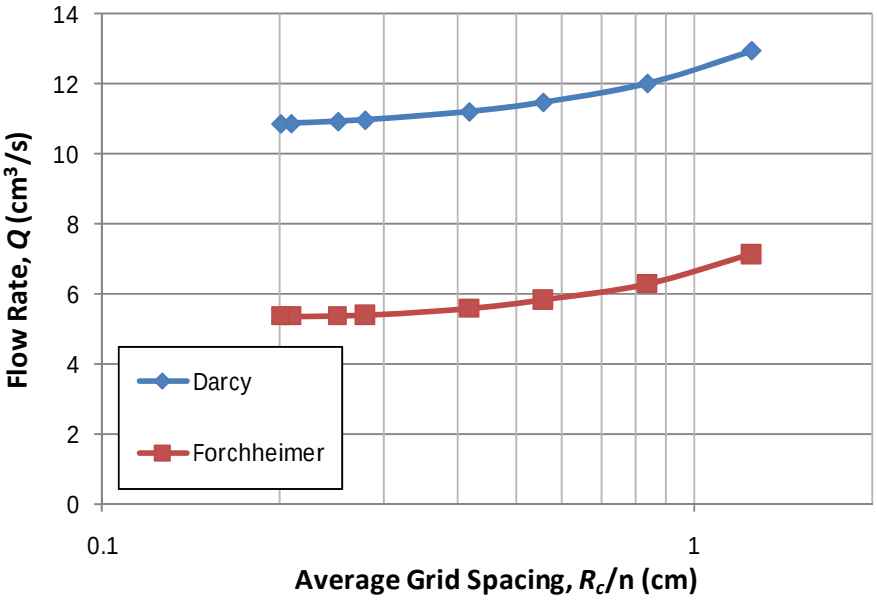

Figure 3-45: Grid refinement for outflow rate

The model inputs used to investigate the grid refinement are as follows: R_s = 2.5 cm, R_c = 10 cm, b_c = 5 cm, a = 1 s/cm, b = 10 s^2/cm^2, and h_s = 1 cm. The outflow rate is graphed as a function of average grid spacing. Due to the expansion ratio, the average grid spacing does not represent the actual grid spacing, but is instead the core radius divided by the number of elements in the radial direction. The domain of the model has the same number of elements in both the radial and vertical directions.

The maximum number of elements for which the model will successfully converge in a reasonable amount of time is 50 elements in both the radial and vertical directions, for a total of 2,500 elements. This was conducted using an Intel Core 2 Duo CPU at 2.2 GHz with 3.5 GB of RAM. When the number of elements is decreased to 36 elements, the percent error in flow rate is less than one percent. The model results described in the previous sections used 40 elements in each direction, for a total of 1,600 elements, or 1,681 nodes. This number of elements results in a percent error in the flow rate of 0.6% for the linear model and 0.3% for the nonlinear model. The smaller percent error for the nonlinear model is desirable since we are primarily interested in the nonlinear results. Not only does a model using 40 elements produce accurate results, but computation times are also relatively small. The typical computation time to run the model for a given value of standpipe head is on the order of approximately two minutes.

Another typical concern in grid refinement is the observed convergence rate of the model. Since a CDS was used for model development, it is expected that the convergence rate should be approximately second-order. This can be tested by using the Richardson extrapolation method (Ferziger and Peric, 2002). The convergence rate p can be found by comparing the head values at similar nodes with differing number of elements:

$$p = \frac{\log\left(\frac{h_{2n} - h_{4n}}{h_n - h_{2n}}\right)}{\log(2)} \tag{3.106}$$

Equation (3.106) estimates the convergence rate of the model by comparing the head value as determined from grids with n, 2n, and 4n elements. For this analysis, n = 12 so that grids of 12×12, 24×24, and 48×48 elements were analyzed. Due to the model grid generation based on expansion ratios, the locations of the nodes change as the number of elements increases. Therefore, the only nodes that are constant for all three grids are at the following locations: r = 0, $z = b_c$ = 5 cm and $r = R_s$ = 2.5 cm, $z = b_c$ = 5 cm. The convergence rate was calculated for these two nodes for both the linear head distribution and nonlinear head distribution. For the linear head distribution, p = 1.74 at both nodes; for the nonlinear head distribution, p = 1.89 at both nodes. Both these values are relatively close to the theoretical convergence rate of p = 2. Therefore, it can be assumed that the model is achieving nearly the desired convergence rate.

3.5.4.2 Nonlinear Solution Limits

One of the primary reasons for choosing the Forchheimer equation to model the nonlinear flow effects observed in PFC is that the Forchheimer equation should approach Darcy's law for either low hydraulic gradients or small values of the nonlinear Forchheimer coefficient. These two limiting cases were investigated in order to determine if the nonlinear model is working properly. Figure 3-46 shows the maximum percent difference between the linear and nonlinear head distributions as a function of standpipe head. The core dimensions used for this analysis are

R_s = 2.5 cm, R_c = 10 cm, and b_c = 5 cm. For different core dimensions, the curves will shift, but the same general trends are observed.

As the standpipe head decreases, the percent difference between the two models decreases as well, so that the nonlinear head distribution approaches the linear head distribution as desired. Furthermore, as mentioned in Section 3.5.3.6, the nonlinear head distribution is solely a function of the value of the nondimensional parameter b/a^2. So the different curves correspond to different relative magnitudes of this nondimensional parameter. Finally, for smaller values of b/a^2, the nonlinear head distribution approaches the linear head distribution at a greater rate. This is expected because as the nonlinear Forchheimer coefficient decreases, one would expect the resulting nonlinear head distribution to approach the linear head distribution.

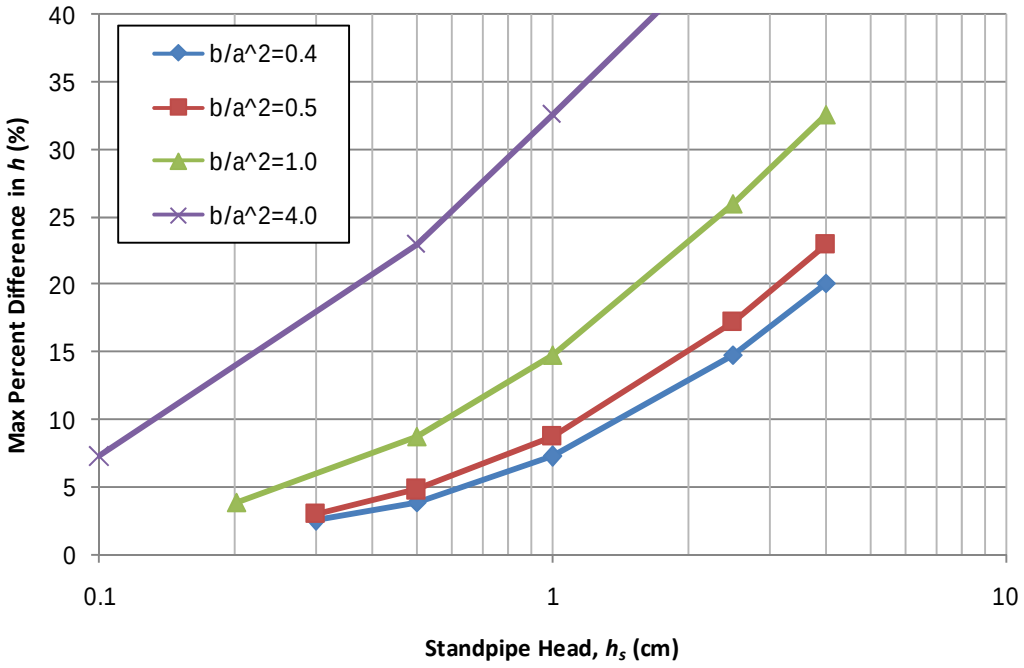

Figure 3-46: Maximum percent difference in head distribution between linear and nonlinear models versus standpipe head for varying magnitudes of nonlinear effect

Another way to investigate how the nonlinear model approaches the linear model is by examining the outflow rate. Figure 3-47 is a similar graph to that shown in Figure 3-46 and shows the percent difference between the linear outflow rate and nonlinear outflow rate. Again, as the standpipe head and/or nonlinear effect decrease, the nonlinear outflow rate approaches the linear outflow rate as expected. A positive percent difference in flow rate is observed when the linear flow rate is greater than the nonlinear flow rate. This means that for the same standpipe head, the nonlinear model will produce a smaller flow rate.

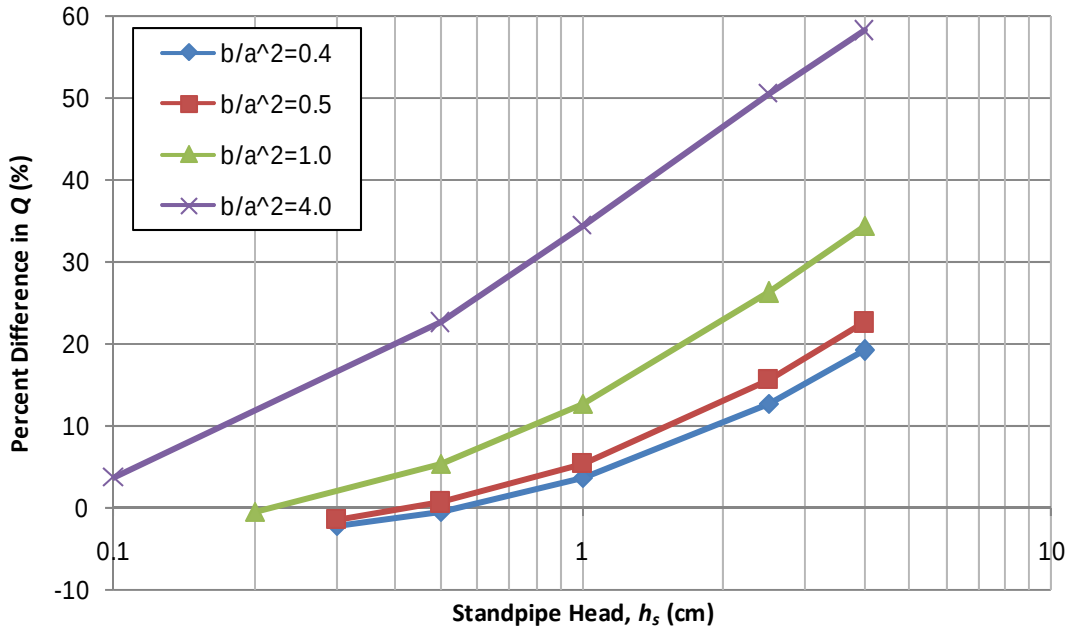

Figure 3-47: Percent difference in outflow rate between linear and nonlinear models versus standpipe head for varying magnitudes of nonlinear effect

As with the change in percent difference for the head distribution, the percent difference in flow rate is solely dependent on the value of b/a^2. This result does not seem immediately obvious because the flow rate is not constant for a given value of b/a^2 (as shown in Equation (3.105)). However, the ratio of the linear flow rate to the nonlinear flow rate (Equation (3.80) divided by Equation (3.105)) is a function of b/a^2. Therefore, this ratio governs the relative magnitudes of the two flow rates such that the curves in Figure 3-47 can also be characterized by the magnitude of the nonlinear effect.

One final method to determine whether the nonlinear numerical model is behaving as we would expect is to compare the results to the Thiem equation for linear flow to a well. The Thiem equation is a solution for steady flow to a well in a confined aquifer for purely radial flow. Although the nonlinear numerical model applies to two-dimensional (vertical and radial) flow, we can compare the model results to the Thiem equation by using a core geometry with $R_s << R_c$ and $b_c << R_c$. In this case, we would expect to see radial flow in the majority of the domain (see comparison of Figure 3-28 and Figure 3-29). Due to the upper and lower no flow boundaries imposed in the numerical model, flow through the PFC core resembles flow through a confined aquifer.

In general, the Thiem equation provides a solution for the head difference between two points as a function of the pumping flow rate out of the well, the transmissivity of the aquifer (hydraulic conductivity times aquifer thickness), and the radial position of the two points being compared. The Thiem equation is given as:

$$h_2 - h_1 = \frac{Q}{2\pi K b_c} \ln\left(\frac{r_2}{r_1}\right) \qquad (3.107)$$

Equation (3.107) compares the head at radial positions r_1 and r_2 from the center of the pumping well. For comparison to the nonlinear numerical model, we will take $r_1 = R_c$ and $r_2 = R_s$ so that $h_1 = 0$ and $h_2 = h_s$. The flow rate must be negative because the Thiem equation is for a pumping well, whereas in our model, the addition of water on the standpipe can be considered an injection well. Therefore, the form of the Thiem equation used for comparison purposes is:

$$h_s = \frac{-Q}{2\pi K b_c} \ln\left(\frac{R_s}{R_c}\right) \tag{3.108}$$

The Thiem equation can be compared to the modified Forchheimer equation for a small nonlinear term. We have already shown that the Forchheimer solution approaches the Darcy solution for low hydraulic gradient and/or specific discharge. Therefore, we would expect in that case that the modified Forchheimer equation will approach the Thiem Equation (3.108). In this limit, the linear modified Forchheimer coefficient could be approximated by:

$$\alpha \approx -\frac{1}{2\pi K b_c} \ln\left(\frac{R_s}{R_c}\right) \tag{3.109}$$

In order to make the comparison, the following core geometry was modeled: R_s = 2.5 cm, R_c = 25 cm, b_c = 2.5 cm, and b = 1 s^2/cm^2; a varies from 1 s/cm to 7 s/cm. The nonlinear numerical model is run and the resulting α value is obtained for each value of a. Figure 3-48 shows a graph of the obtained α value from the numerical model compared to the expected α value obtained from the Thiem equation as given in Equation (3.109).

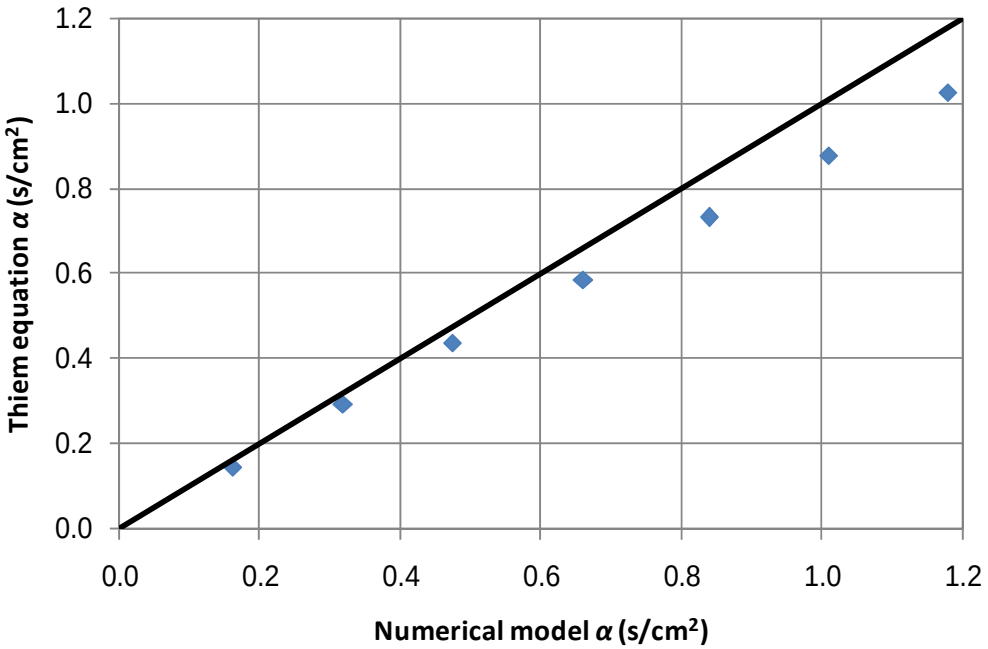

Figure 3-48: Comparison of nonlinear numerical model with Thiem equation

As the numerical data points approach the 1:1 line shown in Figure 3-48, the α value is approaching the value predicted by the Thiem equation, suggesting that the nonlinear numerical model is behaving as we would expect a confined aquifer to respond. The minimum percent difference between the numerical model α and the Thiem equation α is 7% for the data shown above. This analysis again confirms our assumption that the Forchheimer equation should approach Darcy flow results.

3.5.5 Impact of Core Specimen Geometry

3.5.5.1 Methodology for Investigating Impact of Core Geometry

The nonlinear numerical model requires the following inputs: core geometry (R_s, R_c, and b_c), original Forchheimer coefficients (a and b), and standpipe head (h_s). From these inputs, the outflow rate Q is determined and a curve of h_s versus Q is developed for multiple values of h_s. From this curve, the two modified Forchheimer coefficients (α and β) can be determined using a simple regression equation. This allows for a relationship between the modified Forchheimer coefficients and the original Forchheimer coefficients. As shown in the following subsections, the modified and original Forchheimer coefficients are linearly related. Therefore, in order to determine the impact of the core geometry on these linear relationships, a range of core dimensions were simulated. Four values each of R_s, R_c, and b_c were simulated for a total of 64 total combinations. For each core geometry combination, a total of 10 values of a and b were simulated to determine the relationship between the modified and original Forchheimer coefficients. For each combination of a and b, 10 values of h_s were simulated in order to determine the two modified Forchheimer coefficients from regression. Therefore, a total of 6,400 model simulations were conducted in order to investigate the impact of core geometry. The values tested were R_s = 1.5, 2, 2.5, and 3 cm; R_c = 7.5, 10, 15, and 20 cm; and b_c = 2.5, 3.25, 4, and 5 cm. The core specimens collected have a thickness that ranges from 2.8 to 4.8 cm, and radii of roughly 7.5 and 10.9 cm. The standpipe radius used during testing is 1.9 cm. Therefore, it is expected that the range of simulated core dimensions should include the range of core specimens that were extracted from the roadways. Finally, additional simulations will be determined specifically for the CRWR field test apparatus used to measure in-situ hydraulic conductivity because the field test apparatus has core dimensions that lie outside the above mentioned range of core dimensions.

There are two versions of the Forchheimer equation that are of interest. The original Forchheimer equation can be written in one of two ways:

$$I = aq + bq^2 \tag{3.110}$$

$$I = \frac{q}{K}\left(1 + \frac{q}{n}\right) \tag{3.111}$$

where the linear terms are related by $a = 1/K$ and the nonlinear terms are related by $n = a/b$. The modified Forchheimer equation can also be written in one of two ways:

$$h_s = \alpha Q + \beta Q^2 \tag{3.112}$$

$$\frac{h_s}{R_c} = \frac{Q}{\xi}\left(1 + \frac{Q}{\eta}\right) \tag{3.113}$$

where the linear terms are related by $\xi = R_c/\alpha$ and the nonlinear terms are related by $\eta = \alpha/\beta$. These relationships are important in the following regression results to ensure that a conversion between the two forms of the Forchheimer equation exists.

3.5.5.2 Regression of Linear Forchheimer Coefficients

The linear Forchheimer coefficients (a and α) are expected to be linearly related to each other. This relationship cannot be determined analytically and depends on the core geometry. For a core with dimensions R_s = 2.5 cm, R_c = 10 cm, and b_c = 5 cm, Figure 3-49 shows the resulting relationship between a and α. The two linear Forchheimer coefficients are linearly related, and the relationship is perfectly correlated from the numerical simulations.

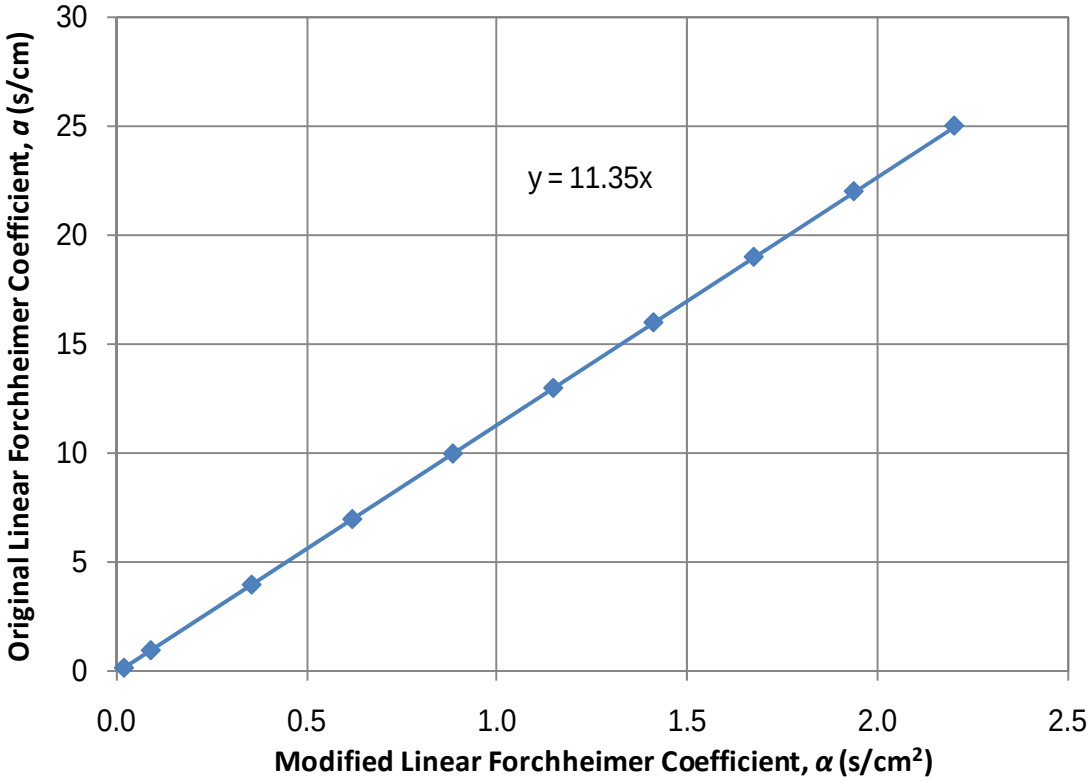

Figure 3-49: Relationship between modified and original linear Forchheimer coefficient for R_s/R_c = 0.25 and b_c/R_c = 0.5

It can be shown that as any of the three core dimensions change, the slope of the line will shift. But in general, the following relationship exists between the two linear Forchheimer coefficients:

$$a = c_1(R_s, R_c, b_c)\alpha \tag{3.114}$$

Equation (3.114) says that the original linear Forchheimer coefficient is linearly related to the modified linear Forchheimer coefficient, where the slope of that relationship c_1 is a function of the core dimensions. The slope c_1 has units of [L]. Using the 64 core geometry combinations described above, the following regression equation was developed for the linear Forchheimer coefficients:

$$a \approx 5.8 R_s \left(\frac{b_c}{R_c} \right)^{0.33} \alpha \qquad (3.115)$$

Equation (3.115) assumes that the slope c_1 of the line relating a to α depends on a power relationship for the three core dimensions. In addition, the grouping of the three core dimensions results in a combination with units of [L]. Therefore, the constant 5.8 is dimensionless and the above equation can be used under any system of units.

The accuracy of the approximation for determining the slope c_1 can be addressed by graphing the slope obtained from Equation (3.115) as a function of the slope obtained from the numerical model. If the regression equation gives a good approximation to the numerical results, the data will plot as a straight line with unit slope. Figure 3-50 shows the comparison between c_1 obtained from regression to c_1 obtained from the numerical simulations. The standard error between the two values of c_1 is 0.422 cm. The average percent difference from the regression equation is nearly 4%, but the maximum percent difference is nearly 18%. This suggests that for the majority of the core dimensions tested, the regression equation produces a very good approximation.

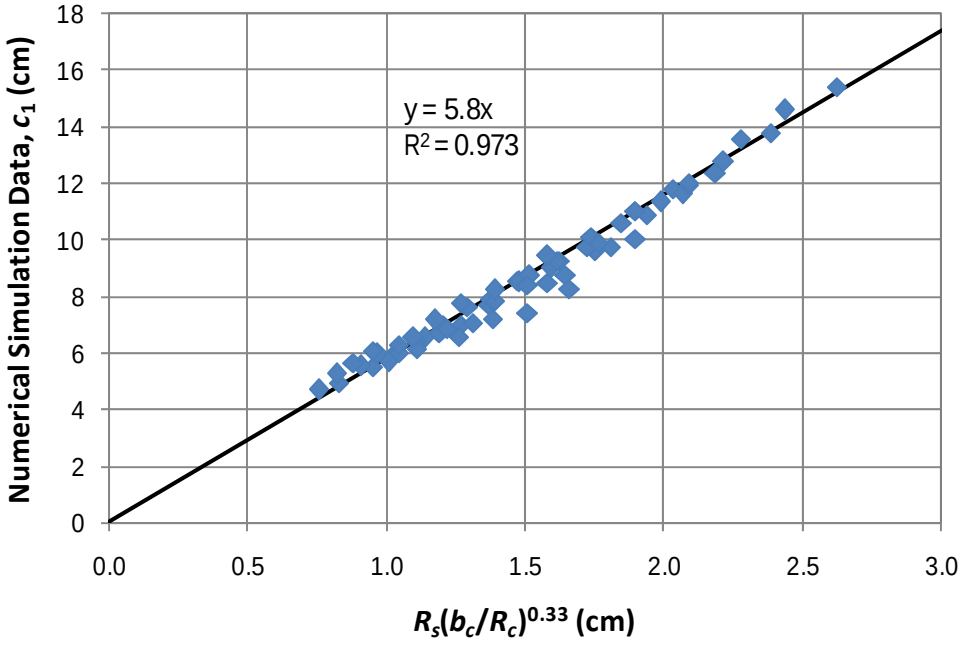

Figure 3-50: Regression results for c_1 (cm)

As mentioned in Section 3.5.5.1, we can express the Forchheimer equation in one of two ways. Looking at the transformed form of the equation, we would expect a linear relationship between the transformed coefficients K and ξ. This equation can be written in a general form as:

$$K = c_3\left(R_s, R_c, b_c\right)\xi \tag{3.116}$$

The slope c_3 in Equation (3.116) has units of [1/L^2]. (Note: The symbol c_3 is used here because c_2 is reserved for the slope relating to the nonlinear coefficients. Slopes c_1 and c_2 will correspond to the first form of the Forchheimer equation, and slopes c_3 and c_4 correspond to the transformed form of the equation.) Conducting a power law regression on the core dimensions results in the following relationship:

$$K \approx \frac{0.175}{R_s R_c^{\,0.67} b_c^{\,0.33}}\xi \tag{3.117}$$

The power terms on each of the core dimensions in Equation (3.117) can be determined from the powers obtained in Equation (3.115) due to the conversions between the two forms of the Forchheimer equation. Therefore, only the constant 0.175 was changed in order to find the correct regression equation. Again, the powers on the core dimensions result in units of [1/L^2] so that the constant 0.175 is dimensionless.

Figure 3-51 shows a plot of the value of the slope c_3 obtained from the numerical simulation to that obtained from the regression Equation (3.117). The resulting standard error is 5.8×10^{-4} 1/cm^2, with an average percent difference of 4.5%, and a maximum percent difference of nearly 17%. Therefore, we see very good agreement from the regression equation and the numerical modeling results, suggesting that the regression equation provides a good approximation to the numerical model.

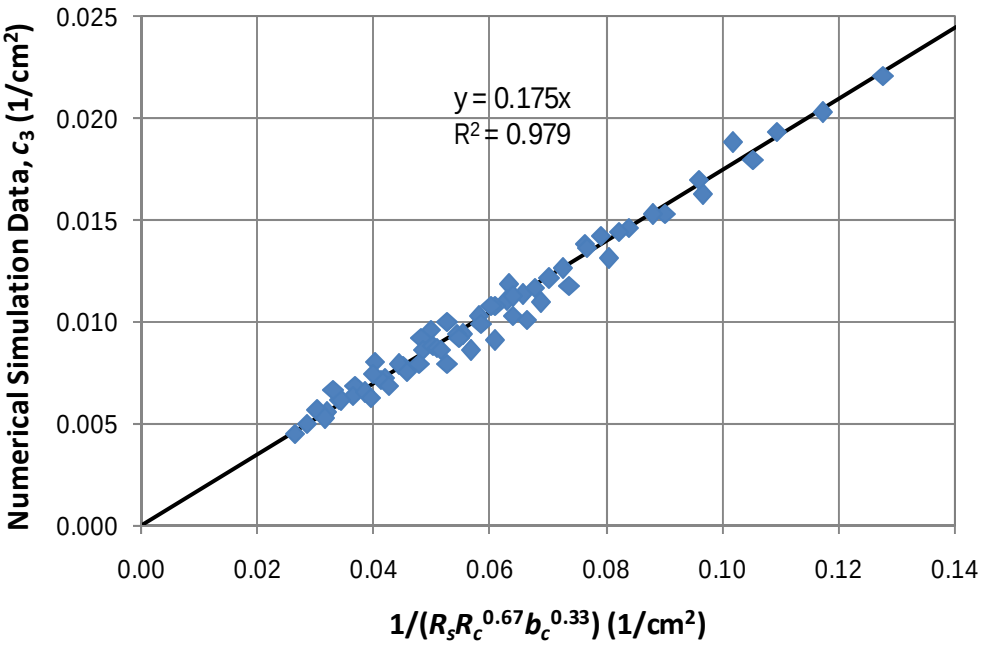

Figure 3-51: Regression results for c_3 (1/cm^2)

One last comment should be made on the choice of a power law regression equation and the resulting errors from these equations. The power law produces desirable results in that the regression equation can be nondimensionalized and used with respect to any system of dimensions. However, errors are produced from this method. For example, we can take a closer look at the slope c_1 and specifically on the power term for the dimension R_s. Equation (3.115) says that the power term on R_s for slope c_1 has a value of one. One way of looking at the error produced by this value is to do a power law regression analysis on the four values of R_s simulated while keeping R_c and b_c constant. The results of this analysis are shown in Figure 3-52.

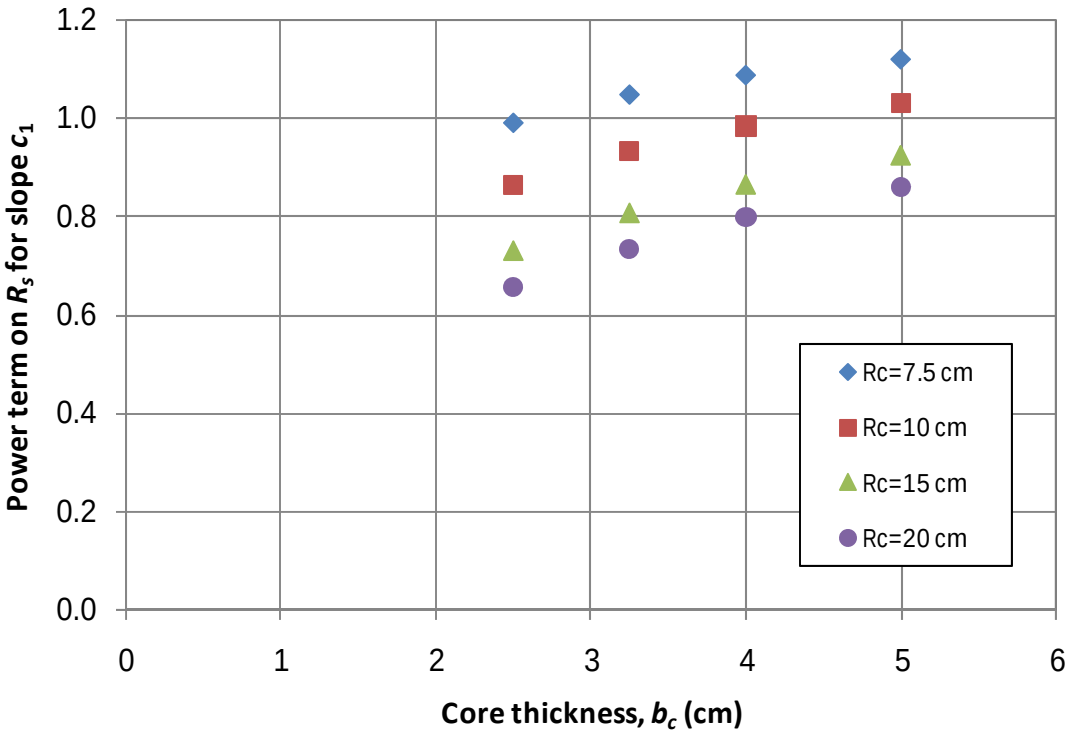

Figure 3-52: Analysis of power law term as function of core dimensions

Figure 3-52 shows that the power on the R_s term is not a constant value of one, but instead changes with the values of R_c and b_c. For this reason, the power law regression will result in error. Due to the trends seen in Figure 3-52, perhaps a more complex regression could be conducted so that the power on one core dimension are functions of the other two core dimensions. However, the complexity of such a model would negate the benefit of having a simple approximation between the original and modified Forchheimer coefficients. Furthermore, the errors produced by the proposed power law relation are typically minimal for most core geometries. These trends can be observed for all the power terms determined from the regression equation and will result in greater errors when conducting regression equations for the nonlinear coefficients.

3.5.5.3 Regression of Nonlinear Modified Forchheimer Coefficients

The nonlinear Forchheimer coefficients (b and β) are also expected to be linearly related to each other. This relationship cannot be determined analytically and depends on the core geometry. For a core with dimensions R_s = 2.5 cm, R_c = 10 cm, and b_c = 5 cm, Figure 3-53 shows the resulting relationship between b and β. The two nonlinear Forchheimer coefficients are linearly related, and the relationship is perfectly correlated from the numerical simulations.

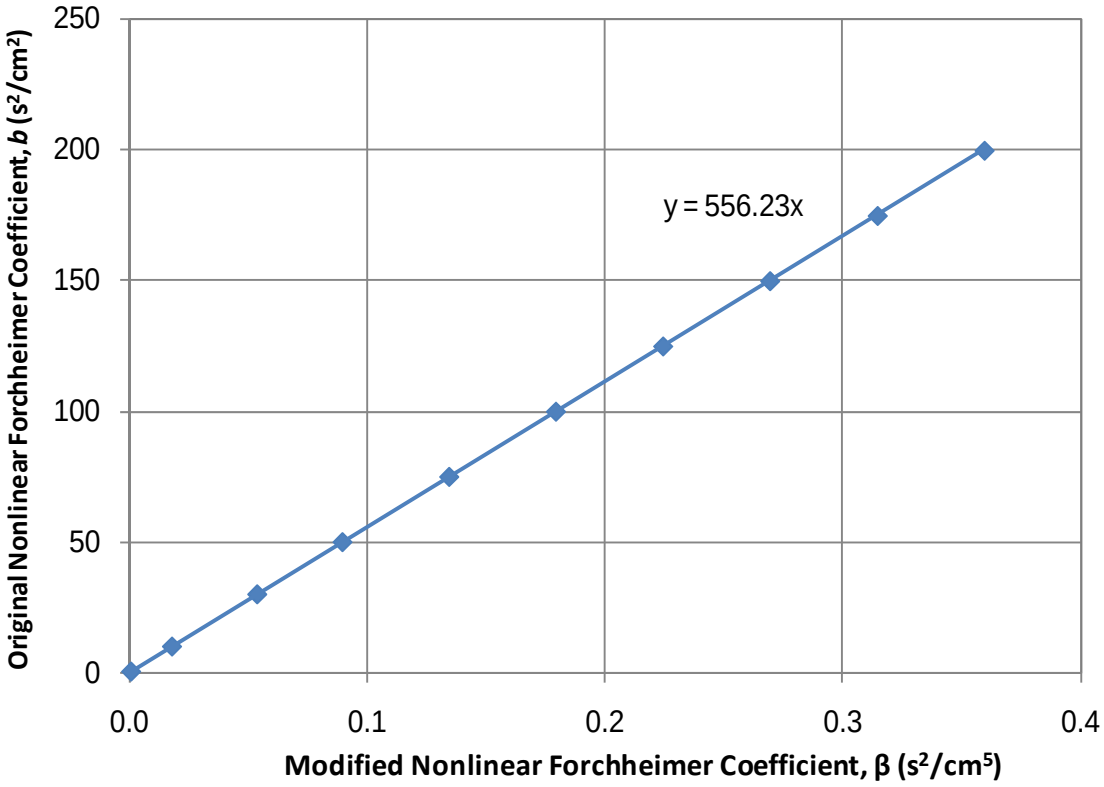

Figure 3-53: Relationship between modified and original nonlinear Forchheimer coefficient for R_s/R_c = 0.25 and b_c/R_c = 0.5

The following relationship exists between the two nonlinear Forchheimer coefficients:

$$b = c_2(R_s, R_c, b_c)\beta \tag{3.118}$$

Equation (3.118) says that the original nonlinear Forchheimer coefficient is linearly related to the modified nonlinear Forchheimer coefficient, where the slope of that relationship c_2 is a function of the core dimensions and has units of [L^3]. The following regression equation was developed for the nonlinear Forchheimer coefficients:

$$b \approx 18.6 R_s^{2.5} (R_c b_c)^{0.25} \beta \tag{3.119}$$

Equation (3.119) makes the same assumptions of a power law relation as before. In addition, the grouping of the three core dimensions results in a combination with units of [L^3] so that the constant 18.6 is dimensionless and the above equation can be used under any system of units.

The accuracy of the approximation for determining the slope c_2 is addressed by graphing the slope obtained from Equation (3.119) as a function of the slope obtained from the numerical model. Figure 3-54 shows this comparison. The standard error between the two values of c_2 is 67 cm^3. This value is much larger than the standard error reported for the linear coefficients in part

due to the significantly larger values of c_2. The average percent difference from the regression equation is 9%, and the maximum percent difference is 25%. This suggests that for the nonlinear coefficient, there is much more uncertainty involved in the regression equation. The cause of this uncertainty follows the error as shown in Figure 3-52. For the nonlinear coefficients, the change in power terms with respect to each dimension varies to a greater extent, causing more error. This is a concern, and a more complex model could be developed to reduce this error. However, as shown in the following sections, the error involved when compared to experimental data is within an acceptable range. In addition, the precise value of the nonlinear coefficient is of secondary concern. The nonlinear coefficient is used primarily to determine when and where nonlinear effects are significant. For the purposes of measuring the hydraulic conductivity of PFC, nonlinear effects will always be significant. Therefore, the precise value of the nonlinear coefficient will not provide any significant information and only an acceptable estimate is needed.

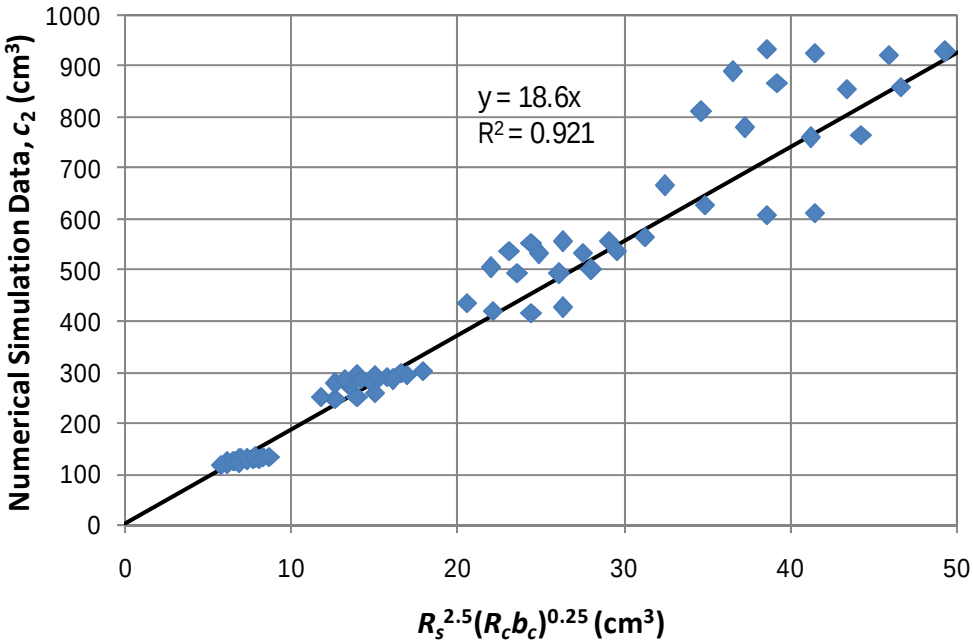

Figure 3-54: Regression results for c_2 (cm^3)

Looking at the transformed form of the Forchheimer equation, we would expect a linear relationship between the transformed coefficients n and η. This equation can be written in a general form as:

$$n = c_4(R_s, R_c, b_c)\eta \qquad (3.120)$$

The slope c_4 in Equation (3.120) has units of [1/L^2]. Conducting a power law regression on the core dimensions results in the following relationship:

$$n \approx \frac{0.3 b_c^{\,0.08}}{R_s^{\,1.5} R_c^{\,0.58}} \eta \qquad (3.121)$$

The power terms on each of the core dimensions in Equation (3.121) can be determined from the powers obtained in Equations (3.115) and (3.119) due to the conversions between the two forms of the Forchheimer equation. Therefore, only the constant 0.3 was changed in order to find the correct regression equation. Again, the powers on the core dimensions result in units of $[1/L^2]$ so that the constant 0.3 is dimensionless.

Figure 3-55 shows a plot of the value of the slope c_4 obtained from the numerical simulation to that obtained from the regression Equation (3.121). The resulting standard error is 4.2×10^{-3} $1/cm^2$, with an average percent difference of 11%, and a maximum percent difference of 30%. The standard error is very small due to the small values of c_4. The percent difference is considerably larger than that obtained for the linear coefficients. As previously mentioned, this is of lesser concern and as shown in the following section, the regression equation produces acceptable results.

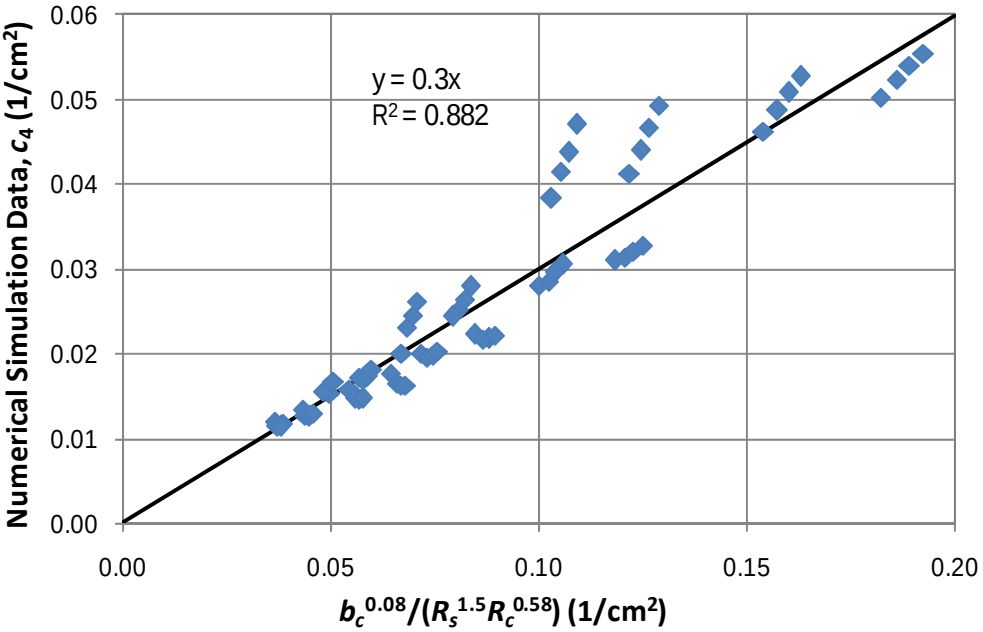

Figure 3-55: Regression results for c_4 ($1/cm^2$)

3.5.5.4 Determination of Hydraulic Conductivity for Core Specimens

Now that we have established a method to relate the original Forchheimer coefficients (a and b) to the modified Forchheimer coefficients (α and β), we can estimate the original coefficients from the measured modified coefficients reported in Section 3.3.4, Tables 3.14 through 3.17 report the estimated original Forchheimer coefficients ($K = 1/a$ and b) obtained from Equations (3.115) and (3.119) for each core specimens tested in the laboratory. In addition, the resulting modified Forchheimer coefficients obtained from the nonlinear numerical model for

the estimated original coefficients are provided. Finally, the percent difference (*P.D.*) in the modified Forchheimer coefficients obtained from the model when compared to the coefficients obtained from laboratory testing is reported. This is the final step necessary in obtaining the hydraulic conductivity for each core specimen.

Table 3.14: Results of numerical simulations for 2007 core specimens

Core ID	K (cm/s)	b (s^2/cm^2)	α (s/cm^2)	β (s^2/cm^5)	*P.D.* in α	*P.D.* in β
1-A-T	0.180	2.785	0.7036	0.0125	0.29	-12.84
1-B-T	2.427	0.584	0.0485	0.0024	1.67	-13.35
2-A-T	0.668	1.812	0.1906	0.0080	1.21	-14.38
2-B-T	0.308	3.034	0.4062	0.0132	0.67	-14.16
3-B-T	0.455	7.206	0.3069	0.0344	3.52	-11.74
3-C-T	0.457	2.679	0.2916	0.0122	1.96	-13.19

Table 3.15: Results of numerical simulations for 2008 core specimens

Core ID	K (cm/s)	b (s^2/cm^2)	α (s/cm^2)	β (s^2/cm^5)	*P.D.* in α	*P.D.* in β
1-1-T	0.801	2.216	0.1530	0.0090	0.66	-2.14
1-1-S	2.328	1.213	0.0547	0.0050	-0.69	-4.22
1-2-T	0.829	2.797	0.1466	0.0113	0.79	-1.39
1-2-S	1.115	2.000	0.1168	0.0083	-0.28	-5.11
1-3-T	1.389	1.529	0.0912	0.0063	-0.36	-4.03
1-3-S	1.820	1.118	0.0734	0.0047	-0.13	-5.59
2-1-T	0.474	4.136	0.2907	0.0176	0.55	-6.07
2-2-T	0.957	2.306	0.1390	0.0097	-0.14	-5.61
2-3-T	0.468	4.060	0.3008	0.0176	0.77	-5.83
3-1-T	0.056	64.297	02.3938	0.2735	-0.29	-5.29
3-2-T	0.048	166.832	3.0816	0.7476	1.74	-5.15
3-3-T	0.228	15.720	0.5850	0.0660	0.01	-5.54

Table 3.16: Results of numerical simulations for 2009 core specimens

Core ID	K (cm/s)	b (s^2/cm^2)	α (s/cm^2)	β (s^2/cm^5)	*P.D.* in α	*P.D.* in β
1-i-T	1.831	1.932	0.0683	0.0079	-0.39	-3.50
1-i-S	2.868	0.875	0.0467	0.0037	-0.17	-5.63
1-ii-T	0.555	3.567	0.2250	0.0146	0.19	-3.33
1-ii-S	2.106	1.613	0.0657	0.0069	0.30	-5.88
1-iii-T	1.334	1.266	0.0927	0.0052	0.29	-2.59
1-iii-S	0.954	3.096	0.1437	0.0132	0.22	-5.87
2-i-T	0.194	4.496	0.7066	0.0193	-0.01	-5.34
2-ii-T	0.437	2.162	0.3090	0.0092	-0.05	-5.69
2-iii-T	0.992	2.007	0.1356	0.0085	0.02	-5.75
3-i-T	0.102	29.132	1.2910	0.1217	-0.34	-5.12
3-ii-T	0.180	12.368	0.7167	0.0513	-0.36	-4.70
3-iii-T	0.241	17.371	0.5413	0.0722	-0.19	-5.14

Table 3.17: Results of numerical simulations for 2010 core specimens

Core ID	K (cm/s)	b (s^2/cm^2)	α (s/cm^2)	β (s^2/cm^5)	*P.D.* in α	*P.D.* in β
1-a-T	0.359	12.721	0.3139	0.0521	4.74	-9.68
1-a-S	1.327	0.795	0.0884	0.0033	1.82	-12.97
1-b-T	2.074	1.067	0.0545	0.0044	4.17	-10.02
1-b-S	1.510	0.630	0.0767	0.0026	2.21	-12.76
1-c-T	0.588	3.909	0.1903	0.0160	5.46	-9.31
1-c-S	1.551	0.466	0.0752	0.0019	1.96	-13.03
3-a-T	0.203	34.789	0.5626	0.1433	2.97	-11.90
3-b-T	0.019	640.386	5.8899	2.6548	2.23	-11.89
3-c-T	0.090	133.903	1.2685	0.5518	2.88	-11.92

From Tables 3.14 through 3.17, we now have a value of the hydraulic conductivity for each core specimen. It is necessary to investigate the error associated with this value of hydraulic conductivity. This is addressed in the comparison between modified Forchheimer coefficients obtained in the lab and from the numerical model. The linear modified Forchheimer coefficient α obtained from the numerical model is at most 3.5% greater than the value obtained in the lab (Core 3-B-T). The majority of the core specimens have a percent difference in the linear modified Forchheimer coefficient of less than one percent. Therefore, the regression equations used to estimate the original linear Forchheimer coefficients are producing very reliable estimates.

The nonlinear modified Forchheimer coefficient has a much greater error associated with it. The maximum percent difference in β is roughly 14% (Core 2-A-T). The smaller diameter cores which were extracted in 2007 and 2010 tend to result in a larger percent difference in the nonlinear term, on the order of over 10% error. This begins to show the limitations of the regression equations presented in Section 3.5.5.3 for the nonlinear coefficients. However, for the larger diameter cores, the nonlinear term has a percent error of typically less than 5%. In general, the regression equations used to estimate the original nonlinear Forchheimer coefficients result in more error to the experimental data. This is of minimal concern because the nonlinear term is typically only necessary to determine when nonlinear effects can be ignored. Clearly, for the hydraulic conductivity test methodology developed for this research study, nonlinear effects will never be negligible. Therefore, we have no need to be extremely precise in our estimates of the nonlinear Forchheimer coefficient.

The above estimates for the original Forchheimer coefficients (a and b) were made using regression Equations (3.115) and (3.119). Similarly, we can use estimates for the transformed original Forchheimer coefficients (K and n) using regression Equations (3.117) and (3.121) in order to determine the percent difference between the modeled and measured modified Forchheimer coefficients. The purpose of this analysis is to determine which set of regression equations provides a more accurate estimate of the measured modified Forchheimer coefficients. Using either set of regression equations results in roughly the same percent difference in the calculated modified Forchheimer coefficients. For example, the percent different in α when determined using the regression equation for a ranges from -0.69% to 5.46%; whereas the percent difference using the regression equation for K ranges from -2.26% to 3.97%. Therefore, although these values shift slightly, the overall range of percent difference for both equations is roughly 6.2%. Similarly, for the nonlinear coefficients, the range of percent difference in β when determined using the equation for b is 15.7%; whereas, the range using the equation for n is

13.3%. Again, both sets of regression equations result in nominally the same precision to the measured lab or field data.

3.5.5.5 Determination of Hydraulic Conductivity for Field Test Apparatus

The dimensions of the CRWR field test apparatus extend beyond the limitations of the dimensions discussed in the previous sections due to the large standpipe and core radii. For this reason, a regression equation was developed specifically for the dimensions of the CRWR field test apparatus with varying PFC thicknesses. The CRWR field test apparatus has dimensions R_s = 5.08 cm and R_c = 22.86 cm. The resulting regression equations based on six different core thicknesses ranging from 2.5 to 5 cm are as follows:

$$a = 5b_c^{0.75}\alpha \tag{3.122}$$

$$b = 482b_c^{1.25}\beta \tag{3.123}$$

$$K = 8.8\times10^{-3}b_c^{-0.75}\xi \tag{3.124}$$

$$n = 0.01b_c^{-0.5}\eta \tag{3.125}$$

These four regression equations apply specifically to the CRWR test apparatus and cannot be used for any other values of R_s or R_c. Furthermore, the constants in Equations (3.122) and (3.125) have units associated with them so that the dimensions used must be expressed in cm.

The above regression equations were used for the CRWR field test results obtained to determine the in-situ hydraulic conductivity and reported in Section 3.4.3.2. The PFC thickness used in the regression equations above is the average PFC thickness from all core specimens extracted for each roadway. For Loop 360, the average thickness is 4.013 cm (1.58 in); for FM 1431, the average thickness is 3.228 cm (1.27 cm); and for RR 620, the average thickness is 3.499 cm (1.38in). Although these thicknesses are not precisely what exist in the field, it should give a good approximation to the actual thickness. The results are reported in Table 3.18. The field test location and date are provided together with the hydraulic conductivity and nonlinear Forchheimer coefficient obtained from the regression equations. The resulting percent difference (*P.D.*) in the modified Forchheimer equations when compared to the values measured in the field are provided as well.

Table 3.18: Results of numerical simulations for CRWR field test

Roadway	Location	Date	K (cm/s)	b (s^2/cm^2)	*P.D.* in α	*P.D.* in β
Loop 360	Shoulder	6-29-08	3.46	0.429	0.65	-3.07
Loop 360	Shoulder	6-29-08	2.78	0.495	0.50	-2.87
Loop 360	Shoulder	9-25-08	2.96	0.451	0.64	-3.05
Loop 360	Shoulder	9-25-08	3.26	0.493	0.72	-3.03
Loop 360	Shoulder	11-9-08	7.61	0.505	0.11	-2.83
Loop 360	Shoulder	11-23-08	7.07	0.346	-0.01	-2.92
Loop 360	Shoulder	2-2-09	2.69	0.541	0.65	-2.95
Loop 360	Travel Lane	2-2-09	3.59	0.547	0.58	-2.99
Loop 360	Shoulder	2-5-10	3.43	0.448	0.90	-3.06
Loop 360	Travel Lane	2-5-10	3.16	0.314	0.37	-2.97
FM 1431	Travel Lane	2-2-09	0.58	5.209	-1.09	-3.38
RR 620	Travel Lane	2-2-09	1.94	2.115	-0.30	-4.05
RR 620	Travel Lane	2-5-10	1.00	2.462	-0.31	-4.08

The average percent difference in the modified linear Forchheimer coefficient is typically less than one percent, whereas the percent difference in the nonlinear coefficient is roughly three percent. These results are much more accurate because the regression equations were developed for only one changing core dimension (b_c). The average hydraulic conductivity on Loop 360 is roughly 3 cm/s (1.2 in/s). This is of the same order of magnitude obtained for the core specimens extracted from Loop 360. The core specimens have much more variability than the field data, which is the reason for conducting the field test in order to remove this variability. There were two field tests on Loop 360 with significantly larger hydraulic conductivity of roughly 7 cm/s (2.8 in/s). These two tests were conducted immediately after the constant head field tests described in Section 3.4.2.3. The large, sustained flow rates used during the constant head tests may have flushed some trapped sediment out of the pore space and/or caused a poor seal from the vacuum grease, resulting in an artificially large value of hydraulic conductivity.

The resulting hydraulic conductivity obtained on FM 1431 matches well with the value obtained in the laboratory. The hydraulic conductivity obtained on RR 620 appears to be slightly larger than what was obtained in the laboratory. There is no explanation for this variability, and further testing may be needed in order to verify these results. As mentioned in Section 3.2.2.4, Kelkar (2000) suggests that the nonlinear Forchheimer coefficient is typically larger when observed in the field than in the laboratory. A comparison of the experimental results presented above show that the field data do not result in significantly greater nonlinear coefficients. Therefore, the claim made by Kelkar (2000) does not apply to this experimental data set.

In order to determine the uncertainty associated with using the average core specimen thickness as the roadway thickness in the above analysis, we can compare the estimates for the original Forchheimer coefficients using plus/minus one standard deviation of the core specimen thickness. For Loop 360, the average thickness plus and minus one standard deviation is 4.588 cm and 3.438 cm, respectively. The larger thickness provides the following estimates: K = 3.13 cm/s and b = 0.507 s^2/cm^2 with a percent difference in α of 1.78% and β of 0.43%. The smaller thickness provides the following estimates: K = 3.89 cm/s and b = 0.354 s^2/cm^2 with a percent difference in α of -0.25% and β of -4.08%. Therefore, using plus/minus one standard deviation in the PFC thickness provides minimal error in the results. The percent difference in the modified

Forchheimer coefficients are of the same order of magnitude as before, suggesting that small changes in the PFC thickness are not expected to result in large errors.

In addition to the regression results obtained for the CRWR field test described above, a regression was also conducted for the field test described by Tan et al. (2002). Their field test has the following dimensions: R_s = 7.5 cm and R_c = 25 cm. A range of PFC thicknesses were simulated to determine the following regression equations in order to estimate the original Forchheimer coefficients:

$$a = 6.5 b_c^{\,0.75} \alpha \tag{3.126}$$

$$b = 680 b_c^{\,1.5} \beta \tag{3.127}$$

$$K = 6.2 \times 10^{-3} b_c^{\,-0.75} \xi \tag{3.128}$$

$$n = 0.01 b_c^{\,-0.75} \eta \tag{3.129}$$

The above equations are specific to the field test used by Tan et al. (2002), and the constants have units associated with them. Therefore, these equations can only be used for the Tan et al. field test when R_s and R_c are expressed in cm. Slightly different relationships are obtained for the Tan et al. field test when compared to the CRWR field test. This is due to the varying dimensions of the test apparatus. Unfortunately, Tan et al. do not provide their falling head data in such a way that these equations can be compared with their experimental results. Therefore, a comparison between the proposed regression equations and the method used by Tan et al. cannot be conducted.

3.6 Analysis of Hydraulic Properties

3.6.1 Statistical Objective and Data

The purpose for accurately measuring the hydraulic properties of PFC is to ultimately be able to determine when the benefits associated with driver safety and improved water quality will no longer persist. Because the pore space of PFC becomes clogged with sediment over time, it is expected that the porosity and hydraulic conductivity will decrease over time as a result. If the pore space becomes too clogged with sediment, it is expected that the benefits of the PFC will degrade. Measuring the in-situ hydraulic conductivity should be an indicator as to whether or not the PFC is adequately allowing for the drainage of stormwater runoff. Therefore, analyzing the trends in hydraulic properties should give an indication as to how these properties are changing.

The objectives of the following statistical analyses are to determine whether the hydraulic properties—porosity and hydraulic conductivity—are changing over time and between each roadway location. The two data sets that will be analyzed are the core specimen porosity and laboratory hydraulic conductivity. Measurement of the porosity is described in detail in Section 3.3. Measurement of hydraulic conductivity is determined based on laboratory evaluation of the modified Forchheimer coefficients (described in Section 3.3) and numerical modeling results to

convert the modified coefficients to the hydraulic conductivity (described in Section 3.5). Figure 3-56 and Figure 3-57 show the raw data for the porosity and hydraulic conductivity, respectively. The statistical tests we will use compare the average of each set with the overall average. Therefore, in these figures, the colored horizontal lines correspond to the average value of each roadway for each year. The thick dashed lines correspond to the overall average for each year, regardless of location. Finally, the thin dotted line gives the overall average of the hydraulic property regardless of year or location. This helps to give an indication of the relative differences in averages.

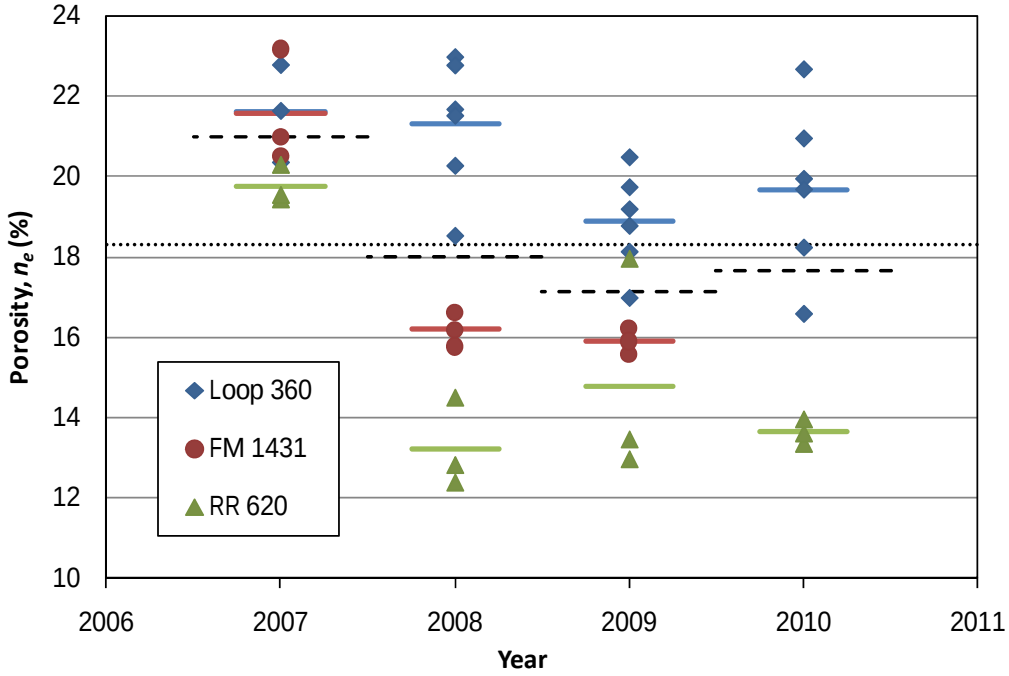

Figure 3-56: Raw porosity data (averages indicated by lines)

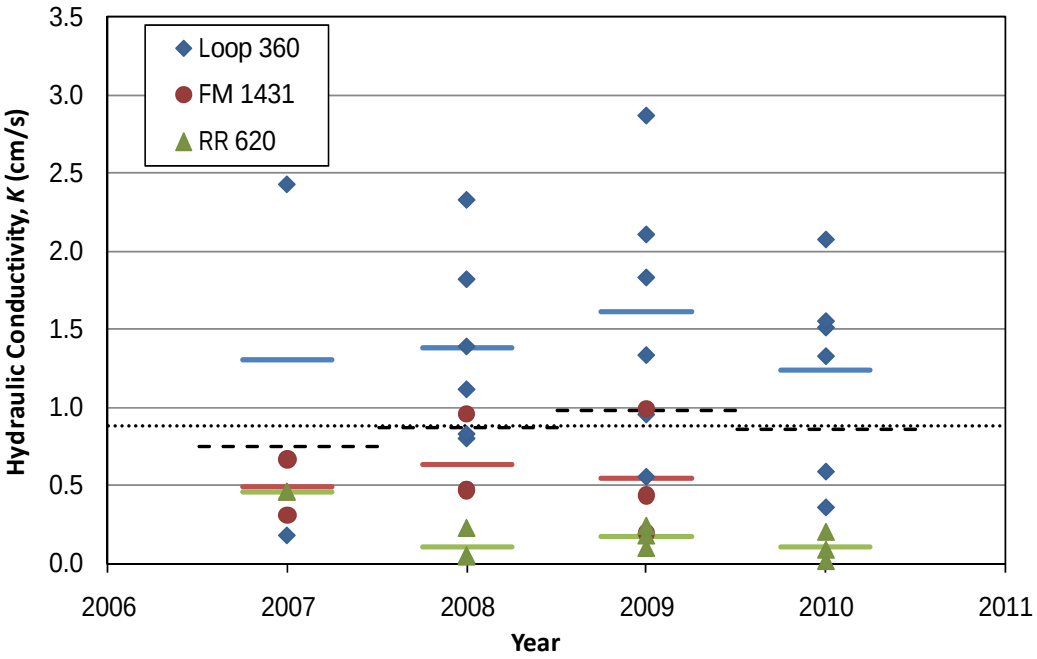

Figure 3-57: Raw hydraulic conductivity data (averages indicated by lines)

In order to gain a clearer view of how the hydraulic properties are changing over time, Figure 3-58 and Figure 3-59 show the average of porosity and hydraulic conductivity, respectively, for each year and each location. The error bars show plus/minus one standard deviation of the data. Based on Figure 3-58, we would expect that the porosity has decreased over time for each roadway and the variability in the porosity is not very large. Figure 3-59 suggests that the hydraulic conductivity has remained relatively constant over time for each roadway but the variability in hydraulic conductivity is much larger. The statistical tests described below will be used to determine whether the observed trends based on the data are statistically significant.

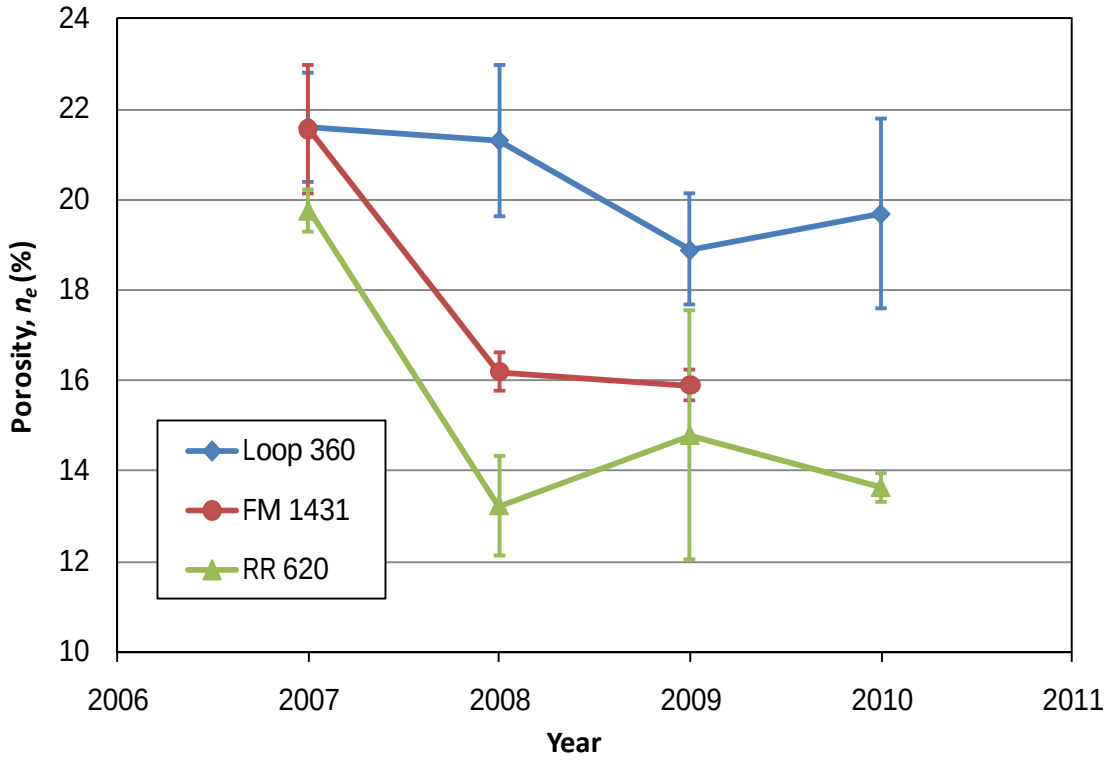

Figure 3-58: Averaged porosity data

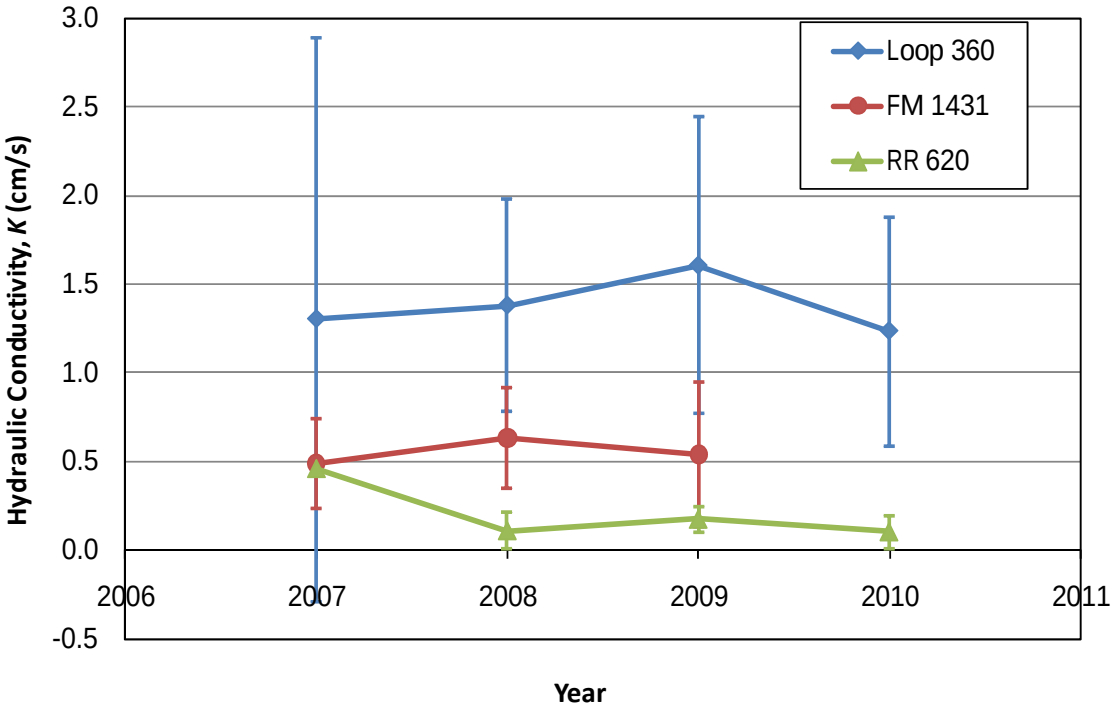

Figure 3-59: Averaged hydraulic conductivity data

Another interesting way to look at the raw data is to compare the hydraulic conductivity as a function of porosity. Ideally there would be some relationship between these two drainage properties so that it is possible to predict one property from the other. Figure 3-60 shows these two properties graphed together for each roadway. There does not appear to be any correlation between these two properties. In general, as the porosity increases, the hydraulic conductivity increases as well. The large variability in this relationship means we cannot use one property to predict the other with any degree of confidence. For this reason, the two properties must be analyzed separately.

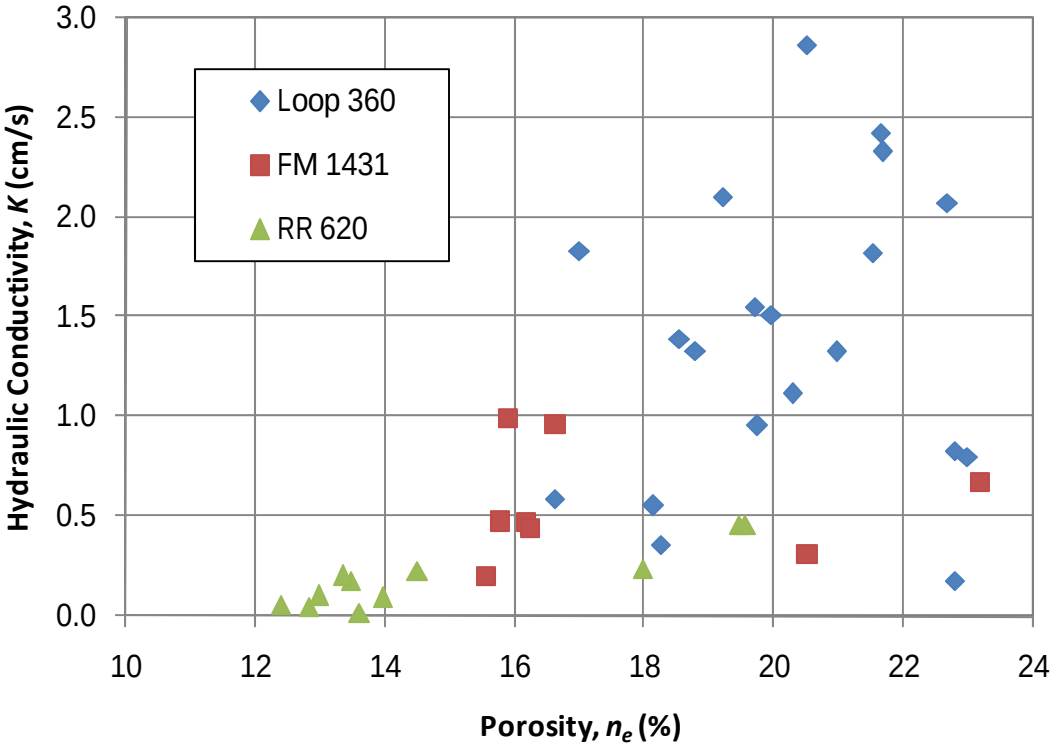

Figure 3-60: Comparison of hydraulic conductivity and porosity data

3.6.2 Nonparametric Statistical Test Descriptions

In order to accomplish the above objective of this statistical analysis, we must use an appropriate statistical test. Only three or six core specimens were extracted at each roadway location for a given year. Therefore, the individual data sets we are interested in comparing are relatively small. This means we cannot make any assumptions about the distribution of the data, and we cannot use a large sample approximation. Due to this constraint, we must use an exact nonparametric statistical test. In order to compare groups of data (three or more groups), we can use the Kruskal-Wallis test. If we want to compare pairs of data we can use the Mann-Whitney test. Both of these tests determine statistics based on the ranks of the data and do not make any assumptions about the distribution of the data. If we had a large number of core specimens and could prove that the data were normally distributed, we would use the more common parametric ANOVA (analysis of variance) test and Students *t*-test, respectively, instead of the nonparametric tests.

3.6.2.1 Kruskal-Wallis Test

The Kruskal-Wallis test is used to determine whether three or more groups of data (either the three roadway locations for a given year or three years for a given roadway location) are statistically similar. This is the nonparametric equivalent to the ANOVA test. The Kruskal-Wallis test ranks the data and performs a nonparametric test on the ranks of the data. No assumptions are made about the distribution of the data. The null hypothesis of the Kruskal-Wallis test is: H_0 = all three groups of data have identical distributions. The alternative hypothesis is: H_a = at least one group differs in its distribution.

Helsel and Hirsch (2002) define the Kruskal-Wallis test statistic as follows:

$$K_W = \frac{12}{N(N+1)} \sum_{j=1}^{3} n_j \left[R_j - \frac{N+1}{2} \right]^2 \tag{3.130}$$

In Equation (3.130), K_W is the Kruskal-Wallis test statistic, N is the total number of data points, n_j is the number of data points in group j, and R_j is the average of the ranks for group j. R_j is defined as follows:

$$R_j = \frac{1}{n_j} \sum_{i=1}^{n_j} R_{ij} \tag{3.131}$$

In Equation (3.131), R_{ij} is the rank of the i^{th} data value in group j. Equation (3.130) gives the exact test statistic when there are no ties in the data. If ties occur, a correction must be made, but for the porosity and hydraulic conductivity data we will analyze, no ties will exist.

The test statistic can be compared to a table of critical K_W values in order to determine the decision on the null hypothesis for a significance level α'. If the calculated test statistic K_{Wcalc} value is greater than or equal to the critical statistic $K_{W\alpha'}$ obtained from the table for the given sample sizes and significance level α', then the null hypothesis is rejected at that significance level and the groups cannot be shown to have identical distributions. In this event, the test gives no indication of which group differs from the others. In order to determine which group is different from the others, the Mann-Whitney test must be conducted.

3.6.2.2 Mann-Whitney Test

The Mann-Whitney test is also typically referred to as the Wilcoxon test or rank sum test. It is an exact nonparametric test that compares the ranks of only two data groups. This is the nonparametric equivalent of the Students *t*-test. Again, no assumptions are made about the distribution of the data sets. The null hypothesis of the Mann-Whitney test is: H_0 = the means of the two groups are the same. The alternative hypothesis is: H_a = the means of the two groups are not equal. Due to the statement of the alternative hypothesis, we must consider a two tailed test.

Conover (1980) defines the Mann-Whitney test statistic as follows:

$$T = \sum_{i=1}^{n} R_i \tag{3.132}$$

In Equation (3.132), T is calculated for the smaller of the two groups with n data points. The larger of the two groups has m data points, for a total of $N = n + m$ data points when combined. Therefore, T is the sum of the ranks of each data point in the small group, R_i. If ties occur in the data, a correction must be made, but we will have no ties for the porosity and hydraulic conductivity data.

The test statistic can be compared to a table of critical values in order to determine the decision on the null hypothesis for a significance level α'. Because we are using a two sided test, we must look at the critical test statistic at level $\alpha'/2$. If the calculated test statistic T_{calc} is less than or equal to the critical test statistic $T_{\alpha'/2}$ obtained from the table for the given sample sizes and significance level α', then the null hypothesis is rejected at that significance level and the groups cannot be shown to have identical means. In this event, the test suggests that the two group means are not equal, but does not give any indication of which mean is larger than the other. This can, in general, be determined based on the value of the means.

3.6.2.3 Critical Test Statistics

Tables 3.19 and 3.20 give the critical test statistics for the Kruskal-Wallis test and Mann-Whitney test, respectively. A significance level of $\alpha' = 0.05$ is used to make the decision on the null hypothesis. Table 3.19 gives the critical values of $K_{W\alpha'}$ based on the number of data values in each group. These critical values were taken from Kanji (2006) or Conover (1980) and only the critical values for the group sizes relevant for these data sets are provided.

Table 3.19: Critical test statistics for Kruskal-Wallis test

n_1	n_2	n_3	$K_{W0.05}$
2	2	2	4.571
2	3	3	5.361
2	6	6	5.410
3	3	3	5.600
3	3	6	5.615
3	6	6	5.625

Table 3.20 gives the critical values of $T_{\alpha'/2}$ based on the number of data points in each group. These critical values were taken from Kanji (2006) or Conover (1980) and only the critical values relevant for the group sizes needed for these data are provided. Since we are using a two sided test, the test statistic is taken at a significance level of $\alpha'/2 = 0.025$, or $\alpha' = 0.05$.

Table 3.20: Critical test statistics for Mann-Whitney test

n	m	$T_{0.025}$
2	2	3.0
2	3	3.0
2	6	3.0
3	3	6.0
3	6	8.0
6	6	27.0
6	9	32.0
9	9	62.0

3.6.3 Statistical Test Results on Porosity

3.6.3.1 Porosity Data Grouped by Year

The first step in analyzing the hydraulic data is to use the Kruskal-Wallis test on the porosity data grouped by year. Each year will be investigated independently and the porosity data for each of the three roadways will be compared for a given year. If the Kruskal-Wallis test shows that there is a difference in porosity for one of the years, we will reject the null hypothesis. In this event, we can conduct the Mann-Whitney test to determine which group (roadway) is different from the others.

Table 3.21 provides the calculated Kruskal-Wallis test statistic for the porosity data grouped by year, together with the critical Kruskal-Wallis test statistic (obtained from Table 3.19) at a significance level of $\alpha' = 0.05$ and the decision on the null hypothesis. We will reject the null hypothesis for $K_{Wcalc} \geq K_{W0.05}$ meaning one of the three groups is different from the others. The core specimens extracted in the year 2010 are not included here as cores were extracted from only two roadways.

Table 3.21: Kruskal-Wallis test results for porosity data grouped by year

Year	K_{Wcalc}	$K_{W0.05}$	Decision
2007	5.422	5.600	Do Not Reject H_0
2008	9.346	5.615	Reject H_0
2009	7.462	5.615	Reject H_0

For the porosity data in 2007, we do not have sufficient evidence to reject the null hypothesis at a significance level of 0.05. This means that the data suggest that the porosity at each of the three roadways have identical distributions for the year 2007. This result is a desirable outcome as it says that the porosity at all three roadways is roughly the same when we started collecting core specimens. Therefore, all three roadways are starting at essentially the same porosity when the first core specimens were collected.

For the porosity data in 2008 and 2009, we reject the null hypothesis, meaning that at least one of the three roadways has a different porosity than the others. Based on visual

inspection of our porosity data, this result is to be expected since there are significant changes in the data. If we would like to determine which road has a different porosity than the others, we must conduct the Mann-Whitney test. These results are summarized in Table 3.22 and 3.23 for the 2008 and 2009 porosity data, respectively. We will reject the null hypothesis for $T_{calc} \leq T_{0.025}$. Table 3.24 shows the Mann-Whitney test results for the 2010 porosity data collected only at Loop 360 and RR 620.

Table 3.22: Mann-Whitney test results for 2008 porosity data

Roadways	T_{calc}	$T_{0.025}$	Decision
Loop 360 & FM 1431	6.0	8.0	Reject H_0
Loop 360 & RR 620	6.0	8.0	Reject H_0
FM 1431 & RR 620	6.0	6.0	Reject H_0

Table 3.23: Mann-Whitney test results for 2009 porosity data

Roadways	T_{calc}	$T_{0.025}$	Decision
Loop 360 & FM 1431	6.0	8.0	Reject H_0
Loop 360 & RR 620	7.0	8.0	Reject H_0
FM 1431 & RR 620	9.0	6.0	Do Not Reject H_0

Table 3.24: Mann-Whitney test results for 2010 porosity data

Roadways	T_{calc}	$T_{0.025}$	Decision
Loop 360 & RR 620	6.0	8.0	Reject H_0

For the year 2008, the Mann-Whitney test suggests that all three roadways have different porosity from each other. However, for 2009, the Mann-Whitney test suggests that FM 1431 and RR 620 have the same porosity. This is due in part to the large variability we observed in the RR 620 porosity data. Due to this large variability, the Mann-Whitney test cannot distinguish between the porosity at these two roadways, so we cannot reject the null hypothesis. Furthermore, for the year 2010, the Mann-Whitney test suggests that the porosity at the two roadways where cores were extracted are different from each other.

This analysis allows for a comparison of porosity data between roadways for each given year core specimens were extracted. Essentially, this tells us that the porosity (or changes in

porosity) at a given roadway do not necessarily follow the same trends observed at another roadway. This should be expected due to the varying traffic volumes, rainfall events, and various other factors that are different at each of the three roadways. Furthermore, parametric tests can be conducted on these data (either the ANOVA test or Students *t*-test) which provide the same decisions on the null hypothesis as determined from the nonparametric tests described above at a significance level of 0.05. Therefore, although it is more appropriate to use a nonparametric test due to the small sample size, the corresponding parametric tests provide support for the same decisions on the null hypothesis.

3.6.3.2 Porosity Data Grouped by Location

We can repeat the above analysis for the data grouped by each roadway in order to determine how the porosity at a roadway changes in time. The results of the Kruskal-Wallis test are shown in Table 3.25. For Loop 360 and RR 620, there are four years worth of data, whereas for FM 1431 there are three years worth of data. However, due to difficulties in determining the critical test statistics for four or more groups, only the first three years worth of data (from 2007 to 2009) are analyzed. All four years worth of data for Loop 360 and RR 620 will be analyzed by using the parametric ANOVA test.

Table 3.25: Kruskal-Wallis test results for porosity data from 2007 to 2009 grouped by roadway

Roadway	K_{Wcalc}	$K_{W0.05}$	Decision
Loop 360	6.225	5.625	Reject H_0
FM 1431	5.600	5.600	Reject H_0
RR 620	5.956	5.600	Reject H_0

For each roadway, we reject the null hypothesis suggesting that the porosity at each roadway location is changing through time from the year 2007 to 2009, which we observed from the original data. Similarly, if we conduct the ANOVA test on these data, we obtain the same decisions on the null hypothesis at a significance level of 0.05. In order to analyze all four years worth of porosity data from Loop 360 and RR 620, we are restricted to using the ANOVA test. The results of that test are provided in Table 3.26.

The p-value is provided, and the decision is made based on the magnitude of the p-value relative to the significance level. If the p-value is greater than the significance level, we do not reject the null hypothesis, meaning the test suggests all four years worth of porosity data are the same.

Table 3.26: ANOVA test results for porosity data from 2007 to 2010 grouped by roadway

Roadway	p-value	Decision
Loop 360	0.058	Do Not Reject H_0
RR 620	0.003	Reject H_0

Table 3.26 suggests that the porosity on Loop 360 is constant over time, whereas the porosity on RR 620 is changing over time. This matches our decision for RR 620 for the first three years worth of data. However, for Loop 360, this contradicts our decision determined from the first three years worth of data and reported in Table 3.25. There are several reasons for this discrepancy. First, the parametric ANOVA test is not expected to be as precise as the Kruskal-Wallis test due the small number of data samples. Second, we cannot determine if the data are normally distributed, as required by the ANOVA test. Finally, the calculated p-value of 0.058 is very nearly equal to our significance level of 0.05. This test suggests that we are 94.2% confident that the porosity data on Loop 360 are changing over time. Due to the assumptions made in using the ANOVA test, perhaps it is appropriate to increase the significance level to 0.10 for the parametric test. In this case, we will reject the null hypothesis for the Loop 360 data suggesting the porosity changes over time, which agrees with our initial test findings for the nonparametric Kruskal-Wallis test.

From the Kruskal-Wallis test results and ANOVA test results provided above, we determined that the porosity has changed over time at each roadway. If we would like to determine which year has porosity different from the other years, we must conduct the Mann-Whitney test. The results for Loop 360, FM 1431, and RR 620 are shown in Tables 3.27, 3.28, and 3.29, respectively.

Table 3.27: Mann-Whitney test results for Loop 360 porosity data

Years	T_{calc}	$T_{0.025}$	Decision
2007 & 2008	16.0	8.0	Do Not Reject H_0
2008 & 2009	26.0	27.0	Reject H_0
2009 & 2010	34.0	27.0	Do Not Reject H_0

Table 3.28: Mann-Whitney test results for FM 1431 porosity data

Years	T_{calc}	$T_{0.025}$	Decision
2007 & 2008	6.0	6.0	Reject H_0
2008 & 2009	9.0	6.0	Do Not Reject H_0

Table 3.29: Mann-Whitney test results for RR 620 porosity data

Years	T_{calc}	$T_{0.025}$	Decision
2007 & 2008	6.0	6.0	Reject H_0
2008 & 2009	8.0	6.0	Do Not Reject H_0
2009 & 2010	10.0	6.0	Do Not Reject H_0

From the above Mann-Whitney test results, we can make the following observations based on our decisions on the null hypothesis. On Loop 360, the porosity data remains constant from 2007 to 2008, decreases in 2009, and remains constant in 2010. For FM 1431, the porosity initially decreases from 2007 to 2008 but then remains constant from 2008 to 2009. Similarly, on RR 620, the porosity initially decreases from 2007 to 2008, but then remains constant for the years 2009 and 2010. These are the general trends we would expect from our raw data, and confirm our decisions obtained from the Kruskal-Wallis test above. This now provides a decision based on a statistical test to confirm our initial guesses. In addition, the RR 620 data appear to increase from 2008 to 2009 (based on Figure 3-58), but our Mann-Whitney test does not support this change in porosity due to the large variability in the 2009 data.

3.6.3.3 Travel Lane versus Shoulder Porosity

One final test to conduct in this research study has to deal with porosity in the travel lane versus porosity on the roadway shoulder. Loop 360 has a large enough shoulder so that core specimens can be extracted from both the travel lane and shoulder. However, only cores extracted in 2008, 2009, and 2010 were obtained from both locations; the 2007 cores were only extracted from the travel lane. Several researchers (c.f. Isenring et al., 1990; Van Heystraeten and Moraux, 1990; Berbee et al., 1999; and Pagotto et al., 2000) suggest that the pumping action of tires in the travel lane will help to remove trapped sediment in the PFC pore space, thereby increasing the porosity and hydraulic conductivity. This is also a concern in terms of design speed on a roadway with a PFC overlay. Typically, a larger design speed (80 km/hr) is considered more desirable due to this assumed pumping action of the tires which will help maintain adequate porosity. In order to test whether our data support this claim, we can use our two statistical tests to make a decision on whether the porosity in the travel lane is larger than the porosity in the shoulder. Figure 3-61 presents the porosity data from Loop 360 divided by travel lane or shoulder. These data are taken from the original data presented in Figure 3-56.

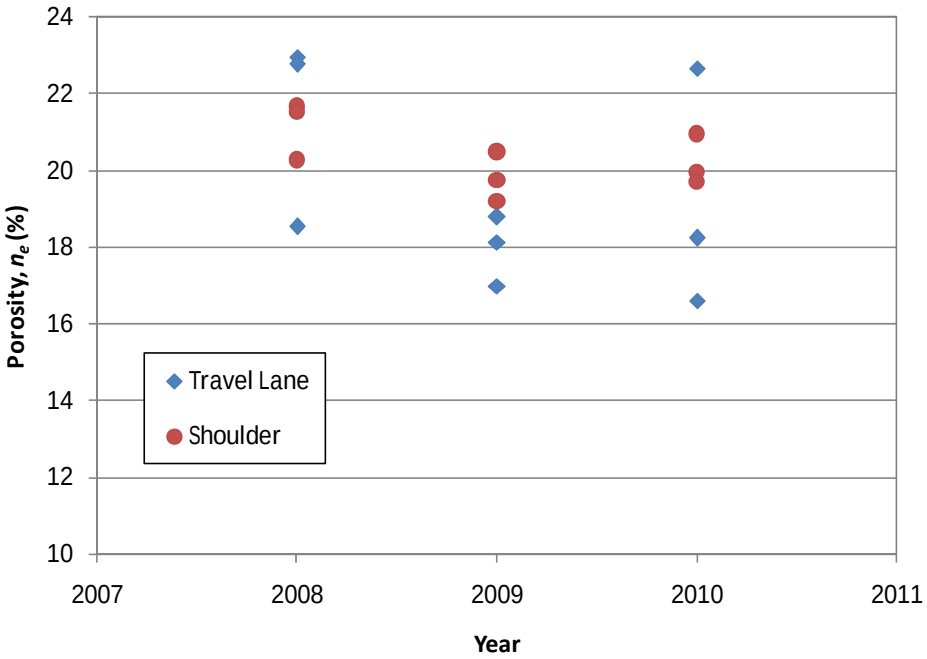

Figure 3-61: Travel lane versus shoulder porosity data on Loop 360

We will start by analyzing the porosity data in the travel lane. Because we only have porosity data in the shoulder for the last three years worth of data, we will only analyze these three years of data for the travel lane as well (2008 to 2010). For the Kruskal-Wallis test, we obtain K_{Wcalc} = 3.289, which when compared to $K_{W0.05}$ = 5.600, we do not reject the null hypothesis. This suggests that the porosity in the travel lane has not changed over time for Loop 360 from 2008 to 2010 and might confirm our claim that the pumping action of tires helps to maintain porosity. This seems to contradict our findings in Table 3.25, which suggest that the porosity does change over time for Loop 360. However, we are now looking at a different data set, which has more relative variability due to the smaller number of data points, making it more difficult for the Kruskal-Wallis test to reject the null hypothesis. We can conduct a similar test on the three years of data for porosity in the shoulder also using the Kruskal-Wallis test. This test gives K_{Wcalc} = 3.467, which when compared to $K_{W0.05}$ = 5.600, we do not reject the null hypothesis. Again, this seems to contradict the previous claim that the porosity in Loop 360 decreases from 2008 to 2010. However, we are again looking at a different data set with a smaller number of data points, meaning we have less confidence in our decision to reject the null hypothesis.

The above test results suggest that the porosity in the travel lane of Loop 360 has not changed with time over the years 2008 to 2010; similarly, the porosity in the shoulder of Loop 360 has not changed with time. We can now compare the porosity in the travel lane to the porosity in the shoulder using the Mann-Whitney test. The results of these data give T_{calc} = 72.0, which when compared to $T_{0.025}$ = 62.0, we do not reject the null hypothesis. This suggests that for our limited data set, we cannot distinguish differences between the porosity in the travel lane and the shoulder. The average porosity in the travel lane from the three years of data is 19.52%, whereas the average porosity in the shoulder for the three years of data is 20.39%. This confirms that the two porosity values cannot be assumed to be different from one another. Therefore, this statistical decision does not support the claim suggesting the pumping action of tires helps to remove sediment from the pore space. However, due to the limited number of data available, there may not be sufficient information to make a reliable decision.

3.6.4 Statistical Test Results on Hydraulic Conductivity

3.6.4.1 Hydraulic Conductivity Data Grouped by Year

The same statistical analysis conducted on the porosity data shown above will be conducted on the hydraulic conductivity data of each core specimen. The hydraulic conductivity is obtained through laboratory testing to determine the modified Forchheimer coefficients. These data are then converted to the original Forchheimer coefficients through the use of numerical modeling, resulting in an accurate measurement of hydraulic conductivity, as reported in Section 3.5.5.4. Each year will be investigated independently and the hydraulic conductivity data for each of the three roadways will be compared for a given year. If the Kruskal-Wallis test shows that there is a difference in hydraulic conductivity for one of the years, we will reject the null hypothesis. In this event, we can conduct the Mann-Whitney test to determine which group is different from the others. For the year 2010, only the Mann-Whitney test will be conducted since core specimens were extracted at only two roadways.

Table 3.30 provides the calculated Kruskal-Wallis test statistic for the hydraulic conductivity data grouped by year, together with the critical Kruskal-Wallis test statistic (obtained from Table 3.19) at a significance level of α' = 0.05 and the decision on the null

hypothesis. We will reject the null hypothesis for $K_{Wcalc} \geq K_{W0.05}$, meaning one of the three groups is different from the others.

Table 3.30: Kruskal-Wallis test results for hydraulic conductivity data grouped by year

Year	K_{Wcalc}	$K_{W0.05}$	Decision
2007	0.000	4.571	Do Not Reject H_0
2008	8.115	5.615	Reject H_0
2009	7.603	5.615	Reject H_0

For the hydraulic conductivity data in 2007, we do not have sufficient evidence to reject the null hypothesis at a significance level of 0.05. This means that the data suggest that the hydraulic conductivity at each of the three roadways have identical distributions for the year 2007. This result is not necessarily expected due to the range of average hydraulic conductivity values at each roadway, but the variability within those averages is very large meaning we do not have sufficient evidence to reject the null hypothesis. This is the same result we determined from the porosity data for the year 2007.

For the hydraulic conductivity data in 2008 and 2009, we reject the null hypothesis meaning that at least one of the three roadways has a different hydraulic conductivity than the others. Based on visual inspection of our hydraulic conductivity data, this result is to be expected since there are significant differences in the data and the variability in the average data has decreased. If we would like to determine which road has a different hydraulic conductivity than the others, we must conduct the Mann-Whitney test. These results are summarized in Tables 3.31, 3.32, and 3.33 for the 2008, 2009, and 2010 hydraulic conductivity data, respectively. We will reject the null hypothesis for $T_{calc} \leq T_{0.025}$.

Table 3.31: Mann-Whitney test results for 2008 hydraulic conductivity data

Roadways	T_{calc}	$T_{0.025}$	Decision
Loop 360 & FM 1431	8.0	8.0	Reject H_0
Loop 360 & RR 620	6.0	8.0	Reject H_0
FM 1431 & RR 620	6.0	6.0	Reject H_0

Table 3.32: Mann-Whitney test results for 2009 hydraulic conductivity data

Roadways	T_{calc}	$T_{0.025}$	Decision
Loop 360 & FM 1431	8.0	8.0	Reject H_0
Loop 360 & RR 620	6.0	8.0	Reject H_0
FM 1431 & RR 620	7.0	6.0	Do Not Reject H_0

Table 3.33: Mann-Whitney test results for 2010 hydraulic conductivity data

Roadways	T_{calc}	$T_{0.025}$	Decision
Loop 360 & RR 620	6.0	8.0	Reject H_0

For the year 2008, the Mann-Whitney test suggests that all three roadways have different hydraulic conductivities from each other. However, for 2009, the Mann-Whitney test suggests that FM 1431 and RR 620 have the same hydraulic conductivity. This is due in part to the large variability we observed in the FM 1431 hydraulic conductivity data. Due to this variability, the Mann-Whitney test cannot distinguish between the hydraulic conductivity at these two roadways, so we cannot reject the null hypothesis. For the year 2010, we reject the null hypothesis. As expected, the hydraulic conductivity at Loop 360 is greater than that at RR 620. It is interesting to note that the decisions made based on the statistical analysis for the hydraulic conductivity data grouped by year is virtually the same as the decisions made on the porosity data.

This analysis provides a comparison of the hydraulic conductivity data between roadways for a given year in order to determine any statistical differences in the data. In general, each roadway has a different hydraulic conductivity than the other roadways. As with the porosity data, this suggests that the magnitudes of the hydraulic conductivity data, as well as any changes, vary depending on roadway location. Of particular interest would be the initial hydraulic conductivity of each roadway immediately after construction of the PFC layer. There are large differences in hydraulic conductivity at each roadway which may be attributed to varying construction methods. Furthermore, as with the porosity data, the equivalent parametric statistical tests provide support for the decision on the null hypothesis as determined from the nonparametric tests.

3.6.4.2 Hydraulic Conductivity Data Grouped by Location

We can repeat the above analysis for the data grouped by each roadway in order to determine how the hydraulic conductivity at a roadway changes in time. The results of the Kruskal-Wallis test are shown in Table 3.34. For Loop 360 and RR 620, there are four years worth of data; whereas for FM 1431 there are three years worth of data. As previously mentioned, due to difficulties in determining accurate critical test statistics for four or more groups, only the first three years worth of data (from 2007 to 2009) are analyzed with the Kruskal-Wallis test. All four years worth of data for Loop 360 and RR 620 will be analyzed using the ANOVA test.

Table 3.34: Kruskal-Wallis test results for hydraulic conductivity data from 2007 to 2009 grouped by roadway

Roadway	K_{Wcalc}	$K_{W0.05}$	Decision
Loop 360	0.267	5.410	Do Not Reject H_0
FM 1431	0.556	5.361	Do Not Reject H_0
RR 620	4.694	5.361	Do Not Reject H_0

For each roadway from 2007 to 2009, we do not reject the null hypothesis suggesting that the hydraulic conductivity at each roadway location is constant through time, which appears to be reasonable from the original data. Therefore, although we observed a decrease in porosity at each roadway over time, the hydraulic conductivity has not been decreasing over time from a statistical standpoint. Similarly, if we conduct the ANOVA test on these three years of data, for Loop 360 and FM 1431, we do not reject the null hypothesis. However, the ANOVA test suggests we reject the null hypothesis for RR 620 with a p-value of 0.011. This suggests that the hydraulic conductivity has changed from the year 2007 to 2009 and contradicts our decision based on the Kruskal-Wallis test. Due to the small sample size, it is expected that the nonparametric Kruskal-Wallis test provides the more accurate decision.

We can also use the ANOVA test in order to analyze the four years of hydraulic conductivity data for Loop 360 and RR 620. The decision of the ANOVA test and the corresponding p-value are provided in Table 3.35.

Table 3.35: ANOVA test results for hydraulic conductivity data from 2007 to 2010 grouped by roadway

Roadway	p-value	Decision
Loop 360	0.868	Do Not Reject H_0
RR 620	0.008	Reject H_0

Table 3.35 suggests that the hydraulic conductivity on Loop 360 is constant over time, whereas the hydraulic conductivity on RR 620 is changing over time. This matches our decision on Loop 360 for the first three years worth of data. However, this contradicts our decision on RR 620 from the Kruskal-Wallis test.

In order to determine whether the hydraulic conductivity data on RR 620 is changing over time, we can conduct the Mann-Whitney test for all four years of data. Table 3.36 provides the analysis of the RR 620 data.

Table 3.36: Mann-Whitney test results for RR 620 hydraulic conductivity data

Years	T_{calc}	$T_{0.025}$	Decision
2007 & 2008	6.0	3.0	Do Not Reject H_0
2008 & 2009	8.0	6.0	Do Not Reject H_0
2009 & 2010	8.0	6.0	Do Not Reject H_0

For the Mann-Whitney test, we do not reject the null hypothesis, meaning there is not sufficient evidence to determine whether there is a change in hydraulic conductivity. This suggests that the hydraulic conductivity data is constant on RR 620 from the year 2007 to 2010. This agrees with our Kruskal-Wallis test results, but contradicts the ANOVA test results. It is expected due to the small sample size and lack of ability to determine whether the data are normally distributed that the nonparametric tests would provide a more accurate decision on the null hypothesis. Therefore, it can be assumed that the hydraulic conductivity data on RR 620 is statistically constant over time, and there is not sufficient evidence to determine a change in hydraulic conductivity. The above statistical analysis suggests that the hydraulic conductivity at each roadway has remained constant over time. Although we observed a statistical decrease in porosity over time at each roadway, this does not correspond to a statistical decrease in hydraulic conductivity at this point in time. The main reason we cannot determine a statistical decrease in hydraulic conductivity over time is the much larger variability in hydraulic conductivity. Because of this variability, the statistical tests do not have enough information to determine a trend in the data.

3.6.4.3 Travel Lane versus Shoulder Hydraulic Conductivity

The final test to conduct on the hydraulic conductivity data is a comparison between the travel lane versus the roadway shoulder. In order to test whether our data support the claim that the pumping action of vehicle tires result in a greater hydraulic conductivity, we can use our two statistical tests to make a decision on whether the hydraulic conductivity in the travel lane is larger than in the shoulder. Figure 3-62 presents the hydraulic conductivity data from Loop 360 divided by travel lane or shoulder. These data are taken from the original data presented in Figure 3-57.

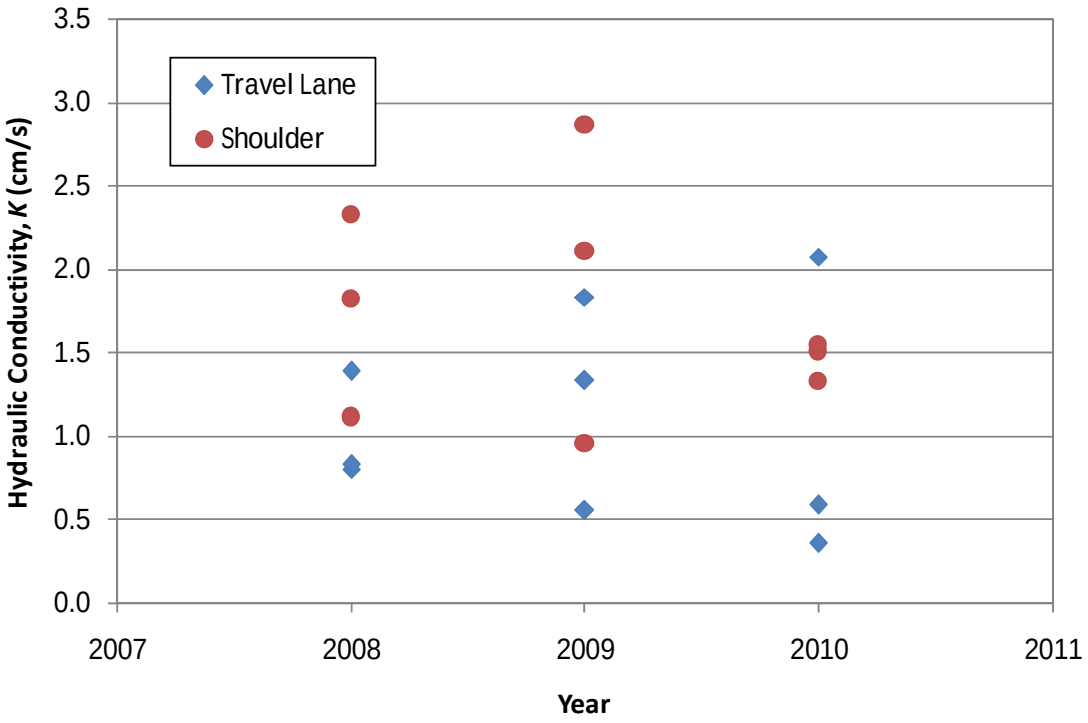

Figure 3-62: Travel lane versus shoulder hydraulic conductivity data on Loop 360

We will start by analyzing the hydraulic conductivity data in the travel lane. Because we only have hydraulic conductivity data in the shoulder for the last three years (2008 to 2010), we will only analyze these three years worth of data in the travel lane. For the Kruskal-Wallis test, we obtain K_{Wcalc} = 0.267, which when compared to $K_{W0.05}$ = 5.600, we do not reject the null hypothesis. This suggests that the hydraulic conductivity in the travel lane has not changed over time for Loop 360. This agrees with our findings in Tables 3.34 and 3.35, which suggest that the hydraulic conductivity remains constant over time for Loop 360. We can conduct a similar test on the three years of data for hydraulic conductivity in the shoulder also using the Kruskal-Wallis test. This test gives K_{Wcalc} = 0.622, which when compared to $K_{W0.05}$ = 5.600, we do not reject the null hypothesis. Again, this agrees with the previous claim that the hydraulic conductivity at Loop 360 remains constant with time.

The above test results suggest that the hydraulic conductivity in the travel lane of Loop 360 has not changed with time. Similarly, the hydraulic conductivity in the shoulder of Loop 360 has not changed with time. We can now compare the hydraulic conductivity in the travel lane to the hydraulic conductivity in the shoulder using the Mann-Whitney test. The results of this data give T_{calc} = 63.0, which when compared to $T_{0.025}$ = 62.0, we do not reject the null hypothesis. This suggests that for our limited data set, we cannot distinguish differences between the hydraulic conductivity in the travel lane and the shoulder. The average hydraulic conductivity in the travel lane from the last three years of data is 1.08 cm/s (0.425 in/s), whereas the average hydraulic conductivity in the shoulder for the three years of data is 1.73 cm/s (0.68 in/s). Although it appears the average hydraulic conductivity in the shoulder is greater than the average hydraulic conductivity in the travel lane, due to the variability in the data we do not have sufficient evidence to statistically distinguish between the two. Therefore, this decision does not

support the claim suggesting the pumping action of tires helps to remove sediment from the pore space. However, due to the limited number of data available, there may not be sufficient information to make a reliable decision.

3.6.5 Experimental Forchheimer Coefficients Compared to Empirical Equations

Various studies have been conducted in the past which attempt to approximate the original Forchheimer coefficients (*a* and *b*) from properties of the fluid and porous medium. Although these empirical approximations typically work well for the material which was being studied, they do not translate to most other porous media that exhibit nonlinear flow. Sidiropoulou et al. (2007) provide a good overview of many of the empirical equations used to estimate the Forchheimer coefficients. These estimates typically depend on the porosity, particle diameter, and fluid properties being tested. Several of these empirical equations will be discussed here and compared to the experimental results obtained for this research study on PFC.

Ergun (1952) was one of the first researchers to develop equations to estimate the Forchheimer coefficients. These equations are based on the Kozeny-Carman model and give the following empirical relations:

$$a = \frac{150\mu(1-n_e)^2}{\rho g n_e^{\ 3} D_p^{\ 2}} \tag{3.133}$$

$$b = \frac{1.75(1-n_e)}{g n_e^{\ 3} D_p} \tag{3.134}$$

Equations (3.133) and (3.134) estimate the Forchheimer coefficients based on the fluid viscosity μ and density ρ as well as the porous medium porosity n_e and particle diameter D_p. For the purposes of this comparison, the PFC particle diameter that will be used is the d_{50} diameter obtained from the particle size distribution used for mix design given in TxDOT (2004b).

Ward (1964) suggests the following empirical equations to estimate the Forchheimer coefficients:

$$a = \frac{360\mu}{\rho g D_p^{\ 2}} \tag{3.135}$$

$$b = \frac{10.44}{g D_p} \tag{3.136}$$

Although the above relationships worked well for the porous media tested, the empirical Equations (3.135) and (3.136) are not functions of the porosity. Therefore, when compared to the PFC results, Ward's equations will not change when the PFC porosity changes. This is problematic because there is no way to measure D_p when the PFC porosity decreases. For comparisons with the PFC experimental data, it is expected that Ward's equations will not

produce reliable estimates. For this reason, the empirical equations presented by Ward will not be compared to the PFC data.

Kovacs (1981) derived the following equations for spherical particles:

$$a = \frac{144\mu(1-n_e)^2}{\rho g n_e^{\ 3} D_p^{\ 2}} \tag{3.137}$$

$$b = \frac{2.4(1-n_e)}{g n_e^{\ 3} D_p} \tag{3.138}$$

Equations (3.137) and (3.138) are very similar to the equations proposed by Ergun. Therefore, we would expect that these two sets of equations produce similar results.

Finally, Kadlec and Knight (1996) present the following equations:

$$a = \frac{255\mu(1-n_e)}{\rho g n_e^{\ 3.7} D_p^{\ 2}} \tag{3.139}$$

$$b = \frac{2(1-n_e)}{g n_e^{\ 3} D_p} \tag{3.140}$$

Again, these equations are similar in form to those proposed by Ergun and Kovacs with slightly different exponential terms. As previously mentioned, the particle diameter used for the comparison is the d_{50} diameter obtained from the mix design for PFC. A sieve analysis on typical PFC mixtures suggests a diameter of 9.525 mm correspond to a range of percent passing particles. This range is from 35% to 60% passing. Therefore, the range of values for d_{50} is between 8.5 mm and 10.5 mm based on the resulting gradation curves. Using an average d_{50} of 9.5 mm for use as D_p in the equations above will provide a comparison to the empirical equations and the experimental values obtained for this research. It should be noted that due to the entrapment of sediment in the pore space, the actual average particle diameter cannot be determined.

Figure 3-63 and Figure 3-64 show the measured PFC core specimen hydraulic conductivity and original nonlinear Forchheimer coefficient, respectively, as determined from the experimental data and numerical modeling compared to the empirical equations in the literature described above. If the empirical equations agree well with the experimental PFC data, then the resulting graph should fall on a 1:1 line. For the hydraulic conductivity data, the empirical equation proposed by Kadlec and Knight (1996) has the best agreement to the experimental data. Although the Kadlec and Knight equation does not fall directly on the 1:1 line shown in Figure 3-63, it does give a same order of magnitude estimate of the hydraulic conductivity. The empirical equations proposed by Ergun (1952) and Kovacs (1981) greatly overestimate the measured PFC hydraulic conductivity. However, as expected, these two empirical equations produce nearly the same estimates. In conclusion, the empirical equation proposed by Kadlec and Knight produce the same order of magnitude estimate of PFC hydraulic

conductivity. The Ergun and Kovacs equations are not recommended for estimating PFC hydraulic conductivity as they overestimate the hydraulic conductivity.

Figure 3-64 shows the measured and empirical nonlinear Forchheimer coefficient. Clearly, the empirical equations drastically underestimate the nonlinear coefficient when compared to the measured data. Four measured values of *b* were so large that they were not included in the above graph. All three empirical equations shown here result in roughly the same estimate. Therefore, in general, these empirical equations for estimating the nonlinear coefficient do not apply to the measured PFC data.

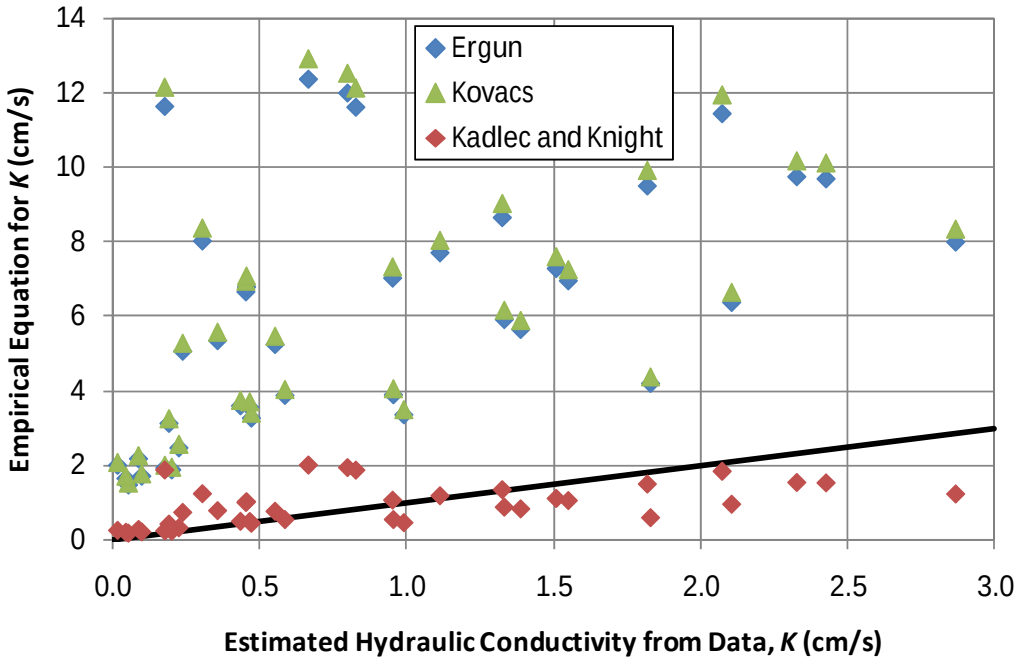

Figure 3-63: Empirical equations for estimating hydraulic conductivity

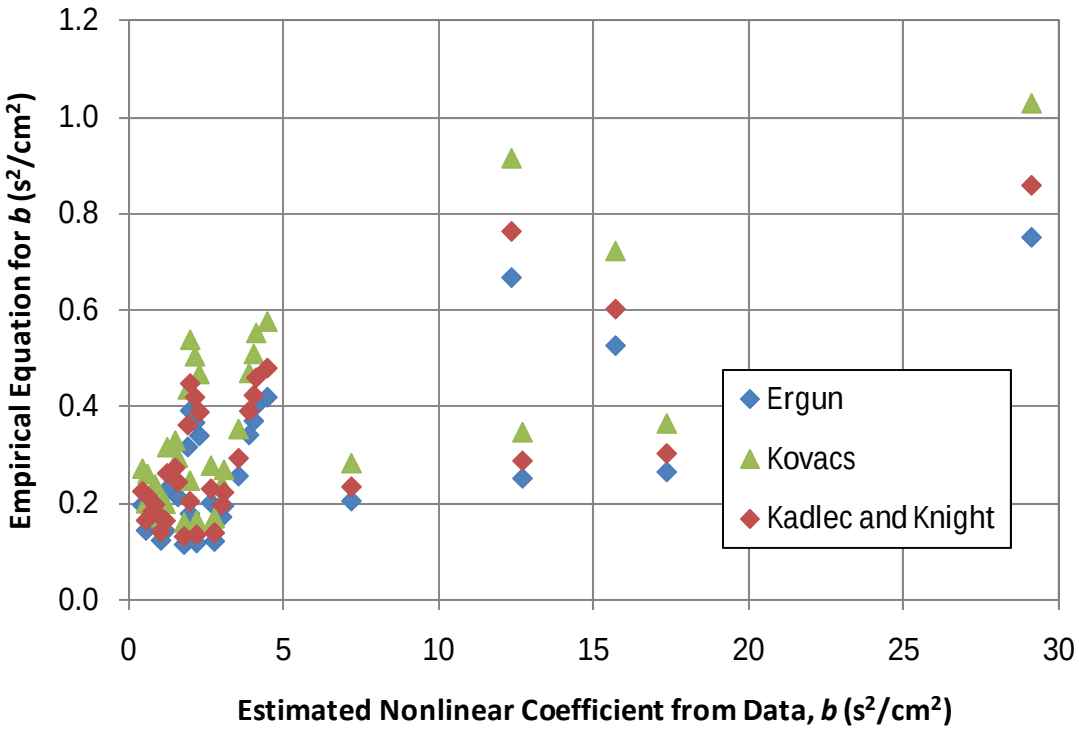

Figure 3-64: Empirical equations for estimating nonlinear Forchheimer coefficient

3.6.6 Sediment Removal Estimate

One of the critical questions remaining about the water quality benefits of PFC is whether the PFC is actually removing pollutants from the stormwater runoff, or simply reducing the source of the pollutants from being washed off of vehicles due to the reduced splash and spray. The removal mechanism which results in an improvement in water quality can be examined by investigating the change in porosity over time together with the expected volume of sediment removed from the stormwater runoff. If the PFC overlay acts primarily as a filter in removing sediment, then the volume of sediment removed from the runoff will result in the observed decrease in porosity over time. On the other hand, if the PFC overlay is simply reducing the source of the sediment by not washing sediment off of cars, then the volume of sediment removed from the runoff will be greater than the volume of sediment needed to decrease the observed porosity.

In this analysis, sediment removal will be estimated as a mass of sediment per surface area of pavement. Two sediment removals will be estimated and then compared to one another. The first sediment removal estimate is based on the observed decrease in core specimen porosity over time. The mass of sediment per volume of PFC layer can be determined by multiplying the change in porosity times an assumed sediment density. This makes the assumption that all of the change in porosity is a result of trapped sediment volume. A sediment density of 2.65 g/cm^3 was used for this analysis. The sediment mass per unit area is determined by multiplying the sediment mass per volume times the average PFC thickness. The PFC thickness is determined from the thickness of the core specimens for all years. Table 3.37 provides the change in porosity and resulting sediment mass per area needed to cause that observed change in porosity from the 2007

cores to the 2010 cores. In general, several hundred milligrams (mg) of sediment per square centimeter surface area of pavement are needed to clog the PFC pore space and result in the observed decrease in porosity.

Table 3.37: Sediment mass estimate for change in porosity

Roadway	Average Thickness (cm)	Decrease in Porosity (%)	Sediment Mass (mg/cm^2)
Loop 360	4.01	2.70	287
FM 1431	3.23	5.65	483
RR 620	3.50	6.53	606

In order to determine the estimated sediment mass per area that we would expect from water quality data, we must investigate the rainfall over the time period together with the average total suspended solids (TSS) concentration and TSS removal observed due to the use of PFC. The rainfall data we will use is specifically for a rain gage located near the core extraction site on Loop 360. Precipitation data was collected from the Lower Colorado River Authority (LCRA) Hydromet data set at the "Bull Creek at Loop 360, Austin" rain gage (LCRA, 2010). Previous research conducted on the water quality benefits of PFC (Stanard, 2008 and Frasier, 2009) measured the TSS concentration in the runoff from a conventional impervious asphalt surface as well as a PFC overlay. These results show that the TSS concentration from PFC runoff is approximately 90% less than from conventional pavement. The difference between the conventional TSS concentration and the PFC TSS concentration is the assumed volume of sediment trapped within the PFC, which causes a decrease in porosity. Therefore, with known values of rainfall depth, average TSS concentration from a conventional roadway, and TSS removal due to the PFC, we can determine the expected mass of sediment trapped per unit area of PFC.

The average TSS concentration from conventional pavement is roughly 135 mg/L as reported by Stanard (2008) and Frasier (2009). This is a general average and varies from storm event to storm event, but is useful for an approximation of the amount of sediment that may be trapped in the PFC pore space. If the PFC is assumed to remove 90% of this concentration according to water quality measurements, then the TSS concentration from a PFC surface is 14 mg/L, meaning 121 mg/L of TSS is expected to be retained within the PFC pore space. The average sediment retained per unit area can be determined by multiplying the TSS concentration times the rainfall for a given period of time. The cumulative rainfall since the first core extraction date to the fourth and final core extraction date is 243.1 cm (LCRA, 2010). This rainfall can be split based on core extraction dates. The rainfall between the first and second set of cores is 97.4 cm for the year 2007. The year 2008 had 42.6 cm of rain, and the year 2009 had 103.1 cm of rainfall. The cumulative rainfall amount times the assumed average TSS concentration retained within the PFC pore space (121 mg/L) results in an average sediment removal of 29.5 mg/cm^2. Clearly this value, when compared to the estimated sediment mass required to change the observed porosity reported in Table 3.37 is significantly less. Therefore, the 90% removal of TSS does not produce nearly enough mass of sediment needed to cause the observed decrease in porosity.

Part of the problem with estimating the trapped mass of sediment in the PFC pore space is that this method only considers the entrapment of sediment in water produced from rainfall runoff. Sediment may become trapped within the PFC pore space even when rainfall is not present. This entrapment of solids during dry conditions is what has caused the PFC porosity to decrease over time. The entrapment of particles during rainfall events most likely produces minimal decreases in porosity. Although the results of this analysis do not provide any definite information on the removal mechanism of suspended solids from runoff, it does show that the observed change in porosity accounts for much more trapped sediment than is expected from water quality data. If the opposite finding was observed, i.e. if the sediment mass from water quality data was greater than the change in porosity, then we could assume that PFC is simply reducing the source of pollutants from being washed off vehicles. Since this finding did not occur, we can at least assume that the PFC has the capacity to retain 90% of the TSS concentration within the stormwater runoff.

3.7 Conclusions

3.7.1 Summary of Problem

Hydraulic testing on PFC core specimens and roadway surfaces reveals a nonlinear flow relationship which can be characterized using the Forchheimer equation. Nonlinear flow is created as a result of the large hydraulic conductivity and large pore space within the PFC layer as well as the large hydraulic gradients imposed on the core specimens during testing. The two-dimensional flow pattern imposed during testing creates an additional complication which can be addressed through numerical modeling. Due to the two-dimensional diverging flow paths, a modified Forchheimer equation for the global conditions of the core specimen must be used. The modified Forchheimer equation relates the change in head through the core specimen to the volumetric flow rate, as opposed to the original Forchheimer equation which relates the local hydraulic gradient and local specific discharge. The modified Forchheimer coefficients obtained from experimental testing are related to the original Forchheimer coefficients through a finite difference numerical model of Forchheimer flow in two-dimensional cylindrical coordinates. Proper modeling of the flow characteristics can relate the measurable PFC hydraulic characteristics to the hydraulic conductivity. This is accomplished with the introduction of a scalar hydraulic conductivity ratio which allows for proper modeling of the original Forchheimer equation in two dimensions. With an accurate measurement of hydraulic conductivity, the extent of clogging over the life of the pavement can be observed in order to determine when maintenance or replacement of the PFC layer, based on drainage capacity, is necessary. Measurement of in-situ hydraulic conductivity is useful as an indicator as to when the driver safety and water quality benefits of the PFC layer are expected to decrease.

3.7.2 Research Objective Conclusions

Four major research objectives are addressed in this chapter and related research study. The first objective addresses laboratory testing on PFC core specimens in order to measure its hydraulic properties: porosity and hydraulic conductivity. The second objective develops a field test methodology for measurement of in-situ hydraulic conductivity. The third objective investigates a numerical model of the two-dimensional nonlinear flow problem necessary to relate the measureable hydraulic characteristics to the true hydraulic conductivity. The fourth objective uses nonparametric statistical tests to analyze the measured hydraulic properties of PFC

over time and at different locations in order to determine any trends or changes in the data which may give an indication of when the benefits of PFC are expected to degrade due to clogging of the pore space by trapped sediment.

3.7.2.1 Conclusions for Evaluation of Hydraulic Properties in the Laboratory

The first research objective investigates laboratory testing on PFC core specimens extracted from three roadways (Loop 360, FM 1431, and RR 620) around Austin, Texas (TX) over the past four years (2007 to 2010) and provides a methodology for determining the porosity and hydraulic characteristics of flow through the core specimen. The extraction of core specimens is accomplished by saw-cutting the roadway surface, which results in a cylindrical core specimen. The PFC core specimen porosity is determined using either an image analysis method or a submerged unit weight method. The submerged unit weight method is preferred as this method leaves the core intact and allows for additional hydraulic testing to be conducted.

Hydraulic testing of PFC core specimens in the laboratory consists of a series of constant head permeability tests. The large hydraulic gradients imposed on the core specimen during testing, combined with the large pore volumes in the PFC cores, result in a nonlinear flow relationship which can be modeled using the Forchheimer equation. The Forchheimer equation was chosen to model the nonlinear effects due to its ability to approximate Darcy's law for low hydraulic gradients and/or low specific discharge. The upper and lower no flow boundary conditions imposed on the core specimen create a two-dimensional cylindrical flow pattern which results in an additional complication due to the inability to directly measure the hydraulic gradient or specific discharge. This problem can be addressed by investigating the global conditions of the core specimen through the use of a modified Forchheimer equation (see Equation (3.30)). The modified Forchheimer coefficients can be determined from the constant head tests but give no indication of the hydraulic conductivity.

The PFC core specimen hydraulic conductivity can be determined through the use of numerical modeling. The result is a well defined test procedure for determining the hydraulic characteristics of two-dimensional nonlinear flow through PFC core specimens, which is both repeatable and reliable. Data collected on PFC core specimens over four years is reported. Core porosity values range from roughly 12% to 23%. A series of laboratory constant head tests allow for the determination of two modified Forchheimer coefficients, α and β, with the following ranges: α = 0.05 to 5.76 s/cm^2 and β = 0.002 to 3.01 s^2/cm^5. Furthermore, falling head tests can be conducted on the core specimens, which result in roughly the same modified Forchheimer coefficients as determined from the constant head tests. Through numerical modeling, the modified Forchheimer coefficients can be related to the original Forchheimer coefficients in order to accurately determine the core specimen isotropic hydraulic conductivity.

3.7.2.2 Conclusions for Evaluation of Hydraulic Conductivity in the Field

Field testing on the PFC roadway surface can be conducted with a falling head test methodology in order to determine the in-situ hydraulic characteristics, which is the goal of the second research objective. In-situ measurement of the hydraulic conductivity is necessary in order to ensure proper drainage capacity of the PFC layer. If the hydraulic conductivity decreases due to trapped sediment in the pore space, the driver safety and water quality benefits are expected to degrade. Therefore, periodic measurement of in-situ hydraulic conductivity is required. A field test apparatus has been developed at the Center for Research in Water Resources (CRWR) specifically for this research study which creates a similar test setup and boundary conditions used in the laboratory. The upper no flow boundary is created with silicon

vacuum grease placed on a metal support base, and the lower no flow boundary is imposed by the underlying impervious roadway surface. These boundary conditions result in two-dimensional cylindrical flow and force water to flow within the PFC pore space as opposed to on the roadway surface. The global flow characteristics can also be modeled with the modified Forchheimer equation for the two-dimensional flow pattern observed in the field. The result of the second research objective not only proposes a well defined test procedure for determining the in-situ hydraulic conductivity, but also proposes a standard piece of equipment used for measurement purposes. This equipment is both simple in design and requires very little instrumentation for proper measurements. The use of a stopwatch with a split function is the only instrumentation needed in order to record the three time-depth measurements used to determine the modified Forchheimer coefficients, α and β, through Equation (3.37). Therefore, any field technician can easily use this field test to accurately determine the in-situ hydraulic conductivity of the PFC layer.

Upon completion of the falling head test, the modified Forchheimer coefficients can be determined which have the following ranges: $\alpha = 0.01$ to 0.14 s/cm^2 and $\beta = 1.2\times10^{-4}$ to 2.5×10^{-3} s^2/cm^5. The simple, nondestructive field test proposed here is needed due to the additional time and effort needed to conduct tests on core specimens in the laboratory. Furthermore, extraction of the core specimens for lab testing may disturb the PFC layer resulting in inaccurate hydraulic data. The in-situ field test is much quicker and does not disturb the PFC layer.

3.7.2.3 Conclusions for Numerical Modeling of Hydraulic Characteristics

The third research objective investigates numerical modeling of the continuity equation in two-dimensional cylindrical coordinates in order to relate the experimentally measured modified Forchheimer coefficients, α and β, to the original Forchheimer coefficients, $a = 1/K$ and b, for determination of the hydraulic conductivity of a PFC core specimen. Due to the nonlinear form of the Forchheimer equation in two dimensions, additional efforts must be made in order to properly model the flow. Previous research has not fully addressed nonlinear flow in two dimensions. Proper modeling of the flow is accomplished through the introduction of a new scalar hydraulic conductivity ratio in order to allow for appropriate invariance properties of the nonlinear equations. The numerical model uses a finite difference scheme to solve the continuity equation in two-dimensional cylindrical coordinates. Expansion ratios are used in both the vertical and radial directions in order to refine the grid near the inflow boundary, where the largest hydraulic gradients occur.

Input parameters to the numerical model are the core dimensions (R_s, R_c, and b_c), the original Forchheimer coefficients (a and b), and the standpipe head (h_s). Both linear and nonlinear solutions of the head distribution through a core specimen are provided. The linear case uses Darcy's law and is solved with an implicit Crank-Nicolson scheme. The linear numerical model results are compared to an approximate analytic solution provided by Carslaw and Jaeger (1959) in order to ensure the model is producing desirable results. The nonlinear case models the Forchheimer equation and uses the iterative Gauss-Seidel method where the initial head value used to iterate about is the solution to the linear model. With the nonlinear head distribution determined, the global flow characteristics can be calculated. The outflow rate is determined from the outflow hydraulic gradient, and the results are fit to the modified Forchheimer equation using a regression equation to determine α and β. In addition, the nonlinear model results approach the linear Darcy flow case for small values of standpipe head and/or small nonlinear coefficients. Therefore, the Forchheimer equation approximates Darcy's law for low hydraulic gradients or specific discharges. This feature of the Forchheimer equation

is the basis for choosing this equation to model the nonlinear flow effects. The value of the scalar hydraulic conductivity ratio provides information as to the location in the core specimen in which nonlinear effects are significant. As expected the hydraulic conductivity ratio shows the large nonlinear effects occur directly under the standpipe at the inflow boundary.

The results of the nonlinear numerical model are used to determine a relationship between the modified and original Forchheimer coefficients for a variety of core geometries. The two linear coefficients, α and a, as well as the two nonlinear coefficients, β and b, are linearly related, where the slope of this relationship depends on the dimensions of the core specimen: R_s, R_c, and b_c. Regression equations using a power law model were developed from 64 numerical simulations of the core geometry and provide useful relationships for estimating the original Forchheimer coefficients based on the measured modified Forchheimer coefficients. Finally, regression equations developed specifically for the CRWR field test apparatus used in this research allow for accurate measurement of the in-situ hydraulic conductivity. These regression equations provide very accurate estimates of the linear Forchheimer coefficient, but produce slightly larger errors in the estimate of the nonlinear Forchheimer coefficient. The estimates of the original Forchheimer coefficients obtained from the regression equations can be used as inputs to the nonlinear numerical model in order to determine the corresponding modified Forchheimer coefficients. A comparison of the modified Forchheimer coefficients obtained from the numerical model and the coefficients obtained from experimental data result in errors within an acceptable range of uncertainty. This allows for an estimate of the hydraulic conductivity and nonlinear original Forchheimer coefficient based on the core geometry and measured modified Forchheimer coefficients from experimental data.

For the PFC core specimens tested in the laboratory, the hydraulic conductivity K and nonlinear Forchheimer coefficient b have the following ranges: K = 0.02 to 2.87 cm/s and b = 0.47 to 640 s^2/cm^2. The in-situ hydraulic conductivity determined using the CRWR field test result in the following range of hydraulic conductivity and nonlinear Forchheimer coefficient: K = 0.6 to 3.6 cm/s (0.24 to 1.42 in/s) and b = 0.31 to 5.21 s^2/cm^2.

3.7.2.4 Conclusions for Analysis of Hydraulic Properties

With four years of porosity and hydraulic conductivity data collected at three roadway sites around Austin, TX, a statistical analysis of the data can be conducted to determine any trends or changes in the data as addressed in the fourth research objective. Nonparametric statistical tests must be conducted on the data due to the small sample size and inability to show the data are normally distributed. The two nonparametric tests used are the Kruskal-Wallis test and Mann-Whitney test. The results of these tests show there have been statistically significant observed decreases in porosity at each roadway location over time. This suggests that the pore space of the PFC is becoming clogged with trapped sediment. In addition, all three roadways have different porosity, suggesting that the varying traffic conditions, construction methods, and environmental or hydrologic conditions at each site affect the porosity of the PFC layer. However, despite the observed statistical decrease in porosity over time, there has been no observed statistically significant decrease in hydraulic conductivity over time. Although the porosity is decreasing due to trapped sediment, this is not yet causing a significant decrease in hydraulic conductivity over time. Each of the three roadways has a different hydraulic conductivity from the other roadways, but these values are not changing in time due primarily to the large variability in hydraulic conductivity data. Furthermore, water quality monitoring from two roadway locations conducted by other researchers has shown the persistence of improved stormwater quality when compared to conventional roadway surfaces. The measurement of

hydraulic conductivity is used as an indicator of when these water quality benefits will decrease. Since there has not been an observed decrease in hydraulic conductivity over time and water quality monitoring shows continued improved stormwater runoff quality to date, an indication of when we expect to see a degradation in drainage benefits due to a decrease in hydraulic conductivity has not been observed.

An estimate of the volume of sediment trapped within the pore space is presented based on the volume of sediment needed to result in the observed decrease in porosity versus the volume of sediment removed from stormwater runoff. This estimate suggests that the removal of total suspended solids from stormwater runoff does not provide a large enough sediment volume to result in the observed decrease in porosity over time. Therefore, the majority of the observed decrease in porosity is due to dry deposition of sediment on the roadway surface between rainfall events. Finally, the measured original Forchheimer coefficients are compared to empirical equations presented in the literature in order to determine the applicability of the empirical equations for use with PFC. Only one empirical equation, presented by Kadlec and Knight (1996), for estimating the linear original Forchheimer coefficient produced reasonable results. Therefore, the Forchheimer coefficients presented in previous literature do not generally apply to use in PFC materials. In conclusion, nonparametric statistical tests conducted on the collected hydraulic data of PFC core specimens show that the measured porosity has decreased over time, but no changes in hydraulic conductivity have been observed to date.

The results of this chapter and associated research study are summarized here. A well-defined methodology for measurement of porosity and hydraulic conductivity on PFC core specimens in the laboratory using a series of constant head tests is presented. Testing involves two-dimensional nonlinear cylindrical flow and is modeled with a modified Forchheimer equation. In order to measure the in-situ hydraulic conductivity, a field test apparatus has been developed using a falling head test with similar boundary conditions created in the laboratory. The field test methodology is both simple and nondestructive allowing for accurate measurement of the modified Forchheimer coefficients. Numerical modeling of the Forchheimer equation in two-dimensional cylindrical coordinates is accomplished through the introduction of a scalar hydraulic conductivity ratio. This allows for a relationship between the measured modified Forchheimer coefficients and the original Forchheimer coefficients to be determined. Regression equations developed on a range of core dimensions allows for an estimate of the original Forchheimer coefficients from measured experimental data. The results of the numerical model also show where nonlinear flow effects are dominate within the core specimen and provide an improved method of modeling nonlinear flow in two dimensions. Finally, a statistical analysis on the measured hydraulic data suggest a decrease in porosity over time due to the entrapment of sediment, but the measured hydraulic conductivity has remained constant through time.

Chapter 4. Steady State Modeling

4.1 Introduction

Figure 4-1 shows a cross-section picture from a PFC core from a roadway near Austin, Texas. The core was taken from the middle of the outside traveled lane and has a diameter of 15 cm. The core was sliced in half vertically and impregnated with fluorescent epoxy to highlight the pores. About 1.5 cm of the underlying pavement is visible at the base of the section. The large typical pore size is evident, as well as the lack of fine-grain material. Due to the nature of placement, large-scale lateral heterogeneity in initial porosity and hydraulic conductivity are not anticipated. However, over time, deposition of suspended solids and other constituents in stormwater runoff are expected to decrease both hydraulic characteristics, and could result in pavement internal characteristics that exhibit large-scale heterogeneity associated with the natural drainage pattern. Such characteristics have not been documented and are one focus of ongoing research efforts.

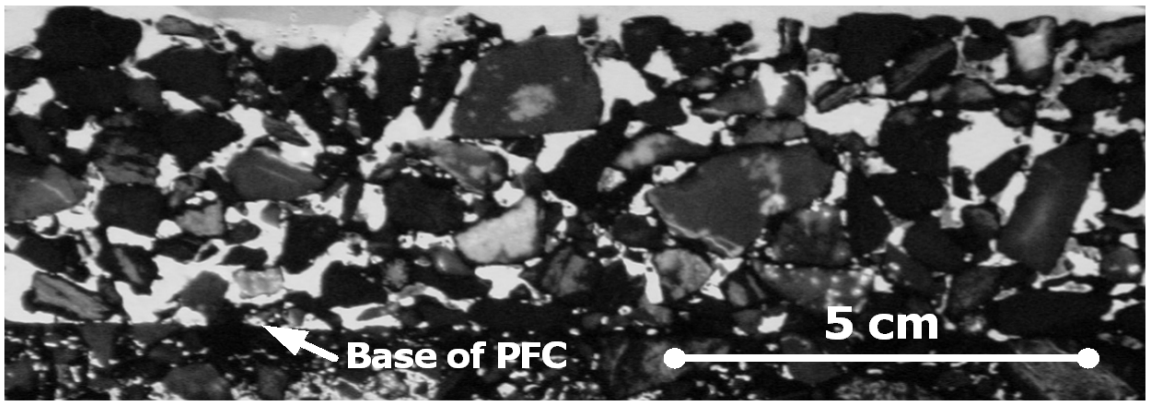

Figure 4-1: Cross section of a PFC core from a roadway near Austin, Texas. Darker color represents soil grain material while light color is pore space

One issue with the use of PFC is that at higher rainfall intensities, the entire volume of runoff cannot be contained within the 50 mm thick porous layer, causing sheet flow on the surface of the road. The sheet flow generally occurs in the outer lanes or in longitudinal sags (regions of local depression) in the roadway. This can present an unexpected danger to drivers who abruptly enter standing water after driving on relatively dry pavement. In addition, the water quality benefits may also be reduced under these circumstances. Interestingly, there are few specifications in the U.S. regarding appropriate design to maintain water within the pavement structure for a given storm intensity. Maintaining the runoff within the pavement may be accomplished by either controlling the thickness of the PFC or providing under drains to reduce the water depth. Potential use and design of under drains is discussed later in this manuscript.

Jackson and Ragan (1974) were among the first researchers to address the issue of flow in porous pavements. Their research was focused on flow within the pavement base course rather than in the pavement itself with the goal of analyzing the effect of subdrain spacing on discharge rates (a subdrain is a drain placed within or beneath the pavement system to enhance stormwater recovery). This was accomplished using numerical solutions to the Boussinesq equation for the situation where the impermeable base had a zero slope.

Ranieri (2002) was the first researcher who published predictions of water depths within PFC itself. He developed a runoff model for PFC that links the hydraulic conductivity of PFC with the geometric characteristics of the road section and rainfall intensity. He validated his theoretical model in the laboratory with a device that simulated rainfall on porous pavements and, at the same time, measured the depth of water over the impervious layer during the seepage motion. Based on the experimental data, a chart for porous pavement design was presented. Ranieri (2007) expands on this earlier work and provides some minor corrections to his original nomographs. In both papers, Ranieri relies on a numerical solution to solve the governing differential equations for water flow within PFC.

Tan et al. (2004) also used a numerical modeling approach to analyze water depths within PFC. They used a three-dimensional finite element program to study the effects of cross and longitudinal slopes on the drainage performance of the porous asphalt surface course. A family of thickness-requirement graphs, based on design rainfall, thickness of surface course layer, width of pavement, and longitudinal and cross slopes, was prepared for use by designers.

The objectives of this current paper are to improve on this earlier modeling by Ranieri (2002, 2007) and Tan et al. (2004) by providing analytical solutions for the governing equations under a variety of boundary and rainfall conditions.

4.2 Linear Sections

4.2.1 Mathematical Analysis

The primary objective of this manuscript is to develop a set of model equations that can be used for design and analysis of PFC systems. Design equations are based on simplifying assumptions that include steady-state flow, constant and uniform rainfall intensity, and homogeneous system properties. For urban drainage, the design rainfall intensity is determined from the size of the drainage area (based on its time of concentration, which for this application is the time to steady-state drainage for constant rainfall intensity) and the design frequency or return period, using the intensity-duration-frequency relationship of the area (Brown et al., 2001; Chow et al., 1988). Flow within PFC is spatially variable porous media flow down a slope with an impermeable base and recharge from infiltrating rainfall. Among the features that distinguish PFC flow from groundwater flow are the typically larger hydraulic conductivity and the small thickness of the seepage layer. The primary assumptions in drainage hydraulics of PFC are that the flow can be modeled as one-dimensional, steady-state Darcy-type flow, and that slopes are sufficiently small so that the Dupuit-Forchheimer assumptions apply (Charbeneau, 2000). Figure 4-2 shows a schematic cross-section along a flow path that is determined by the roadway cross-slope and longitudinal slope. The pavement has slope $s = \tan(\alpha)$, length L from the crown to the end of the overlay, and PFC thickness b_p. Slope s generally ranges from 0.02 to 0.06, length L on the order of 5–15 meters, and thickness b_p 3–8 cm. The infiltration rate r [L/T] is constant and uniform, and the PFC is underlain by impermeable pavement. The hydraulic head is $H(x)$ while the drainage layer thickness within the pavement is $h(x)$. The flow per unit width is $U(x)$ [L^2/T]. If the capacity of the PFC is exceeded, then drainage occurs as a combination of PFC flow plus overland sheet flow.

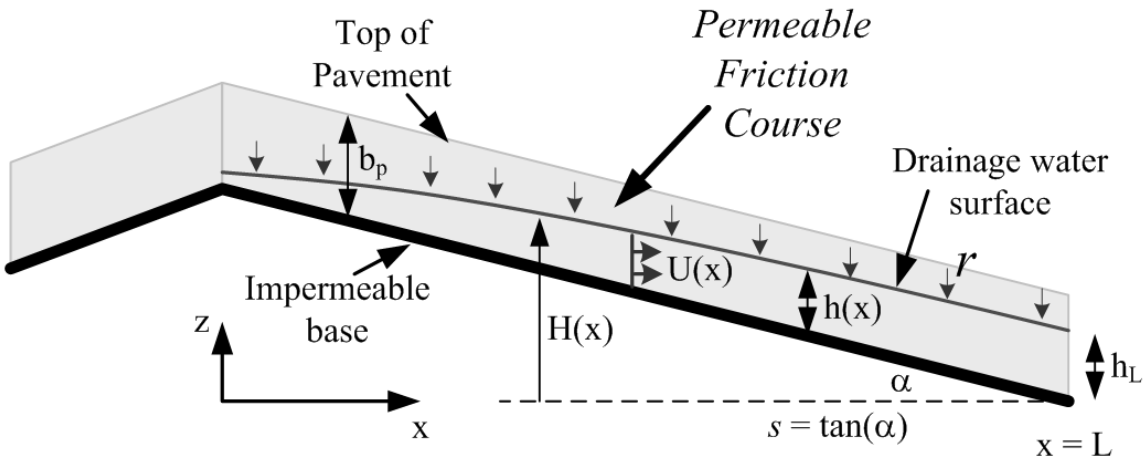

Figure 4-2: Schematic cross section of permeable friction course

The flow per unit width is the integral of the Darcy velocity over the saturated thickness and is proportional to the slope of the drainage water surface (water table).

$$U = -K\,h\frac{dH}{dx} \tag{4.1}$$

In equation (4.1) K is the PFC hydraulic conductivity. Figure 4-2 shows that the hydraulic head and saturated thickness are related through

$$H(x) = (L - x)\,s + h(x) \tag{4.2}$$

Thus

$$\frac{dH}{dx} = \frac{dh}{dx} - s \tag{4.3}$$

Equation (4.3) implies that the flow per unit width may be written

$$U = -K\,h\frac{dh}{dx} + K\,h\,s \tag{4.4}$$

For one-dimensional steady-state flow conditions with recharge at a rate r, the principle of continuity gives

$$\frac{dU}{dx} = r$$

$$U(x) = U_o + r\,(x - x_o) \tag{4.5}$$

From Figure 4-2, the origin of the x-axis ($x = x_o = 0$) is the roadway crown and acts as a no-flow boundary. Thus equation (4.5) may be written

$$U = r\,x \tag{4.6}$$

Combining equations (4.4) and (4.6) one finds

$$\frac{dh}{dx} = \left(s - \frac{r\,x}{K\,h} \right) \tag{4.7}$$

Equation (4.7) describes the change in drainage flow thickness through PFC. A couple of points are of interest.

i) The origin is automatically a no-flow boundary since for x = 0, this equation requires $dh/dx = s$, and from equation (4.3), this implies $dH/dx = 0$.

ii) Since $s > 0$, the flow thickness initially increases ($dh/dx > 0$).

iii) At the location of maximum depth within the flow profile $dh/dx = 0$, and the following relationship must hold among the variables

$$h_{\max} = \frac{r\,x_{\max}}{K\,s} \tag{4.8}$$

iv) The location of maximum depth changes with flow conditions.

Methods for estimating the upstream thickness $h(0)$ are not well defined by problem conditions, and specification of a downstream boundary condition $h(L) = h_L$ is more useful.

Equation (4.7) is a homogeneous ordinary differential equation (Boyce and DiPrima, 1969, pg. 43) that may be solved using variable transformation followed by separation of variables. Use the following variable transformation

$$\begin{aligned} \eta &= \frac{h}{x} \\ \frac{dh}{dx} &= x\frac{d\eta}{dx} + \eta \end{aligned} \tag{4.9}$$

With this transformation, equation (4.7) can be written

$$x\frac{d\eta}{dx} + \eta = \left(s - \frac{R}{\eta} \right) \tag{4.10}$$

Equation (4.10) states that the variable η (= h/x) depends only on distance x with parameters s and relative recharge rate $R = r/K$. The relative magnitude of these parameters is important. The variables in equation (4.10) may be separated to give

$$-\frac{dx}{x}=\frac{d\eta}{\eta-s+R/\eta}=\frac{\eta\,d\eta}{\eta^2-s\eta+R} \tag{4.11}$$

Formally the problem now becomes one of quadrature. Integration gives

$$\frac{1}{s}\ln\left(h^2-shx+Rx^2\right)+\int\frac{d\eta}{\eta^2-s\eta+R}=0 \tag{4.12}$$

The last term in equation (4.12) determines the form of the solution, and it depends on the sign of the quantity

$$\Phi=4R-s^2. \tag{4.13}$$

First consider the case for $\underline{\Phi<0}$ which corresponds to low rainfall intensity. For this case equation (4.12) gives

$$\frac{1}{s}\ln\left(h^2-shx+Rx^2\right)+\frac{1}{\sqrt{-\Phi}}\ln\left(\frac{2\eta-s-\sqrt{-\Phi}}{2\eta-s+\sqrt{-\Phi}}\right)=const \tag{4.14}$$

The constant is evaluated by applying a boundary condition with known thickness at a specified location. One may use $h(L) = h_L$ to find (with $\eta_L = h_L/L$)

$$\frac{1}{s}\ln\left(\frac{h^2-shx+Rx^2}{h_L{}^2-sh_LL+RL^2}\right)+\frac{1}{\sqrt{-\Phi}}\ln\left(\frac{\left(2\eta-s-\sqrt{-\Phi}\right)\left(2\eta_L-s+\sqrt{-\Phi}\right)}{\left(2\eta-s+\sqrt{-\Phi}\right)\left(2\eta_L-s-\sqrt{-\Phi}\right)}\right)=0 \tag{4.15}$$

Next consider the special case for $\underline{\Phi = 0}$ so that $R = s^2/4$. For this case equation (4.11) becomes

$$-\int\frac{dx}{x}=\int\frac{\eta\,d\eta}{(\eta-s/2)^2}$$

$$-\ln(x)=\ln(\eta-s/2)-\frac{s/2}{\eta-s/2}+const \tag{4.16}$$

With $h(L) = h_L$ the result is

$$\ln\left(\frac{h-sx/2}{h_L-sL/2}\right)-\frac{sx/2}{h-sx/2}+\frac{sL/2}{h_L-sL/2}=0 \tag{4.17}$$

The last case is for $\underline{\Phi > 0}$. For this case equation (4.12) gives

$$\frac{1}{s}\ln\left(h^2 - shx + Rx^2\right) + \frac{2}{\sqrt{\Phi}}\tan^{-1}\left(\frac{2\eta - s}{\sqrt{\Phi}}\right) = const \tag{4.18}$$

With $h(L) = h_L$ the result is

$$\frac{1}{s}\ln\left(\frac{h^2 - shx + Rx^2}{h_L{}^2 - sh_L L + RL^2}\right) + \frac{2}{\sqrt{\Phi}}\tan^{-1}\left(\frac{2h/x - s}{\sqrt{\Phi}}\right) - \frac{2}{\sqrt{\Phi}}\tan^{-1}\left(\frac{2h_L/L - s}{\sqrt{\Phi}}\right) = 0 \tag{4.19}$$

4.2.2 Analysis and Discussion

The three solutions for cases with (1) $\Phi < 0$, (2) $\Phi = 0$, and (3) $\Phi > 0$ are given by equations (4.15), (4.17), and (4.19) for boundary condition $h(L) = h_L$. These cases are discussed separately.

4.2.2.1 Case 1: $\Phi < 0$

Equation (4.15) provides the solution

$$F_1(h, x; s, R, L, h_L) = \frac{1}{s}\ln\left(\frac{h^2 - shx + Rx^2}{h_L{}^2 - sh_L L + RL^2}\right) + \frac{1}{\sqrt{-\Phi}}\ln\left(\frac{\left(2\eta - s - \sqrt{-\Phi}\right)\left(2\eta_L - s + \sqrt{-\Phi}\right)}{\left(2\eta - s + \sqrt{-\Phi}\right)\left(2\eta_L - s - \sqrt{-\Phi}\right)}\right) = 0 \tag{4.20}$$

The notation used in equation (4.20) is meant to specify that h and x are variables for the function F_1, while s, R, L, and h_L are function parameters. The function F_1 defines the relationship $h(x)$ implicitly, and in order to extract this relationship one must invert the function using a selected numerical technique. If the appropriate root of $F_1 = 0$ can be bracketed, then the method of bi-section is easy to implement (Press et al., 1992). Investigation of function behavior shows that the critical parameters are the roots of the quadratic equation appearing in the numerator of the first term on the left side. The symbol h has been used to denote the flow depth within the PFC; the special case for roots of the quadratic equation is denoted by h', so that values of h' are found as solutions of the quadratic equation

$$\begin{aligned} h'^2 - sh'x + Rx^2 &= 0 \\ h' &= (x/2)\left(s \pm \sqrt{-\Phi}\right) \end{aligned} \tag{4.21}$$

In particular, for the roots evaluated at $x = L$ one finds

$$\begin{aligned} h'_L(+) &= (L/2)\left(s + \sqrt{-\Phi}\right) \\ h'_L(-) &= (L/2)\left(s - \sqrt{-\Phi}\right) \end{aligned} \tag{4.22}$$

The magnitude of h_L compared with $h_L'(-)$ and $h_L'(+)$ determines the range that must be searched for the appropriate root of $F_1 = 0$. These are given explicitly as follows.

$$
\begin{aligned}
&h_L \le h_L'(-): \quad 0 \le h(x) \le (x/2)\left(s - \sqrt{-\Phi}\right) \\
&h_L'(-) < h_L \le h_L'(+): \quad (x/2)\left(s - \sqrt{-\Phi}\right) < h(x) \le (x/2)\left(s + \sqrt{-\Phi}\right) \\
&h_L'(+) < h_L: \quad (x/2)\left(s + \sqrt{-\Phi}\right) < h(x) \le h_L
\end{aligned}
\qquad (4.23)
$$

In the special case, of minor interest, where h_L is equal to one of the roots given by equation (4.22), then the drainage profile is a straight line.

Figure 4-3 shows the solution from equation (4.20) for three different downstream depth values corresponding to the three different ranges specified by equation (4.23). The dashed lines correspond to the 'root' equations. For Case 1 ($\Phi < 0$), the water level profiles do not cross the root equations. Also, if $h_L \le (L/2)\left(s + \sqrt{-\Phi}\right)$, then $h(0) = 0$.

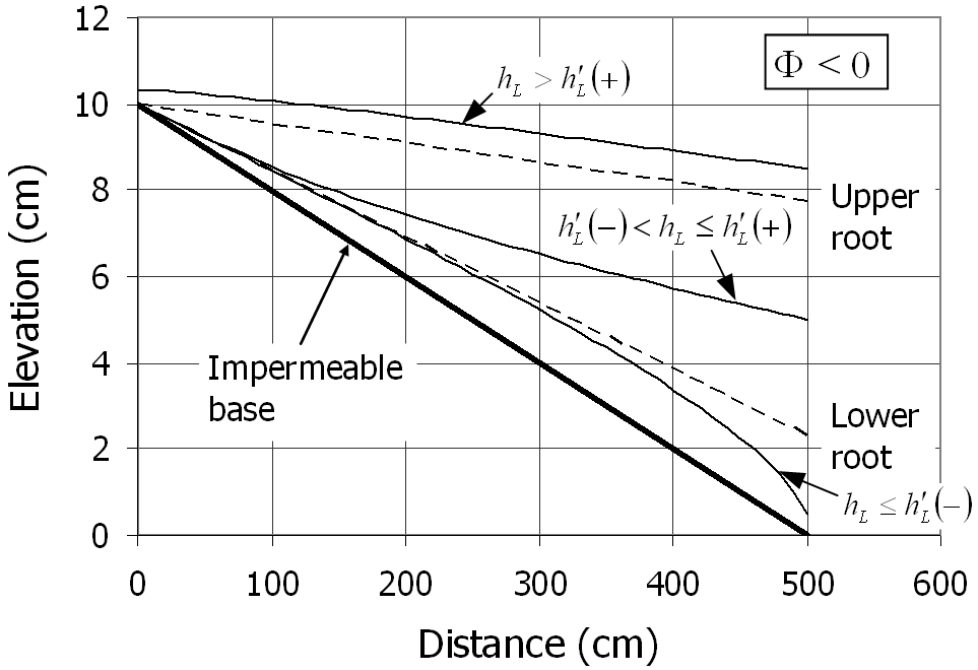

Figure 4-3: PFC drainage profiles for Case 1 (Φ<0) with r=0.25cm/hr, s=0.02, L=500cm, K=1cm/s, and downstream depth values h_L =0.5, 5, and 8.5cm.

Note: The characteristic root values are hL=2.24 and 7.76cm, and the root curve equations corresponding to the second of equation (4.21) are shown as the lower and upper dashed lines.

4.2.2.2 Case 2: $\Phi = 0$

Case 2 ($\Phi = 0$) represents a special (limited) condition with $r = K\,s^2/4$. In essence, the solution corresponds to the limit $\Phi \rightarrow 0$ from the Case 1, so that the roots corresponding to equation (4.21) or (4.22) collapse to a double root with $h_L = sL/2$. The middle range in equation (4.23) does not exist. The solution gives a drainage profile that is similar to either the lower or

upper profiles shown in Figure 4-3. The root equation gives $h'(x) = s\,x/2$. The drainage profile is found from roots of the function

$$F_2(h, x; s, L, h_L) = \ln\left(\frac{h - sx/2}{h_L - sL/2}\right) - \frac{sx/2}{h - sx/2} + \frac{sL/2}{h_L - sL/2} = 0 \qquad (4.24)$$

4.2.2.3 Case 3: $\Phi > 0$

Case 3 ($\Phi > 0$) corresponds to higher rainfall rates, is of greater interest, and appears to be fundamentally different from Cases 1 and 2 in terms of mathematical behavior of the solution. The flow profile is found from solution of equation (4.19), written as follows.

$$F_3(h, x; s, R, L, h_L) =$$
$$\frac{1}{s}\ln\left(\frac{h^2 - shx + Rx^2}{h_L{}^2 - sh_L L + RL^2}\right) + \frac{2}{\sqrt{\Phi}}\tan^{-1}\left(\frac{2h/x - s}{\sqrt{\Phi}}\right) - \frac{2}{\sqrt{\Phi}}\tan^{-1}\left(\frac{2\,h_L/L - s}{\sqrt{\Phi}}\right) = 0 \qquad (4.25)$$

The first term in the function F_3 is the same as in the function F_1, and thus the roots of the quadratic are also given by equation (4.21). The fundamental difference is that in the function F_3, $\Phi > 0$ so the roots are complex conjugates. There are no roots corresponding to singularities of the function on the real axis. A simple method is used for bracketing the root of $F_3 = 0$. Start with $h_i = R\,x/s$, which is the solution corresponding to $dh/dx = 0$ in equation (4.7). The lower limit is then found by the sequence $h_{i+1} = 0.9 * h_i$ until the condition $F_3(h_{i+1},\ldots) < 0$ is met. Similarly, the sequence $h_{i+1} = h_i + h_L$ is evaluated until the condition $F_3(h_{i+1},\ldots) > 0$ is met. The method of bi-section is then used to find the solution to $F_3 = 0 \rightarrow h(x)$.

Figure 4-4 shows drainage profiles corresponding to rainfall rates r = 0.25, 0.5, 1.0, and 2.5 cm/hr with other conditions specified in the caption. For these parameters, the critical rainfall intensity corresponding to $\Phi = 0$ is $r = K\,s^2/4$ = 0.0001 cm/s (0.36 cm/hr), so that the lower profile corresponds to $\Phi < 0$ while the upper three profiles have $\Phi > 0$. Summary results from this example are shown in Table 4.1. As anticipated, the maximum drainage depth increases with rainfall intensity, as does the specific storage (volume per unit width) which is calculated from the integral of the drainage depth over the profile and an assumed porosity n = 0.2. What may not be expected is that the mean residence time (specific volume divided by rainfall recharge rate to the pavement) decreases with increasing rainfall rate. Discussion of the equilibrium time (time of concentration) is presented below.

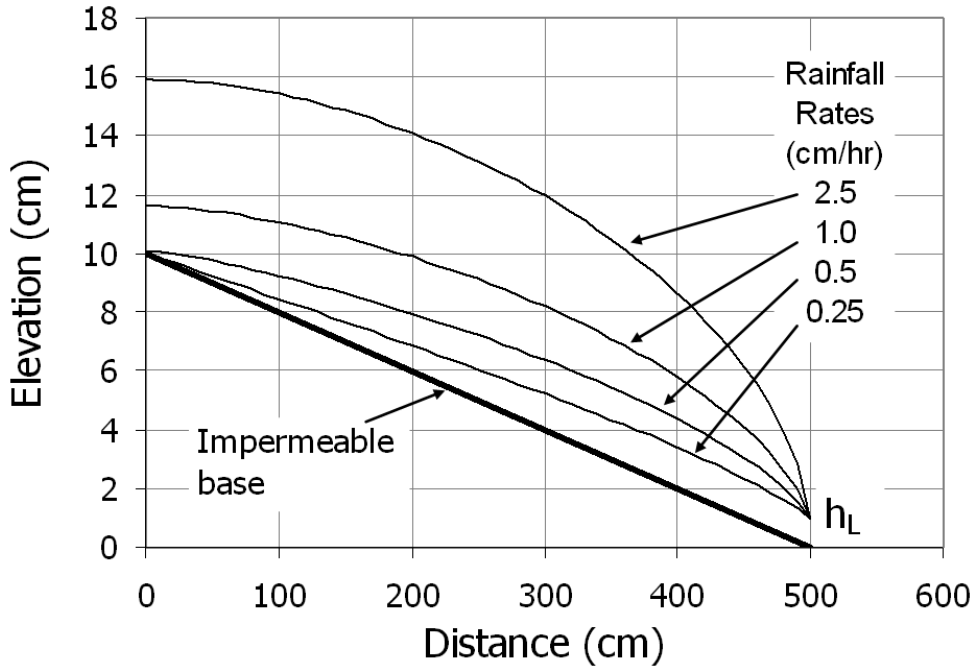

Figure 4-4: Drainage depth profiles corresponding to rainfall rates r = 0.25, 0.5, 1.0 and 2.5 cm/hr with s = 0.02, K = 1cm/s, L = 500cm and h_L = 1cm.

Table 4.1: Summary results from Figure 4-3 example

	r = 0.25	r = 0.5	r = 1.0	r = 2.5 cm/hr
Max. depth (cm)	1.42	2.45	4.19	8.14
Spec. Vol. (L/cm)	0.09	0.18	0.34	0.70
Mean Res. Tm. (hr)	0.73	0.71	0.68	0.56
Equil. Time (hr) [Eq. 42]	1.14	0.98	0.84	0.81

4.2.3 Drainage Profile near x=0

One cannot directly evaluate the functions F_1, F_2, or F_3 at $x = 0$. For F_1 and F_2 one knows that if $h_L \le h_L'(+)$, then $h(0) = 0$. For other cases the $h(0)$ value is found by extrapolating from the two adjacent points x_1 and x_2, and fitting a quadratic using the following algorithm. The general quadratic is

$$h = ax^2 + bx + c$$

$$\frac{dh}{dx} = 2ax + b \qquad (4.26)$$

Obviously, from equation (4.26), $h(0) = c$. From equation (4.7) one finds

$$\frac{dh}{dx}(0) = s = b \tag{4.27}$$

One then can write

$$\begin{aligned} h_1 &= ax_1^{\,2} + sx_1 + c \\ h_2 &= ax_2^{\,2} + sx_2 + c \end{aligned} \tag{4.28}$$

These equations are used to find

$$h(0) = c = h_1 - \left(\frac{(h_1 - h_2) - s(x_1 - x_2)}{x_1^{\,2} - x_2^{\,2}} \right) x_1^{\,2} - sx_1 \tag{4.29}$$

This is consistent with the upper boundary being a no-flow boundary ($dH/dx = 0$).

4.2.4 Upslope Drainage

Depending on conditions near the upstream edge of a PFC, the boundary may not act as a no-flow boundary, but rather as a drainage boundary as shown in Figure 4-5. In this case there must be a drainage divide located at some station along the pavement surface. The coordinate system is located at this station, so that the boundary condition $dH/dx(0) = 0$ applies for both upstream and downstream drainage. The flow depth at the divide is $h(0) = h_0$.

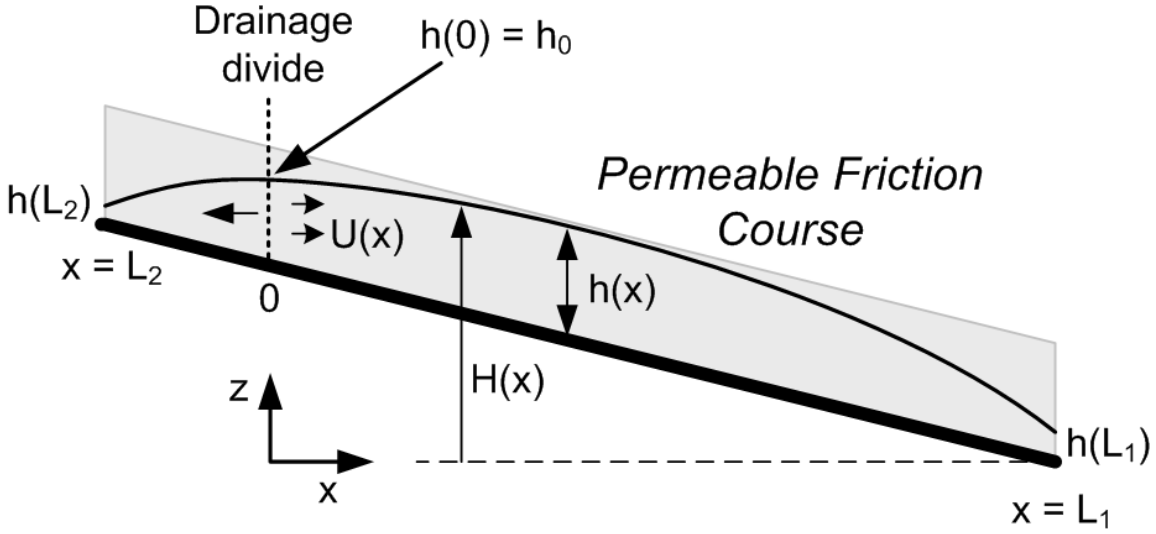

Figure 4-5: Schematic cross section of permeable friction course showing drainage divide with both upstream and downstream drainage

The solution for upstream drainage is essentially the same as that already considered. To simplify notation let $\xi = -x$. Then the flow per unit width in the upstream direction is given by $U = -K\,h\,dH/d\xi$. Also, $H(\xi) = h(\xi) + \xi\,s$. Combining these with continuity ($U = r\,\xi$) gives

$$\frac{dh}{d\xi} = -\left(s + \frac{R\xi}{h}\right) \tag{4.30}$$

Comparing equation (4.30) with equation (4.7) shows that the only change is in the sign of the slope (*s* is still considered a positive number). The solution development remains the same, and the critical parameter for solution behavior is still the magnitude of Φ. Practically, only the solution for Φ > 0 is of interest, and this solution is still given by equation (4.25) with the sign of s changed. The interesting question is how to match the upstream and downstream solutions. One must have $h(0)$ the same from both sides, where $x = 0$ is the location of the divide. For a given slope, rainfall intensity, etc., one solves both problems with selected L_1 and $L_2 = L - L_1$ values, and compare the depth $h(0)$ from the two solutions. The value of L_1 is adjusted until the solutions match. An example profile with r = 1.0 cm/hr, h_{L1} = 1 cm, and h_{L2} = 0.5 cm (other conditions are the same as in Figure 4-4) is shown in Figure 4-6. For this example, L_1 = 469.4 cm and L_2 = 30.6 cm. The mean residence time for downstream drainage is 0.64 hr while that for upstream drainage is 0.09 hr. The maximum flow depth within the PFC is 3.94 cm.

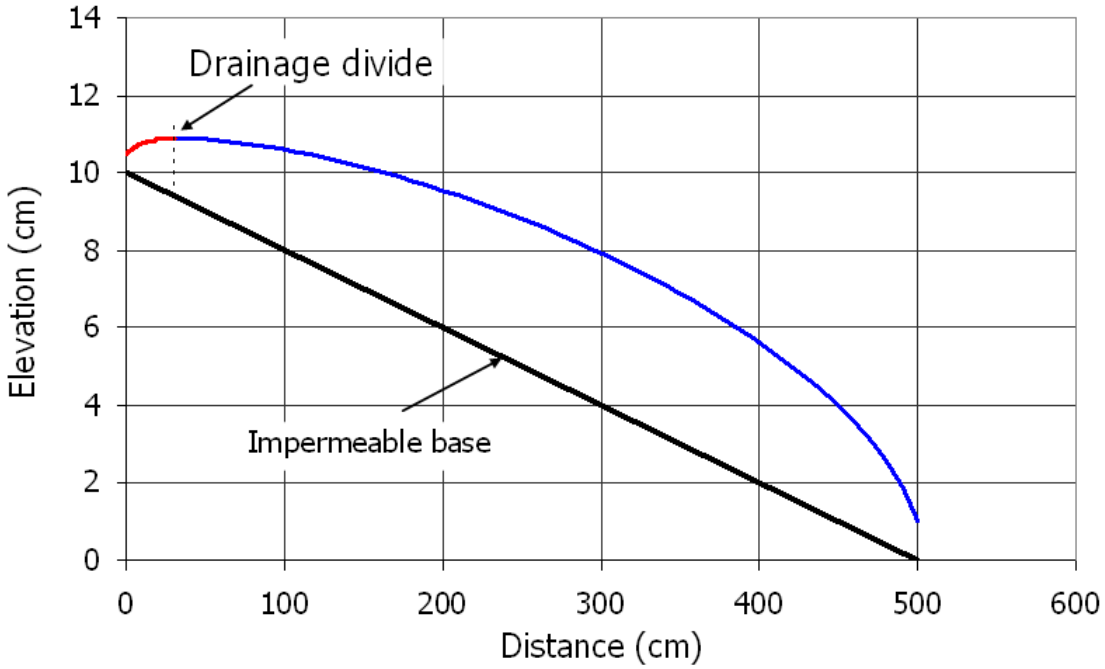

Figure 4-6: Water profile with upstream and downstream drainage for rainfall intensity r = 1.0 cm/hr.

Note: The divide occurs approximately 0.3m from the upstream edge of pavement.

4.2.5 Combining Overland (Sheet) and PFC Flow

The discussion so far has considered PFC as if it had an infinite thickness. However, because the thickness is finite (and generally small), one will often find conditions where stormwater drains from the roadway through a combination of PFC drainage plus overland sheet flow upon the roadway surface. Because the depth of overland flow is very small (even

compared with the PFC thickness b_p), the maximum hydraulic gradient for the saturated PFC is limited to

$$-\frac{dH}{dx} \le s \tag{4.31}$$

Once overland flow occurs, continuity gives

$$U = rx = Ts + U_{sheet} \tag{4.32}$$

In equation (4.32) the PFC transmissivity is defined by $T = K\, b_p$.

At the location of 'initial sheet flow' (x = Ls), the sheet flow discharge (U_{sheet}) is zero and the distance from the drainage divide or upstream edge of pavement is found from

$$L_s = \frac{K\, b_p\, s}{r} \tag{4.33}$$

Substituting x = Ls and h = b_p in Eq. (4.7) shows that at the location of initial sheet flow, dh/dx(x=Ls) = 0. Thus the relevant range of integration of Eq. (4.7) is from the origin where dh/dx = s to the location where dh/dx = 0. When a seepage divide occurs, Eq. (4.7) must also be integrated in the upstream direction, as described previously.

For the sheet flow per unit width one may use either the Darcy-Weisbach equation or Manning's equation. The sheet flow Reynolds number is generally very small, and the friction factor can be expressed as $f = K_{DW}/Re = K_{DW}\ \nu/U_{sheet}$, where K_{DW} is the Darcy-Weisbach coefficient, $Re = U_{sheet}/\nu$ is the Reynolds number, and ν is the kinematic viscosity. With laminar flow on a smooth surface, K_{DW} = 24 (Chow, 1959). However, because the roadway surface is rough, and because of the impacts from rainfall, K_{DW} is much larger for PFC applications. With the Darcy-Weisbach equation the thickness of sheet flow $h_s(x)$ is calculated using

$$h_s = \left[\frac{K_{DW}\nu\,(rx - Ts)}{8gs}\right]^{1/3} \tag{4.34}$$

A schematic view of combined PFC and sheet flow is shown in Figure 4-7. This figure shows the water saturation thickness (h) within the PFC with total PFC thickness b_p, the elevation of the water surface above a datum (H), the locations of a possible drainage divide (lateral coordinate origin, x = 0) and initiation of sheet flow (Ls) as measured from the upstream edge-of-pavement or drainage divide. The pavement slope (s) is shown, and the uniform rainfall intensity (r) is not shown. At the upstream edge-of-pavement is a potential seepage face which may function with an assumed seepage face height to allow outflow of upstream drainage from the groundwater divide, if one occurs. The possible function of the seepage face and location of a groundwater divide are determined through the solution procedure.

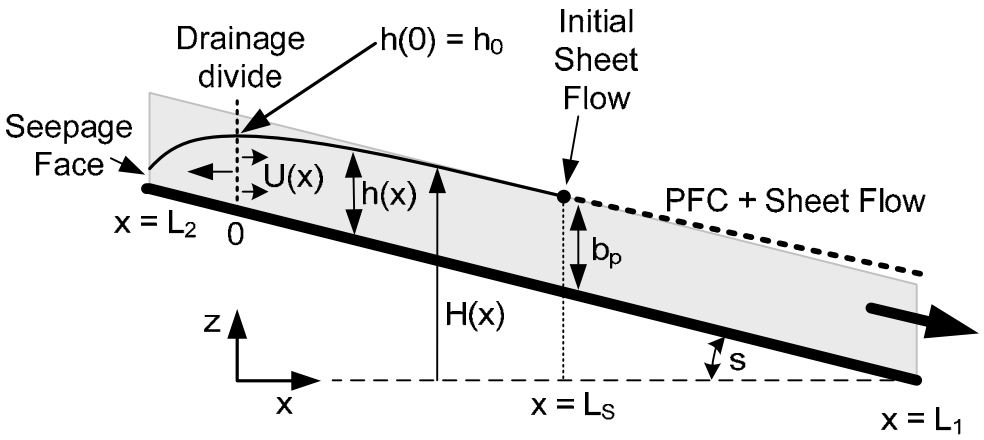

Figure 4-7: Schematic view of porous friction course with drainage divide and sheet flow

The general solutions presented in Section 4.2.2 remain valid. However, if the problem of interest is generation of sheet flow on PFC surfaces, then the 'initial point' on the solution curve is not arbitrary. One should specify $h = b_p$ at a station $x = Ls$ downstream from the drainage divide. Sheet flow commences downstream of $x = Ls$, and both PFC and sheet flow occur.

Figure 4-8 shows an example with drainage profiles corresponding to rainfall intensity r = 5, 2, 1.5, 1, and 0.4 cm/hr (from upper to lower curves shown). An assumption made in calculating this series of profiles is that a seepage face height of 1 cm is established. If the PFC thickness at the drainage divide is less than this magnitude, then it is assumed that the upstream boundary acts as a no-flow boundary. Otherwise, there is upstream discharge. As the magnitude of rainfall increases, the locations of the drainage divide moves downstream and the quantity of upstream drainage increases. This conceptual model formulation with regard to seepage face and upstream drainage remains to be verified experimentally.

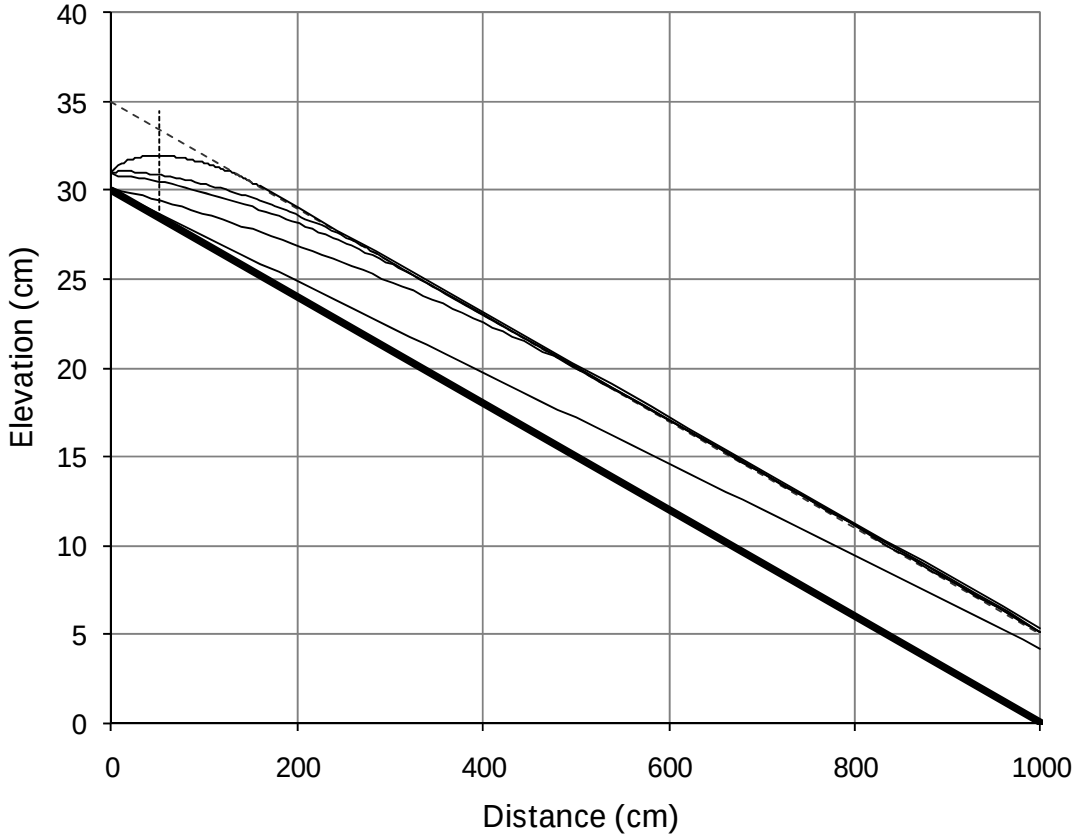

Figure 4-8: Drainage profile curves corresponding (from upper to lower curve) to rainfall intensity r = 5, 2, 1.5, 1, and 0.4 cm/hr.

Note: The point of initial sheet flow for r = 0.4 cm/hr lies beyond the domain; this location does not preclude the use of the point for calculating the drainage curve.

4.2.6 Estimation of Drainage Equilibrium Time (Time of Concentration)

The analyses presented in this manuscript have focused on steady-state flow, which is conventional for engineering design. A constant rainfall rate is estimated based on the time of concentration and the intensity-duration-frequency curve for the location (ASCE, 1992; Brown et al., 2001). The time of concentration is often estimated using the kinematic wave method, where the estimate depends on the rainfall intensity, so that the procedure can be iterative. There are no methods for estimating the time of concentration of drainage segments including porous pavement.

An estimate of the minimum possible equilibrium drainage time corresponds to the mean stormwater residence time that is calculated as the ratio of the steady-state storage volume (from the drainage profile) to the discharge (rainfall intensity multiplied by the drainage path length). Izzard (1947) assumes that the equilibrium time for surface drainage is twice the residence time, as calculated above. A more fundamental approach is based on analysis of the continuity equation for transient drainage in PFC.

Combining equation (4.5) with the one-dimensional transient continuity equation gives

$$n\frac{\partial h}{\partial t}+\frac{\partial}{\partial x}\left(-Kh\frac{\partial h}{\partial x}+Khs\right)=r \tag{4.35}$$

In equation (4.35) the leading term uses the porosity *n* in place of the specific yield since estimates of the specific retention of PFC are not available, and it is expected that $r << K$ so that the specific retention is small. The initial condition is

$$h(x,0)=0 \tag{4.36}$$

Formulation of boundary conditions is not considered since no attempt at solving equation (4.35) directly is made. For early time and within the interior of the domain, the depth gradient vanishes and equation (4.35) simplifies to the following form:

$$n\frac{\partial h}{\partial t}+Ks\frac{\partial h}{\partial x}=r \tag{4.37}$$

Equation (4.37) is a linear, first-order hyperbolic equation which may be solved using the method of characteristics. The wave celerity (c) is constant and equal to

$$c=\frac{dx}{dt}=\frac{Ks}{n} \tag{4.38}$$

Along each characteristic within this region the depth is equal to

$$h(x,t)=\frac{rt}{n} \tag{4.39}$$

An approximate estimate for the equilibrium drainage time (time of concentration) may be taken as the time duration required for the hyperbolic wave depth to reach the maximum drainage depth within the profile. With equations (4.38) and (4.39) this gives

$$T_c=\frac{h_{\max}n}{r}=\frac{x_{\max}n}{Ks} \tag{4.40}$$

In equation (4.40), T_c = time of concentration, h_{max} = maximum drainage depth within the PFC profile, and x_{max} = location of the maximum depth. Equation (4.40) is consistent with equation (4.8). Estimates of the equilibrium drainage time using equation (4.40) are presented in Table 4.1 for comparison with the mean residence time values.

4.2.7 Example Application

Stormwater quality and runoff hydrology and hydraulics from PFC are monitored at a station along Loop 360 in Austin, Texas. Loop 360 is a four lane divided highway. At the monitoring station the two-lane roadway width is 10.4 m and the longitudinal and cross slope are 0.023 and 0.02, respectively. The PFC has b_p = 5 cm. It is of interest to evaluate the reduction in

direct runoff from pavement surfaces due to placement of PFC, and the required spacing between drains beneath the PFC that could be placed across the roadway to meet certain objectives. These issues are discussed in this example.

Lateral drains for PFC drainage enhancement are slots cut into the base pavement that can be filled with coarse material or metal drains before placement of the PFC. A schematic layout is shown in Figure 4-9. The placement of the drains is shown perpendicular to the roadway alignment, though this is not necessary. The drainage path is 'down slope' based on the longitudinal and cross slope, s_L and s_c. For this location s = 0.0305, and the drainage path length is L = 15.85 m. It is assumed that K = 1 cm/s (no measurements have been made for this location; the estimated value is based on literature values for porous media gravel material [0.1–10 cm/s] (Charbeneau, 2000), and on estimates for PFC from European experience [1–2 cm/s], Ranieri, 2007b).

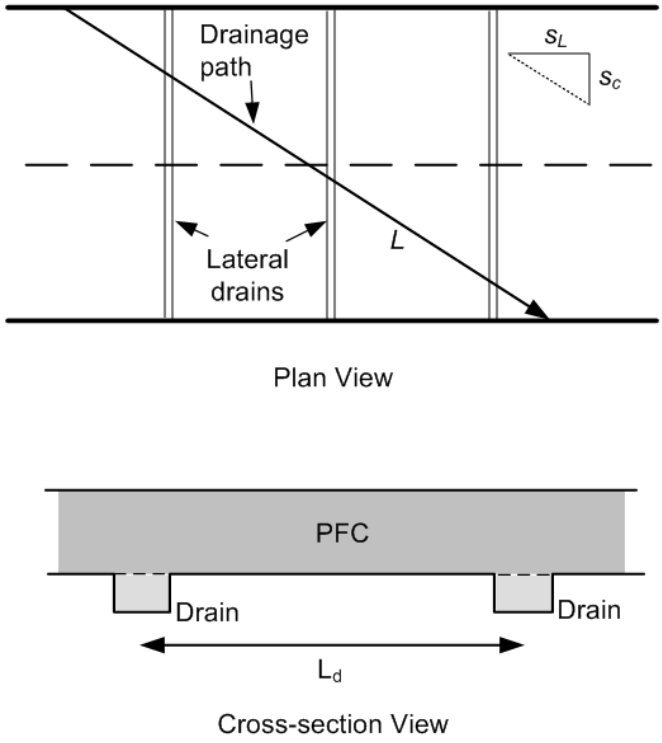

Figure 4-9: Schematic view of a roadway section with lateral drains

Figure 4-10 shows the cumulative rainfall intensity curve for Austin, Texas area based on 15-minute rainfall data from 1987 to 2004 collected as part of the City of Austin's Flood Early Warning System. The curve gives the fraction of the total rainfall duration over that period that occurred at intensities less than the given value.

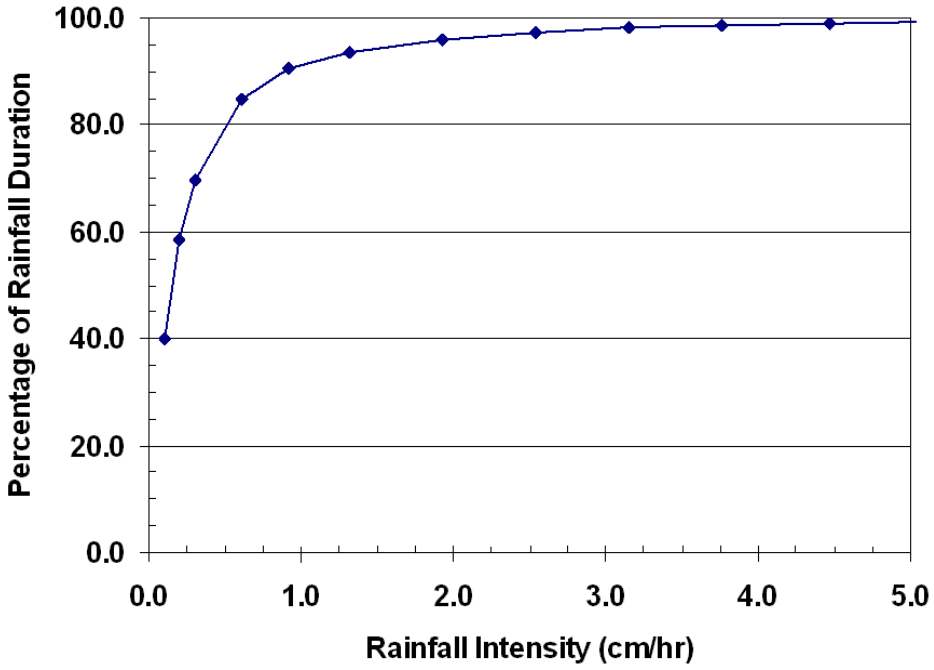

Figure 4-10: Cumulative rainfall intensity curve for Austin, Texas, showing percent of duration corresponding to a given rainfall intensity

The model equations were used to estimate the maximum rainfall intensity that would not result in overland flow from the pavement surface under steady-state conditions. For a drainage path length of 15.85 m with slope s = 0.0305, rainfall of intensity less than 0.425 cm/hr will not cause overland flow. With this rainfall intensity and the data shown in Figure 4-10, it is estimated that just over 75 percent (0.758) of the rainfall duration is at intensities that will not cause direct pavement surface runoff. Such estimates are approximate because they are based on a steady-state flow model, and natural rainfall events exhibit significant variability and drainage flow is transient.

One option for design of drain spacing is to control water quality (and/or splash from traffic caused by sheet flow on roadways) for ninety percent of the annual rainfall events, which for this case, would give a design rainfall intensity of 0.88 cm/hr. The model equations were used to investigate the drainage profile for rainfall intensity r = 0.88 cm/hr and slope s = 0.0305. The drainage path length was adjusted to allow for both upstream and downstream drainage with h_{L1} = 1 cm and h_{L2} = 0.5 cm, and the maximum drainage depth was limited to $h < b_p$ = 5 cm. The results are shown in Figure 10. The maximum drainage path depth is L = 850 cm and results in only downstream drainage, which corresponds to a longitudinal distance between drains L_d = 850 (0.023/0.0305) = 641 cm. The Reynolds number (based on Darcy velocity and effective grain diameter from Hazen's formula [Fetter, 2001]) ranges from 0.15 to 0.76. Also shown in Figure 10 is the flow profile for conditions where the drainage path length is increased to L = 900 cm (with the same rainfall intensity). Sheet flow occurs on the pavement surface with a maximum depth h_s = 1.36 mm at the downstream pavement edge. However, nearly seventy percent (0.693) of the drainage occurs through the PFC.

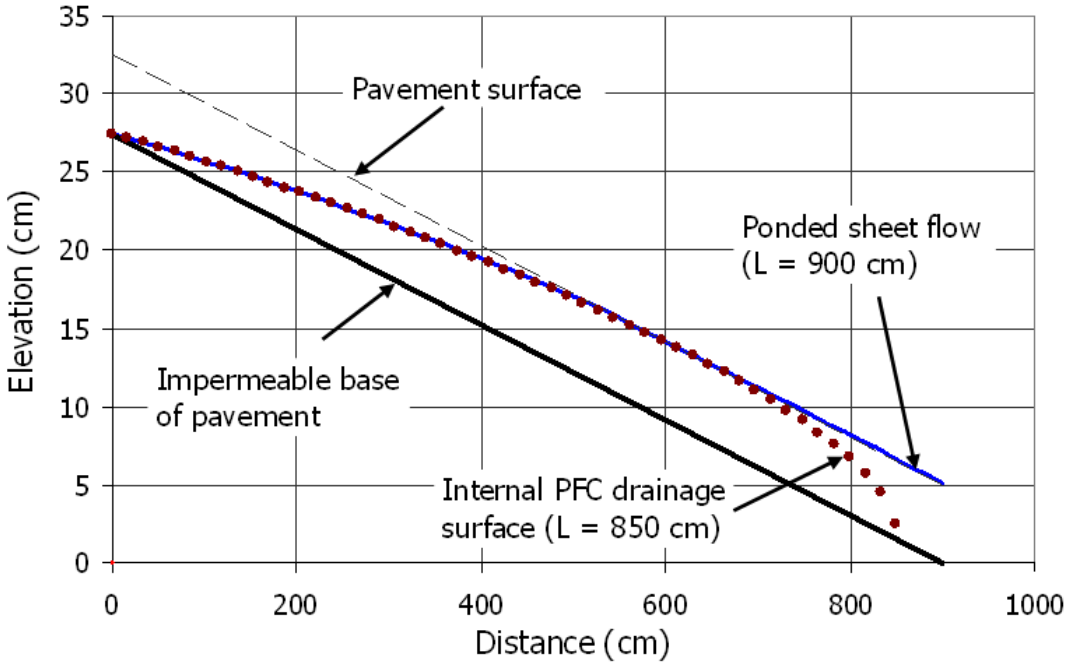

Figure 4-11: Drainage profiles for PFC with drainage path length L = 850 cm (dotted profile with drainage profile within PFC) and L = 900 cm (profile with surface drainage)

4.2.8 Summary and Conclusions

This chapter describes solutions to the hydraulic equations that govern flow in permeable friction courses (PFC). The primary assumptions used in this analysis are that the flow can be modeled as one-dimensional, steady-state Darcy-type flow, and that slopes are sufficiently small so that the Dupuit-Forchheimer assumptions apply. Solutions are derived for three distinct cases that represent low rainfall intensity, high intensity, and a point of singularity that divides the two previous cases. At low rainfall intensities, three different water surface profiles are predicted based on the selected downstream boundary condition (water depth at the edge of pavement). At higher rainfall rates the mathematical solution is substantially different. The maximum drainage depth increases with rainfall, as does the specific storage; however, the mean residence time (specific volume divided by rainfall recharge rate to the pavement) decreases with increasing rainfall rate. Depending on conditions near the upstream end of a PFC, this boundary may not act as a no-flow boundary, but rather as a drainage boundary. In this case there must be a drainage divide located at some station along the pavement surface, and a search algorithm may be used to locate the drainage divide and apportion down slope and upslope drainage.

These solutions have considered PFC as if it had an infinite thickness; however, because the thickness is finite, one will often find conditions where stormwater drains from the roadway through a combination of PFC drainage plus overland sheet flow upon the roadway surface. A solution is also presented for this case. Finally, a method for estimating the time of concentration from the steady-state flow profiles is presented.

For design rainfall intensity, the mathematical solutions provide estimates of the maximum drainage depth within PFC, and the maximum ponded depth of sheet flow on the roadway surface when the PFC drainage capacity is exceeded. These variables depend on the

rainfall intensity, PFC hydraulic conductivity, roadway slope, and maximum drainage path length. Necessary spacing between under drains for controlling surface flow on pavement surfaces can also be calculated using the model equations.

4.3 Curved/Converging Sections

The steady state solution for PFC flow on a linear domain is given by Charbeneau and Barrett (2008). Steady-state solutions for sheet flow on linear and converging sections are given by Eck et al. (2010), and also Jeong et al. (2010). What is missing is the solution for PFC flow on a converging section, which is the topic of the present subsection.

Consider a section of roadway having a constant radius of curvature and constant cross-slope as shown in Figure 4-12. Geometrically, this shape is equivalent to an inverted cone. A cross section view along the radius is shown in Figure 4-13. It is important to realize the coordinate system is arranged so that flow moves from a large radial position to a smaller radial position as it moves down the slope.

At steady state, the volumetric flow-rate into an area equals the flow-rate out of that area. For a converging section, the discharge is radial. The flow rate is the rainfall rate times the contributing area. The area is found by subtracting the area of the sector at radius R from the area of the sector at R_{max}.

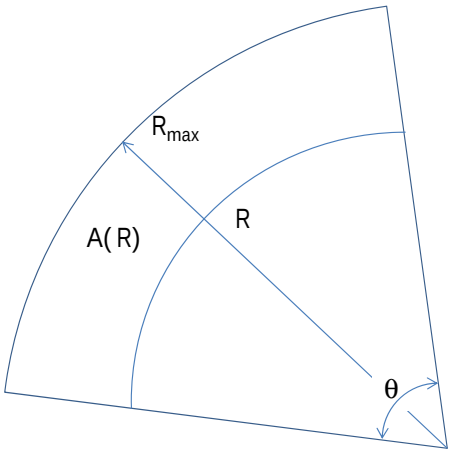

Figure 4-12: Schematic of converging section

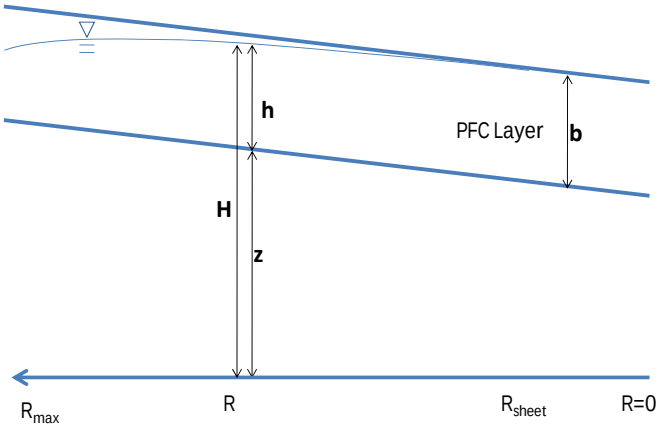

Figure 4-13: Cross section view

For the discharge through station R, the area is:

$$A(R) = \frac{\theta}{2\pi}\pi Rmax^2 - \frac{\theta}{2\pi}\pi R^2 = \frac{\theta}{2} * (R_{max}^2 - R^2) \tag{4.40}$$

where θ is the included angle. The flow rate is given by:

$$Q(R) = r * A(R) = \frac{r\theta}{2}(R_{max}^2 - R^2) \tag{4.41}$$

The unit flux past radius R is the flow rate divided by the arc length at R:

$$U(R) = \frac{Q(R)}{\theta R} = \frac{r}{2R}(R_{max}^2 - R^2) \tag{4.42}$$

Because flow through a PFC is the problem of interest, Darcy's law is the appropriate form of the momentum equation:

$$U = K * h * \frac{dH}{dR} \tag{4.43}$$

The hydraulic gradient decomposes as:

$$\frac{dH}{dR} = \frac{dh}{dR} + \frac{dz}{dR} = \frac{dh}{dR} + s \tag{4.44}$$

where s is the slope, which due to the choice of coordinate system is positive for a down-slope flux.

In order to agree with this convention, a positive hydraulic gradient in Darcy's law should cause a down-slope flux. This requirement is satisfied because the coordinate system for this problem is reversed from our usual system—the origin is at the down-hill end of the domain rather than the uphill end.

Combining Equations (4.42), (4.43), and (4.44) the ODE for PFC flow on a converging section:

$$Kh\left(\frac{dh}{dR} + s\right) = \frac{r}{2R}(R_{max}^2 - R^2)$$
$$\text{or} \tag{4.45}$$
$$\frac{dh}{dR} = -s + \frac{r}{2Kh}\left(\frac{R_{max}^2 - R^2}{R}\right)$$

This ODE is first-order, but non-linear, and an analytical solution is not known at this time. The same general features of the ODE for the linear section (see Charbeneau and Barrett, 2008) also apply to the ODE for the converging section:

1. The location of maximum radius, R_{max}, is automatically a no-flow boundary because for $R = R_{\max}$, $\frac{dh}{dR} = -s$, and from (4.44) this implies $\frac{dH}{dR} = 0$.
2. The thickness initially increases as the radius decreases because $s > 0$.
3. At the location of maximum depth $\frac{dh}{dR} = 0$ and the variables are related by
4.

$$h_{\max} = \frac{r}{Ks}\frac{R_{\max}^2 - R^2}{2R} \tag{4.46}$$

The ODE of Equation (4.45) applies on a domain where flow is completely contained within the PFC. To integrate the ODE, an initial point is needed somewhere on the solution curve. The appropriate initial point depends on problem conditions. When flow is completely contained in the PFC the saturated thickness at the edge of the domain can be specified; in the case of combined PFC and sheet flow the appropriate point is the PFC thickness taken at the location where sheet flow begins. This location is found by equating (4.42) and (4.43) and setting the hydraulic gradient to the pavement slope. Note that a hydraulic gradient equal to the pavement slope is a requirement for sheet flow to occur.

$$r * \left(\frac{R_{max}^2 - R^2}{2R}\right) = K * b * s \tag{4.47}$$

Applying the quadratic formula gives the location where sheet flow begins:

$$R_{sheet} = \frac{1}{2}\left(-\frac{2Kbs}{r}\right) + \frac{1}{2}\sqrt{\left(\frac{2Kbs}{r}\right)^2 + 4R_{max}^2}$$

or (4.48)

$$R_{sheet} = \left(-\frac{Kbs}{r}\right) + \sqrt{\left(\frac{Kbs}{r}\right)^2 + R_{max}^2}$$

As an analytical solution is not known at this time, a numerical solution was developed using a fourth order Runge-Kutta scheme (Figure 4.14). Comparisons between linear and converging sections are discussed in Section 5.4.3 of this report.

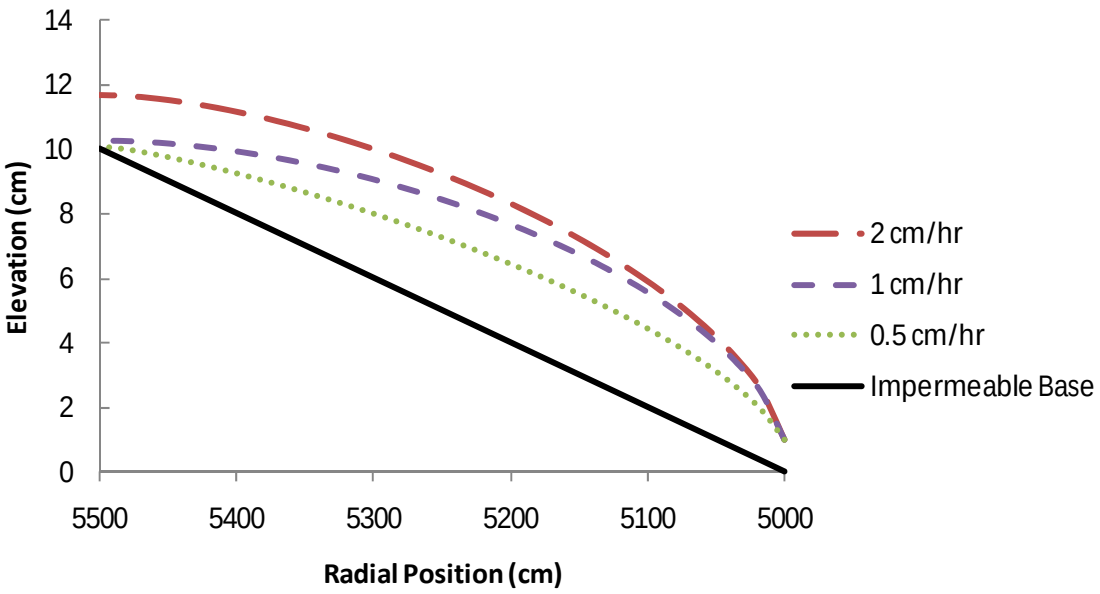

Figure 4-14: Drainage depth profiles for a converging section with maximum radius of 55m, hydraulic conductivity 1cm/s, slope of 2%, initial depth of 1cm at R=5000cm and range of rainfall rates.

Chapter 5. Unsteady Modeling

5.1 Introduction

5.1.1 Background and Motivation

Although usually placed in a 50mm layer, the PFC thickness may be selected so that all of the rainfall for a design event drains within the pavement. However, structural and cost concerns prevent the use of an arbitrarily thick porous layer. Additionally, PFC has been shown to clog over time, resulting in lower subsurface drainage capacity (NCHRP, 2009). Therefore, some storms will exceed the installed capacity, forcing drainage to occur both on the pavement surface and within the porous matrix. Understanding this coupled flow process is the goal of this research.

A precise description of PFC's response to rainfall events is needed for several reasons including driver safety, water quality, and basic science. From a safety perspective, flow over traffic lanes can cause vehicles to hydroplane. Hydroplaning is especially hazardous when right and left tires encounter different water depths—the difference in resistance imposes a torque on the vehicle, potentially causing the driver to lose control. A detailed runoff model for PFC could identify areas of excessive sheet flow depth so that additional drainage can be provided. Such a model also has implications for water quality. Field studies of runoff from PFC have shown that runoff concentrations of pollutants are lower for PFC than conventional pavement, but the mechanisms responsible for lower concentrations have not been identified (Stanard, 2008). Possible mechanisms include reduced wash-off from vehicles, filtration and absorption within the pavement, and even biological activity. Studying these mechanisms in detail requires an accurate hydraulic model. Finally, the proposed model is of general scientific interest because the problem of flow over porous media appears in numerous applications. Civil engineering applications include surface irrigation, watershed modeling, and sediment transport. The concept of flow over porous media has also been applied to biological systems such as blood flow within the arterial wall (Dabaghmeshin, 2008). A better technical understanding of flow in PFC will contribute to a diverse scientific field and promote wider use of the material, thereby improving driver safety and the environment.

Figure 5-1 shows a photograph of a PFC layer. The PFC overlay is very thin compared to the length and width of the roadway section. A cross section of typical PFC roadway is shown in Figure 5-2 and a more detailed schematic of the PFC layer is shown in Figure 5-3.

Figure 5-1: Photograph of PFC layer on Loop 360, Austin, Texas

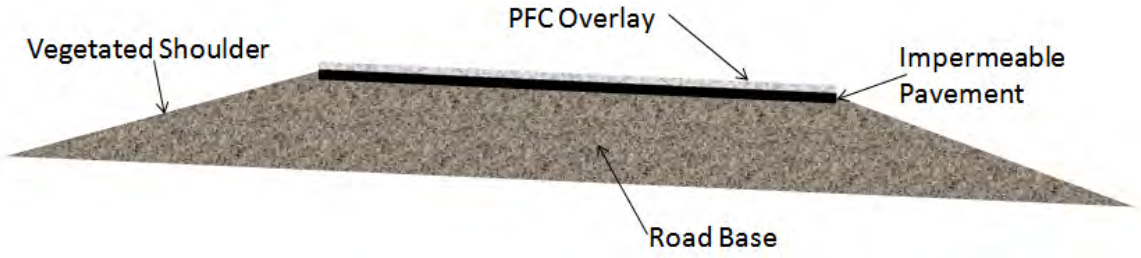

Figure 5-2: Cross section of a typical PFC roadway

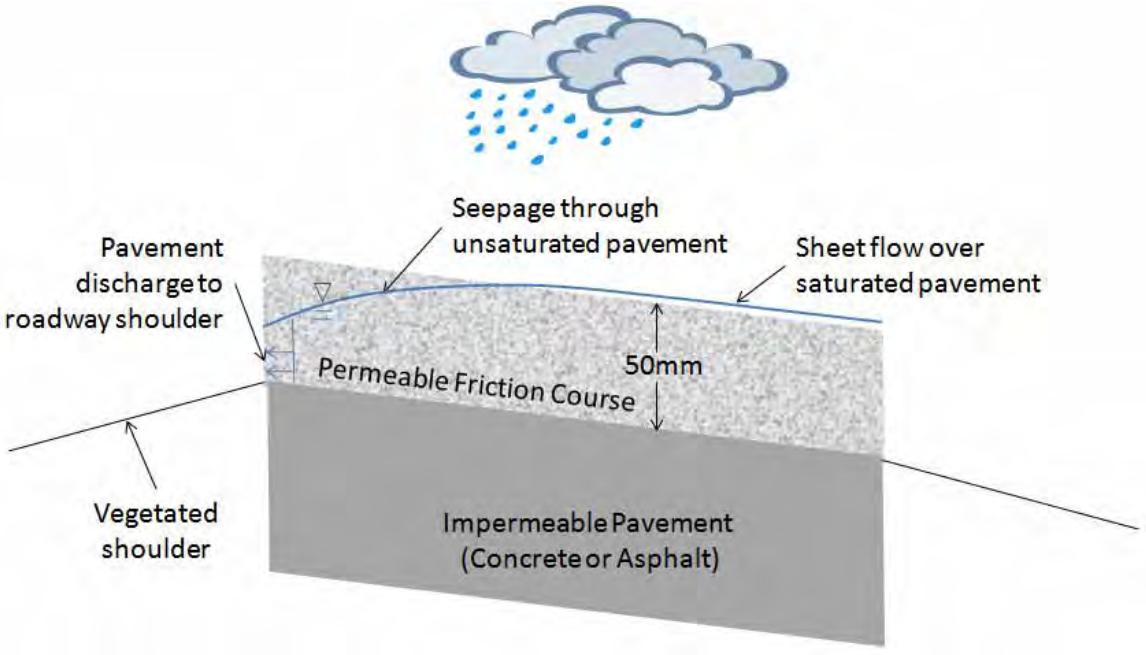

Figure 5-3: Schematic cross section of a roadway with a PFC overlay

5.1.2 Research Objectives

The goal of this chapter is to understand the coupling between overland flow and porous media flow in roadway applications. In this context, understanding the coupling means predicting water depths at a fine enough scale to assess the risk of hydroplaning. To accomplish this goal, a numerical model that predicts water surface elevations on roads overlain with PFC has been developed and validated. The model has as inputs the roadway geometry, rainfall intensity, and porous media properties. The model has been formulated to accommodate roadway geometries where the horizontal alignment may be straight or curved and to accommodate variable rainfall intensity.

Based on these inputs, the goal of understanding coupled flow between the surface and subsurface will be pursued through the following research objectives:

1. Identify governing equations for surface and subsurface flow for the geometry of interest
2. Develop a scheme to couple flow between the surface and subsurface
3. Implement the coupling scheme and numerical methods in a computer model that represents roadway geometry using a coordinate transformation
4. Validate the model using analytical solutions
5. Compare model predictions of runoff rates with values measured at an existing monitoring site

During the preparation of this work, the National Cooperative Highway Research Program (NCHRP) issued Report 640 entitled “Construction and Maintenance Practices for Permeable Friction Courses” (NCHRP, 2009). The report signifies the growing popularity and

importance PFC layers for highways in the USA. Several of the future research needs listed in the report are addressed in part by this chapter:

- Field work to document how water flows within a PFC layer
- Methods for selecting the minimum PFC thickness
- Consideration for water sheets on the PFC surface

Field work included constructing a monitoring site to measure runoff hydrographs from a PFC roadway. The dynamic simulation model developed in this chapter accounts for sheet flow on the PFC surface and seepage through the porous layer; it can be used to evaluate methods for selecting the thickness of a PFC layer. Another important and related research need identified in the report is a method to determine the permeability of PFC layers. The work of Klenzendorf (2010) addresses the hydraulic conductivity of PFC and this chapter uses his results to simulate PFC flow on highways.

5.1.3 Organization of the Chapter

This chapter is organized into six sections. Section 5.1 has introduced the work and defined the research objectives. Section 5.2 reviews selected literature that bears on the work. A method for developing a predictive model for PFC drainage is given in Section 5.3. The proposed model is essentially a specialized hydrologic model so Sections 5.2 and 5.3 are organized around hydrologic processes. The methods of Section 5.3 have been implemented in a Fortran computer model called PerfCode. Section 5.4 validates the model's numerics by comparing model results with independently obtained solutions for simplified cases. Section 5.4 also discusses the model's stability and convergence properties. Section 5.5 applies the model to a field monitoring site, facilitating a comparison of modeled results with field measurements. Section 5.6 concludes the chapter with a summary of the findings and possible avenues for future work.

5.2 Literature Review

This review summarizes the literature that provides the theoretical foundation for this research. Developments related specifically to permeable friction course (PFC) are given first. A general discussion of subsurface flow is given next and readers who are unfamiliar with flow in porous media may prefer to review it prior to the section on PFC. A section on overland flow is given next, followed by a discussion of coupling schemes and models of coupled surface/subsurface systems. The final section identifies gaps in the literature that are addressed by this research.

5.2.1 Permeable Friction Course

5.2.1.1 Water Depth Predictions

Three authors have published predictions of water depth in PFC for straight roadway sections under constant rainfall. Ranieri (2002) gives a numerical solution to the governing equation. Tan et al. (2004) use a commercially available finite element program to model flow through PFC. Both Ranieri (2002) and Tan et al. (2004) provide charts to find the required

thickness of PFC from slope information and rainfall intensity. Charbeneau and Barrett (2008) provide an analytical solution for the saturated thickness along the flow path.

These three papers consider the same roadway geometry: a straight road with a longitudinal slope and a cross slope. The drainage slope is the Pythagorean sum of the longitudinal slope and the cross slope. In these papers, the drainage slope is a constant, making the problem one dimensional—that is the saturated thickness only varies along the drainage path. Under the assumption of constant rainfall intensity the system reaches a steady state. It is this one-dimensional steady state solution that these authors present.

A comparison of their predictions for a single point reveals that Charbeneau and Barrett (2008) and Ranieri (2002) have essentially identical results. Tan et al. obtain a different result, predicting a thinner porous layer than the other workers. The reasons for this discrepancy are difficult to uncover because Tan et al. used a commercial finite element program for analysis.

The problem of drainage within a PFC layer of constant slope and under steady rainfall is analogous the problem of hillslope seepage under constant recharge. Most solutions make the Dupuit-Forchheimer assumptions of horizontal flow with the local discharge proportional to the slope of the water table. Equivalent results to those of Charbeneau and Barrett (2008) and Ranieri (2002) have been presented by Yates, Warrick and Lomen (1985) and also by Loaiciga (2005).

Very little has been mentioned in the literature regarding the coupling between surface and subsurface flow in PFCs. Charbeneau and Barrett (2008) address the issue briefly and provide an estimate of sheet flow thickness based on the Darcy-Weisbach equation. Eck et al. (2010) refined the coupling between PFC and sheet flow by using a different boundary condition for the PFC equation. The idea was to compute the location that sheet flow begins based on the principle of continuity and use that location and the pavement thickness as the initial point to integrate the first order ODE that governs the PFC part of the problem.

5.2.2 Saturated Porous Media Flow

Saturated porous media flow refers to the movement of fluid through a porous medium when the pore space is filled with fluid. The boundary between saturated and unsaturated zones of a porous medium is the water table. The water table is at atmospheric pressure. Below the water table the media is saturated. Above the water table the media is considered unsaturated, though a small area of saturated pores may exist above the water table due to capillary effects. Quantitative predictions of saturated porous media flow apply Darcy's law or the Forchheimer equation to relate the hydraulic gradient and the specific discharge.

5.2.2.1 Darcy's Law

The usual way of characterizing flow through porous media is Darcy's law. Darcy's law states that the relationship between the hydraulic gradient and seepage velocity is linear when velocities are low enough to neglect inertia (Charbeneau, 2000). A simple statement of Darcy's law is:

$$Q = KIA \tag{5.1}$$

where Q is the volumetric flow rate, I is the hydraulic gradient, A is the cross sectional area of the flow, and K is a parameter called the hydraulic conductivity that depends on the properties of the porous medium and the fluid. Darcy's law is frequently presented in terms of the velocity obtained by dividing the flow rate by the area:

$$q = KI \tag{5.2}$$

where q is the fictitious velocity known as the Darcy velocity, or the specific discharge. The relative contributions of the porous medium and the fluid to the hydraulic conductivity can be seen by expressing the hydraulic conductivity as:

$$K = \frac{\rho g k}{\mu} \tag{5.3}$$

where ρ is the fluid density, g is the constant of gravitational acceleration, μ is the dynamic viscosity of the fluid , and k is a property of the medium called the intrinsic permeability which is related to the grain size distribution of the medium. From an analysis of the Fanning friction factor, one relationship between permeability and grain size is (Charbeneau, 2000):

$$k = \frac{d^2}{2000} \tag{5.4}$$

Bear (1972) gives several correlations between the mean or effective grain size and the intrinsic permeability. The hydraulic conductivity is typically preferred in groundwater hydrology because water is the only fluid of interest. In contrast, the petroleum industry uses the intrinsic permeability because several fluids are often of interest.

5.2.2.2 Dupuit-Forchheimer Assumptions

So far, this review has discussed several ways to predict how the hydraulic gradient (or pressure gradient) in a porous medium varies in space, but has not directly addressed the pressure distribution through the medium. In the case of flow through a PFC, the porous medium flow is always bounded above by a free surface so the flow is said to be unconfined. If the velocities are essentially horizontal, then the hydraulic head will be the same on any vertical line and the pressure distribution will be hydrostatic (Bear, 1972). In this case, the discharge is proportional to the hydraulic gradient. The assumptions that the head is independent of depth, and that the discharge is proportional to the hydraulic gradient are the Dupuit-Forchheimer assumptions (Charbeneau, 2000).

Irmay (1967) studied the error in predicting the hydraulic head using the Dupuit-Forchheimer assumptions. He gives formulas for computing the relative error at different depths for flat and inclined aquifers. For a flat aquifer, the maximum error occurs at mid depth and depends mostly on the hydraulic gradient. A hydraulic gradient of 10% caused a maximum error of 0.25% in the hydraulic head. As most roadways have a drainage slope smaller than 10%, the Dupuit-Forchheimer assumptions provide a good approximation.

5.2.3 Unsaturated Porous Media Flow

Unsaturated porous media flow occurs when the pore space is not completely filled with a single fluid. Unsaturated flow is more difficult to describe than saturated flow because the hydraulic conductivity and capillary pressure change with the water content. Richard’s equation governs unsaturated flow and considers the variation of hydraulic conductivity and capillary pressure with water content:

$$\frac{\partial \theta}{\partial t} = div\left(-K_{us}(\theta)\frac{d\Psi}{d\theta}\, grad(\theta)\right) + \frac{\partial K_{us}(\theta)}{\partial z} \tag{5.5}$$

In Richard's equation θ is the water content, Ψ is the capillary pressure head, and K_{us} is the unsaturated hydraulic conductivity (Charbeneau, 2000).

For PFC drainage, unsaturated flow is essentially vertical and the primary effect of interest is the travel time through the unsaturated zone. For this purpose, Richard's equation may be simplified by considering only vertical flow and neglecting capillary pressure gradients. This leads to the kinematic form of Darcy's law:

$$q = K_{us}(\theta) \tag{5.6}$$

where q is the specific discharge and K_{us} is the unsaturated hydraulic conductivity which depends on the water content, θ. This form of Darcy's law applies specifically to vertical flow so the hydraulic gradient is unity.

In order to apply the kinematic form of Darcy's law a relationship between the hydraulic conductivity and water content must be obtained. One such relationship is the power law model of Brooks and Corey (Charbeneau, 2000):

$$K_{us} = K\Theta^{3+2/\lambda} \tag{5.7}$$

where K_{us} is the unsaturated hydraulic conductivity, K is the saturated hydraulic conductivity, Θ is the water content assuming zero field capacity, and λ is the pore size distribution index.

Using Equations (5.6) and (5.7), Charbeneau (2000) estimates the average pore-water velocity using an average value of the water content:

$$v = \frac{G}{\theta_r + (n-\theta_r)\left(\frac{G}{K}\right)^{\frac{\lambda}{3\lambda+2}}} \tag{5.8}$$

where G is net recharge rate (assumed equal the rainfall rate for the PFC), θ_r is the irreducible water content, K is the saturated hydraulic conductivity, and λ is the pore size distribution index. With this average velocity, the travel time through the unsaturated zone can be estimated:

$$t = \frac{L}{v} \tag{5.9}$$

where L is the depth to the water table. The equations presented in this section are used in Section 5.3.2.3 to evaluate the effect of unsaturated flow in the model.

5.2.4 Overland Flow

Overland flow is governed by a simplification of the Navier-Stokes equations first presented by Saint-Venant in 1871 (Chow et al., 1988). The full Saint-Venant equations retain all of the terms of the Navier-Stokes equations including terms for inertial, viscous, and gravitational forces, along with convective accelerations. For the purpose of predicting flow at shallow depths, various levels of approximation to the Saint-Venant equations have been applied

(Chow et al., 1988). The kinematic wave approximation retains only the gravitational and viscous terms. The diffusion wave approximation adds the pressure term. The full Saint-Venant equations, with no simplifications, are known as the dynamic wave model.

Three non-dimensional parameters are important in characterizing the overland flow problem: (1) Reynolds number, (2) Froude number, (3) Kinematic wave number. Reynolds number is defined in Equation (5.10). The Froude number is defined as:

$$F = \frac{v}{\sqrt{gh}} \tag{5.10}$$

where v is the velocity, g is the gravitational constant, and h is the flow depth. The Froude number compares the speed of the flow with the speed of a gravity wave (White, 1999).

The kinematic wave number is defined as:

$$N_k = \frac{SL}{hF^2} \tag{5.11}$$

where S is the slope, L is the length, h is the depth and F is the Froude number. The symbol N_k is used here instead of the usual symbol K to avoid confusion with the saturated hydraulic conductivity. The kinematic wave number reflects the length and slope of the plane as well as the normal flow variables (Woolhiser and Liggett, 1967).

The ranges of applicability for the levels of approximation to the Saint-Venant equations are studied in terms of the Froude number and kinematic wave number by Daluz Vieira (1983). The author produced a plot showing the range of applicability for the kinematic wave, diffusion wave, and full Saint-Venant equations (Figure 5-4).

On smooth urban slopes the kinematic wave number lies between 5 and 20 (Daluz Vieira, 1983) so the diffusion wave approximation is appropriate for the full range of Froude numbers.

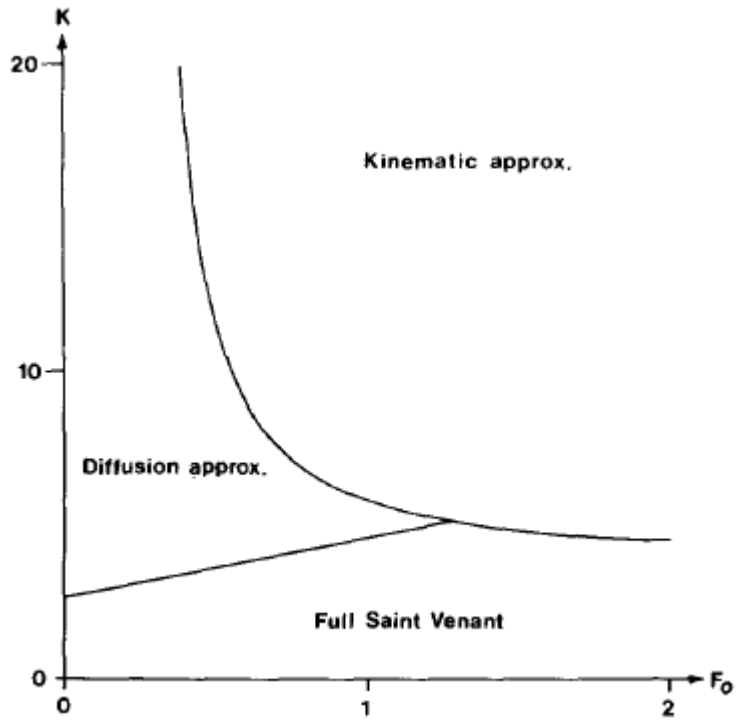

Figure 5-4: Range of applicability for sheet flow models (Daluz Vieira, 1983); used with permission

5.2.5 The CRWR Approach to Modeling Highway Drainage

The results presented in this chapter are the latest advance in a long tradition of work in highway drainage hydraulics conducted at the Center for Research in Water Resources (CRWR) at The University of Texas at Austin. The present sub-section describes how different aspects of the previous research have been incorporated into the present work.

Previous highway drainage research at CRWR has included both experimental measurements and numerical modeling. Experimental work included measuring the sheet flow thickness on a laboratory roadway section under simulated rainfall. The roadway section is rectangular and situated so that the elevation of three corners can be adjusted to achieve a range of longitudinal and cross slopes. Sheet flow thicknesses and unit discharge were measured on three surfaces having different roughness under a range of slopes and rainfall conditions. Charbeneau et al. (2009) analyzed this data and evaluated depth-discharge relationships. They concluded that Manning's equation had equivalent accuracy to logarithmic boundary layer theory, and that the hydraulic effects of rainfall on sheet flow were negligible.

Previous research at CRWR in the area of numerical modeling developed a hydrodynamic diffusion wave model for sheet flow in superelevation transitions (Jeong, 2008). Beyond implementing the diffusion wave model for sheet flow, this work developed a curvilinear grid generation scheme that is well suited for highway drainage hydraulics. The idea of the grid generation scheme is that each point along a roadway centerline lies on the circumference of a circle. The coordinates of the center of the circle may be given explicitly, or estimated from neighboring points. The radius of curvature is assumed to vary linearly along the centerline between known points. The radius of curvature is very large for straight sections and

smaller for curved sections. This approach to grid generation accommodates a wide range of roadway geometry, and gives models developed from it a consistent basis.

The superelevation transition study also formulated kinematic boundary conditions for a 2D diffusion wave model using the method of characteristics. Boundary conditions for highway drainage can be quite complicated, especially in unsteady conditions. Making the kinematic approximation is often reasonable and provides at least some dynamic behavior at drainage boundaries. Applying the method of characteristics along the drainage path allows the boundary condition to be physically reasonable, and to vary in time.

5.2.6 Coupling Schemes

The need to couple fluid behavior on the surface with that in the subsurface comes from the hydrologic cycle. Rain falls on the earth's surface as precipitation and infiltrates the soil to become groundwater. Various approaches to coupling surface and subsurface flow have been proposed. An early study by Beavers and Joseph (1967) investigated the interface region and detected a slip velocity at the interface. In hydrologic models the conductance method (Anderson and Woessner, 1992) is widely used. In this method, the flux between the phases is the gradient times the conductance. This approach is acceptable for a distinct boundary between phases, but the high surface roughness of PFC blurs this boundary. Recently, Kollet and Maxwell (2006) proposed coupling the surface and subsurface by requiring the pressure to be constant right at the land surface.

5.2.7 Coupled Surface-Subsurface Models

There many examples of hydrologic models that couple surface and subsurface flow processes. Most models focus on flow in only one phase, and use the other phase as a boundary condition. For example, in an irrigation system, the detailed solution of the groundwater system is not terribly important; the objective is a good representation of surface flow and infiltration. In the same way, subsurface flow models such as MODFLOW focus on the solution to the groundwater system, which is usually unaffected by the sheet flow dynamics. In contrast, models of entire watersheds do attempt to represent surface flow, infiltration, and subsurface flow. However, a detailed solution for overland flow is rarely found along with a detailed groundwater solution. Two notable exceptions are discussed below.

Researchers at the University of Mississippi recently published a paper entitled "Coupled Finite-Volume Model for 2D Surface and 3D Subsurface Flows" (He et al., 2008). This model couples a diffusion wave model on the surface with Richard's equation in the subsurface. The coupling is accomplished by requiring the pressure to be continuous right at the land surface. This formulation treats overland flow as a boundary to subsurface flow. The model predicts the variation of surface water depth through time over the watershed.

The MIKE-SHE model—maintained by the Danish Hydrologic Institute, Inc (DHI)—is a commercial software package for watershed simulation. The model simulates the major hydrological processes that occur in the land phase of the hydrologic cycle, including surface flow and groundwater flow (Refsgaard and Storm, 1995). For coupling between surface and subsurface phases, the program calculates the exchange flux from Darcy's law. The MIKE-SHE model has been used widely to model many watersheds and is often used to evaluate new models (e.g. He et al., 2008).

Numerous models that couple surface and subsurface processes have been reviewed by Furman (2008). In his review, Furman categorizes models according to the type of surface flow

and subsurface flow that the model uses. In his summary of 26 models, there are seven models that deal with surface flow in two dimensions—of these only one deals with the subsurface as a groundwater problem instead of only infiltration or partial saturation. The one model that does both is a unique application by Liang et al. (2007) where buildings in the floodplain are modeled as a porous medium. In their formulation, Liang et al. (2007) restrict the solution at any point in the system to either surface flow or subsurface flow. The coupling is horizontal; water from the flood wave flows laterally into the buildings.

5.3 Model Development

This section describes the development of the permeable friction course drainage code (PerfCode). A statement of the research problem is given first along with a discussion of the physical processes involved. With this basis, a mathematical formulation is developed for each physical process. A discussion of major assumptions is provided next. The mathematical models are applied on a control volume to formulate the numerical model that will provide the predictions of interest. The section concludes with a discussion of model tolerances and the technique used for the transition between sheet flow and PFC flow.

5.3.1 Problem Statement

The research problem is predicting the elevation of the water surface throughout a PFC roadway during a rainstorm. PFC is a permeable pavement placed in a 50mm layer on top of regular, impermeable pavement. During rain events, water seeps into the porous layer and flows to the side of the road by gravity. When the rainfall intensity is small, all of the drainage is contained within the pavement. Under higher rainfall intensities drainage occurs both within and on top of the pavement. The model predicts depths in both cases.

For the straight roadway shown in Figure 5-5, the road has a longitudinal slope and a cross slope. The resultant of these slopes is the drainage slope, along which water particles move to the edge of the pavement. For straight roadway sections without shoulders the problem is one dimensional along the drainage slope. However, the drainage problem becomes two-dimensional when shoulders have a different slope than the traffic lanes or when the roadway is curved. PFC is frequently used to improve driving conditions in these cases. Some specific configurations of interest are:

- Roadways with shoulders
- Curved sections
- Superelevation transitions
- Sag vertical curves

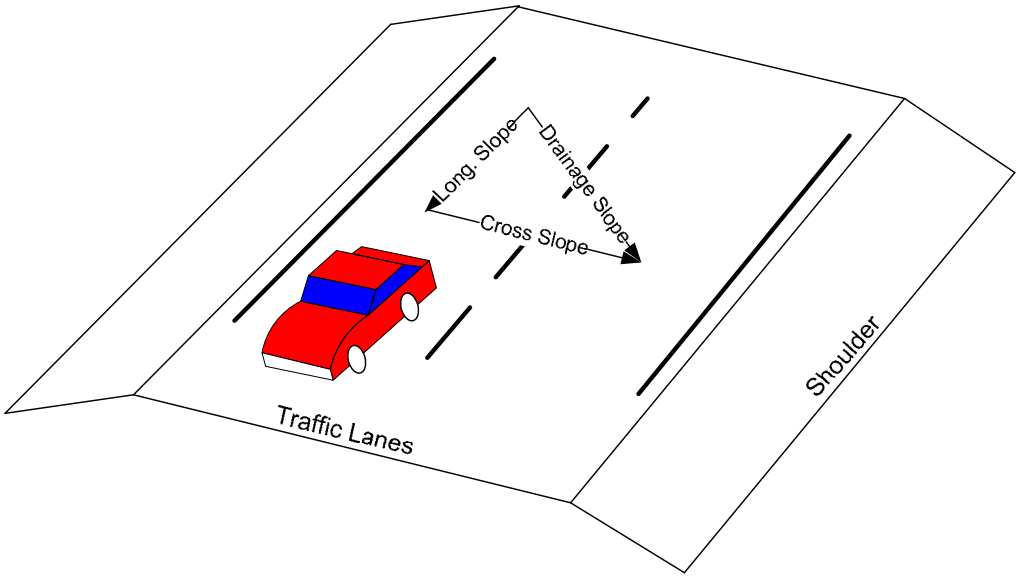

Figure 5-5: Straight roadway section

5.3.2 Physical Processes

In order to achieve the model aims, several physical processes must be considered. Modeling drainage from a PFC roadway can be considered as a specialized watershed model. As such, the physical processes may be categorized in terms of the hydrologic cycle. The hydrologic processes that occur in this system are: precipitation, evaporation, infiltration, unsaturated porous media flow, saturated porous media flow, and overland flow. One of these processes is important for the present work if it has a meaningful effect on the mass of water in the system or affects the travel time of a water particle moving through the system. The significance of each hydrologic process with respect to the model is evaluated in the following sub-sections.

5.3.2.1 Precipitation and Evaporation

Precipitation is the process by which water that has condensed in the atmosphere falls to earth. Precipitation can take the form of rain, sleet, snow or hail depending on atmospheric conditions. For the purposes of this research, rain is the only form of precipitation considered. The rainfall rate is a model input, assumed to be a known function of time.

Evaporation is the process of water changing from the liquid phase to the vapor phase. Key factors in determining the evaporation potential are the solar radiation and relative humidity (Charbeneau, 2000). In this work evaporation is neglected because most drainage occurs during or immediately following rainfall events while the relative humidity is high.

5.3.2.2 Infiltration

Infiltration is the process of rainfall entering the porous medium. Infiltration is governed by hydraulic conductivity, porosity and moisture content of the medium. For infiltration to be an important process with respect to PFC drainage, the process of water entering the pavement would have to cause a meaningful delay in the travel time of a water particle. Such a delay would cause water to pond on the pavement surface before the pore space was filled. According to the Green-Ampt method for calculating infiltration, ponding will not occur unless the rainfall intensity exceeds the hydraulic conductivity (Charbeneau, 2000). As an example, consider a five minute rainfall of one inch (2.54cm), which exceeds the 100-year 5-minute rainfall event for the

entire eastern United States (Chow et al. 1988, pg 447). Such an event corresponds to a rainfall rate of 0.0085 cm/s—far below the 1 cm/s order of PFC hydraulic conductivity. Since the hydraulic conductivity of PFC is much higher than rainfall rates, infiltration is not expected to play an important role in this problem and is neglected in the model formulation.

5.3.2.3 Unsaturated Porous Media Flow

Although infiltration occurs very quickly for a PFC, unsaturated porous media flow from the pavement surface to the water table may play an important role. To quantify the effect of this process an estimate of the travel time for a range of rainfall intensities was made using Equations (5.8) and (5.9) and the results plotted in Figure 5-6.

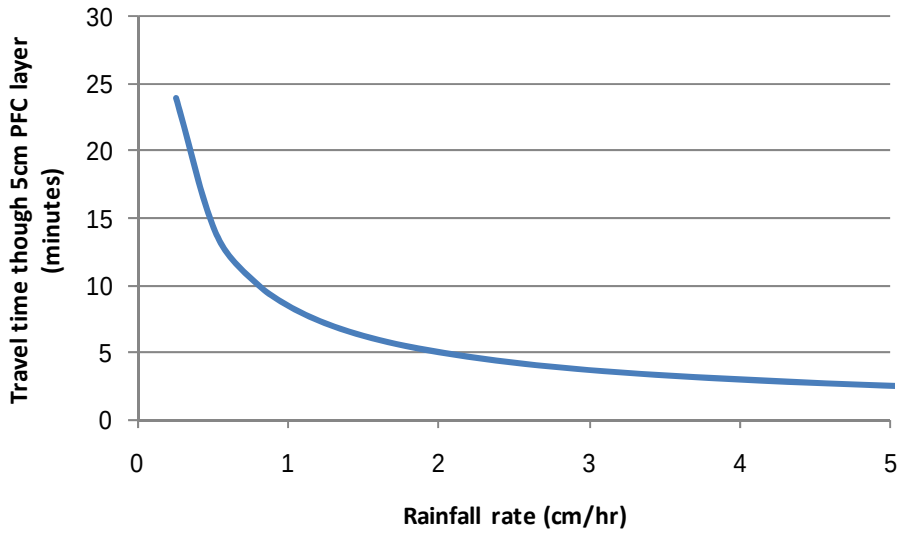

Figure 5-6: Travel time though an unsaturated PFC layer having a thickness of 5cm, irreducible water content of zero, pore size distribution index of 1.7, and a saturated hydraulic conductivity of 1 cm/s

Figure 5-6 shows that travel times are longer at lower rainfall intensities, but that the travel time is on the order of minutes. The significance of this delay depends on the model time step. Model time steps for this work are on the order of seconds, suggesting that the delay may be important. However, rainfall measurements necessarily report rainfall accumulation over a time period, frequently five or fifteen minutes. Considering the reporting period for rainfall data compared to the expected travel time, flow through the unsaturated PFC is neglected in this model.

5.3.2.4 Saturated Porous Media Flow

Saturated porous media flow refers to the movement of fluid through a porous medium when the pore space is filled with fluid. The boundary between saturated and unsaturated zones of a porous medium is the water table. At the water table, the pressure is atmospheric. Below the water table the media is saturated. Above the water table the media is considered unsaturated, though a small area of saturated pores may exist above the water table due to capillary effects. Saturated porous media flow is an essential process for the model because drainage to the edge

of pavement occurs horizontally. This model treats all of the drainage through the PFC as saturated porous media flow.

Quantitative predictions of saturated porous media flow apply Darcy's law or Forchheimer's equation to relate the hydraulic gradient and the specific discharge. This model assumes that Darcy's law characterizes PFC drainage.

5.3.2.5 Overland Flow

Overland flow is the process of water flowing on the land surface, usually in a thin layer. Hydrologists categorize overland flow as either Hortonian overland flow or saturation overland flow (Chow et al., 1988). The distinction is the source of the flow. Hortonian overland flow occurs when the rainfall rate exceeds the infiltration capacity of the surface. Saturation overland flow occurs when the subsurface becomes saturated and discharges flow onto the land surface, usually at the bottom of a hill. In PFC drainage, overland flow occurs through the latter mechanism.

Overland flow velocities are generally much higher than subsurface flow velocities because viscous forces are smaller due to differences in surface area. Because of the higher velocities, overland flow drains water more quickly from the roadway than subsurface flow. The high drainage capacity of overland flow makes it an important process for modeling drainage from PFC roadways.

5.3.2.6 Summary of Physical Processes

The physical processes that occur during drainage from a PFC roadway have been identified and evaluated. The processes of precipitation, saturated porous media flow, and overland flow were found to be important for the current work. The interaction between these processes is shown in Figure 5-7.

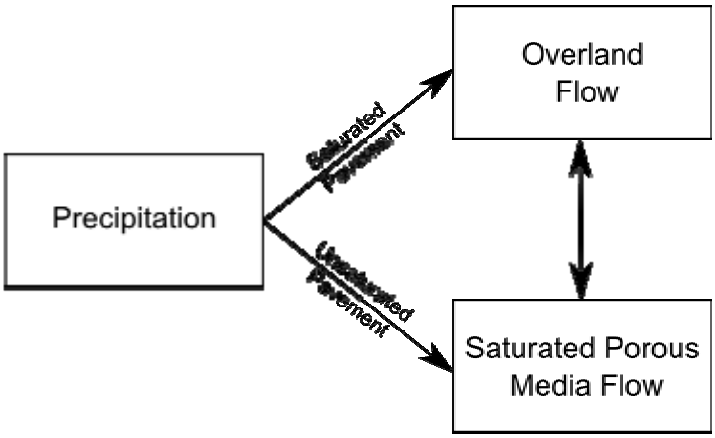

Figure 5-7: Interaction between physical processes in PerfCode

5.3.3 Mathematical Model Development

Now that the important physical processes for PFC drainage have been identified, a mathematical description of each process is needed. For the precipitation process, the variation of rainfall over time is assumed to be known so no further description is required. Models for saturated porous media flow and overland flow are developed in the following sections. A sketch

of the dimensional variables used to represent different physical quantities is shown in Figure 5-8.

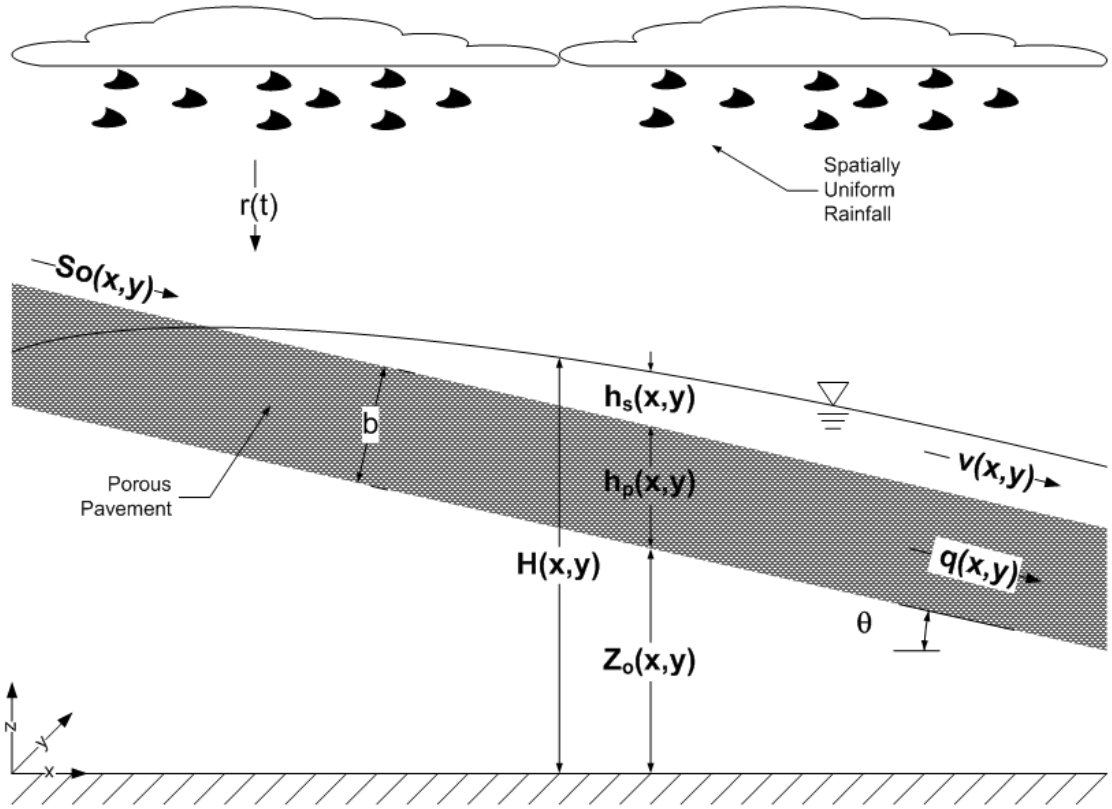

Figure 5-8: Cross section along drainage path

The rainfall rate $r(t)$ is assumed to be spatially uniform, but variable in time. The elevation of the bottom of the PFC layer with respect to a datum is $Z(x,y)$. The PFC layer has a thickness b, which is taken as constant throughout the domain. The saturated thickness of water in the PFC layer is $h_p(x,y)$ where the subscript refers to the pavement. The specific discharge through the PFC is $q(x,y)$. On the pavement surface, the thickness of sheet flow is h_s and the average velocity is $v(x,y)$. The total head of water at any point in the domain is $H(x,y)$.

5.3.3.1 Mathematical Model of Saturated Porous Media Flow

The equations of motion for saturated flow in a porous media consist of the continuity equation and the momentum equation. This development follows Halek and Svec (1979). Consider first the equation of continuity:

$$\frac{\partial q_x}{\partial x} + \frac{\partial q_y}{\partial y} + \frac{\partial q_z}{\partial z} = 0 \tag{5.12}$$

where q is the Darcy velocity in each of the coordinate directions. If the drainage slope is small enough, the only vertical fluxes are from rainfall or movement of the free surface. In the present

problem, rainfall is prescribed and the free surface position is of interest. Integrating the continuity equation over the saturated thickness gives:

$$\int_0^{h_p}\left(\frac{\partial q_x}{\partial x}+\frac{\partial q_y}{\partial y}+\frac{\partial q_z}{\partial z}\right)dz=\frac{\partial}{\partial x}\left(q_x h_p\right)+\frac{\partial}{\partial y}\left(q_y h_p\right)+q_{h_p}-q_0 \tag{5.13}$$

This integration makes use of Leibnitz's rule to interchange the order of differentiation and integration. By assuming that the PFC has no resistance to flow in the vertical direction, the effects free surface movement and rainfall may be separated into q_{hp} and q_0, respectively. The movement of the free surface (within the PFC) in time is given by $q_{h_p}=n_e\frac{\partial h_p}{\partial t}$ and the rainfall may be expressed as $q_0= r(t)$. Making these substitutions and rearranging:

$$n_e\frac{\partial h_p}{\partial t}=-\frac{\partial}{\partial x}\left(q_x h_p\right)-\frac{\partial}{\partial y}\left(q_y h_p\right)+r(t) \tag{5.14}$$

For the case of non-inertial flow, the momentum equation reduces to Darcy's law for each coordinate direction.

$$q_x=-K_x\frac{\partial H}{\partial x}, q_y=-K_y\frac{\partial H}{\partial y} \tag{5.15}$$

where q and K are the Darcy velocity and hydraulic conductivity in the coordinate directions. For the present case, horizontal anisotropy will be neglected so that $K_x=K_y=K$. Substituting Darcy's law into the vertically integrated continuity equation gives:

$$n_e\frac{\partial h_p}{\partial t}=K\left[\frac{\partial}{\partial x}\left(\frac{\partial H}{\partial x}h_p\right)+\frac{\partial}{\partial y}\left(\frac{\partial H}{\partial x}h_p\right)\right]+r(t) \tag{5.16}$$

Equation (5.16) is known as the Boussinesq equation. It describes unsteady two-dimensional flow in an unconfined porous medium with spatially uniform recharge.

5.3.3.2 Mathematical Model of Overland Flow

The following development of the mathematical model for overland flow follows that of Jeong (2008), except that the velocity is used as the primary variable rather than unit discharge. The dynamics of shallow water flow over the pavement surface are described by the Saint-Venant equations, which comprise a continuity equation and a momentum equation for each component direction. The continuity equation is expressed as:

$$\frac{\partial h_s}{\partial t}+\frac{\partial(v_x h_s)}{\partial x}+\frac{\partial\left(v_y h_s\right)}{\partial y}=r(t) \tag{5.17}$$

where h_s is the thickness of water on the surface, v is the average velocity in each coordinate direction, and $r(t)$ is the rainfall rate. The two full momentum equations are:

$$\frac{\partial(v_x h_s)}{\partial t} + \frac{\partial({v_x}^2 h_s)}{\partial x} + \frac{\partial(v_x v_y h_s)}{\partial y} + g h_s \left(Sf_x + \frac{\partial H}{\partial x}\right) = 0$$
$$\frac{\partial(v_y h_s)}{\partial t} + \frac{\partial({v_y}^2 h_s)}{\partial y} + \frac{\partial(v_x v_y h_s)}{\partial x} + g h_s \left(Sf_y + \frac{\partial H}{\partial y}\right) = 0 \quad (5.18)$$

This system of three partial differential equations may be reduced to a single equation by applying the diffusion wave approximation—neglecting local and convective accelerations. Neglecting inertial terms and dividing by $g\ h_s$ gives the simplified momentum equations:

$$S_{f_x} = -\frac{\partial H}{\partial x} \quad S_{f_y} = -\frac{\partial H}{\partial y} \quad (5.19)$$

To combine continuity and momentum into a single equation, the velocity components (v_x and v_y) must be expressed in terms of the friction slope. Manning's equation relates the velocity and friction slope as follows:

$$v = \frac{1}{n} R^{2/3} S_f^{1/2} \quad (5.20)$$

where v is the velocity, n is the Manning roughness coefficient, R is the hydraulic radius, and S_f is the friction slope. Manning's equation is a scalar equation that applies in the direction of flow. In order to apply the Manning's equation to this problem it needs to be formulated using the vector components of Equation (5.18). Inserting these components and approximating the hydraulic radius as the depth as is common for shallow flows yields:

$$\left(v_x^2 + v_y^2\right)^{1/2} = \frac{1}{n} h_s^{2/3} \left({S_f}_x^2 + {S_f}_y^2\right)^{1/2} \quad (5.21)$$

The friction slope term may also be expressed in terms of both vector components and the magnitude:

$$\left(v_x^2 + v_y^2\right)^{1/2} = \frac{1}{n} \frac{h_s^{2/3}}{\sqrt{Sf}} \left({S_f}_x^2 + {S_f}_y^2\right) \quad (5.22)$$

This formulation shows that Manning's equation can be written as the vector sum of the velocity components. Using the momentum result of Equation (5.19), the friction slope may also be written in terms of the hydraulic gradient.

$$v_x = \frac{1}{n} \frac{h_s^{2/3}}{\sqrt{S_f}} S_{f_x} = -\frac{1}{n} \frac{h_s^{2/3}}{\sqrt{S_f}} \frac{\partial H}{\partial x}$$
$$v_y = \frac{1}{n} \frac{h_s^{2/3}}{\sqrt{S_f}} S_{f_y} = -\frac{1}{n} \frac{h_s^{2/3}}{\sqrt{S_f}} \frac{\partial H}{\partial y} \quad (5.23)$$

Substituting these velocity components into the continuity equation yields a single partial differential equation that contains the essential physics of the overland flow problem.

$$\frac{\partial h_s}{\partial t} + \frac{\partial}{\partial x}\left(-\frac{1}{n}\frac{h_s^{2/3}}{\sqrt{S_f}}\frac{\partial H}{\partial x}h_s\right) + \frac{\partial}{\partial y}\left(-\frac{1}{n}\frac{h_s^{2/3}}{\sqrt{S_f}}\frac{\partial H}{\partial y}h_s\right) = r(t) \tag{5.24}$$

This equation may be simplified by lumping the non-differential terms within the spatial derivatives into a single coefficient,$D(h_s)$. Additionally, the time derivative must be converted from depth to elevation above datum. From Figure 5-8 the variables are related by $H = Z + h_p + h_s$. Taking the time derivative, dz/dt is zero and $\frac{\partial}{\partial t}h_p$ is zero when there is flow on the surface. That is, during surface flow, the saturated depth of the PFC will be equal to the pavement thickness. Making these substitutions gives the desired PDE:

$$\frac{\partial H}{\partial t} + \frac{\partial}{\partial x}\left(-D(h_s)\frac{\partial H}{\partial x}\right) + \frac{\partial}{\partial y}\left(-D(h_s)\frac{\partial H}{\partial y}\right) = r(t) \tag{5.25}$$

where $D(h_s) = \frac{1}{n}\frac{h_s^{5/3}}{\sqrt{S_f}}$ and other terms are defined previously. This approach to describing surface flow is a two-dimensional diffusion wave model.

5.3.4 Mathematical Model Assumptions

The forgoing development made simplifying assumptions about the physical system. In particular it was assumed that the saturated subsurface varies hydrostatically, that porous media flow is slow enough to neglect inertial effects, and that inertial effects can also be neglected for overland flow. Each of these assumptions is discussed in the following sections.

5.3.4.1 Dupuit-Forchheimer Assumptions

In developing the mathematical model for saturated porous media flow, it was assumed that pressure varied hydrostatically and that the subsurface discharge was proportional to the hydraulic gradient. These are the Dupuit-Forchheimer assumptions.

Irmay (1967) studied the error made in predicting the hydraulic head using the Dupuit-Forchheimer assumptions. He gives formulas for computing the relative error at different depths for flat and inclined aquifers. For a flat aquifer, the maximum error occurs at mid depth and depends mostly on the hydraulic gradient. A hydraulic gradient of 10% caused a maximum error of 0.25% in the hydraulic head. As most roadways have a drainage slope smaller than 10%, the Dupuit-Forchheimer assumptions provide a good approximation.

5.3.4.2 Diffusion Wave Approximation

The reasons for selecting the diffusion wave approximation are discussed more thoroughly in the literature review. Briefly, the diffusion wave model provides a balance between accuracy and computational efficiency. The kinematic wave approximation is too simplified because it cannot deal with adverse slopes or backwater effects. The dynamic wave model would be ideal, but comes at a high computational cost and is not expected to give substantially different results than the diffusion wave model.

5.3.5 Computational Grid

In order to implement the mathematical models of the physical processes for real roadways, a computational grid for the roadway must be developed. This research uses the same grid generation employed by Jeong (2008), which is summarized below.

The idea of the grid generation scheme is that each point along a roadway centerline lies on the circumference of a circle. The coordinates of the center of the circle may be given explicitly, or estimated from neighboring points. The radius of curvature is assumed to vary linearly along the centerline between known points. The radius of curvature is very large for straight sections and smaller for curved sections.

The center and radius of curvature can be obtained by specifying them directly as was done in this work, or by analyzing a digital elevation model as was done by Jeong (2008). In either approach, a point along the roadway centerline has the following attributes:

- Cartesian X,Y coordinates (input)
- Coordinates of center of curvature, (x_{cc}, y_{cc}) (output)
- Radius of curvature, R (output)
- Angle (from positive horizontal axis) of ray from center of curvature to centerline point, Θ (output)

Considering adjacent DEM points, the difference in radius of curvature and angular position are ΔR and $\Delta\Theta$, respectively. Using these quantities the curvilinear roadway can be mapped to a rectangular representation through the coordinate transformation functions (Jeong 2008):

$$\begin{aligned} x(\xi,\eta) &= \left(\mathrm{x_{cc1}} + \xi(\mathrm{x_{cc2}} - \mathrm{x_{cc1}})\right) + (\mathrm{R_1} + \xi\Delta\mathrm{R} + (\eta - 0.5)\mathrm{W})\cos\left(\Theta_1 + \xi\Delta\Theta\right) \\ y(\xi,\eta) &= (\mathrm{y_{cc1}} + \xi(\mathrm{y_{cc2}} - \mathrm{y_{cc1}})) + (\mathrm{R_1} + \xi\Delta\mathrm{R} + (\eta - 0.5)\mathrm{W})\sin\left(\Theta_1 + \xi\Delta\Theta\right) \end{aligned} \tag{5.26}$$

In Equation (5.26), ξ and η are parameters that range from 0 to 1; W is the width of the roadway. This equation only applies between adjacent DEM points.

The length ℓ, and width $\mathcal{w}$ of a line segment centered at the point (ξ, η) are computed using the partial derivatives of the coordinate transformation functions:

$$\begin{aligned} \ell(\xi,\eta) &= \Delta\xi\sqrt{\left(\frac{\partial x}{\partial \xi}\right)^2 + \left(\frac{\partial y}{\partial \xi}\right)^2} \\ \mathcal{w}(\xi,\eta) &= W\Delta\eta \end{aligned} \tag{5.27}$$

with $\Delta\xi = 1/N_\xi$ and $\Delta\eta = 1/N_\eta$, N being the number of elements between DEM points in each direction.

The area of a grid cell is computed from the Jacobian of the transformation functions:

$$\Delta A = J(\xi, \eta) = \begin{vmatrix} \frac{\partial x}{\partial \xi} & \frac{\partial x}{\partial \eta} \\ \frac{\partial y}{\partial \xi} & \frac{\partial y}{\partial \eta} \end{vmatrix} \tag{5.28}$$

Equations (5.27) and (5.28) provide the information needed to develop a numerical formulation in the computational space. The coordinate transformation process is depicted visually in Figure 5-9.

5.3.6 Numerical Formulation

The major goal of this research is the development of a numerical model for the drainage of water from a PFC. The Boussinesq equation and the diffusion wave model developed above provide the theoretical basis for the system of interest. However, predicting flow behavior in a real system requires that the surface and subsurface behaviors interact.

The numerical formulation uses the finite volume method with central differencing in space and the Crank-Nicolson method in time. A mass balance is developed for an interior grid cell with flux components for rainfall, subsurface flow, and surface flow. The flux across each face of the grid cell is estimated using Darcy's law and the diffusion wave model. The mass balance is initially expressed in terms of the total head at adjacent cells and then re-expressed in terms of the depth at adjacent cells.

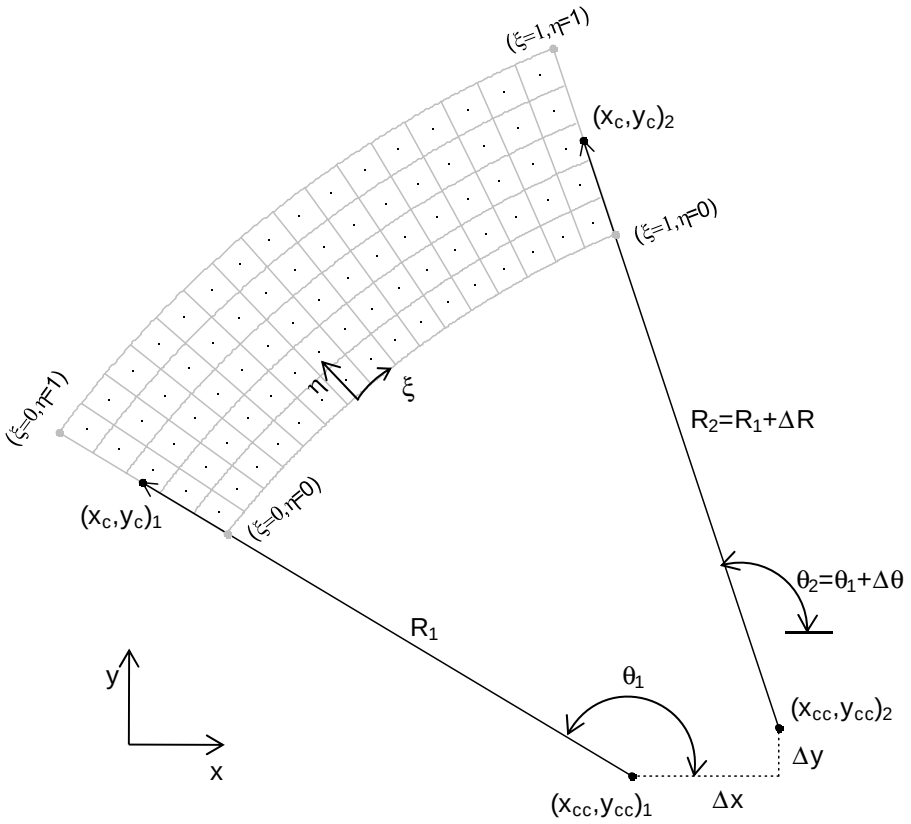

Figure 5-9: Development of computational grid from roadway geometry

5.3.6.1 Mass Balance on a Grid Cell

An interior grid cell is shown in Figure 5-11 and Figure 5-11 with horizontal dimensions in computational space. The total head for the center of the grid cell is:

$$H = z + h_p + h_s \tag{5.29}$$

where z is the elevation above the datum, h_p is the saturated thickness in the pavement and h_s is the thickness on the pavement surface. The volume of the grid cell is:

$$V = Area * Depth = \Delta A(H - z) = \Delta A(h_p + h_s) \tag{5.30}$$

The volume of *water* in the grid cell must account for the porosity, and is given by:

$$V_{H_2O} = \Delta A h_p n_e + \Delta A h_s \tag{5.31}$$

where n_e is the effective porosity of the pavement.

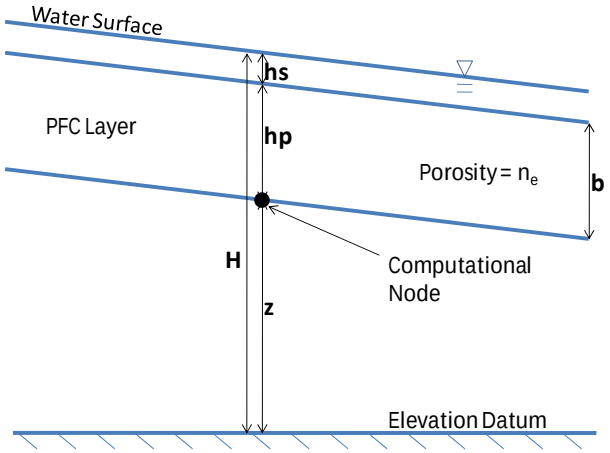

Figure 5-10: Profile view of interior grid cell

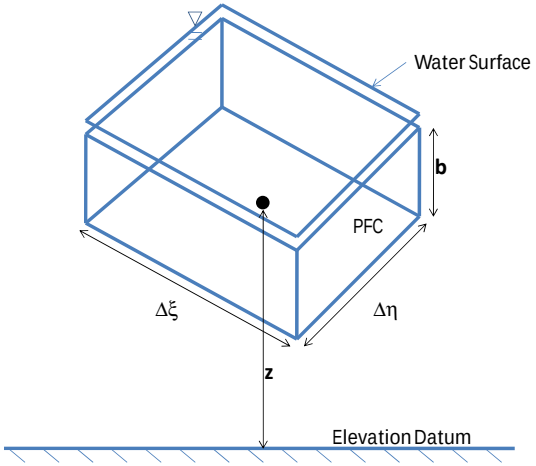

Figure 5-11: Isometric View of Interior Grid Cell

The change in volume of water in the cell over time is found from the partial derivative of Equation (5.31). This derivative must consider the physical constraint that either $\frac{\partial h_p}{\partial t}$ or $\frac{\partial h_s}{\partial t}$ will be zero at all times according to the location of the free surface with respect to the pavement surface.

$$\frac{\partial V_{H_2O}}{\partial t} = \begin{cases} \Delta A\, n_e \dfrac{\partial h_p}{\partial t} & for\ h_p < b \\ \Delta A \dfrac{\partial h_s}{\partial t} & for\ h_p \geq b \end{cases} \tag{5.32}$$

The principle of continuity states that the time rate of change of volume is equal to the net flow rate, which can be expressed mathematically as:

$$\frac{\partial V_{H_2O}}{\partial t} = Q_{in} - Q_{out} \tag{5.33}$$

The volume of water in the cell changes by rainfall, subsurface flow, and surface flow. Flow into the grid cell is considered positive. To estimate the flow rate due to each component, consider an interior control volume and its adjacent cells as in Figure 5-12. The central cell in the figure has node i, j at the center. The faces of the center cell are identified with the compass directions.

Note that the grid in computational space is uniform—each cell has the same value of $\Delta\eta$ and $\Delta\xi$ and the grid is situated so that the cell faces lie halfway between the cell centers. The grid in physical space is not uniform because cells have different lengths in the longitudinal direction according their radial position. In the figure, the subscripts of $\Delta\eta$ and $\Delta\xi$ refer to the metric coefficients, which do vary in space.

In the indexing scheme for the model, the *i* index changes longitudinally through the domain and the *j* index changes transversely. These indices are related to the compass directions within a grid cell for convenience. In terms of coordinate directions, the local north and south compass directions correspond to the positive and negative η directions.

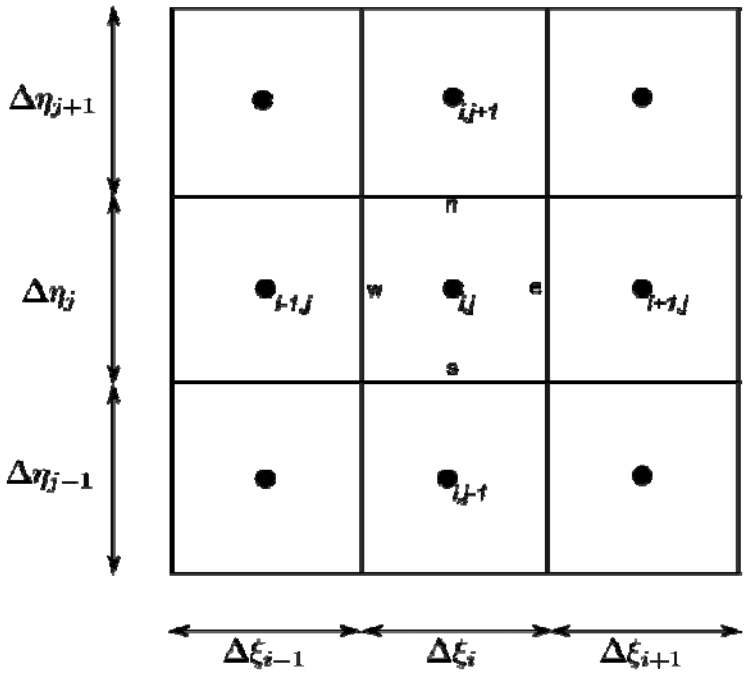

Figure 5-12: Top View of Grid in Computational Space

For cell i, j the flow rate due to rainfall is given by the rainfall intensity and the cell area:

$$Q_{rain} = r(t) * \Delta A \tag{5.34}$$

The flow rate due to subsurface flow can be estimated using Darcy's law, ($Q = KIA$), where K is the hydraulic conductivity, I is the hydraulic gradient, and A is the cross sectional area. The hydraulic gradient and cross sectional area must be estimated using the physical lengths of the cells. Considering Figure 5-12, the head gradient with respect to ξ at location w can be approximated as:

$$\left.\frac{\partial H}{\partial \xi}\right|_w = \frac{H_{i-1,j} - H_{i,j}}{1/2\,(\Delta\xi_{i-1} + \Delta\xi_i)} \tag{5.35}$$

Since ξ is dimensionless, this equation does not have the dimensions of hydraulic gradient. In order to estimate the hydraulic gradient at cell face w, cell size computed in Equation (5.27) must be used. Applying the transformation gives an estimate for the hydraulic gradient:

$$\left.\frac{\partial H}{\partial \ell}\right|_w = \frac{H_{i-1,j} - H_{i,j}}{1/2\,(\ell_{i-1,j} + \ell_{i,j})} \tag{5.36}$$

Using this formulation for the hydraulic gradient, the subsurface flow into the each face of cell i, j is expressed:

$$
\begin{aligned}
Q_{p,w} &= K\frac{H_{i-1,j}-H_{i,j}}{1/2\,(\ell_{\mathrm{i-1,j}}+\ell_{\mathrm{i,j}})}h_{p,w}w_{i,j}\\
Q_{p,e} &= K\frac{H_{i+1,j}-H_{i,j}}{1/2\,(\ell_{\mathrm{i+1,j}}+\ell_{\mathrm{i,j}})}\,h_{p,e}w_{\mathrm{i,j}}\\
Q_{p,s} &= K\frac{H_{i,j-1}-H_{i,j}}{1/2\,(w_{\mathrm{i,j-1}}+w_{\mathrm{i,j}})}\,h_{p,s}\ell_{\mathrm{i,j,s}}\\
Q_{p,n} &= K\frac{H_{i,j+1}-H_{i,j}}{1/2\,(w_{\mathrm{i,j+1}}+w_{\mathrm{i,j}})}\,h_{p,n}\,\ell_{\mathrm{i,j,n}}
\end{aligned}
\tag{5.37}
$$

Here the hydraulic gradient at the cell boundary is estimated as the difference in head divided by the distance between nodes. The cross sectional area is the saturated thickness times the length of the cell boundary. The length of the cell boundary has the same value for the east and west faces ($w_{i,j}$), but differs for the north and south faces $\left(\ell_{i,j,s}\ or\ \ell_{i,j,n}\right)$ because the radius of curvature is different.

The flow rates due to surface flow can be estimated using the diffusion wave model according to the equation:

$$
Q = V * A = \frac{1}{n}\frac{h_s^{\frac{2}{3}}}{\sqrt{S_f}}\frac{\partial H}{\partial x} * h_s\Delta\mathrm{y} \tag{5.38}
$$

Here, h_s is the thickness on the pavement surface and S_f is the magnitude of the slope of the water surface. Using the same estimate of the hydraulic gradient as for subsurface flow gives the following estimates for the flow rate into cell i,j at each of the cell boundaries.

$$
\begin{aligned}
Q_{s,w} &= \frac{1}{n}\frac{h_{s,w}^{\frac{2}{3}}}{\sqrt{S_{f,w}}}\left(\frac{H_{i-1,j}-H_{i,j}}{1/2\,(\ell_{\mathrm{i-1,j}}+\ell_{\mathrm{i,j}})}\right) * h_{s,w}w_{i,j}\\
Q_{s,e} &= \frac{1}{n}\frac{h_{s,e}^{\frac{2}{3}}}{\sqrt{S_{f,e}}}\left(\frac{H_{i-1,j}-H_{i,j}}{1/2\,(\ell_{\mathrm{i+1,j}}+\ell_{\mathrm{i,j}})}\right) * h_{s,e}w_{i,j}\\
Q_{s,s} &= \frac{1}{n}\frac{h_{s,s}^{\frac{2}{3}}}{\sqrt{S_{f,s}}}\left(\frac{H_{i-1,j}-H_{i,j}}{1/2\,(w_{\mathrm{i,j-1}}+w_{\mathrm{i,j}})}\right) * h_{s,s}\ell_{\mathrm{i,j,s}}\\
Q_{s,n} &= \frac{1}{n}\frac{h_{s,n}^{\frac{2}{3}}}{\sqrt{S_{f,n}}}\left(\frac{H_{i-1,j}-H_{i,j}}{1/2\,(w_{\mathrm{i,j+1}}+w_{\mathrm{i,j}})}\right) * h_{s,n}\ell_{\mathrm{i,j,n}}
\end{aligned}
\tag{5.39}
$$

Now that flow rates for each cell boundary have been developed, the water balance on a grid cell can be expressed in terms of the flow rates. All of the flow rates are formulated as being positive because of the arrangement of the $H_{i,j}$ term. If the head in cell i,j is lower than the cell it is subtracted from, water will flow into cell i,j. The flow rates were formulated this way to make it easier to check the equations. For the 2D case, the mass balance has nine flow components:

$$\frac{\partial V_{H_2O}}{\partial t} = Q_{p,w} + Q_{s,w} + Q_{p,e} + Q_{s,e} + Q_{p,s} + Q_{s,s} + Q_{p,n} + Q_{s,n} + Q_{rain}$$

or (5.40)

$$\frac{\partial V_{H_2O}}{\partial t} = Q_{p,w} + Q_{s,w} + Q_{p,e} + Q_{s,e} + Q_{rain}$$

Substituting the flow rates for rainfall, subsurface, and surface flow into the continuity equation gives a mass balance for an interior grid cell:

$$\begin{aligned}\frac{\partial V_{H_2O}}{\partial t} = \\ K\frac{H_{i-1,j} - H_{i,j}}{1/2\left(\ell_{\mathrm{i-1,j}} + \ell_{\mathrm{i,j}}\right)} h_{p,w} w_{i,j} + \frac{1}{n}\frac{h_{s,w}^{\frac{2}{3}}}{\sqrt{S_{f,w}}}\left(\frac{H_{i-1,j} - H_{i,j}}{1/2\left(\ell_{\mathrm{i-1,j}} + \ell_{\mathrm{i,j}}\right)}\right) * h_{s,w} w_{i,j} \\ + K\frac{H_{i+1,j} - H_{i,j}}{1/2\left(\ell_{\mathrm{i+1,j}} + \ell_{\mathrm{i,j}}\right)} h_{p,e} w_{\mathrm{i,j}} + \frac{1}{n}\frac{h_{s,e}^{\frac{2}{3}}}{\sqrt{S_{f,e}}}\left(\frac{H_{i-1,j} - H_{i,j}}{1/2\left(\ell_{\mathrm{i+1,j}} + \ell_{\mathrm{i,j}}\right)}\right) * h_{s,e} w_{i,j} \\ + K\frac{H_{i,j-1} - H_{i,j}}{1/2\left(w_{\mathrm{i,j-1}} + w_{\mathrm{i,j}}\right)} h_{p,s} \ell_{\mathrm{i,j,s}} + \frac{1}{n}\frac{h_{s,s}^{\frac{2}{3}}}{\sqrt{S_{f,s}}}\left(\frac{H_{i-1,j} - H_{i,j}}{1/2\left(w_{\mathrm{i,j-1}} + w_{\mathrm{i,j}}\right)}\right) * h_{s,s} \ell_{\mathrm{i,j,s}} \\ + K\frac{H_{i,j+1} - H_{i,j}}{1/2\left(w_{\mathrm{i,j+1}} + w_{\mathrm{i,j}}\right)} h_{p,n}\, \ell_{\mathrm{i,j,n}} + \frac{1}{n}\frac{h_{s,n}^{\frac{2}{3}}}{\sqrt{S_{f,n}}}\left(\frac{H_{i-1,j} - H_{i,j}}{1/2\left(w_{\mathrm{i,j+1}} + w_{\mathrm{i,j}}\right)}\right) * h_{s,n} \ell_{\mathrm{i,j,n}} \\ + r(t) * \Delta\mathrm{A}\end{aligned} \quad (5.41)$$

Equation (5.41) contains four dependent variables: $V_{H_2O}, H, h_p, and\ h_s$. A fifth variable, the total thickness h, may be formed as the sum of the thickness in the pavement and the thickness on the surface.

$$h = h_p + h_s \quad (5.42)$$

So the total head is:

$$H = z + h \quad (5.43)$$

In order to solve the problem, Equation (5.41) must be expressed in terms of the total head or total thickness. Choosing the total head is perhaps more intuitive, and makes the equations simpler, but the total thickness is a better choice numerically because it avoids subtracting two large numbers (the elevation being much larger than the total thickness). The equation will be expressed first in terms of the head, and then expressed again in terms of the thickness.

5.3.6.2 Formulation using Total Head

To express the equations in terms of the head, h_s , h_p and S_f must be expressed at the cell center and the boundaries in terms of H. Each of these terms will be examined in turn, starting

with those on right hand side of Equation (5.41). In the development, it will also be convenient to define conveyance coefficients and a porosity function.

Saturated Thickness and Sheet Flow Depth

The saturated thickness at the grid cell boundaries—$h_{p,*}$—can be estimated from the total head at the cell centers by linear interpolation. Since the computational grid is evenly spaced, the interpolation is just the average of the head values. To find the saturated thickness at the boundary, the total head at the cell boundary is estimated from the adjacent nodes, and the elevation at the boundary is subtracted to give the saturated thickness:

$$\begin{aligned} h_{p,w} &= \frac{\mathrm{H_{i,j}}\ell_{i-1,j} + H_{i-1,j}\ell_{i,j}}{\ell_{i,j} + \ell_{i-1,j}} - z_w \\ h_{p,e} &= \frac{\mathrm{H_{i,j}}\ell_{i+1,j} + H_{i+1,j}\ell_{i,j}}{\ell_{i,j} + \ell_{i+1,j}} - z_e \\ h_{p,s} &= \frac{\mathrm{H_{i,j}}w_{i,j-1} + H_{i,j-1}w_{i,j}}{w_{i,j} + w_{i,j-1}} - z_s \\ h_{p,n} &= \frac{\mathrm{H_{i,j}}w_{i,j+1} + H_{i,j+1}w}{w_{i,j} + w_{i,j+1}} - z_n \end{aligned} \tag{5.44}$$

The surface flow thickness at the grid cell boundaries—$h_{s,*}$—is estimated in the same way as the saturated thickness. The elevation at the cell boundary and the PFC thickness are subtracted from the interpolated total head at the boundary to give an estimate of the thickness of sheet flow:

$$\begin{aligned} h_{s,w} &= \frac{\mathrm{H_{i,j}}\ell_{i-1,j} + H_{i-1,j}\ell_{i,j}}{\ell_{i,j} + \ell_{i-1,j}} - z_w - b \\ h_{s,e} &= \frac{\mathrm{H_{i,j}}\ell_{i+1,j} + H_{i+1,j}\ell_{i,j}}{\ell_{i,j} + \ell_{i+1,j}} - z_e - b \\ h_{s,s} &= \frac{\mathrm{H_{i,j}}w_{i,j-1} + H_{i,j-1}w_{i,j}}{w_{i,j} + w_{i,j-1}} - z_s - b \\ h_{s,n} &= \frac{\mathrm{H_{i,j}}w_{i,j+1} + H_{i,j+1}w}{w_{i,j} + w_{i,j+1}} - z_n - b \end{aligned} \tag{5.45}$$

The approximations given in Equation (5.44) and (5.45) must consider the physical constraints on and interdependence of the saturated thickness and surface thickness. The saturated thickness must be greater than or equal to zero and less than or equal to the thickness of the PFC layer. The surface thickness must be positive, and must be zero when the saturated thickness is less than the thickness of the PFC layer. These constraints are expressed mathematically as:

$$\begin{aligned} 0 \le h_p \le b \\ h_s = 0\ for\ h_p < b \end{aligned} \tag{5.46}$$

These constraints are imposed on the estimates of thickness at the cell boundaries using minimum and maximum functions. Examples of how these functions are used are given for the western boundary. The other boundaries are calculated in a similar way.

$$h_{p,w} = \min\left(b\,;\ \frac{\mathrm{H_{i,j}}\ell_{i-1,j} + H_{i-1,j}\ell_{i,j}}{\ell_{i,j} + \ell_{i-1,j}} - z_w\right)$$
$$h_{s,w} = \max\left(0\,;\ \frac{\mathrm{H_{i,j}}\ell_{i-1,j} + H_{i-1,j}\ell_{i,j}}{\ell_{i,j} + \ell_{i-1,j}} - z_w - b\right) \tag{5.47}$$

Use of these functions means that the overall mass balance equation is no longer smooth in the mathematical sense; however the physical system under consideration is not smooth either. There is a shift in the behavior of the system when the PFC layer becomes saturated and sheet flow begins, or when sheet flow disappears into the pavement because the rainfall intensity decreased. The minimum and maximum functions have the advantages of ease implementation in a numerical scheme and of facilitating the use of a single equation to describe subsurface flow and combined surface/subsurface flow.

Friction Slope

By the Dupuit-Forchheimer assumptions, the friction slope is the same as the hydraulic gradient. This is a vector quantity, so the component in each coordinate direction will be estimated. Estimates of the component in the proper direction and the overall magnitude are needed for the sheet flow part of the problem.

The ξ-component of the friction slope at the middle of the west and east faces are computed from the node values of neighboring cells.

$$S_{f\xi,w} = \frac{H_{i-1,j} - H_{i,j}}{1/2\,(\ell_{\mathrm{i-1,j}} + \ell_{\mathrm{i,j}})}$$
$$S_{f\xi,e} = \frac{H_{i+1,j} - H_{i,j}}{1/2\,(\ell_{\mathrm{i+1,j}} + \ell_{\mathrm{i,j}})} \tag{5.48}$$

Similarly, the η-component of the friction slope at the middle of the south and north faces are computed from the node values of neighboring cells.

$$S_{f\eta,s} = \frac{H_{i,j-1} - H_{i,j}}{1/2\,(w_{\mathrm{i,j-1}} + w_{\mathrm{i,j}})}$$
$$S_{f\eta,n} = \frac{H_{i,j+1} - H_{i,j}}{1/2\,(w_{\mathrm{i,j+1}} + w_{\mathrm{i,j}})} \tag{5.49}$$

The other friction slope component for each face is found from a weighted average of the component in that direction from the nearest four faces where it was computed. This means the η-component at the western face is estimated as the weighted average of the η-component at the north and south faces of the central cell and its western neighbor.

$$S_{f\eta,w} = \frac{(S_{f\eta,n} + S_{f\eta,s})\ell_{i-1,j} + \left(S_{f\eta,n} + S_{f\eta,s}\right)_{i-1}\ell_{i,j}}{2(\ell_{i,j} + \ell_{i-1,j})}$$
$$S_{f\eta,e} = \frac{(S_{f\eta,n} + S_{f\eta,s})\ell_{i+1,j} + \left(S_{f\eta,n} + S_{f\eta,s}\right)_{i+1}\ell_{i,j}}{2(\ell_{i,j} + \ell_{i+1,j})} \tag{5.50}$$

The ξ-component of the friction slope at the southern and northern faces is estimated in a similar way:

$$S_{f\xi,n} = \frac{\left(S_{f\xi,e} + S_{f\xi,w}\right)w_{i,j+1} + \left(S_{f\xi,e} + S_{f\xi,w}\right)_{i,j+1}w_{i,j}}{2\left(w_{i,j} + w_{i,j+1}\right)} \tag{5.51}$$

Note that Equations (5.50) and (5.51) could equivalently use the metric coefficients corresponding to each cell face rather than the actual lengths and widths. The magnitude of the total friction slope at any location is the Pythagorean sum of the components.

$$S_{f,w} = \sqrt{{S_{f\xi,w}}^2 + {S_{f\eta,w}}^2} \tag{5.52}$$

Conveyance Coefficients

Now that all of the terms on the right hand side of the mass balance given in Equation (5.41) are expressed in terms of the total head, we return to the overall equation. Collecting like terms and dividing by the cell area gives the model equation where terms in square brackets are defined to be conveyance coefficients:

$$\begin{aligned}\frac{1}{\Delta A}\frac{\partial \forall_{H_2O}}{\partial t} = &\left[\left(K * h_{p,w} + \frac{1}{n}\frac{h_{s,w}^{\frac{5}{3}}}{\sqrt{S_{f,w}}}\right)\left(\frac{2w_{i,j}}{\ell_{i-1,j} + \ell_{i,j}}\right)\left(\frac{1}{\Delta A}\right)\right] * \left(H_{i-1,j} - H_{i,j}\right) \\ &+ \left[\left(K * h_{p,e} + \frac{1}{n}\frac{h_{s,e}^{\frac{5}{3}}}{\sqrt{S_{f,e}}}\right)\left(\frac{2w_{i,j}}{\ell_{i+1,j} + \ell_{i,j}}\right)\left(\frac{1}{\Delta A}\right)\right] * \left(H_{i+1,j} - H_{i,j}\right) \\ &+ \left[\left(K * h_{p,s} + \frac{1}{n}\frac{h_{s,s}^{\frac{5}{3}}}{\sqrt{S_{f,s}}}\right)\left(\frac{2l_{i,j}}{w_{\mathrm{i,j-1}} + w_{\mathrm{i,j}}}\right)\left(\frac{1}{\Delta A}\right)\right] \\ &* \left(H_{i,j-1} - H_{i,j}\right) \\ &+ \left[\left(K * h_{p,n} + \frac{1}{n}\frac{h_{s,n}^{\frac{5}{3}}}{\sqrt{S_{f,n}}}\right)\left(\frac{2l_{i,j}}{w_{\mathrm{i,j+1}} + w_{\mathrm{i,j}}}\right)\left(\frac{1}{\Delta A}\right)\right] \\ &* \left(H_{i,j+1} - H_{i,j}\right)\end{aligned} \tag{5.53}$$

In Equation (5.53) the terms in square brackets are conveyance coefficients. There is a conveyance coefficient for each face of the grid cell. The thickness estimates at the cell boundary appear only in the conveyance coefficient. Substituting the thickness estimates of Equation (5.47) yields the final conveyance coefficients for the faces. The conveyance coefficient for the western boundary is:

$$C_w = \left(\begin{array}{l} K * \min\left(b\,;\ \dfrac{\mathrm{H_{i,j}}\ell_{i-1,j} + H_{i-1,j}\ell_{i1,j}}{\ell_{i,j} + \ell_{i-1,j}} - z_w \right) \\ \\ + \dfrac{1}{n} \dfrac{\max\left(0\,;\ \dfrac{\mathrm{H_{i,j}}\ell_{i-1,j} + H_{i-1,j}\ell_{i1,j}}{\ell_{i,j} + \ell_{i-1,j}} - z_w - b \right)^{\frac{5}{3}}}{\sqrt{S_{f,w}}} \end{array} \right) \left(\frac{2w_{i,j}}{\ell_{i-1,j} + \ell_{i,j}} \right) \left(\frac{1}{\Delta A} \right) \quad (5.54)$$

Conveyance coefficients allow the mass balance equation to be expressed more concisely:

$$\begin{aligned} \frac{1}{\Delta A}\frac{\partial \forall_{H_2O}}{\partial t} = {} & C_w * \left(H_{i-1,j} - H_{i,j} \right) + C_e * \left(H_{i+1,j} - H_{i,j} \right) + C_s * \left(H_{i,j-1} - H_{i,j} \right) \\ & + C_n * \left(H_{i,j+1} - H_{i,j} \right) + r(t) \end{aligned} \quad (5.55)$$

Porosity Function

With the right hand side of the mass balance expressed in terms of the total head we turn to the left hand side of Equation (5.55) and recall that the volume of water in a grid cell must consider the porosity of the PFC. Considering Equation (5.32), the left hand side of Equation Equation (5.55) can be expressed as:

$$\frac{1}{\Delta A}\frac{\partial \forall_{H_2O}}{\partial t} = \begin{cases} n_e \dfrac{\partial h_p}{\partial t} & for\ h_p < b \\ \dfrac{\partial h_s}{\partial t} & for\ h_p \geq b \end{cases} \quad (5.56)$$

The constraints on h_p and h_s are imposed by the physical system are that either $\frac{\partial h_p}{\partial t}$ or $\frac{\partial h_s}{\partial t}$ will be zero at all times. In other words the time derivative of the total head, $\frac{\partial H}{\partial t}$, will be completely given by $\frac{\partial h_p}{\partial t}$ when the flow is contained within the pavement. For the case of combined surface/subsurface flow, the pavement is saturated, therefore the saturated thickness is constant and $\frac{\partial h_p}{\partial t}$ is zero, leaving changes in the total head to the surface component. Table 5.1 summarizes these cases.

Table 5.1: Flow Cases

	Flow Condition	Time Derivative of Total Head	Left Hand Side of Mass Balance
Case 1	Flow completely within pavement	$\frac{\partial H}{\partial t} = \frac{\partial h_p}{\partial t}$	$n_e \frac{\partial h_p}{\partial t}$
Case 2	Combined surface/subsurface flow	$\frac{\partial H}{\partial t} = \frac{\partial h_s}{\partial t}$	$\frac{\partial h_s}{\partial t}$

The difference between these flow conditions is reflected in the mass balance equation through the porosity. When the water is contained in the pavement, changes in the volume of water in the grid cell are reflected in the head through the porosity. Consider for example, a cell having an area of 1 square meter that receives 1 mm of rainfall and has no other fluxes. In either case 1 or case 2 the volume of water in the cell increases by 1 liter. In case 1 the total head increases by $1mm/n_e$, while in case 2 the head increases by only 1mm.

To combine the time derivatives into a single term, we must apply the porosity to the right hand side based on the flow condition. For this purpose a "porosity function" is defined to accomplish switching between the phases. This function says to divide by the porosity if the flow is contained within the pavement, but not change anything if the pavement is saturated.

$$pf(H, z, b, n_e) = \begin{cases} 1 & for\ H - z \geq b \\ 1/n_e & for\ H - z < b \end{cases} \tag{5.57}$$

Model Equation in terms of Total Head

With the use of the porosity function, we can combine the time derivatives of thickness into the time derivative of total head, and express the mass balance for a grid cell in terms of the total head and problem parameters. The equation is arranged in order of the bands that appear in the coefficient matrix.

$$\frac{\partial H}{\partial t} = pf * [C_w H_{i-1,j} + C_s H_{i,j-1} - (C_w + C_s + C_n + C_e) H_{i,j} + C_n H_{i,j+1} + C_e H_{i+1,j} + r(t)] \tag{5.58}$$

Equation (5.58) accomplishes the goals set out for this numerical formulation. The mass balance is expressed in terms of the total head at the center of a grid cell and a single equation applies for both subsurface flow and combined surface/subsurface flow. When the saturated thickness (h_p) is less than the thickness of the PFC layer, the porosity function is active, the max function removes the surface flow part of the conveyance coefficient, and Equation (5.58) reduces to the Boussinesq equation. When the saturated thickness is equal to or greater than the thickness of the PFC layer, the porosity function turns off, the minimum function forces the saturated thickness to the PFC layer thickness, and the surface flow part of the conveyance coefficient is non-zero.

5.3.6.3 Depth Formulation, Time Discretization, Linearization

As mentioned earlier, the discretized equations will now be re-expressed in terms of the thickness rather than the total head. This is accomplished by making the substitution $H = h + z$. The time derivative converts directly because the elevation does not change in time.

$$\begin{aligned}\frac{\partial h_{i,j}}{\partial t} = \; pf * [&C_w(h+z)_{i-1,j} + C_s H(h+z)_{i,j-1} \\ &- (C_w + C_s + C_n + C_e)(h+z)_{i,j} + C_n(h+z)_{i,j+1} \\ &+ C_e(h+z)_{i+1,j} + r(t)]\end{aligned} \tag{5.59}$$

To solve Equation (5.59) the time dimension is discretized using the Crank-Nicolson method. The resulting non-linear system is linearized by lagging the conveyance coefficients using an inner iteration loop. The Crank-Nicolson method is summarized as follows, using the superscript n as the time level (Ferziger and Peric, 2002).

$$\frac{h_{i,j}^{n+1} - h_{i,j}^{n}}{\Delta t} = \frac{1}{2}[\,RHS]^{n+1} + \frac{1}{2}[\,RHS]^{n} \tag{5.60}$$

Now the system is arranged for solving as a linear system by moving the unknowns—the depths at time level $n + 1$—to the left side of the equation and moving the known quantities to the right.

$$h_{i,j}^{n+1} - \frac{\Delta t}{2}[\,RHS\,]^{n+1} = \frac{\Delta t}{2}[\,RHS\,]^{n} + h_{i,j}^{n} \tag{5.61}$$

Let A, B, C, D, E be the bands of the penta-diagonal coefficient matrix and F be the right side of the linear system, or force vector. A linear index is needed to relate grid points using i, j indices to a single index for the matrix system. The linear index is formed by numbering the grid cells consecutively along the columns starting in the southwest corner of the domain. Taking the largest value of the domain column index as j_{max} the linear index k for any grid cell is computed from:

$$k(i,j) = (i-1) * j_{max} + j \tag{5.62}$$

Using the linear index, the system can be written as:

$$A_k\, h_{k-j_{max}}^{n+1} + B_k\, h_{k-1}^{n+1} + C_k\, h_k^{n+1} + D_k\, h_{k+1}^{n+1} + E_k\, h_{k+j_{max}}^{n+1} = F_k \tag{5.63}$$

where the expressions for the matrix coefficients are (with the conveyance coefficients at the n+1 level):

$$
\begin{aligned}
A_k &= -\frac{\Delta t}{2} * pf * {C_w}^{n+1} \\
B_k &= -\frac{\Delta t}{2} * pf * {C_s}^{n+1} \\
C_k &= \frac{\Delta t}{2} * pf * \left({C_w}^{n+1} + {C_s}^{n+1} + {C_n}^{n+1} + {C_e}^{n+1}\right) + 1 \\
D_k &= -\frac{\Delta t}{2} * pf * {C_n}^{n+1} \\
E_k &= -\frac{\Delta t}{2} * pf * {C_e}^{n+1}
\end{aligned}
\tag{5.64}
$$

The right hand side of the system is:

$$
\begin{aligned}
F_k = \; & pf^n \, \frac{\Delta t}{2} \left\{ \begin{array}{c} C_w h_{i-1,j} + C_s h_{i,j-1} - \\ (C_w + C_s + C_n + C_e) h_{i,j} + \\ C_n h_{i,j+1} + C_e h_{i+1,j} + \\ C_w z_{i-1,j} + C_s z_{i,j-1} - \\ (C_w + C_s + C_n + C_e) z_{i,j} + \\ C_n z_{i,j+1} + C_e z_{i+1,j} + \; r(t) \end{array} \right\}^n + h_{i,j}^n \\
& + pf^{n+1} \, \frac{\Delta t}{2} \left\{ \begin{array}{c} C_w z_{i-1,j} + C_s z_{i,j-1} - \\ (C_w + C_s + C_n + C_e) z_{i,j} + \\ C_n z_{i,j+1} + C_e z_{i+1,j} + r(t) \end{array} \right\}^{n+1}
\end{aligned}
\tag{5.65}
$$

Note that the value of in each band for an interior grid cell depends upon the four cells on its borders and on itself so the computational molecule is comprised of five cells and the coefficient matrix is penta-diagonal.

The values of the coefficient matrix (A, B, C, D, E) depend on the conveyance coefficients, which in turn depend on the unknown thicknesses so the system of equations is non-linear. Linearization is accomplished using the fixed point method—conveyance coefficients are computed using old values of the depths and these coefficients are then used to compute new depths (Ferziger and Peric, 2002). The new depths are used to update the conveyance coefficients and this process is repeated until values of the depths stop changing within the iteration. At each iteration, the linearized system of equations is solved using the Gauss-Seidel method for solving linear systems of equations.

5.3.7 Initial Conditions and Boundary Conditions

Solution of the governing equations requires suitable initial conditions and boundary conditions. In the following sections initial conditions are discussed first, followed by the no-flow boundary condition. The subsequent section proposes a new boundary condition for PFC flow—the kinematic condition. A formulation for kinematic boundary conditions in the case of sheet flow is also given, followed by an algorithm combining the kinematic condition for PFC and sheet flow.

5.3.7.1 Initial Conditions

The initial condition for the entire system is that of zero depth, corresponding to a PFC roadway that is completely dry at the onset of rainfall. Any known depth could theoretically be used as an initial condition, but the zero depth condition arises frequently in practice.

5.3.7.2 No Flow Boundaries

A no flow boundary is a Neumann type condition because the derivative is specified at the boundary. For a no-flow boundary, the conveyance coefficient for the cell face corresponding to the boundary is set to zero, effectively enforcing the condition of a zero head gradient.

$$\frac{dH}{d\eta} = 0 \tag{5.66}$$

Considering Equation (5.53), which shows the conveyance coefficients in brackets, setting the conveyance coefficient equal to zero is equivalent to the zero gradient condition. Note that this approach works for PFC flow and sheet flow.

5.3.7.3 Kinematic Boundary Conditions for PFC Flow

Boundary conditions other than no-flow boundaries are difficult to formulate for PFC roadways. Boundary conditions are classified as Dirichlet type when the solution is prescribed at the boundary, Neumann type when the first derivative is specified at the boundary and as Robin type when some combination of the solution and its derivative are specified at the boundary (Kreyszig, 1999). Formulating boundary conditions for PFC flow—especially under unsteady conditions—is difficult because the solution at the boundary varies according to the external forcing (rainfall), the solution within the domain, and the geometry of the domain itself. In addition, the boundary condition should be able to transition back and forth between sheet flow conditions.

Strictly speaking, the edge of a PFC is a seepage face because the pressure at any point along the edge is atmospheric. Treating the edge of pavement as a seepage surface is problematic for at least two reasons: (1) the velocity field near a seepage face has a strong vertical component (see the experiments of Simpson et al. 2003) but the model equation excludes vertical velocities; and (2) the Dupuit-Forchheimer assumptions on which the model is based do not allow for a seepage surface since they require the pressure to vary along a vertical line.

As a way to overcome these challenges it is desirable to specify the saturated thickness at the center of a boundary grid cell based on the forcing, geometry, and solution from the previous time step. The center of a boundary cell is a nodal unknown, the value of which is referred to by the adjacent cells. Specifying the value at such a location is a Dirichlet condition because the value of the solution is prescribed.

The following formulation develops a new method for specifying boundary conditions to a Dupuit-Forchheimer flow model. The principle assumption is that of kinematic flow. In the following three subsections, the algorithm is developed for a linear roadway; the effect of the algorithm on the steady state solution is investigated; and the applicability to curved roads is assessed.

Linear Roadways

The saturated thickness at the center of a boundary cell may be estimated by applying the method of characteristics (MOC) to the PDE for one-dimensional flow under kinematic conditions. The MOC is a mathematical solution technique for PDEs of first-order and for hyperbolic PDEs of second-order (Street, 1973). The concept of kinematic flow refers to the case where pressure and acceleration are neglected in the momentum equation.

The continuity equation for flow in a porous medium under unsteady conditions and with a free surface is given by Equation (5.14); considering only the x direction the equation becomes

$$n_e \frac{\partial h}{\partial t} + \frac{\partial}{\partial x}(q * h) = r \tag{5.67}$$

where n_e is the effective porosity, h is the saturated thickness, r is the rainfall rate and the Darcy velocity is

$$q = -K\frac{\partial H}{\partial x} = -K\frac{\partial h}{\partial x} - KS_0 \tag{5.68}$$

Making this substitution and expanding the terms gives

$$n_e \frac{\partial h}{\partial t} - Kh\frac{\partial^2 h}{\partial x^2} - K\left(\frac{\partial h}{\partial x}\right)^2 - KS_0\frac{\partial h}{\partial x} = r \tag{5.69}$$

The assumption of kinematic conditions means that the depth gradient is neglected in the Darcy velocity, which removes the higher order terms in Equation (5.69) and gives

$$n_e \frac{\partial h}{\partial t} - KS_0\frac{\partial h}{\partial x} = r \tag{5.70}$$

Removing the higher order terms destroys the parabolic nature of the PDE. This is not a typical approximation for porous media flow and does introduce some error in the solution. However, neglecting these terms allows the formulation of a boundary algorithm that considers the problem parameters and can transition smoothly to sheet flow conditions.

The MOC procedure given by Street (1973) is followed here. The solution of Equation (5.70) can be considered as a surface in $x, t, h(x,t)$ space. The tangent plane to the surface is given by the total differential

$$dh = \frac{\partial h}{\partial t}dt + \frac{\partial h}{\partial x}dx \tag{5.71}$$

and the normal vector to this tangent plane is $(\frac{\partial h}{\partial t}, \frac{\partial h}{\partial x}, -1)$. This normal vector is tangent to the vector $(n_e, -KS_0, r)$because their dot product is zero by Equation (5.70).

$$\left(\frac{\partial h}{\partial t}, \frac{\partial h}{\partial x}, -1\right) \cdot (n_e, -KS_0, r) = n_e \frac{\partial h}{\partial t} - KS_0 \frac{\partial h}{\partial x} - r = 0 \tag{5.72}$$

The vector $(n_e, -KS_0, r)$ must be tangent to the solution surface because it is orthogonal to the surface normal. A position vector for a point on the solution surface can also be represented parametrically as $(x(s), t(s), h(s))$. Its tangent vector is $\left(\frac{dx}{ds}, \frac{dt}{ds}, \frac{dh}{ds}\right)$. The fact that components of the tangent vectors must be proportional leads to the MOC formulation of the problem:

$$\frac{(d\,x/ds)}{n_e} = \frac{(d\,t/ds)}{-KS_0} = \frac{(d\,h/ds)}{r} \tag{5.73}$$

This formulation is usually presented after ds has been eliminated from the equations:

$$\frac{dt}{n_e} = \frac{dx}{-KS_0} = \frac{dh}{r} \tag{5.74}$$

To obtain a Dirichlet type boundary condition for the domain, we need to estimate the saturated thickness in the boundary cell at the new time level based on the solution from the previous time-step. Since the solution travels along characteristic curves, the idea is to figure out how far the solution will move along a characteristic during a time-step. In this way the solution at time level n+1 is estimated by going up the characteristic by the proper distance. In other words, if A and B are points along the characteristic curve, the solution at point A and time level n can be used to find the solution at point B for time level n+1. The problem now is to find the distance from point B to point A. This estimate comes from integrating Equation (5.74).

Integrating the second and third terms of Equation (5.74) gives an estimate of the boundary value in terms of the distance up the characteristic curve

$$\frac{x_2 - x_1}{-KS_0} = \frac{h_2 - h_1}{r} \rightarrow h_2 = h_1 - \frac{r}{KS_0}(x_2 - x_1) \tag{5.75}$$

Integrating the first and second terms of Equation (5.74) yields an estimate of the distance in terms of the time-step:

$$\frac{t_2 - t_1}{n_e} = \frac{x_2 - x_1}{-KS_0} \rightarrow \Delta x = -\frac{KS_0 \Delta t}{n_e} \tag{5.76}$$

Substituting Equation (5.76) into Equation (5.75) gives the desired estimate:

$$h_2 = h_1 + \frac{\mathrm{r}\,\Delta t}{n_e} \tag{5.77}$$

The value of h_1 is estimated as the solution at time level n a distance Δx up the drainage slope from point h_2.

The kinematic approximation implies a maximum value for the saturated thickness that is not reflected in the algorithm of Equations (5.76) and (5.77). At steady state there is no change with time so $\Delta t = 0$, which makes $\Delta x = 0$ and puts h_1 and h_2 at the same location. Since the hydraulic gradient was approximated as the pavement slope, the Darcy velocity is constant (see Equation (5.68)) and the saturated thickness is determined by the flow rate per unit width. For the one dimensional case, the steady state flow rate per unit width is given by the rainfall rate, r, and length of the drainage path, L.

$$h_{ss} = \frac{rL}{KS_0} \tag{5.78}$$

When the kinematic condition is applied to a 1D problem, the boundary is the edge of pavement and the approximation gives a maximum depth as just described. A 2D problem has boundaries at both the edge of pavement and the ends of the domain, where the road continues beyond the modeled area. The kinematic boundary condition can also be applied at the end of the domain, but the boundary values—having neglected the depth gradient in Darcy's law—will be inconsistent with the domain interior. This inconsistency results in a boundary effect. The model domain should be expanded so that this effect does not influence the area of interest. One approach is to ensure the drainage path for a water particle starting at the boundary exits the model domain rather than entering the area of interest, thereby "washing out" the error. The required distance is found from the longitudinal and cross slopes and the width.

Effect on Steady State Solution

The steady state solution for 1D drainage in PFC is given by an ODE and an initial point along the solution curve is needed to integrate the equation (Charbeneau and Barrett, 2008). The kinematic approximation described above is one approach to specifying such an initial point based on the problem parameters. Figure 5-13 shows that the shape of the solution curve, especially near the boundary, depends upon the value that was specified at the boundary (hL). The solution curves show that the kinematic approximation does not allow the solution to 'draw down' near the boundary as is usual near a seepage face (Simpson et al., 2003). This draw down is required because the phreatic surface must be tangent to the seepage face (Bear, 1972). This draw-down decreases the saturated thickness but increases the hydraulic gradient. In contrast, the approximation over-estimates the saturated thickness and reduces the hydraulic gradient. Which one of the curves is closest to the true physical solution is unknown, but a range of possible solutions has now been established.

In Figure 5-13, the solutions collapse to a single curve away from the downstream boundary, but this behavior depends on the problem parameters. Doubling the rainfall rate for example pushes the point at which the curves collapse to the left, provided that the thickness of the PFC layer is sufficient to contain the additional flow (Figure 5-14). If the PFC thickness is 5cm, then doubling the rainfall rate to 1cm/hr causes sheet flow and the boundary condition for the region of PFC flow is given by the pavement thickness (Eck et al., 2010). In general, a finite pavement thickness means that the uncertainty in the boundary value matters most for low rainfall rates. Together, these examples illustrate that:

- the predicted value of the saturated thickness depends on the boundary value;
- the boundary value is unknown only for low rainfall rates; and
- the solution is less sensitive to the boundary value in this case.

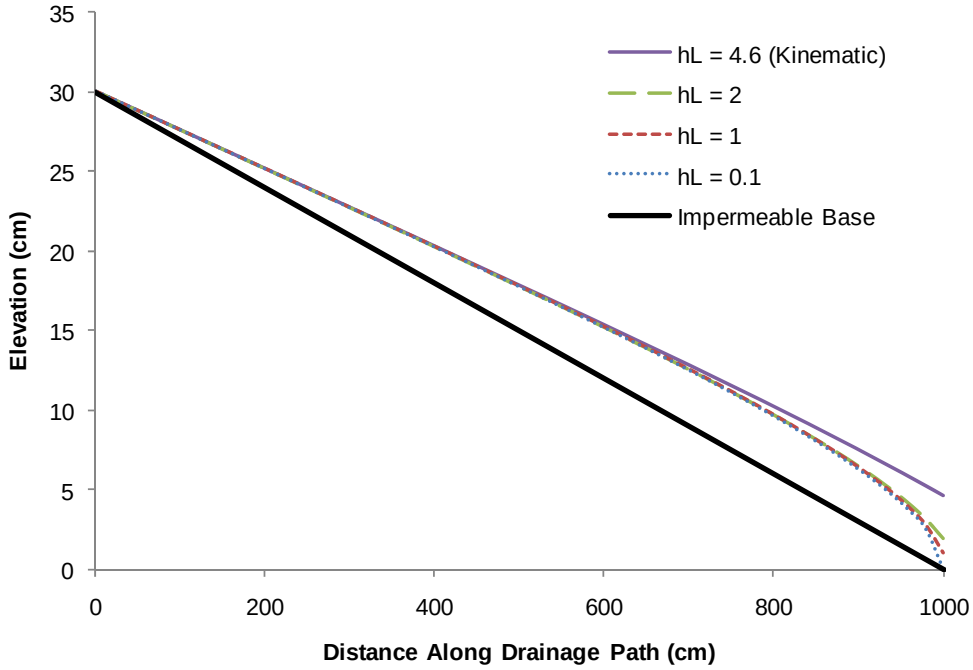

Figure 5-13: Steady state drainage profile for different boundary values; all cases used K=1cm/s, S_0=3%; r=0.5cm/hr

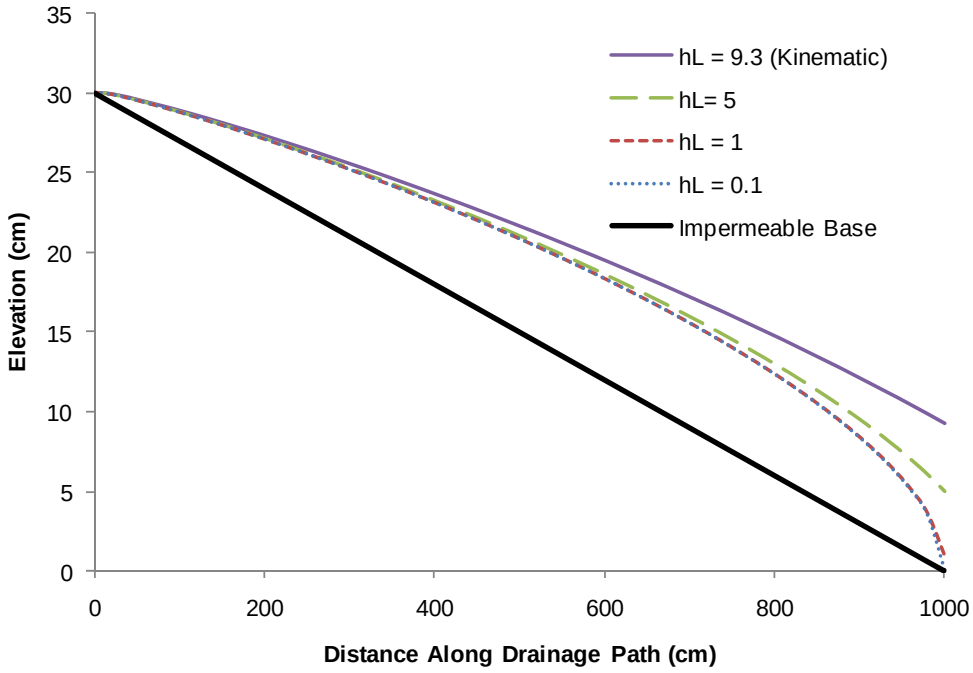

Figure 5-14: Steady state drainage profile for different boundary values; all cases used K=1cm/s, S_0=3%; r=1cm/hr

Kinematic Boundary for Curved Roadways

The algorithm outlined in Equations (5.76) and (5.77) was developed under the assumption of a straight roadway section and not a curved one. An order of magnitude approach is used to assess the applicability of the linear algorithm for curved sections.

The continuity equation for radial flow is

$$n_e \frac{\partial h}{\partial t} + \frac{1}{R}\frac{\partial}{\partial R}(Rq_R) = r \tag{5.79}$$

where R is the radial coordinate and r is the rainfall rate. Darcy's law for radial flow is

$$q_R = -Kh\frac{\partial h}{\partial R} + KhS_o \tag{5.80}$$

Neglecting depth gradients in Darcy's law and using the continuity equation for one-dimensional radial flow gives a PDE in $h(R,t)$.

$$n_e \frac{\partial h}{\partial t} + \frac{KhS_o}{R} + KS_o\frac{\partial h}{\partial R} = r \tag{5.81}$$

Using the method of characteristics approach described above gives the formulation:

$$\frac{dt}{n_e} = \frac{dR}{KS_o} = \frac{dh}{r - \frac{KhS_o}{R}} \tag{5.82}$$

The order of magnitude for the quantities in Equation (5.82) can be estimated as r = 5cm/hr ~ 10^{-3}cm/s; h~1cm; So~0.03; R=10^4cm. Using these values, $KhS_0/R = 3(10)^6$ cm/s, which is much less than the rainfall rate of 10^{-3}cm/s. This result suggests that the linear domain kinematic approximation should be adequate for calculating boundary conditions to curved domains of interest.

5.3.7.4 Kinematic Boundary Conditions for Sheet Flow

Kinematic boundary conditions for sheet flow were derived by Jeong (2008). The resulting algorithm is repeated here for completeness. The distance up the drainage path is estimated in terms of the time-step and the boundary depth, h_2, at time level n.

$$\Delta s = \frac{\sqrt{S_0}}{n\, r}\left((h_2^n + r\Delta t)^{\frac{5}{3}} - (h_2^n)^{\frac{5}{3}}\right) \tag{5.83}$$

The solution at the upstream point is obtained using bi-linear interpolation, and the value of the boundary depth at time level $n + 1$ is

$$h_2^{n+1} = \left((h_1^n)^{\frac{5}{3}} + (h_2^n + r\Delta t)^{\frac{5}{3}} - (h_2^n)^{\frac{5}{3}}\right)^{0.6} \tag{5.84}$$

5.3.7.5 Combined Kinematic Boundary Condition for PFC and Sheet flow

The algorithms for kinematic boundary conditions for sheet flow and PFC flow have been developed separately, but need to be combined so that the appropriate condition is used within the model. The combined algorithm must select between the PFC and sheet flow equations, handle the case of zero rainfall, and provide for a transition between PFC and sheet flow. This is accomplished through nested if-then statements as depicted in Figure 5-15.

When the flow depth is less than the pavement thickness, the PFC algorithm is used. The distance up the drainage slope is computed from Equation (5.76) and the solution at this location is estimated using bi-linear interpolation. Then the boundary value for the next time-step is computed from Equation (5.77). No modification to the algorithm is required for zero rainfall. The computed boundary value is compared to the maximum depth of Equation (5.78).

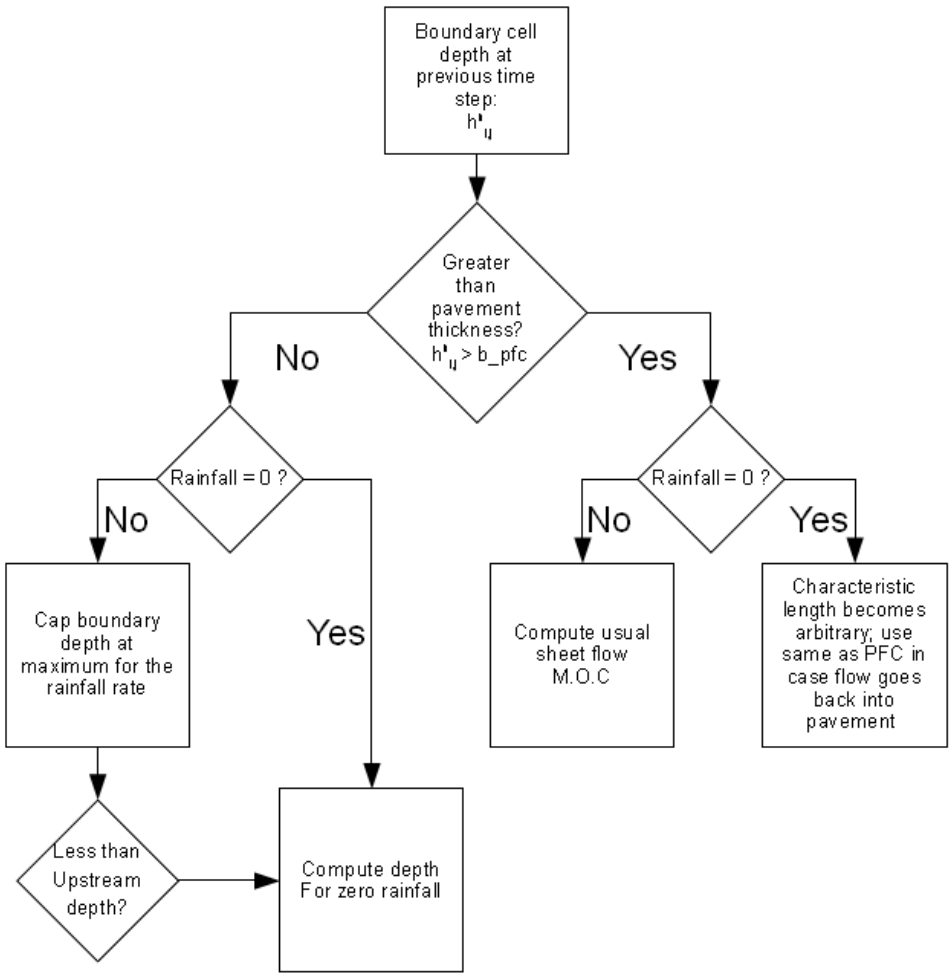

Figure 5-15: Combined algorithm for kinematic boundary condition

Implementation of the sheet flow algorithm is more complex due to the possibilities of zero rainfall and transition back to PFC flow. If the rainfall rate is zero, the distance to interpolate up the drainage path becomes arbitrary; the PFC distance is used in case a transition back to PFC flow is indicated. If the rainfall rate is greater than zero the interpolation distance is computed according to Equation (5.83) and the solution is estimated using bi-linear interpolation. If the interpolated value suggests PFC flow then the boundary value is estimated using the PFC equations, otherwise the sheet flow equation is used.

5.3.8 Solution Procedure and Tolerances

The numerical formulation and boundary conditions described in this section have been implemented in a Fortran computer code. The general solution procedure can is outlined as follows and depicted in flow chart form (Figure 5-16):

- Read model parameters, geometry information and rainfall from input files
- Create a curvilinear grid for the domain. The grid includes the coordinates, length, width and area of each grid cell.

- Assign elevations to the center of each grid cell.
- Loop through the time steps, recording details of the solution at each step
- Within a time-step, iteratively compute the depths using the fixed point method.
- Within each iteration, solve the linearized system of equations using the Gauss-Seidel method.

A vector of errors or residuals is calculated at each iteration in order to determine when the non-linear iteration loop has converged. Absolute errors are computed when the solution is near zero and relative errors are computed when the solution is away from zero. Two norms of the error vector are checked; the L_∞ norm is simply the largest value in the error vector, and the L_2 norm is the square root of the sum of the squared errors (Kreyzig, 1999). Both the L_2 norm and the L_∞ norm must be less than the tolerance for the loop to converge. A typical tolerance value of 10^{-3} was used for simulations.

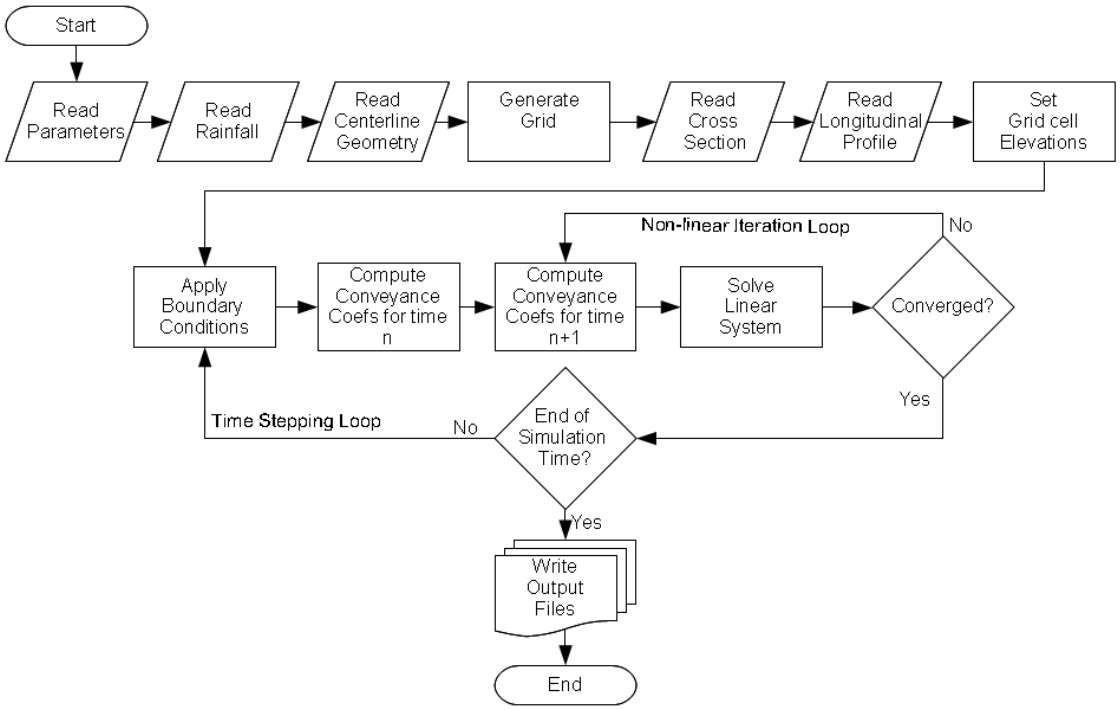

Figure 5-16: Flow chart of solution process

5.3.9 Convergence and the Transition to Sheet Flow

Trial runs during the model development process revealed numerical difficulties regarding the transition from PFC flow to sheet flow. During the time step that a grid cell transitioned from PFC flow to sheet flow the solution frequently oscillated between the PFC and sheet flow states, never reaching a solution. Physically, this transition represents a change in the character of the flow. Mathematically, there is a change in the governing equations. Given these changes, some oscillatory behavior was not wholly unexpected.

Several schemes were tried in order to overcome the numerical difficulties but the most successful approach was using an under-relaxation factor. This approach is based on the method of successive over relaxation for solving linear systems (Ferziger and Peric, 2002). The idea in successive over relaxation is to reduce the number of iterations by amplifying the change at each step using an over-relaxation factor. The under-relaxation approach aims to increase the number of iterations by making smaller changes at each step. In this way, only part of a large oscillation is taken, thus reducing the overshoot of the actual solution.

Under relaxation was found to reduce the errors by an order of magnitude, but even still a looser iterative tolerance was needed for convergence. During a simulation, the model detects a transition time-step, loosens the tolerance by a factor of 10 (changes the tolerance from 10^{-3} to 10^{-2}) and applies under-relaxation. When no grid cells are switching between PFC and sheet flow no relaxation factor is applied and the usual tolerance is imposed. An example of the relaxation factor's effect is given at the end of Section 5.5.3.

5.4 Model Validation

This section presents modeling results from PerfCode for two simplified geometries: a linear section or straight road and a converging section or curved road. The purpose of the section is to demonstrate that solutions obtained by simulating the domain through time agree with steady state solutions, which were obtained independently of the model. Three simulations are presented for each geometric configuration: (1) PFC flow only, (2) sheet flow only, and (3) combined PFC and sheet flow. The unsteady simulations provide runoff hydrographs, which are also discussed.

5.4.1 Linear Section (Straight Roadway)

The linear section selected for testing is 10m wide and 20m long with a 3% cross slope. Other parameters common to all simulations were a hydraulic conductivity, porosity and rainfall rate (Table 5.2). Holding these parameters constant, the PFC thickness was set to 15cm, 0cm, and 5cm to simulate PFC flow only, sheet flow only, and combined PFC/sheet flow.

Table 5.2: Model parameters for simulating a linear section

Parameter	Unit	Value
Roadway width	m	10
Domain length	m	20
Cross Slope	%	3
Hydraulic Conductivity	cm/s	1
Porosity	--	0.2
Rainfall Rate	cm/hr	1

A plan view of the model domain for the linear section (Figure 5-17) shows elevation contours, locations of grid cell centers and boundary conditions imposed on the model. Because the objective of these simulations was a comparison with analytical solutions, the domain and boundary conditions were chosen to make the flow one-dimensional.

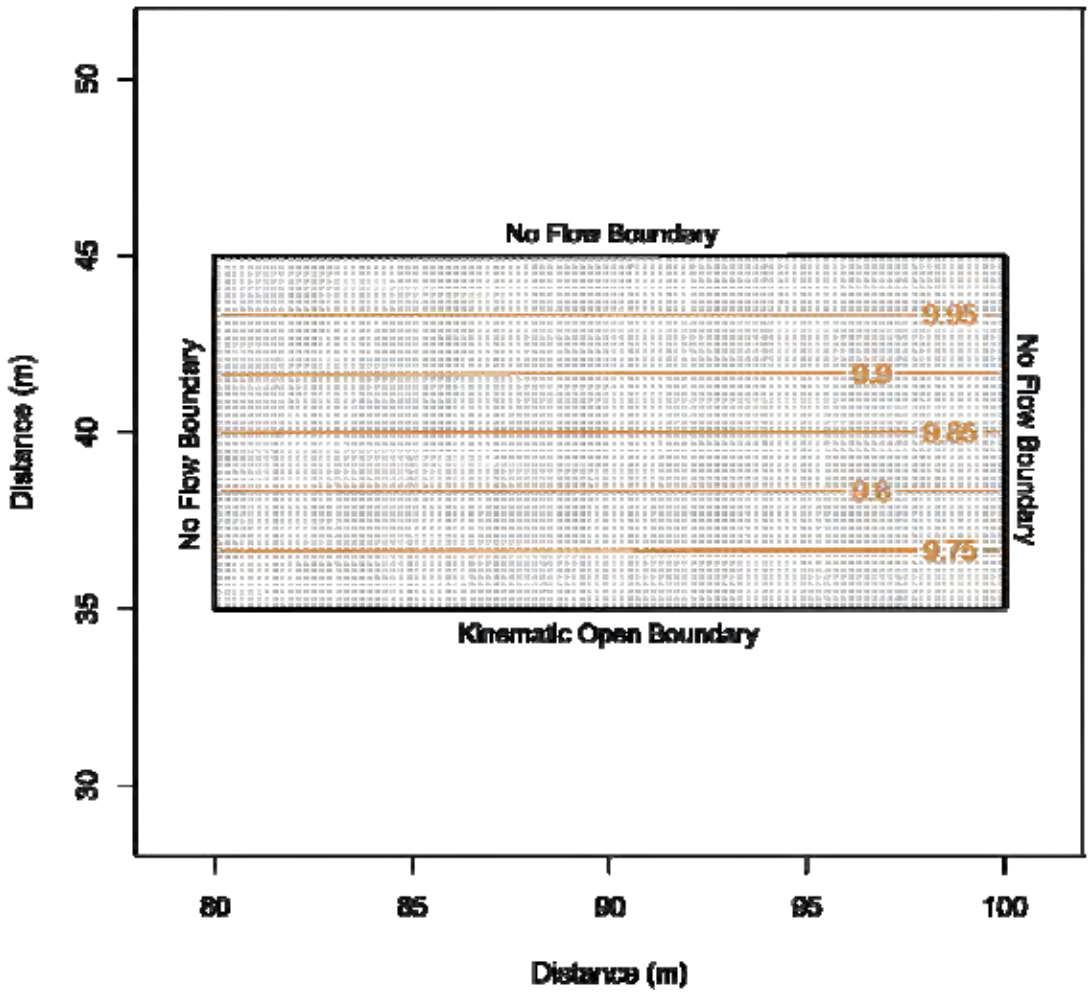

Figure 5-17: Linear domain showing elevation contours, grid cell centers, and boundary conditions

5.4.1.1 PFC Flow Only

This first simulation sets the PFC thickness at 15cm so that the steady state drainage profile will stay within the pavement. The model starts from an initial condition of zero depth and continues until steady state is reached. The model converged to a steady state solution after 20,480 seconds of rainfall. In computing the steady state solution, the initial point for integrating the ODE was found from

$$h_L = \frac{rx}{Ks} = \frac{1\frac{cm}{hr} * 1000cm}{1\frac{cm}{s} * 3\%} = 9.26cm \tag{5.85}$$

This value corresponds to the kinematic boundary condition used in the model—the hydraulic gradient is only due to the slope of the pavement.

Modeled values of the saturated thickness along the drainage path agreed closely with the analytical solution (Figure 5-18). In the figure, the normalized width variable η is plotted on the abscissa. For the linear section a value of $\eta = 1$ corresponds to the no flow boundary at the edge of pavement and a value of $\eta = 0$ corresponds to the kinematic drainage boundary at the edge of pavement. The scale on the figure has been plotted in reverse order so that drainage occurs from left to right.

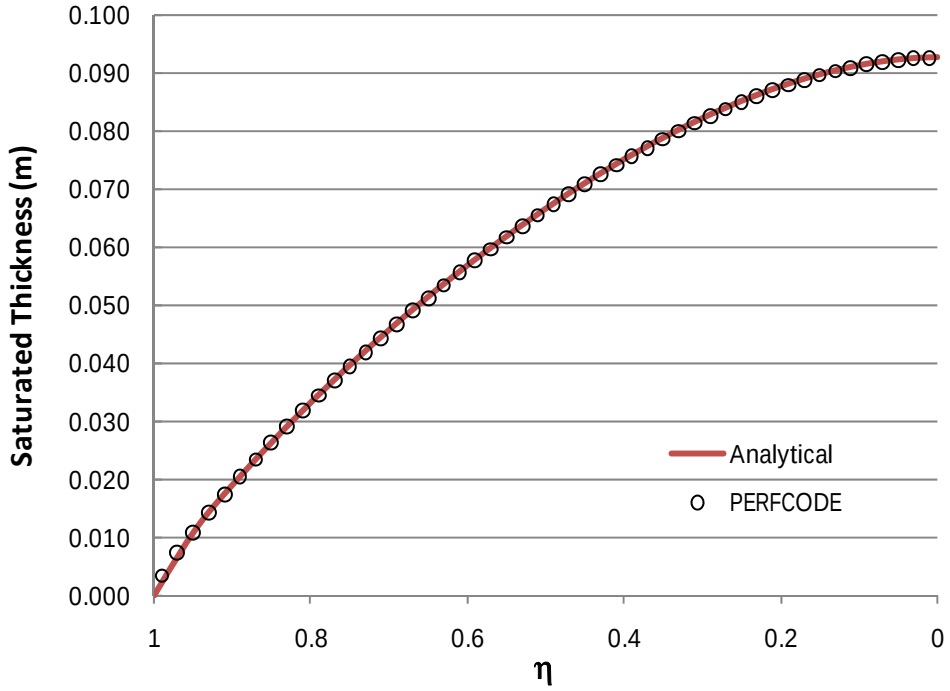

Figure 5-18: Depth profile for linear section with drainage by PFC flow only

5.4.1.2 Sheet Flow Only

The next simulation set the PFC thickness to zero so that all drainage occurs as sheet flow. The sheet flow simulation converged to a steady state solution after 252 seconds of rainfall. The flow thickness along the drainage path compares well with the analytical solution from the kinematic model (Figure 5-19). Sheet flow reaches steady state much faster PFC flow. The difference in time scales for transport via sheet flow versus PFC flow foreshadows some challenges of modeling the coupled flow process.

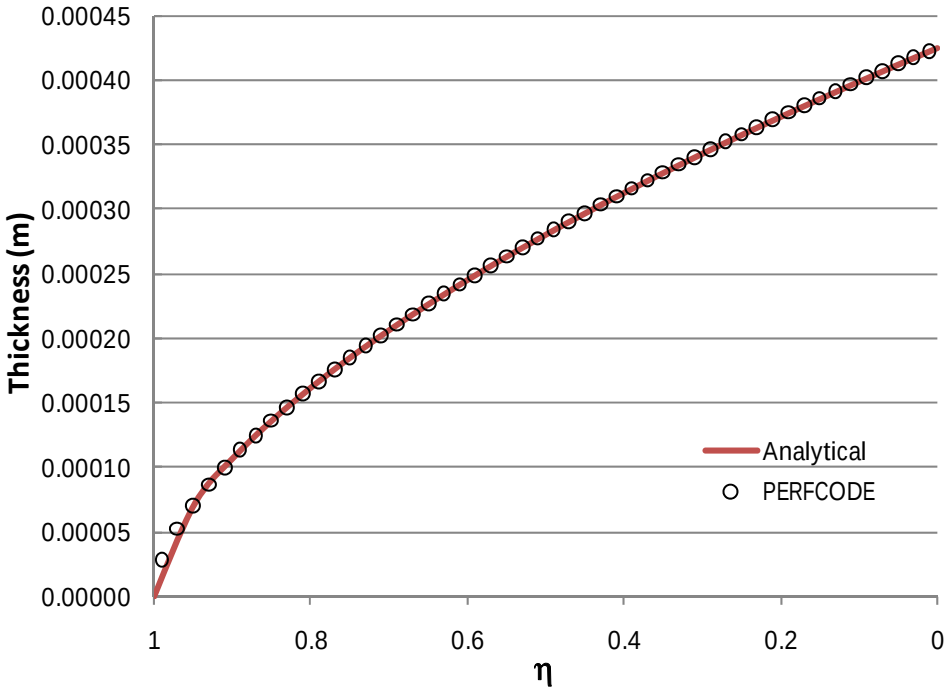

Figure 5-19: Depth profile for linear section with drainage by sheet flow only

5.4.1.3 Combined Flow

For the combined flow simulation, the PFC thickness was set to 5cm. Steady state was reached after 5,128 seconds of rainfall. Good agreement was again obtained between the numerical and analytical solutions (Figure 5-20).

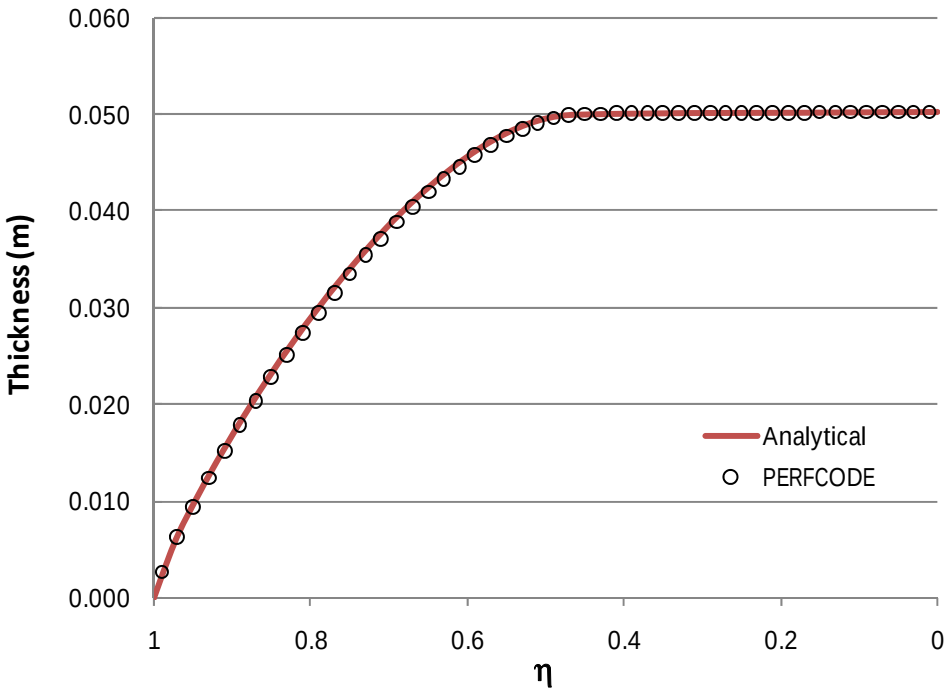

Figure 5-20: Depth profile for linear section with drainage by PFC and sheet flow

5.4.1.4 Runoff hydrographs

For each simulation the discharge from the outflow boundary was tracked through time. These rising hydrographs are plotted on a logarithmic scale on account of the wide range of times required to reach steady state (Figure 5-21). Several points of interest are noted on the hydrographs.

- The presence of a PFC layer delays the initial discharge from the roadway, in this case by about 1 minute from when rainfall begins.
- PFC delays the peak flow by nearly 10,000 seconds—much longer than most actual storms.
- For the combined case, the transition to sheet flow is evidenced as a sharp increase in the slope of the hydrograph.
- For the PFC flow only, the break in slope corresponds to the time when the outflow boundary reaches the maximum depth allowed by the kinematic condition.

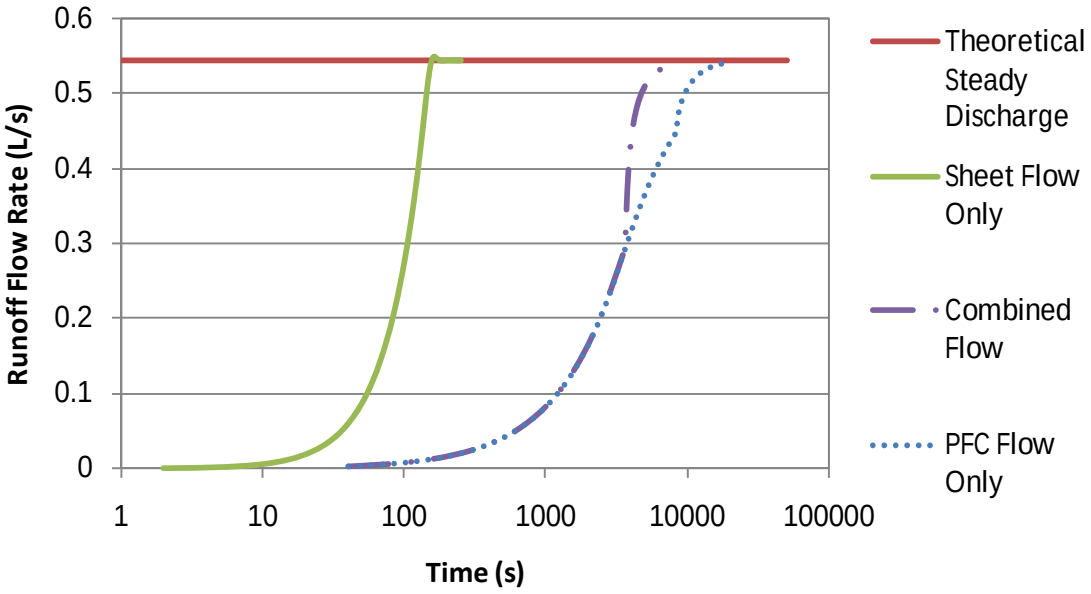

Figure 5-21: Runoff hydrographs from a linear section

5.4.2 Converging Section (Curved Roadway)

The next geometry investigated in the validation process was a fully super-elevated roadway section with a constant radius of curvature. For the purposes of this discussion such a geometry is called a *converging section.* This roadway geometry is of interest for evaluating the model's ability to simulate flow on a curved road. Keeping the cross-slope and radius of curvature constant makes the problem one-dimensional.

The converging section selected for testing is similar to the linear section, except that the radius of curvature at the roadway center is 60m. Simulation parameters are summarized in Table 5.3. A plan view of the model domain for the converging section (Figure 5-17) shows elevation contours, locations of grid cell centers and boundary conditions imposed on the model. Holding these parameters constant, the PFC thickness was set to 15cm, 0cm, and 5cm to simulate PFC flow only, sheet flow only, and combined PFC/sheet flow.

Table 5.3: Model parameters for simulating a converging section

Parameter	Unit	Value
Roadway width	m	10
Domain length	m	20
Cross Slope	%	3
Radius of curvature at roadway center	m	60
Hydraulic Conductivity	cm/s	1
Porosity	--	0.2
Rainfall Rate	cm/hr	1

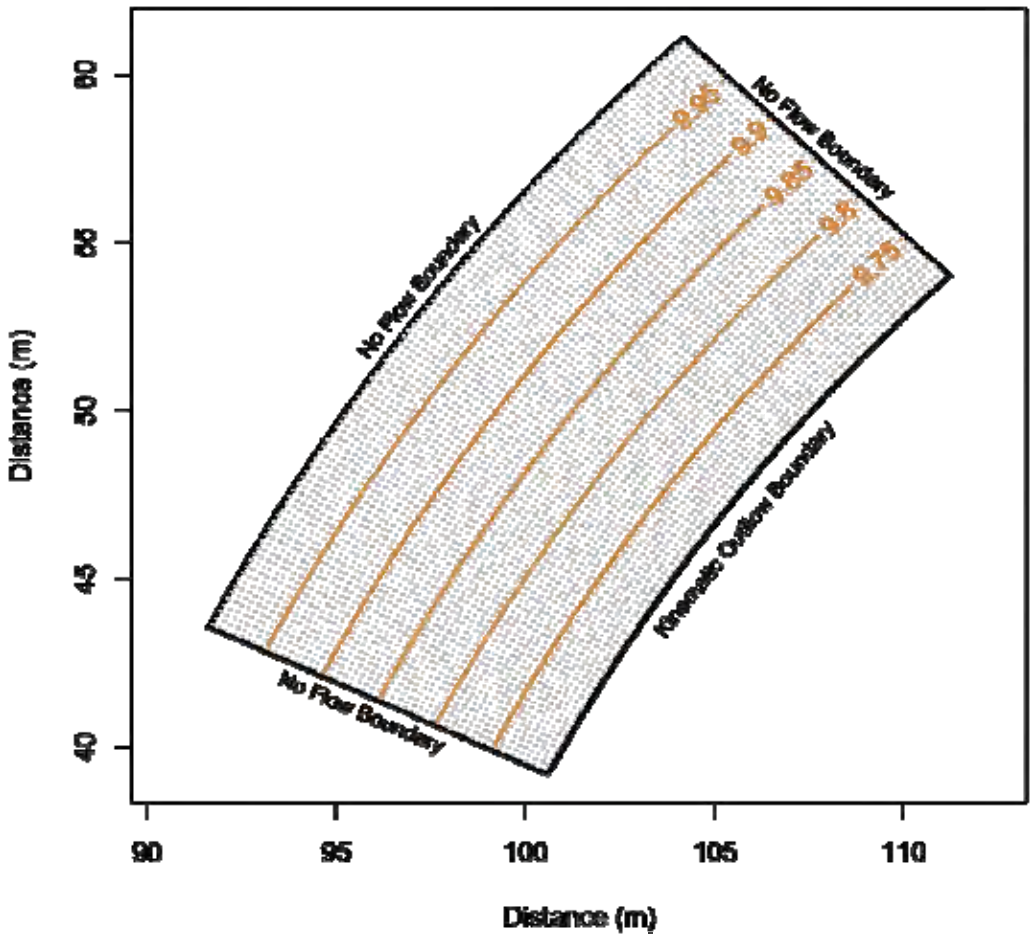

Figure 5-22: Converging domain showing elevation contours, grid cell centers, and boundary conditions

5.4.2.1 PFC Flow Only

The first simulation of the converging section set the PFC thickness to 15cm so that all of the drainage would be contained in the pavement. The model reached a steady state solution after 21,760 seconds of rainfall and showed good agreement with the steady state ODE (Figure 5-23). The linear kinematic boundary condition of Equation (5.1) was applied to the converging section. An order of magnitude analysis suggests that this approximation is appropriate (see Section 5.3.7.3).

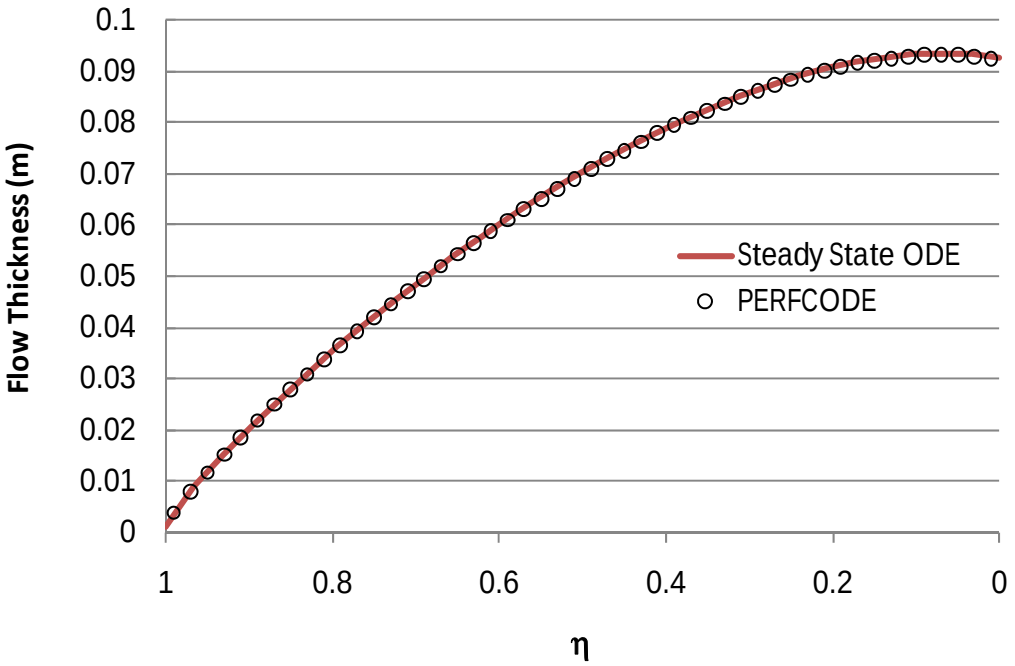

Figure 5-23: Depth profile for converging section with drainage by PFC flow only

5.4.2.2 Sheet Flow Only

The next simulation set the PFC thickness to zero so that all drainage occurred as sheet flow. Steady state was reached in 196 seconds and had good agreement with the analytical solution (Figure 5-24).

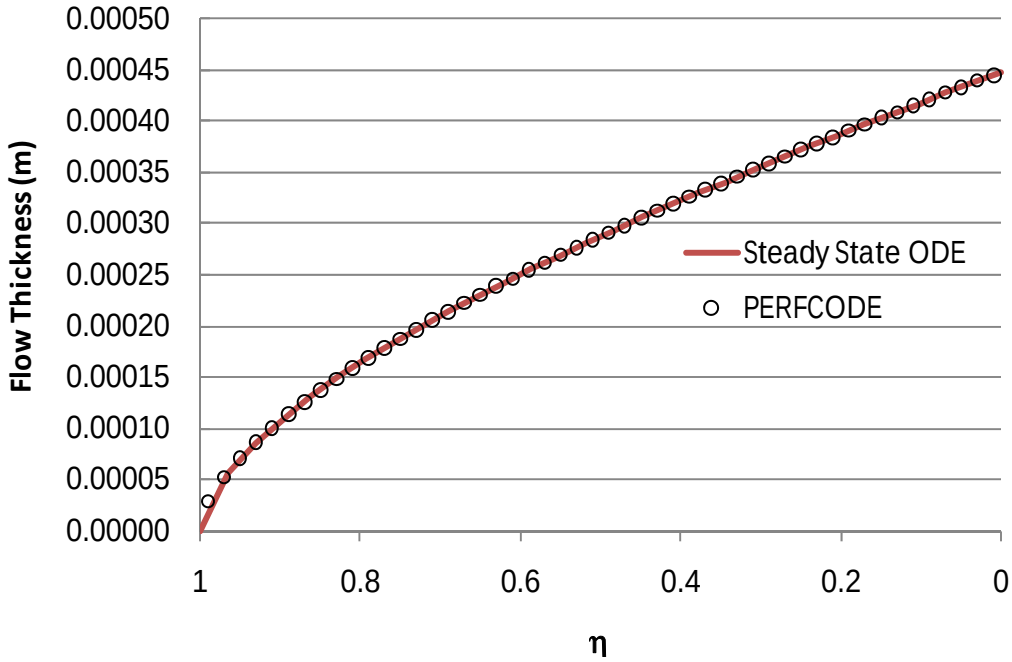

Figure 5-24: Depth profile a converging section with sheet flow only

5.4.2.3 Combined Flow

This simulation set the PFC thickness to 5cm so that drainage occurred both within the pavement and on the surface. The model reached a steady state solution in 5,398 seconds, and showed generally good agreement with the analytical solution (Figure 5-25).

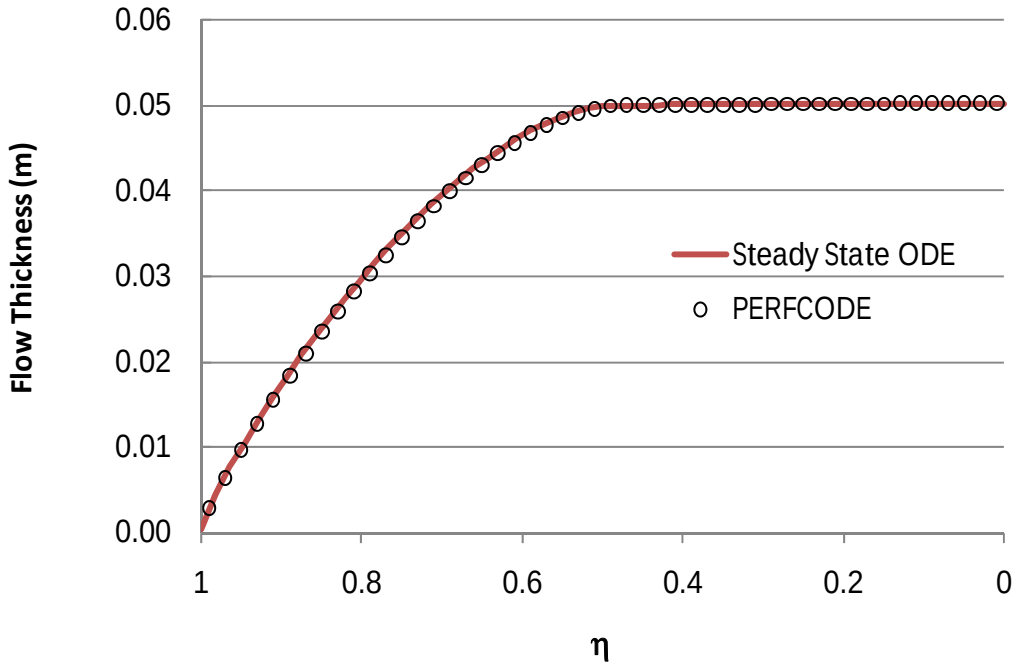

Figure 5-25: Depth profile for a converging section with combined PFC and sheet flow

5.4.2.4 Runoff Hydrographs

For each simulation the discharge from the outflow boundary was tracked through time. These rising hydrographs are plotted on a logarithmic scale on account of the wide range of times required to reach steady state (Figure 5-21). Hydrographs from the converging section show the same general trends as the linear section (see page 228). A comparison of the linear and converging cases is presented in the next section.

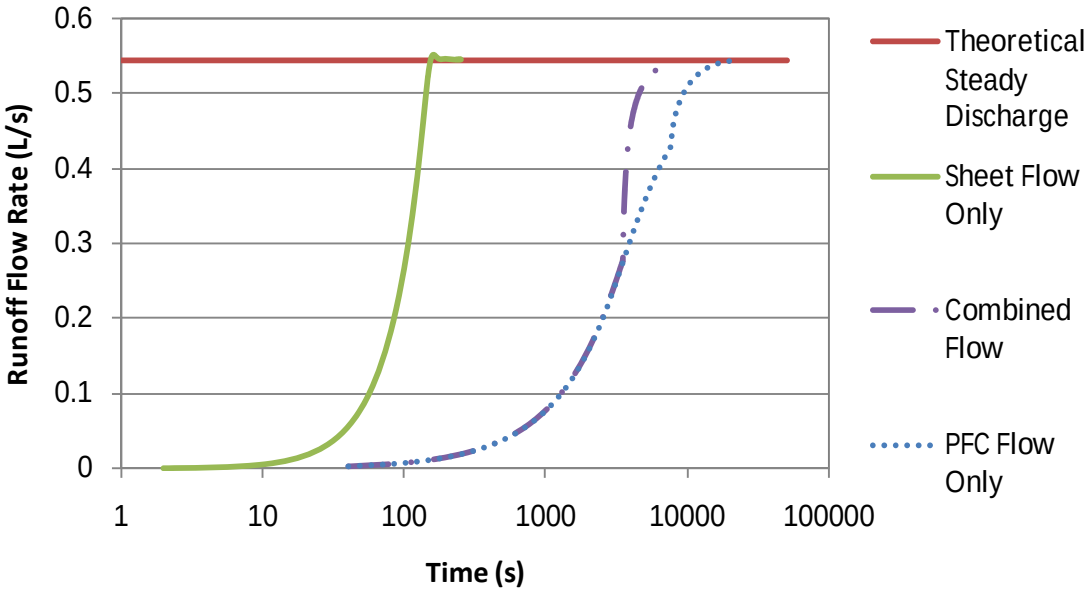

Figure 5-26: Runoff hydrographs for converging section

5.4.3 Comparison of Linear and Converging Sections

So far, this section has considered two extremes of roadway geometry: perfectly straight and perfectly curved. Most real roads fall into neither category, but these extreme cases are useful for bounding the range of problems likely to be encountered in practice.

A converging section has the effect of increasing the flow depth along the drainage path. This increase occurs because the width available for drainage decreases as the flow moves toward the center of a curve. How much the depth increases compared to a linear section depends on the radius of curvature and on the road width.

Depth profiles for the combined flow scenarios (10m width, 3% cross slope, 1 cm/hr rainfall, 5cm PFC thickness, 1 cm/s PFC hydraulic conductivity, 60m radius of curvature at center) are shown in Figure 5.27.

As expected, the flow thickness for the converging section is slightly higher than the linear section and the difference increases as the effect of convergence becomes more pronounced moving down the slope. The difference drops sharply near the transition to sheet flow because the porosity no longer amplifies the depth. Sheet flow also begins slightly higher on the converging section.

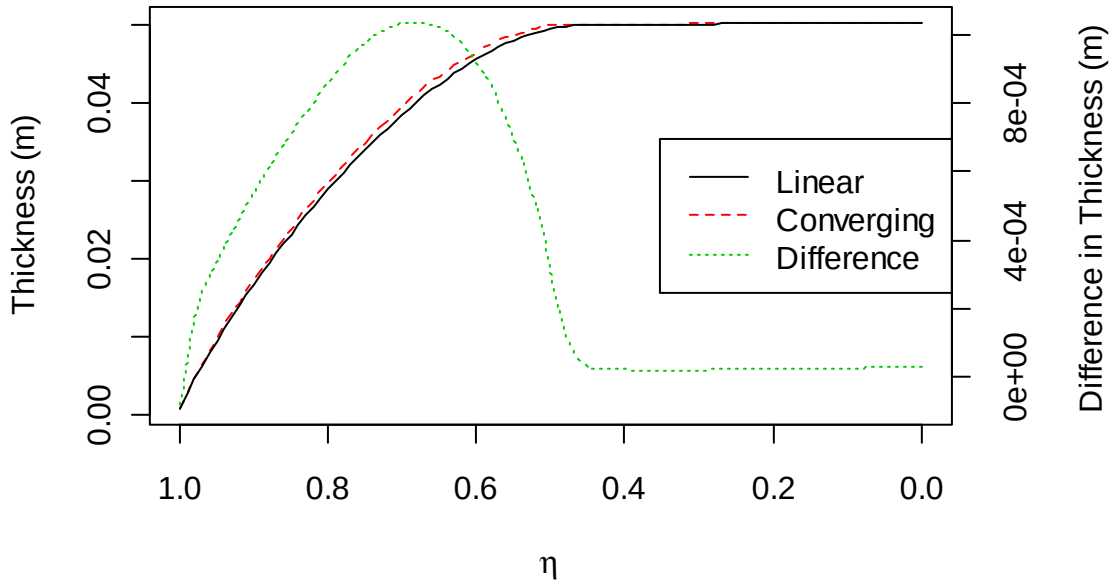

Figure 5-27: Comparison of exact solutions for steady state flow thickness on linear and converging sections, other parameters given in Table 5.2 and 5.3

The effect of a converging section on flow depth can be determined from the steady state ODEs, but the influence on the outflow hydrograph requires numerical simulation. The hydrographs for the combined PFC/Sheet Flow scenarios from Figure 5-21 and Figure 5-26 are plotted together in Figure 5-28 to illustrate the effect of convergence on the outflow hydrograph. Unlike previous the figures, an arithmetic scale is used because the relevant time range is smaller. The converging section begins sheet flow earlier than the linear section by 110 seconds. The figure also shows the evolution of the depth at the domain boundary. Adding this line to the plot emphasizes that the sharp increase in the flow rate is associated with the transition to sheet flow.

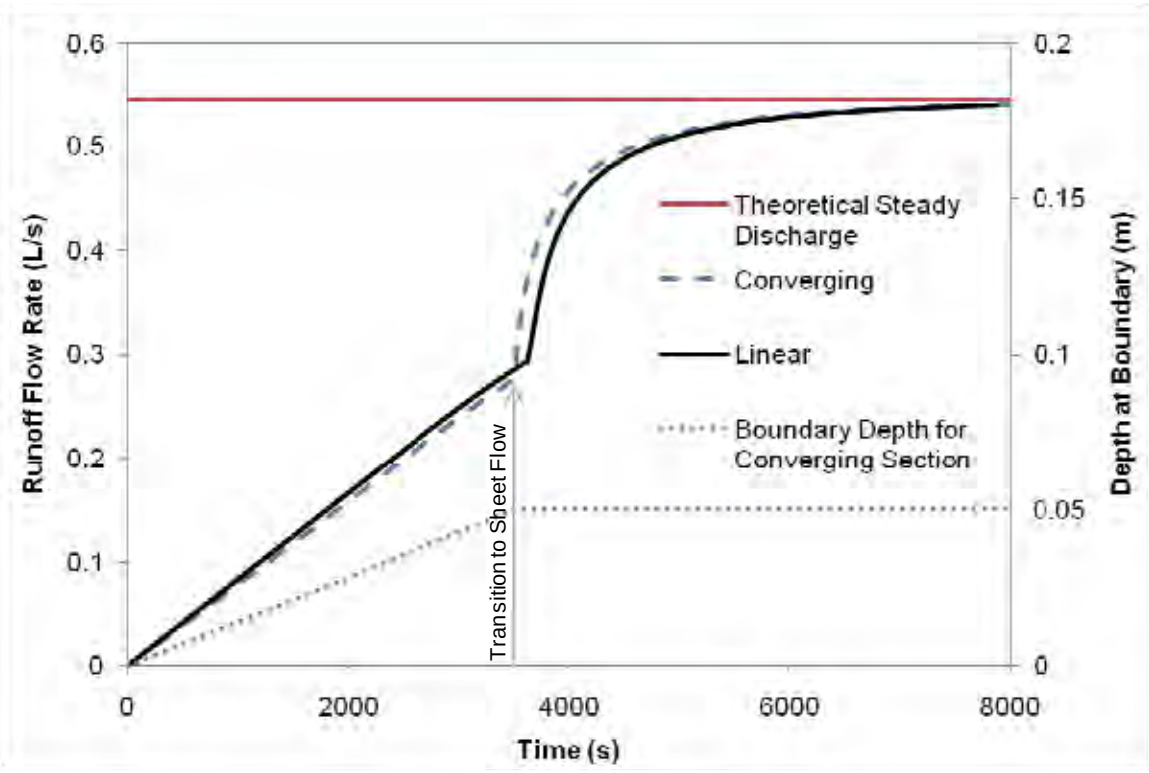

Figure 5-28: Hydrograph comparison for linear and converging sections, PFC thickness was 0.05m

5.4.4 Stability

A numerical method is considered to be stable if errors introduced into the solution are not amplified by the method (Ferziger and Peric, 2002). An amplification factor for a method may be computed by introducing a small error into the solution (as a Fourier component) at time level n and seeing how the error grows by time level $n+1$. The amplification factor is the ratio of these errors. An amplification factor of less than unity is required for a method to be stable. This analysis of stability is called the von Neumann stability analysis. The von Neumann approach applies only to linear problems; there are no comprehensive methods for assessing stability of non-linear problems (Ferziger and Peric, 2002). The non-linear coefficients are frozen here so that the von Neumann approach may be used.

The model equation for stability this analysis is formulated in terms of the total head (see Equation (5.53)) rather than the depth for simplicity. With reference to Equation (5.53), the substitutions $\ell = \Delta x;\ \imath w = \Delta y;\ \Delta A = \Delta x \Delta y;\ D = K * h + \frac{h^{\frac{5}{3}}}{n\sqrt{S_0}}$ give a simplified expression of the model equation

$$\frac{\partial H_{i,j}}{\partial t} = \frac{D}{\Delta x^2}\left(H_{i-1,j} - 2H_{i,j} + H_{i+1,j}\right) + \frac{D}{\Delta y^2}\left(H_{i,j-1} - 2H_{i,j} + H_{i,j+1}\right) + r \qquad (5.86)$$

In this formulation the diffusion coefficient D is assumed to be a constant so the equation is linear. Applying Crank-Nicolson to the time dimension gives

$$\begin{aligned}\frac{H_{i,j}^{n+1}-H_{i,j}^{n}}{\Delta t} &= \frac{1}{2}\frac{D}{\Delta x^2}\left(H_{i-1,j}^{n}-2H_{i,j}^{n}+H_{i+1,j}^{n}\right)\\ &+\frac{1}{2}\frac{D}{\Delta y^2}\left(H_{i,j-1}^{n}-2H_{i,j}^{n}+H_{i,j+1}^{n}\right)\\ &+\frac{1}{2}\frac{D}{\Delta x^2}\left(H_{i-1,j}^{n+1}-2H_{i,j}^{n+1}+H_{i+1,j}^{n+1}\right)\\ &+\frac{1}{2}\frac{D}{\Delta y^2}\left(H_{i,j-1}^{n+1}-2H_{i,j}^{n+1}+H_{i,j+1}^{n+1}\right)+r\end{aligned} \tag{5.87}$$

The value of the solution at $H_{i,j}^{n}$ can be expressed as a Fourier component

$$H_{i,j}^{n}=A^{n}e^{Ipi\Delta x}e^{Iqj\Delta y} \tag{5.88}$$

where A is the amplitude at time level n, $I=\sqrt{-1}$, and p and q are the wave numbers in the x and y directions and i,j are the indices of the grid cell. The details of the substitution of Equation (5.88) into Equation (5.87) are shown for the first term on the right side of Equation (5.87).

$$\frac{1}{2}\frac{D}{\Delta x^2}\left(A^{n}e^{Ip(i-1)\Delta x}e^{Iqj\Delta y}-2A^{n}e^{Ipi\Delta x}e^{Iqj\Delta y}+A^{n}e^{Ip(i+1)\Delta x}e^{Iqj\Delta y}\right) \tag{5.89}$$

Making similar substitutions for the remaining terms and dividing by $A^{n}e^{Ipi\Delta x}e^{Iqj\Delta y}$ gives

$$\begin{aligned}&\frac{1}{\Delta t}\left(\frac{A^{n+1}}{A^{n}}-1\right)\\ &\quad=\ \frac{1}{2}\frac{D}{\Delta x^2}\left(e^{-Ip\Delta x}-2+e^{Ip\Delta x}\right)+\frac{1}{2}\frac{D}{\Delta y^2}\left(e^{-Iq\Delta y}-2+e^{Iq\Delta y}\right)\\ &\quad+\frac{1}{2}\frac{D}{\Delta x^2}\left(\frac{A^{n+1}}{A^{n}}e^{-Ip\Delta x}-\frac{2A^{n+1}}{A^{n}}+\frac{A^{n+1}}{A^{n}}e^{Ip\Delta x}\right)\\ &\quad++\frac{1}{2}\frac{D}{\Delta y^2}\left(\frac{A^{n+1}}{A^{n}}e^{-Iq\Delta y}-\frac{2A^{n+1}}{A^{n}}+\frac{A^{n+1}}{A^{n}}e^{Iq\Delta y}\right)\end{aligned} \tag{5.90}$$

Making use of the identity:

$$e^{-Ip\Delta x}+e^{Ip\Delta x}=2\cos(p\Delta x) \tag{5.91}$$

and defining the amplification factor $G=\frac{A^{n+1}}{A^{n}}$ the linearized model equation can be written as an equation for the amplification factor

$$\frac{1}{\Delta t}(G-1) = \frac{D}{\Delta x^2}(\cos(p\Delta x)-1) + \frac{D}{\Delta y^2}(\cos(q\Delta y)-1) + G\left(\frac{D}{\Delta x^2}\right)(\cos(p\Delta x)-1) + G\left(\frac{D}{\Delta y^2}\right)(\cos(p\Delta y)-1) \quad (5.92)$$

Solving this expression for the amplification factor gives

$$G = \frac{1}{1 + 4\left(\frac{D}{\Delta x^2}\right)\sin^2\left(\frac{p\Delta x}{2}\right) + 4\left(\frac{D}{\Delta x^2}\right)\sin^2\left(\frac{p\Delta y}{2}\right)} \quad (5.93)$$

Equation (5.93) shows that the amplification factor will always be less than unity because the coefficient D is always positive and $\sin^2$ is also always positive. This stability analysis has shown that the Crank-Nicolson method is unconditionally stable for a linear diffusion problem. The actual model equations however are non-linear and so may exhibit some stability problems.

5.4.5 Model Convergence

A numerical solution is said to converge if the errors in the solution decrease as the grid is refined. This model was developed using central differencing scheme. Based on a Taylor series expansion, central differencing schemes can be shown to have a second-order truncation error (Ferziger & Peric, 2002). This means that the largest term in the neglected part of the Taylor series expansion contains the grid spacing term raised to the second power. The observed order of the truncation error for a model can be obtained by comparing model runs for different grid sizes.

The model domain selected for the convergence study is the same domain studied in Section 5.4.2.3—10m width, 3% cross slope, 1 cm/hr rainfall, 5cm PFC thickness, 1 cm/s PFC hydraulic conductivity, 60m radius of curvature at the roadway centerline. Double precision variables were used for the convergence study to assure that differences in the solution at the various grid sizes were due to truncating the Taylor series approximations for derivatives and not due to floating point errors. Even with double precision variables, the solutions using a 10cm grid was indistinguishable from the solution using a 5cm grid. A plot of the solution for various grid sizes shows that the model converges to the same solution independent of the grid size (Figure 5-29).

For the purposes of this convergence study, the model solution for a nominal grid spacing of 5cm was used as the exact solution. The difference between the model solution and the exact (5cm) solution, or the residual, was computed for each point. The portion of the domain in PFC flow had higher residuals than the sheet flow part of the domain (Figure 5-30). That the sheet flow and PFC flow parts of the domain would have different behaviors is not completely unexpected because the governing equations differ. What should be consistent though, is the rate at which the errors change with grid size.

The observed convergence rate of the model was investigated by computing the residual with respect to the 5cm grid at several locations along a cross section in the center of the domain (at different points along the cross-section for the longitudinal station in the middle of the domain). The grid refinement study (Figure 5-31) shows that the model gives second order behavior as the grid is refined.

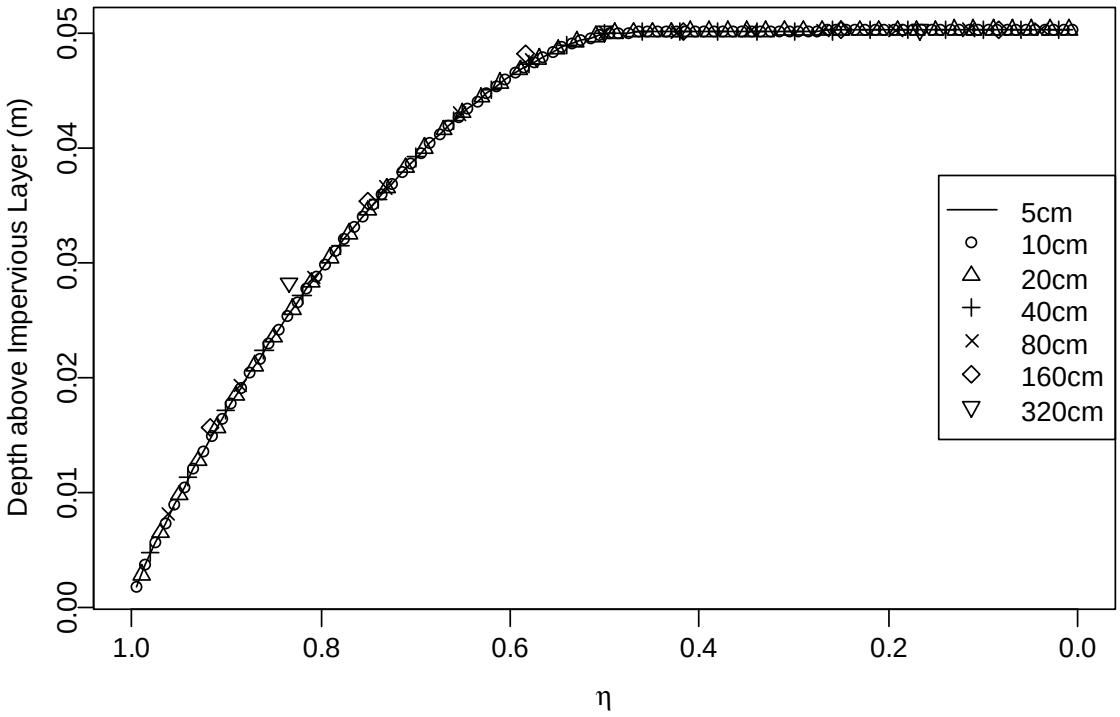

Figure 5-29: Steady state depth profile for various grid sizes

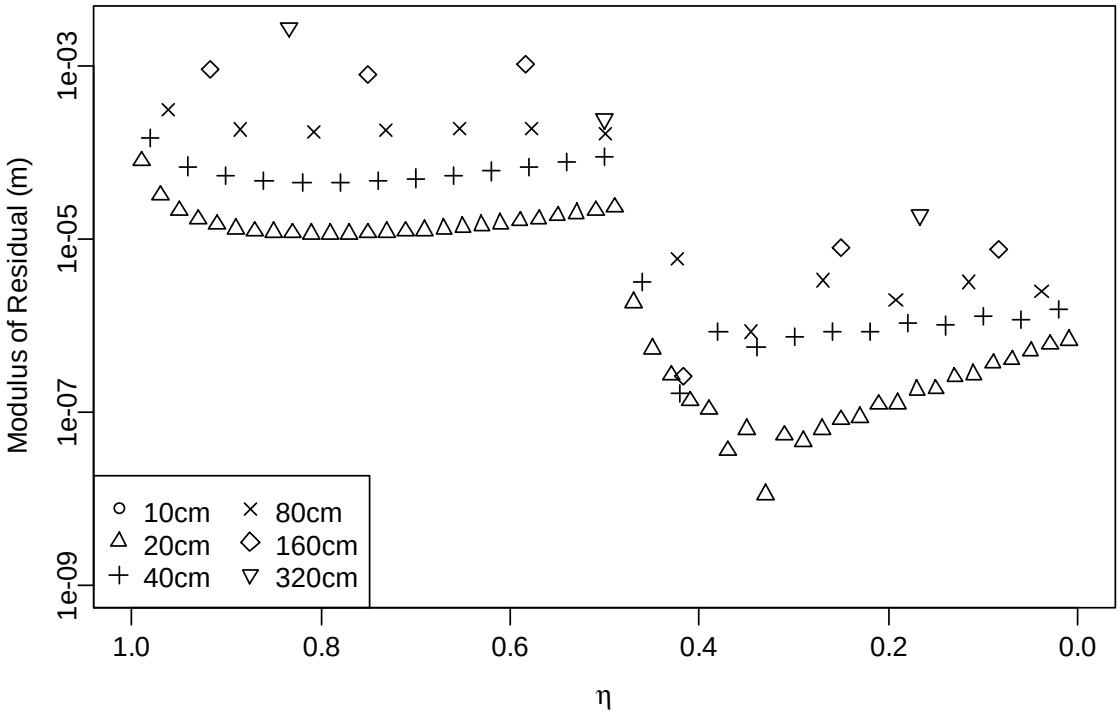

Figure 5-30: Residual with respect to 5cm grid by location, all residuals for 10cm grid were zero

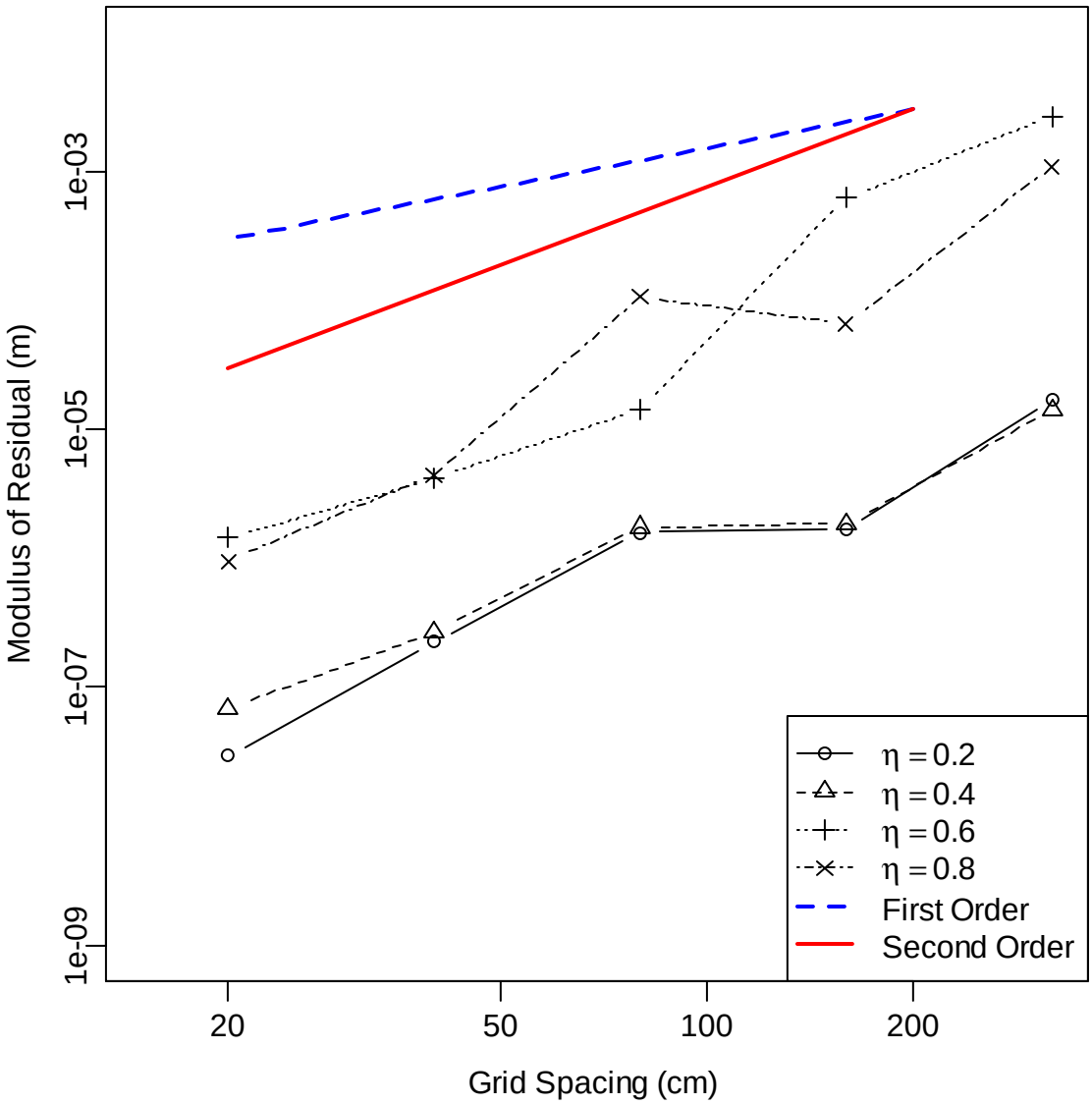

Figure 5-31: Grid refinement study

5.5 Comparison with Field Data

This section compares model results with field data from a monitoring site constructed on Loop 360, near Austin, Texas. The variable of interest remains the water depth on the highway, but measurements of this quantity are difficult to make. Indeed, one motivation for developing a model is to estimate quantities that are difficult to measure. What has been measured is the rainfall depth and runoff hydrograph at the monitoring site. The measured rainfall is taken as input and the variation of water depth through the storm is computed along with the runoff hydrograph. Reasonable agreement between the modeled and measured hydrographs lends credibility to the associated depth predictions.

5.5.1 Construction of Field Monitoring Site

The monitoring site, located on southbound Loop 360 near Austin, Texas (Figure 5-32), was initially established as a monitoring site for stormwater runoff in 2004. Later that year, the highway was repaved with PFC. Lower concentrations of total suspended solids and total heavy metals were observed in the runoff, which generated interest in additional research.

In the autumn of 2006 equipment for automatic sample collection was installed at the Loop 360 monitoring site. The field site was designed to measure the runoff hydrograph and to collect water quality samples. A drainage system was constructed using 4-inch PVC pipe to collect runoff from an 18m (60 ft) length of roadway and direct it to the sampler. A 6-inch H-flume was used to measure the flow rate from the drainage pipe. An ISCO 4230 bubbler flow meter measured the water depth in the H-flume and calculated the flow rate. An ISCO 3700 portable sampler used the flow rate to collect flow-weighted water samples. An ISCO 674 tipping bucket rain gage recorded rainfall. Both rainfall and runoff were recorded in five-minute intervals, rainfall as the total depth and runoff as the average flow rate. Refer to Stanard (2008) for additional details on the construction of the monitoring site and programming of the equipment.

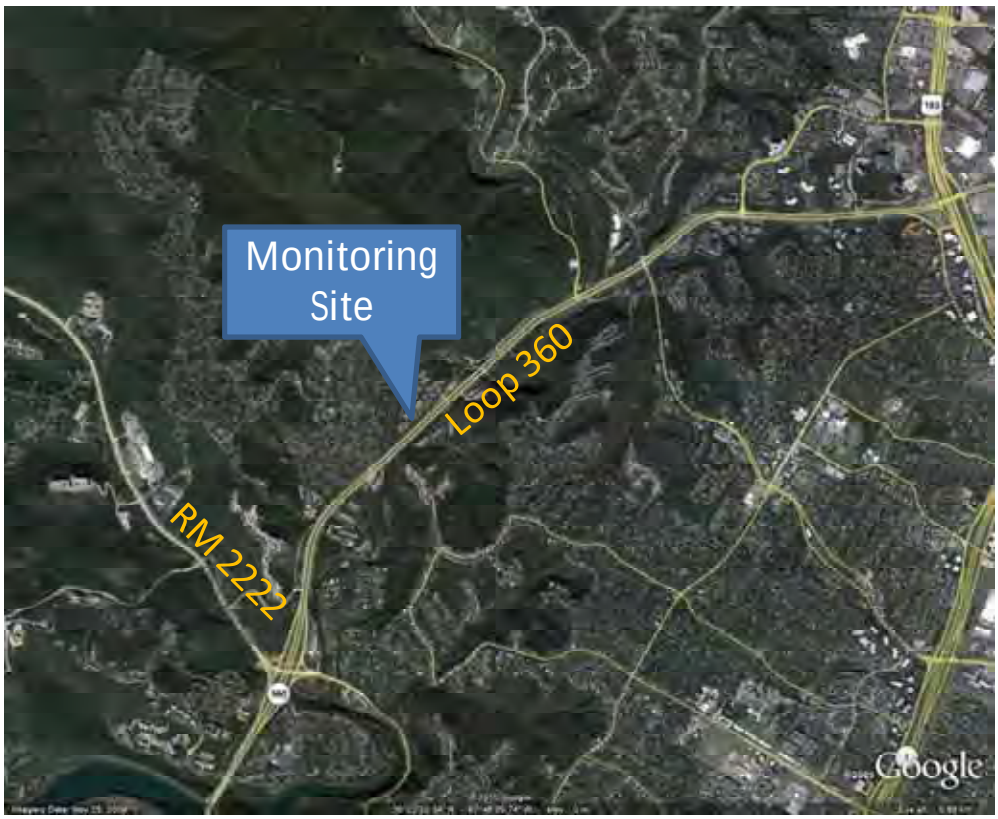

Figure 5-32: Aerial map of Loop 360 monitoring site (Google 2010)

Figure 5-33: Photograph of H-flume and drainage pipe at Loop 360 monitoring site

5.5.2 Model Inputs and Parameters

At the location of the monitoring site, Loop 360 is a four-lane divided highway. The monitoring site is situated on the right-hand shoulder of the south-bound traffic lanes. The traffic lanes (24ft) and right hand shoulder (10ft) slope to the driver's right-hand side at cross-slopes of 2% and 4%, respectively. The left shoulder (6ft) drains to the left at a cross-slope of 4%. The entire section has a longitudinal slope of 2.3%.

The roadway geometry for Loop 360 was used to develop input files for the model. The model domain was extended beyond the 60ft length monitored so that errors in the kinematic condition on the east and west boundaries would not influence the solution in the domain of interest. Kinematic boundary conditions were used on all four sides of the domain. In Figure 5-34, the middle third of the domain corresponds to the location of the drainage pipe at the monitoring site.

The storm event of July 20, 2007 was selected for simulation because it was a large enough to cause substantial sheet flow. The hydraulic conductivity and porosity for this simulation correspond to values measured by Klenzendorf (2010) for a nearby location on the same highway. Values of Manning's n have not been measured for PFC, but a value of 0.015 s / $m^{1/3}$ appears appropriate considering the analysis of Charbeneau et al. (2009). Table 5.4 summarizes the model parameters.

Table 5.4: Model Parameters for Loop 360 Monitoring Site

Parameter	Unit	Value
Roadway width	m	12.2
Domain length	m	36.6
Cross Slope	%	various
Hydraulic Conductivity	cm/s	3
PFC Thickness	cm	5
Porosity	--	0.2
Manning's n	$s/m^{1/3}$	0.015
Rainfall Rate	cm/hr	various

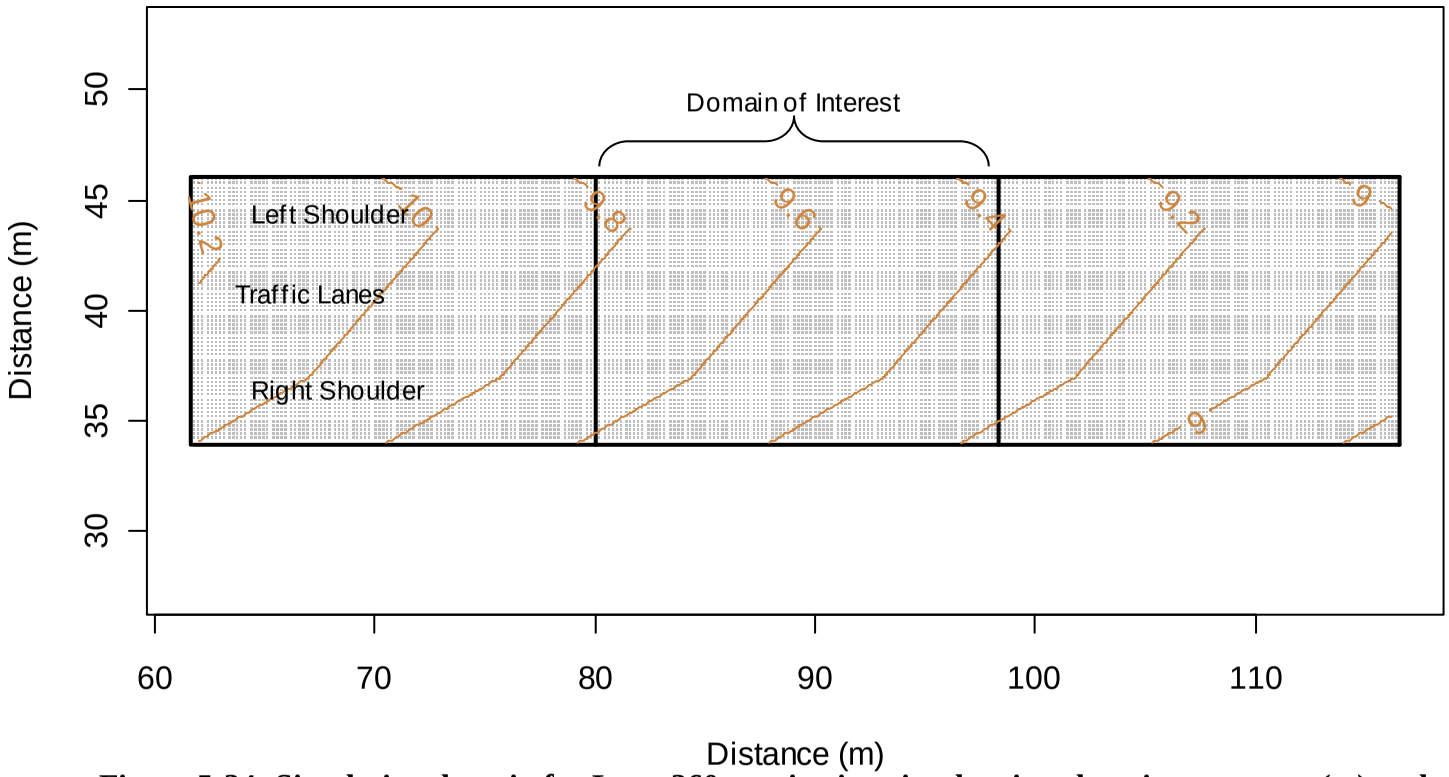

Figure 5-34: Simulation domain for Loop 360 monitoring site showing elevation contours (m) and location of grid cell centers

The storm of July 20, 2007 occurred during an unusually wet summer, and was a particularly large storm. A total of 48mm (1.9 in) of rainfall were recorded at the monitoring site over a 5.6 hour period. The peak rainfall depths on a five, fifteen and sixty minute basis were 6.6mm 18mm, and 39mm (0.26in, 0.71in, 1.56in), respectively. On a sixty minute basis, the storm corresponded to a return period of about 2 years (Chow et al., 1988 pg. 450) The highest five-minute rainfall intensity was 80mm/hr.

The field measurements provided the time at the end of five-minute periods for which the rainfall total was reported. This information was prepared for use in the model by computing the rainfall intensity (mm/hr or m/s) and inserting points at the beginning of each five-minute interval (Figure 5-35). The purpose of this approach was to facilitate use of a linear interpolation routine for selecting the proper rainfall rate for any time during the model simulation.

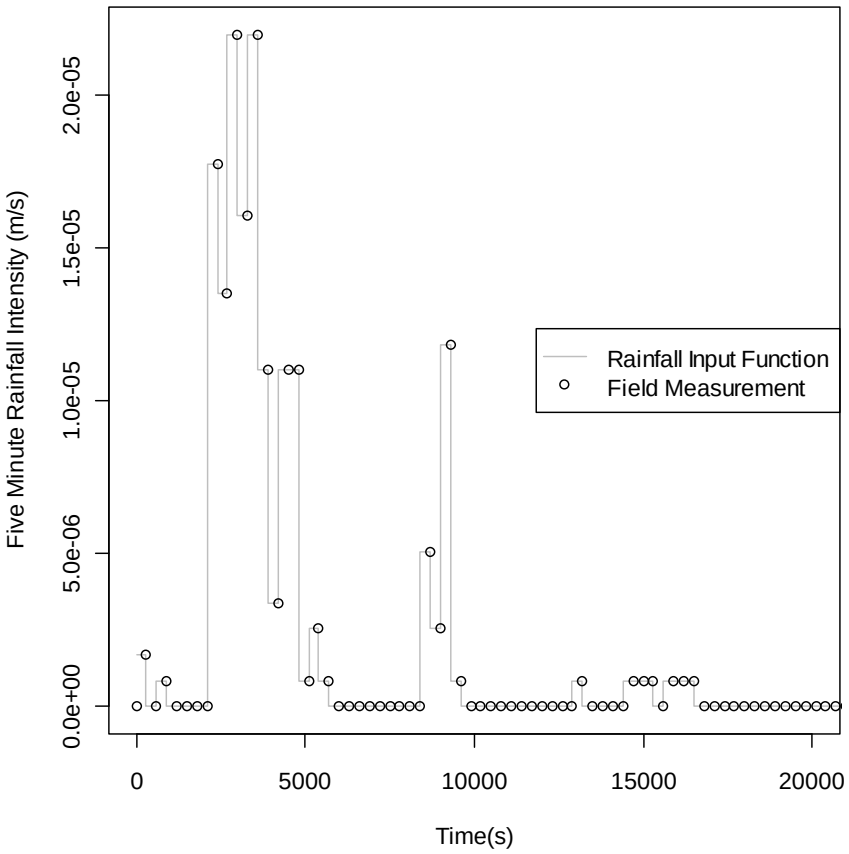

Figure 5-35: Measured rainfall and model input function for Loop 360 monitoring site on July 20, 2007

5.5.3 Results and Discussion for event of July 20, 2007

The rainfall function and other parameters were used as inputs for a simulation over 20,000 seconds. During the simulation, the runoff through the domain's southern boundary and was computed for each time step. The overall maximum depth and the maximum depth in the middle of the domain were also tracked throughout the simulation. This distinction in the depths was necessary due to oscillations near the boundary.

A model time step of 5s was used when the all of the drainage was contained within the pavement, but a step of 0.1s was needed during sheet flow for the model to remain stable. In order to make a fair comparison with the field measurements, the calculated flow rates were averaged over five minute intervals. A weighted average flow rate was used so that a five-minute interval containing two sizes of time step has the proper flow rate. These averaged flow rates showed generally good agreement with the field measurements (Figure 5-36). The model predicted peak flows of the proper time and magnitude, and the shape of the hydrograph generally matches the field observations.

The model predicted a peak flow 3.7 L/s, which is 97% of the measured value of 3.8 L/s. The difference between the modeled and measured flow rates (residual) had a mean -0.029L/s, median 0.021 L/s, standard deviation 0.24 L/s and standard error of the mean 0.029 L/s. The largest residuals were associated with high flow rates. This comparison suggests that the model parameters were consistent with field conditions and lends credibility to the associated depth predictions.

A plot of the model solution for maximum depth conditions shows sheet flow occurring in both traffic lanes and on the right hand shoulder (Figure 5-37). Within the domain of interest, the depth contours are parallel to the roadway centerline. This result is consistent with a straight road and constant slopes. Some oscillations in the depth contours appear outside of the domain of interest, especially near the western boundary. It is believed that these oscillations are related to using the kinematic outflow boundary condition from the east end of the domain on the inflow boundary at the west end.

During this simulation, maximum depth in the domain of interest was 0.05142m above the impervious layer, which represents a sheet flow depth of 1.4mm. This maximum occurred near the edge of the right traffic lane (Figure 5-38). The exact location was 3.2m from the southern edge of the domain; since the shoulder width is 3.05m, the maximum depth occurred 15cm from the shoulder. This peak occurred 1 hour after rainfall began (3599.9s) and during the peak rainfall intensity of 80 mm/hr.

The model results show that sheet flow begins 1.6m due south of the grade break for the left hand shoulder (Figure 5-38). Under most conditions, this break in slope acts as a no-flow boundary within the domain; the no flow condition is assumed here for purposes of comparison with the analytical model even though some flow does occur. At the peak rainfall rate for this storm, the analytical model (see Charbeneau & Barrett 2008 and Eck et al. 2010) predicts sheet flow at 2m down the drainage slope or 1.4m due south of the grade break (2% cross slope, 2.3% longitudinal slope; 3.048% drainage slope). This seems a reasonable match, considering that the numerical model is not at steady state, and that boundary condition is approximate.

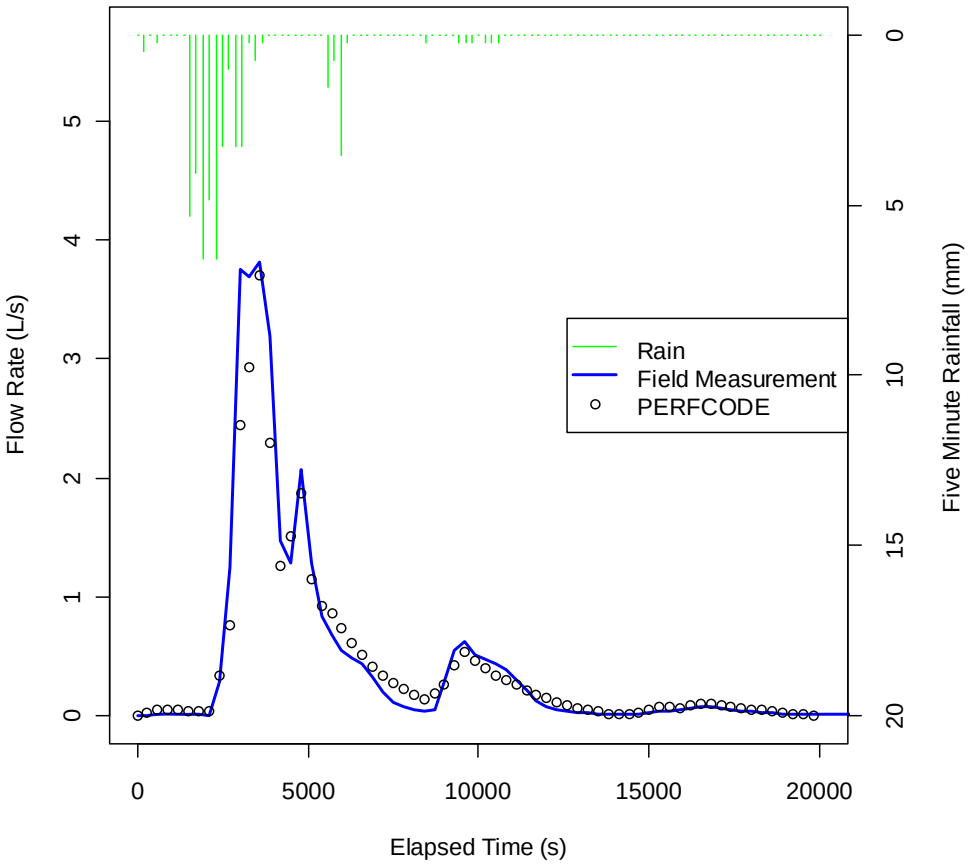

Figure 5-36: Comparison of modeled and measured hydrographs for storm of July 20, 2007

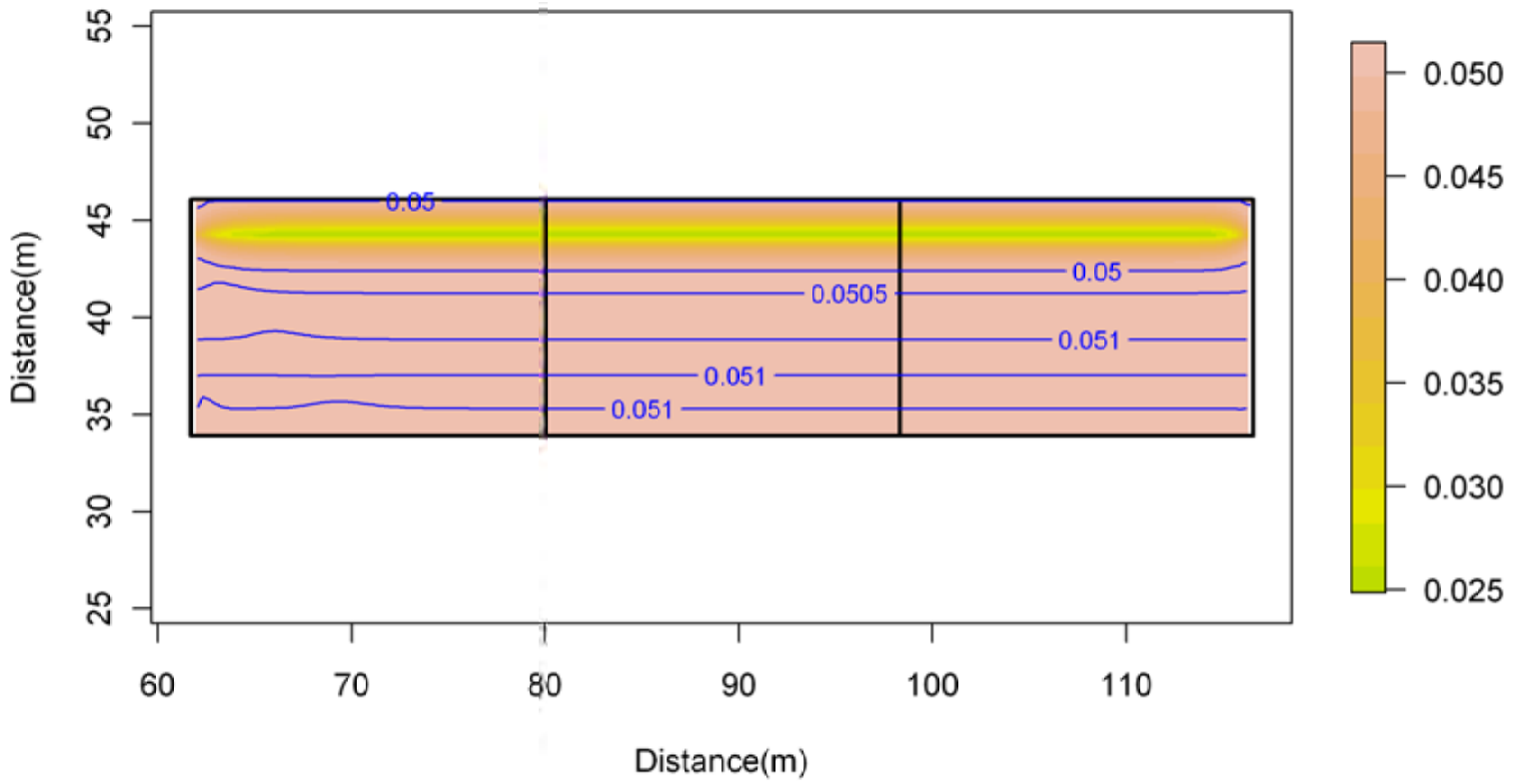

Figure 5-37: Water depth above impervious layer (m) for Loop 360 during maximum depth conditions on July 20, 2007. The PFC thickness was 0.05m; contours correspond to sheet flow conditions.

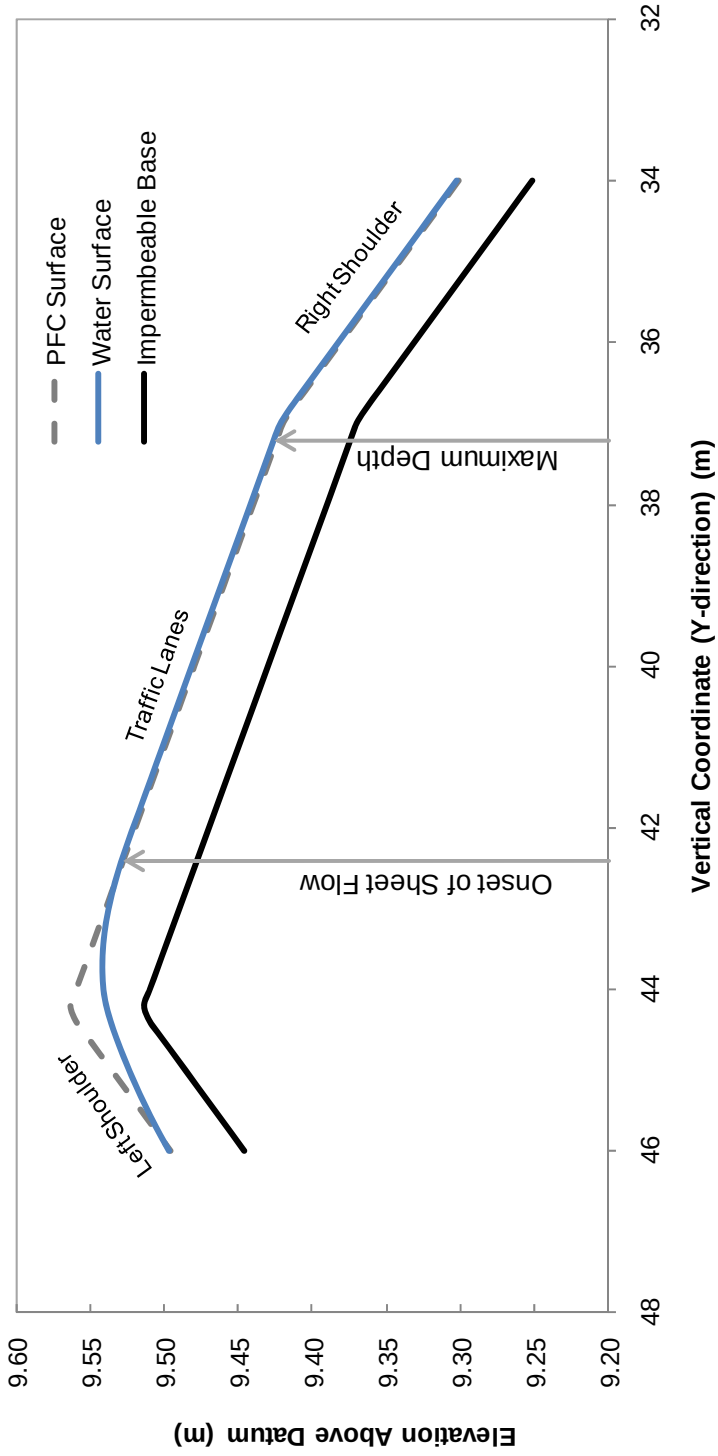

Figure 5-38: Profile through maximum depth section; the horizontal coordinate is 94.42m

In addition to examining water depths during an actual rainstorm, this example also provides an opportunity to illustrate the effect of using an under-relaxation factor in the non-linear iteration loop. Figure 5-39 shows how the solution at a grid cell just on the right shoulder evolves during a time step shortly after peak rainfall has started (time 2821.9s). At the previous time-step the traffic lanes have sheet flow and the shoulder is in PFC flow. The model is trying to determine if the shoulder is also now in sheet flow or if it remains in PFC flow. Without the under-relaxation, the solution bounces between inside and outside of the PFC surface, the grid cell shown has the largest error, and the solution does not converge for the time step. This 'hunting' behavior does not occur with the relaxation factor and the model concludes that the depth at this location remains in the PFC for this time-step.

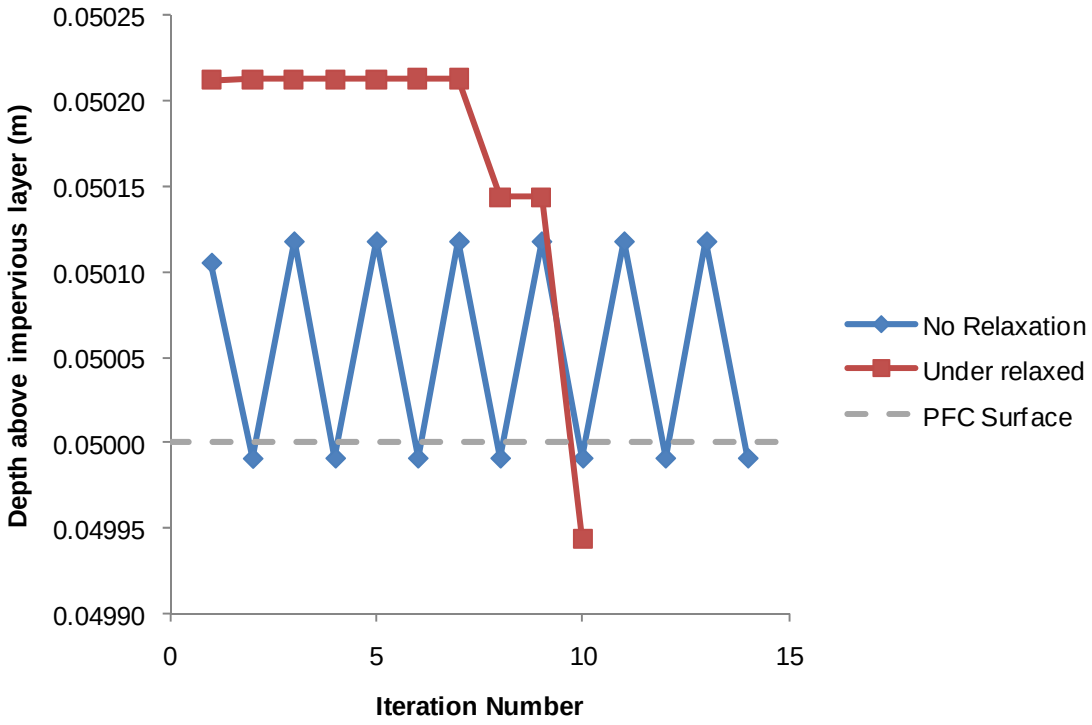

Figure 5-39: Solution history for an interior point (grid cell 2138) with and without under-relaxing the non-linear iteration

5.5.4 Loop 360 with and without PFC

One opportunity afforded by the simulation model is to compare results with and without PFC for the same storm event. Such an analysis gives direct insight about how PFC changes the drainage hydraulics as compared to conventional pavement and is the topic of this section. The same roadway geometry and simulation parameters used for the comparison with field measurements were used in this simulation, except that the thickness of the PFC layer was set to zero so that all drainage occurred as sheet flow.

The simulated hydrograph for Loop 360 without PFC is shown in Figure 5-40 along with the simulated hydrograph corresponding with a 5cm PFC layer. Both hydrographs have been time averaged over the reporting period for rainfall measurements (5 minutes). The absence of a

PFC layer appears to make the hydrograph rise and fall faster, especially later in the storm (10,000s) when flow would be contained within the PFC. The PFC layer reduced the magnitude of this small peak by about 70% and delayed it five minutes, or one averaging period.

A PFC layer might be expected to delay the runoff hydrograph due to storage within the pavement, but that effect is not observed in this case. The high rainfall intensity quickly overwhelmed the capacity of the PFC layer, causing most of the drainage to occur as sheet flow so the hydrographs exhibit a similar shape.

The presence of a PFC layer reduced the sheet flow thickness during this event (Figure 5-41). The PFC layer prevented sheet flow entirely for the left part of the left lane and also on the left shoulder. In regions where sheet flow occurred over PFC, the PFC layer reduced the depth by an average of 0.35mm. Some small oscillations are noted in the sheet flow profile near the right shoulder and were associated with sharp change in cross slope.

In addition to reducing the magnitude of sheet flow on the highway, PFC also reduced the duration that sheet flow was present. Simulation results showed that sheet flow depths in excess of 0.1mm were present for about 1600 seconds when the PFC layer was present and for 8580 seconds without the PFC layer.

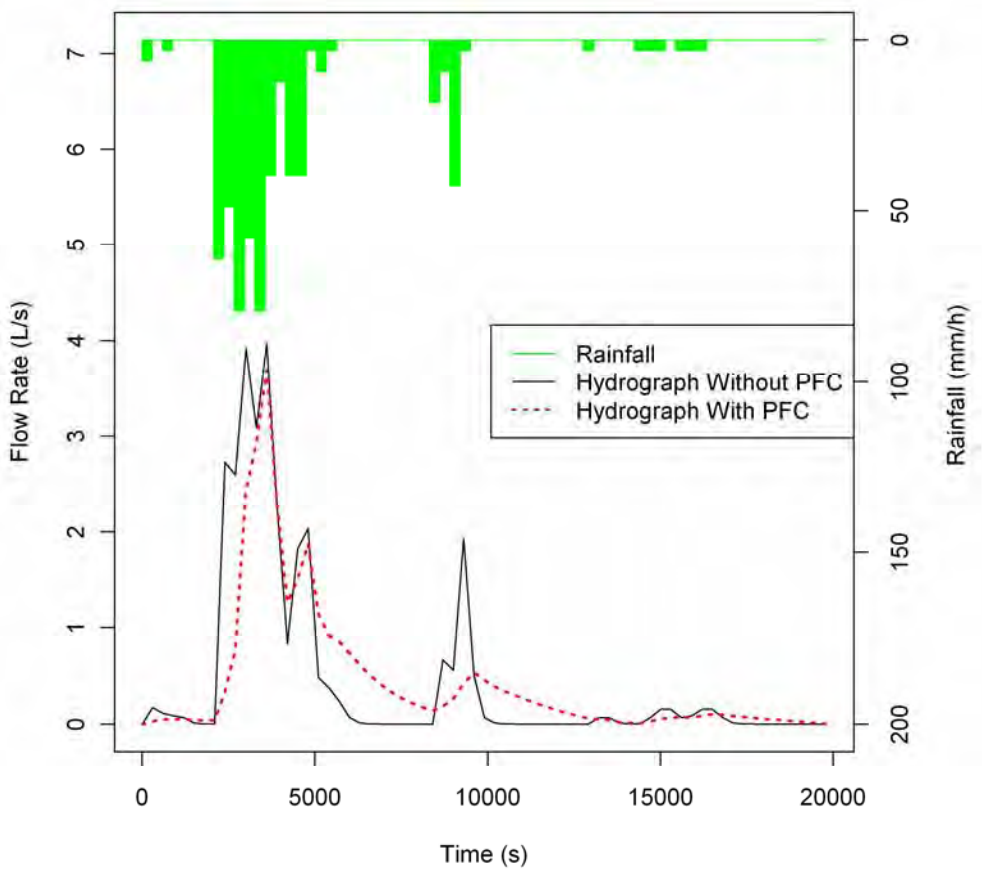

Figure 5-40: Comparison of modeled hydrographs with and without a PFC layer for Loop 360 on July 20, 2007. Plotted flow rates are five minute averages.

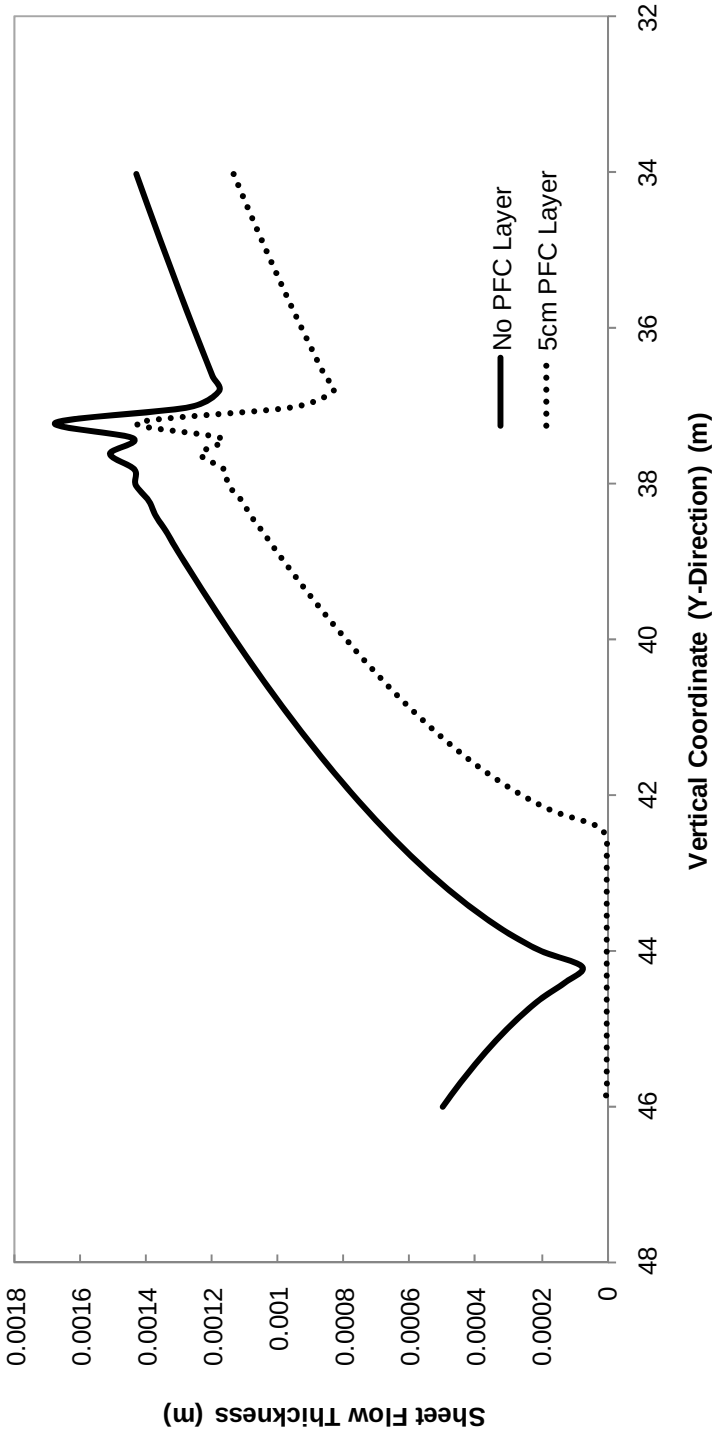

Figure 5-41: Comparison of sheet flow depths with and without a PFC layer horizontal coordinate of 94.42m at Loop 360 on July 20, 2007

5.5.5 Storm event of June 3, 2007

A comparison between model results and field measurements was made for a second storm event to confirm that the results obtained for July 20, 2007 were not coincidental. The event of June 3, 2007 was selected for analysis because the total rainfall depth was around 1-inch and because 90% of the rainfall was measured as runoff, a reasonable mass balance for field sampling. The measured rainfall data was prepared for simulation as outlined previously; all other simulation parameters remained the same.

The modeled hydrograph again shows reasonable agreement with the measured one (Figure 5-42). The model predicted a peak discharge of 2.6 L/s, which is 76% of the measured peak discharge of 3.4 L/s. Statistics of the residuals (the differences between modeled and measured values) are reported in Table 5.5. Compared to the July 20 event, the peak discharge was not modeled as well, but the statistics of the residuals were comparable between the events, suggesting that the model performed consistently in both cases.

A contour plot of the model domain during maximum depth conditions shows that sheet flow occurred over most of the roadway and that sheet flow depths were on the order of 1mm (Figure 5-43). The onset of sheet flow occurred 2.2m from the left hand shoulder and the maximum sheet flow depth of 1.3mm occurred near the right shoulder (Figure 5-44). These values compare favorably to the steady state model, which predicts sheet flow 3.4m from the left shoulder and a maximum sheet flow depth of 1.3mm.

Table 5.5: Summary of statistics of model residuals, all in units of L/s

Statistic	July 20, 2007	June 3, 2007
Mean	-0.029	0.016
Median	0.021	0.035
Standard Deviation	0.24	0.16
Standard Error of the Mean	0.029	0.02

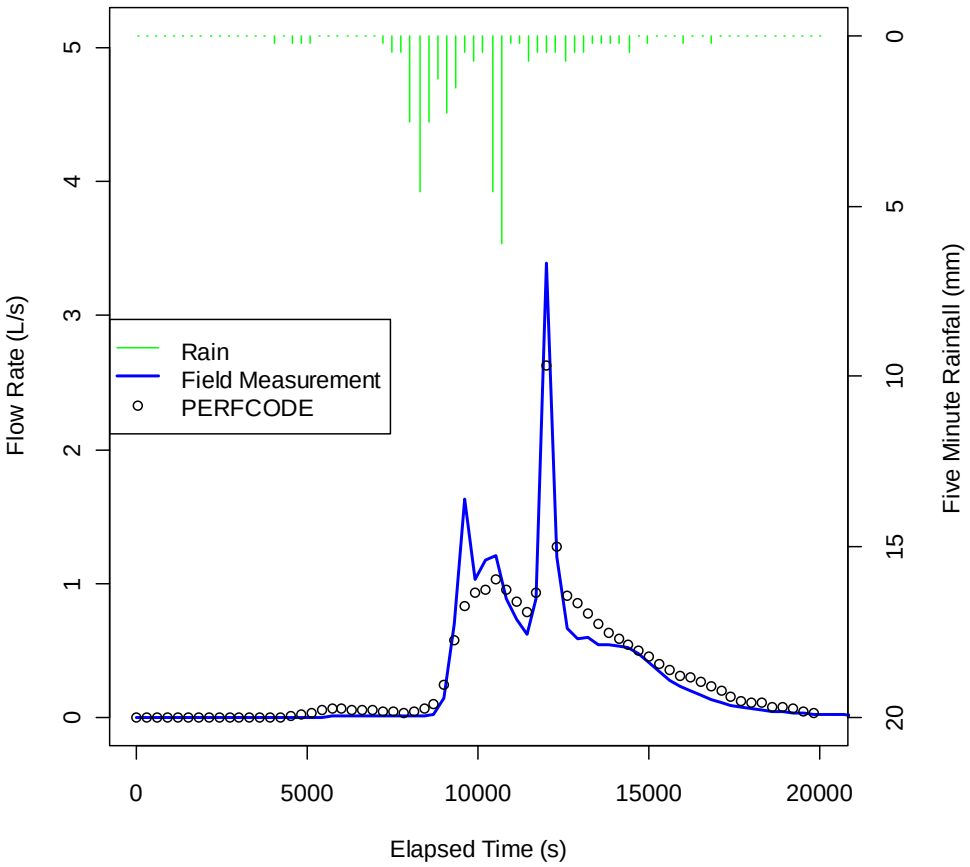

Figure 5-42: Comparison of modeled and measured hydrographs for June 3, 2007

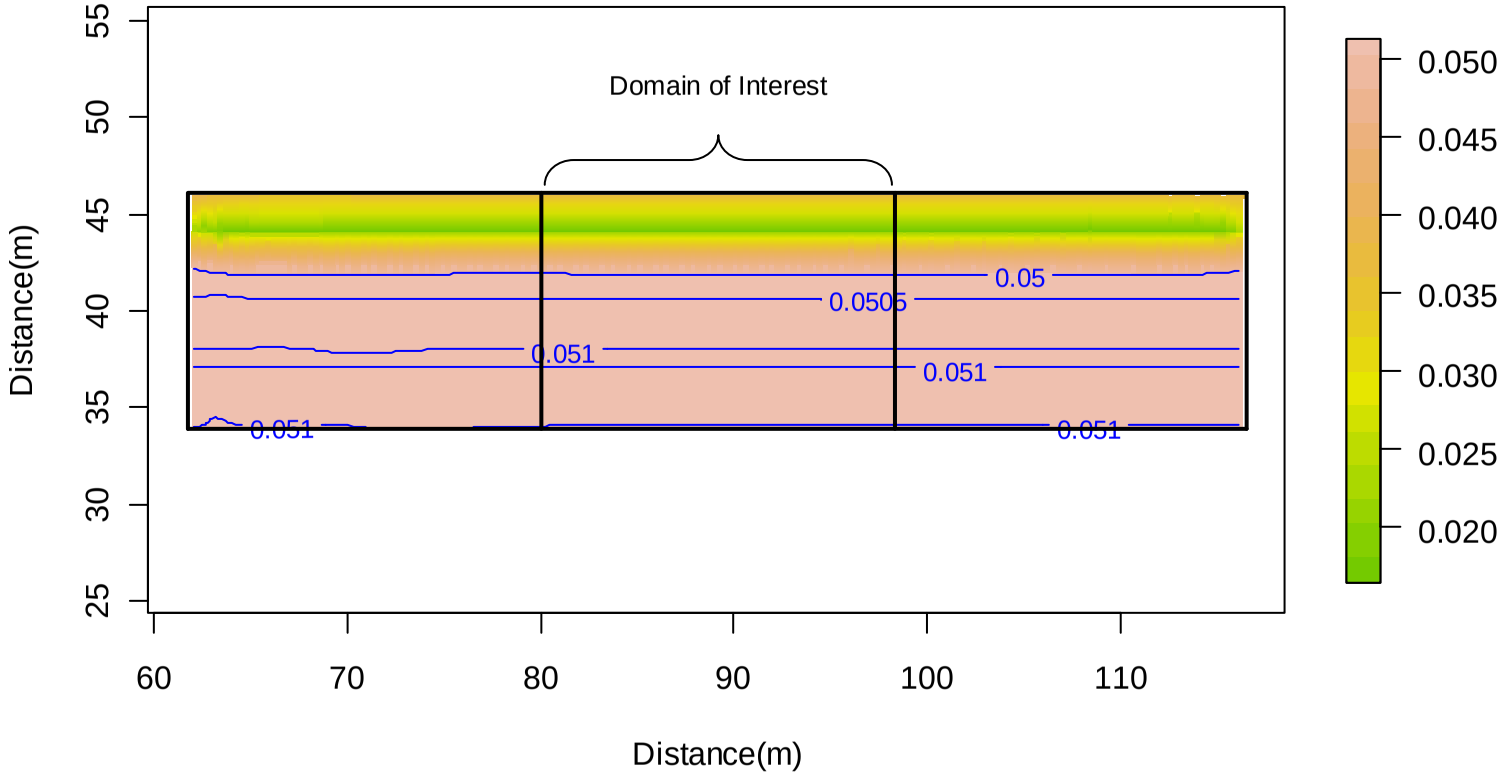

Figure 5-43: Water depth above impervious layer (m) for Loop 360 during maximum depth conditions on June 3, 2007. The PFC thickness was 0.05m; contours correspond to sheet flow conditions.

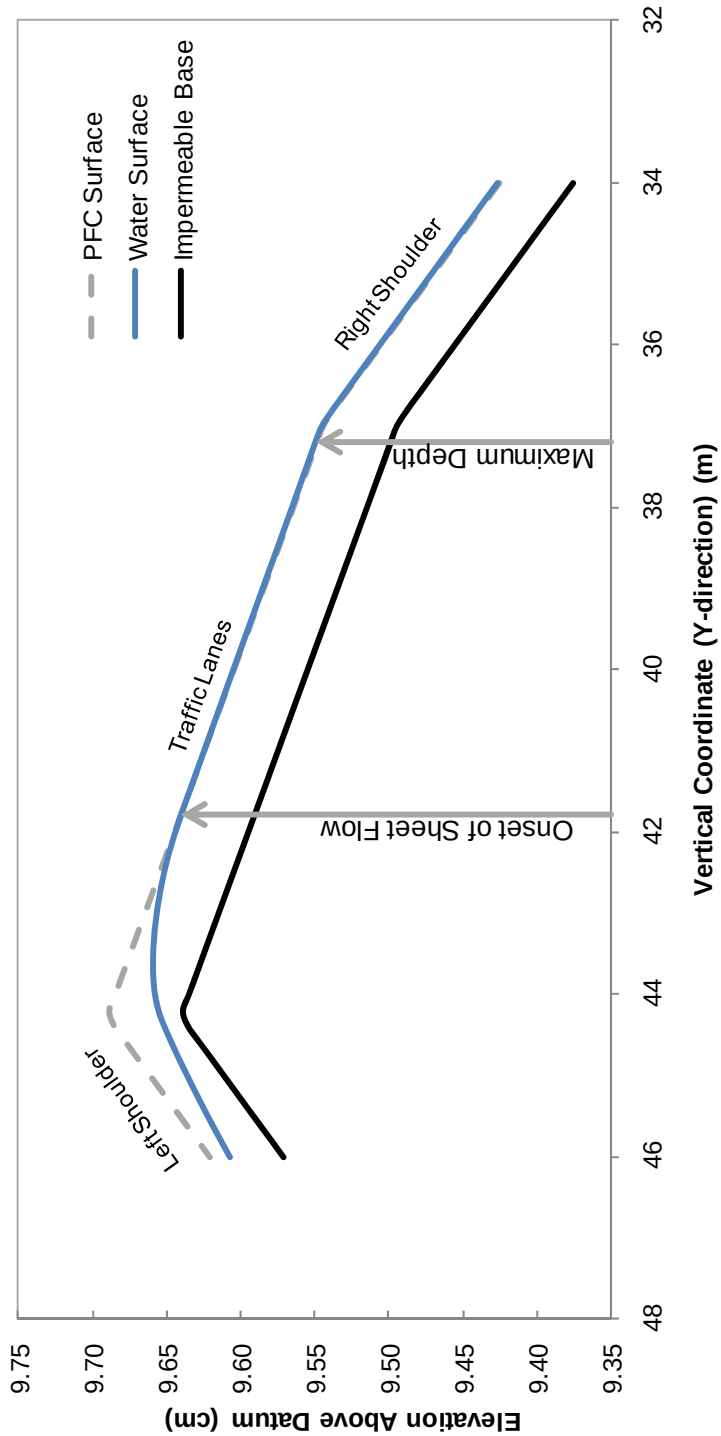

Figure 5-44: Profile through maximum depth section; the horizontal coordinate is 94.42m

5.6 Conclusions and Future Work

5.6.1 Project Summary

This chapter has documented the development, validation, and application of a numerical model that couples the dynamics of overland flow with porous media flow for PFC roadways. The model represents overland flow using the 2-D diffusion wave approximation to the Saint-Venant equations. Porous media flow is described by the Boussinesq equation. Coupling these equations together facilitated water depth predictions at a fine spatial scale. This work has addressed the research objectives which were established in Section 5.1 and are repeated here for reference:

1. Identify governing equations for surface and subsurface flow for the geometry of interest
2. Develop a scheme to couple flow between the surface and subsurface
3. Implement the coupling scheme and numerical methods in a computer model that represents roadway geometry using a coordinate transformation
4. Validate the model using analytical solutions
5. Compare model predictions of runoff with values measured at an existing monitoring site

The governing equations for surface and subsurface flow have been identified and applied to roadway geometry. A scheme to couple the surface and subsurface flow components has been developed. The proposed scheme uses a mass balance approach and adjusts conveyance coefficients based on the flow conditions. A computer model has been developed and validated against steady state solutions that were obtained independently. Predictions of the runoff hydrograph were compared to measured values for the field monitoring site.

Several aspects of this work represent new and unique contributions to the fields of hydraulics and porous media flow:

- The model itself—PerfCode—is a unique tool for understanding highway drainage. It builds on a long tradition of research in highway drainage hydraulics at The University of Texas at Austin.
- The way in which PFC flow and sheet flow are coupled within the model led to a better understanding of the interaction between PFC flow and sheet flow (see Eck et al. 2010).
- The ODE for PFC flow on a converging section has been derived and a numerical solution provided. The solution is useful for understanding how roadway geometry influences drainage behavior and for validating more comprehensive numerical treatments.
- A new boundary condition—the kinematic condition—for PFC flow has been developed and found to have reasonable agreement with field measurements.

5.6.2 Conclusions

Developing the simulation model and applying it to linear sections, converging sections, and the field monitoring site provided insight into the drainage behavior of PFC highways. Conclusions from this work are as follows:

- The kinematic boundary condition developed for PFC flow addresses an important gap in the literature of porous pavement hydraulics: the depth at the boundary can now be estimated for steady state or transient conditions. At the edge of pavement this condition gives a maximum depth in the PFC layer; but at the ends of the domain depth estimates are inconsistent with the domain interior, resulting in a boundary effect. The model domain should therefore be expanded to remove this effect from the area of interest. Use of this boundary condition yielded hydrographs that were consistent with field measurements.
- Predictions of runoff hydrographs for PFC roadways are available for the first time. These hydrographs show that PFC delays the initial discharge from the roadway compared to conventional pavement and that flow in a PFC layer requires a long time to reach steady state. For a constant rainfall case, PFC delayed the initial discharge by 60 seconds and required 50 times more rainfall to reach steady state, though these values depend on problem parameters.
- One dimensional steady state equations remain a powerful tool for engineering design. For the storm investigated in Section 5.5, the 1D steady state equations predicted the location that sheet flow begins within 20cm (7.9 in) of the PerfCode's prediction. The location and magnitude of the maximum sheet flow depth were also closely predicted by the 1D steady state equations. This result confirms that the steady state equations (Charbeneau and Barrett, 2008 and Eck et al., 2010) are suitable for designing the PFC thickness on straight roads.
- The presence of a PFC layer did not affect the timing or magnitude of the peak discharge for the storm that was analyzed, but a later and smaller peak in the runoff hydrograph was delayed and reduced by the PFC layer. This result suggests that PFC has a negligible effect on the hydrology of large events, but can reduce the peak discharge of smaller events.
- During intense storms a PFC layer cannot prevent sheet flow altogether, but it can reduce the time during which sheet flow conditions persist. In the example studied, PFC reduced the duration of sheet flow conditions by about 80% and reduced the maximum sheet flow depth by 25%.

5.6.3 Recommendations for Future Work

Based on the research reported in this chapter, several areas that should be considered for future research are as follows:

- The model required very small time-steps to simulate the measured rainfall. An infinite number of rainfall patterns are consistent with the five-minute rainfall data that was measured. Future work could include using a smoother rainfall function to

see if the model's stability properties could be improved (e.g. take larger time-steps).

- Measured values of the hydraulic conductivity for PFC are at the high end of the acceptable range for Darcy's law on typical roadway slopes. Related experimental and modeling efforts conducted by Klenzendorf (2010) used the Forchheimer equation to model flow through PFC and found the Forchheimer coefficients. Future work could update the model developed here to use Forchheimer's equation in place of Darcy's law. Such an update need only modify the subroutine for computing conveyance coefficients. Since the Darcy's law problem is already non-linear, the non-linearity introduced from Forchheimer's equation would be handled within the existing non-linear iteration loop.
- Small time steps (0.1s) were needed for non-smooth rainfall functions and high rainfall intensities. This small time step dramatically increased the time required for a model run. It also is based on the lowest common denominator—it is likely that larger time steps would be stable for part of the simulation time. An adaptive time stepping scheme could improve the run time while maintaining stability.
- The statistics of the residuals (modeled minus measured discharges) were similar for the two storms investigated. Future work should simulate additional storm events to further quantify the uncertainty in the model predictions.
- The model formulation is intended to allow simulations of more complex roadway geometry such as a superelevation transition or sag vertical curves. Although it is believed that major changes would not be required to deal with such geometries, they have not been attempted.

Chapter 6. Test Procedure

6.1 Introduction

An accurate, repeatable field test protocol is essential for determining the in-situ hydraulic conductivity of a PFC overlay throughout its life. Such a test will give an indication of the extent of clogging that has occurred in the pore space of the PFC. In addition, determining the in-situ hydraulic conductivity is necessary to determine if the PFC provides adequate drainage to prevent surface runoff during rainfall events. Tracking the hydraulic conductivity over time will help indicate whether other benefits, specifically the water quality benefits, of the PFC are expected to persist in the near future.

TxDOT currently has a field test protocol which is defined in specification Tex-246-F "Permeability or Water Flow of Hot Mix Asphalt" of the TxDOT Construction Division. The field test procedure is an empirical test that is most useful to confirm that excessive compaction did not occur during construction. The test can be performed immediately following roller compaction during construction or on an existing PFC overlay. The current TxDOT PFC field test consists of a falling head test in which water flows vertically through a 6 inch diameter PVC pipe which is 18 inches in length. At the interface between the PVC pipe and the PFC surface, plumber's putty is used to create a seal and avoid any leakage at the interface. Time measurements are started at a water depth of 14.5 inches above the PFC surface, and the time measurement is stopped at a water depth of 3.5 inches above the PFC surface. Therefore, the data collected consists of the time for the PFC to drain roughly 311 in^3 of water. The TxDOT specification suggests that the typical time measurement for newly constructed PFC overlays should be less than 20 seconds. However, there is no indication of what the hydraulic conductivity for this measurement might be. Figure 6-1 shows the TxDOT test apparatus during testing.

Figure 6-1 Current TxDOT Field Test Apparatus

Although the current TxDOT field test is useful to determine when adequate compaction of the PFC overlay has been achieved during the construction process, it cannot be used to measure the hydraulic conductivity because the region of saturated flow is not controlled. To overcome this limitation, a new field test using a similar falling head procedure is proposed together with a theoretical basis for determining the hydraulic conductivity of the PFC overlay.

6.2 Theoretical Basis

Due to the lack of ability of the current TxDOT field test protocol to estimate the in-situ hydraulic conductivity, a new field test protocol is proposed. The proposed test can be used to determine the hydraulic conductivity from a theoretical basis. The flow conditions through PFC have been shown to follow a nonlinear relationship. This nonlinear relationship is characterized using a modified Forchheimer equation. The flow distribution through PFC is similar to the flow of heat through a disk. Using this analogy, a solution to the heat problem given by Carslaw and

Jaeger (1959) can be applied to the PFC case. Modifications to the Carslaw and Jaeger analytic equations allow for an estimate of the hydraulic conductivity under nonlinear flow conditions.

Flow through PFC under the large head values experienced during the field test results in a nonlinear flow relationship. This relationship does not follow the typical linear flow relationship in porous media defined by Darcy's Law. The nonlinear flow relationship can be characterized through the modified Forchheimer equation as follows:

$$h_s(t) = \alpha Q + \beta Q^2 \qquad (6.1)$$

In Equation (6.1), hs is the head in the standpipe which is a function of time, Q is the volumetric flow rate, α and β are the modified Forchheimer coefficients specific to the PFC porous media and geometry of the test setup. The modified Forchheimer coefficients must be determined from the falling head data in order to determine the hydraulic conductivity. Three time-depth measurements are needed to experimentally determine the two Forchheimer coefficients. Equation (6.1) can be solved for Q to obtain:

$$Q = \frac{\alpha}{2\beta}\left[\sqrt{1+\frac{4\beta h_s}{\alpha^2}} - 1\right] \qquad (6.2)$$

For a falling head permeability test, the flow rate is set equal to the negative change in head in the standpipe times the area of the standpipe. Therefore, the falling head equation can be defined as:

$$-\pi R_s^{\,2}\frac{dh_s}{dt} = \frac{\alpha}{2\beta}\left[\sqrt{1+\frac{4\beta h_s}{\alpha^2}} - 1\right] \qquad (6.3)$$

R_s is the radius of the standpipe which is equal to two inches for the proposed test apparatus. As previously mentioned, the test procedure requires three time-depth measurements. Therefore, h_s will be measured at three times, and these measurements will be used to determine α and β. Equation (6.3) can be integrated with respect to time to give the following:

$$\frac{t}{\pi R_s^{\,2}\alpha} = \sqrt{1+\frac{4\beta h_s(0)}{\alpha^2}} - \sqrt{1+\frac{4\beta h_s(t)}{\alpha^2}} + \ln\left(\frac{\sqrt{1+4\beta h_s(0)/\alpha^2}-1}{\sqrt{1+4\beta h_s(t)/\alpha^2}-1}\right) \qquad (6.4)$$

Equation (6.4) is the modeled time for nonlinear flow during a falling head test. The values of α and β can be determined from Equation (6.4) by providing a first estimate for each coefficient and then changing these values until the modeled times from Equation (6.4) match the measured times from data collected during the falling head test.

The first estimates for α and β can be determined by analyzing Equation (6.1) with only one parameter. To determine the first estimate for α, we would have $h_s = \alpha Q$. This can then be solved for Q and used in the falling head equation to obtain the following:

$$\frac{t}{\pi R_s^{\,2}\alpha} = \ln\left(\frac{h_s(0)}{h_s(t)}\right) \tag{6.5}$$

Similarly, β can be found from the nonlinear portion of the Forchheimer equation $h_s = \beta Q^2$. Integrating the falling head equation gives:

$$\frac{t}{2\pi R_s^{\,2}\sqrt{\beta}} = \sqrt{h_s(0)} - \sqrt{h_s(t)} \tag{6.6}$$

Equations (6.5) and (6.6) can be used to provide an initial estimate for the coefficients α and β, respectively.

Once the Forchheimer coefficients have been determined from the experimental data, the hydraulic conductivity can be calculated as follows:

$$K = \frac{1}{4R_s\alpha F} \tag{6.7}$$

K is the hydraulic conductivity and F is a shape factor that depends on the geometry of the flow conditions. Equation (6.7) is derived from Carslaw and Jaeger (1959, pg. 215) with a modification to account for the nonlinear flow relationship and the no flow boundary conditions created by the test apparatus and underlying impervious asphalt surface. The shape factor F depends on the radius of the standpipe R_s, the radius for which flow is forced through the PFC (as opposed to surface runoff) R_c, and the thickness of the PFC layer b_c. The thickness of the PFC layer is estimated from core samples extracted from the roadway. For the proposed test apparatus described in the next section, the shape factor is $F = 0.66$. However, the thickness of the PFC overlay is not uniform, so this value cannot be determined precisely in the field.

The above theoretical basis makes several assumptions about the flow distribution. First, it is assumed that the pore space in the PFC is completely saturated such that no air voids exist. Second, it assumes that flow exits the porous media sample of interest in a purely radial flow direction. This means that there is no surface runoff and no vertical flow at the outflow boundaries. Third, the only governing equation is the continuity equation (conservation of mass). This means that the effects of gravity are not important. Fourth, the Carslaw and Jaeger analysis is for steady state conditions. Finally, the hydraulic conductivity is determined based only on the α coefficient. This will give the maximum hydraulic conductivity of the PFC, which will exist for very small flow rates. The range of flow rates during actual rainfall events is expected to be within the small flow rate range such that the hydraulic conductivity calculated is representative of actual flow conditions.

6.3 Field Test Development

This section describes the proposed field test apparatus and the development of the test procedure. A discussion is included for various issues experienced in the field and how these issues were addressed during the test development. Sensitivity to the time measurements obtained during testing is analyzed to determine the errors that may be involved during the testing process.

6.3.1 Test Apparatus

The proposed field test apparatus is shown in Figure 6-2. The apparatus consists of a solid metal base plate with a diameter of 18 inches. The vertical standpipe has a diameter of 4 inches (R_s = 2.0 inches) and a length of 18 inches. Vacuum grease is placed on the underneath side of the base plate to prevent water from flowing at the interface between the PFC surface and the plate. The vacuum grease enters the surface voids of the PFC and prevents vertical flow under the base plate. Therefore, radial porous media flow is created for a radius of R_c = 9.0 inches. Outside of the base plate, surface runoff occurs, and the theoretical basis for determining the hydraulic conductivity is no longer valid. This flow distribution allows for use of the Carslaw and Jaeger (1959) equations described in the previous section. The proposed field test apparatus serves to create vertical inflow from the standpipe which turns and flows radially under the base plate.

The field test is conducted by first flushing a volume of water through the standpipe in order to saturate the pore space beneath the base plate. The standpipe is then filled with water and three time-depth measurements are recorded. Time is started at an initial head value, an intermediate time is taken at half the initial head value, and time is stopped at the final head value.

Figure 6-2 Proposed Field Test Apparatus

6.3.2 Investigation of Saturated Pore Space

One of the assumptions in the theoretical development of the test process is the pore space must be completely saturated. Due to the slope of the roadway in the field, water is constantly flowing down gradient toward the roadway shoulder by gravity. This suggests that the

pore space may not be entirely saturated despite the initial volume of water allowed to drain through the test apparatus prior to testing. In the event that the pore space is not completely saturated, the hydraulic conductivity measurement would result in an artificially high hydraulic conductivity. This increase in hydraulic conductivity is a result of some of the water acting to fill the pore space of the PFC.

In order to determine whether or not saturated conditions were achieved, a diffuser was built that will drip water into the PFC pore space upstream from the testing location. The diffuser consists of a five foot long piece of PVC pipe attached to a 50 gallon water supply tank. The diffuser and water supply tank are shown in Figure 6-3 and Figure 6-4, respectively. The diffuser has nine holes of ¼ inch diameter drilled through the PVC. The holes are spaced six inches apart and allow water to drip out. The flow rate from the diffuser can be controlled by a valve attached upstream of the diffuser.

Figure 6-3 Testing Prior to Using Diffuser Upstream

Figure 6-4 50 Gallon Water Supply Tank

Prior to using the diffuser, three falling head field tests were conducted. The average of these three tests were used to determine the hydraulic conductivity. The diffuser was then allowed to drip water for 10 minutes. A total of roughly 20 gallons of water entered the PFC pore space. It appeared with this volume of water in the pore space, that the pores had become completely saturated. A second set of three falling head field tests were conducted after use of the diffuser to determine the hydraulic conductivity. Prior to the use of the diffuser, the hydraulic conductivity was calculated as 1.24 in/s (3.14 cm/s). After the diffuser presumably saturated the pore space, the hydraulic conductivity was measured as 1.36 in/s (3.45 cm/s). These two values are sufficiently close that it can be assumed the PFC pore space was completely saturated in both cases. Furthermore, the hydraulic conductivity after use of the diffuser was slightly higher than prior. If the pore space was not saturated, we would expect to see a decrease in hydraulic conductivity after using the diffuser. This confirms our assumption of saturated conditions.

6.3.3 Comparison with Constant Head Field Test

The Carslaw and Jaeger equation to determine the hydraulic conductivity is based on steady state conditions. This would apply to a constant head permeability test, as opposed to the falling head test used in the field. A falling head test serves to theoretically represent an infinite number of constant head tests. In order to determine whether a series of constant head tests is equivalent to a falling head test, several constant head tests were attempted in the field. These tests require a large amount of water to conduct due to the ease of flow through the PFC as well as the time required to reach steady state conditions. The head is measured as a constant in the standpipe, and the flow rate is measured with a stopwatch and graduated bucket. In addition, it is difficult to obtain precise measurements due to the large flow rates needed. Figure 6-5 shows a constant head test being conducted. The water supply comes from the same 50 gallon water tank, which must be refilled with water from smaller buckets during the test in order to maintain a constant water level in the tank. The constant water level in the tank is necessary to obtain a constant flow rate.

Figure 6-5 Constant Head Test

Four constant head tests were conducted in the field, followed by one falling head test. The results are shown in Figure 6-6 below. The Forchheimer coefficients in Equation (6.1) can be determined by fitting a curve to the four constant head data points by minimizing the standard error between the model and the four constant head tests. The blue curve is the nonlinear flow relationship obtained by fitting to the four constant head tests. The pink curve is the nonlinear flow relationship produced from the falling head test. The similar shape between the constant head and falling head test results suggest that the falling head test serves as a good comparison to a series of constant head tests.

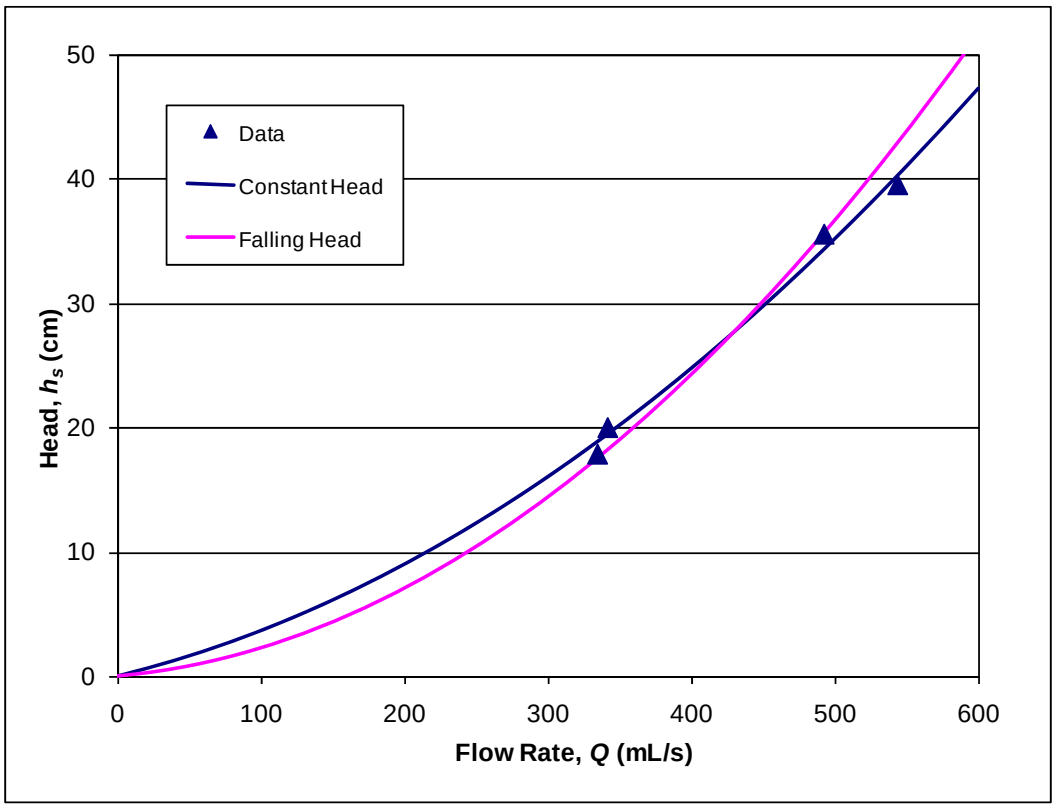

Figure 6-6 Comparison between Constant and Falling Head Tests

6.3.4 Effect of Roadway Slope

The final assumption that was investigated is the impact of gravity on the flow conditions. The longitudinal slope and cross slope of the roadway surface create a constant conveyance of water through the PFC overlay due to gravity alone. Therefore, gravity may have an effect on the field conditions, which would result in an artificially high hydraulic conductivity measurement. This is because water will be transported through the porous media by the established head in the standpipe as well as by gravity. Since gravity is not included in any of the falling head equations, the transport of water by gravity would be attributed to the head difference, resulting in a high hydraulic conductivity estimate.

In order to determine the impact of the slope of the roadway, we can estimate the flow rate that is produced by gravity alone and then compare that to the actual flow rate that we create in the falling head test. During a typical falling head test using the proposed field test, the total water drained is roughly 180 in^3. The falling head test takes roughly 12 seconds on Loop 360. This results in an average flow rate of approximately 15 in^3/s. To determine the flow rate produced by the roadway slope, we can use the Forchheimer equation. With a roadway slope of 4.0% for flow across the width of the test apparatus (18 inches), gravity alone will produce a flow rate of approximately 0.015 in^3/s or 0.1% of the flow produced by the falling head test. Therefore, since the roadway slope produces such a small flow rate compared to the flow rate produced by the falling head test, the effect of the roadway slope can be neglected. This means the only significant governing equation is the continuity equation, which is the basis of our theoretical model.

6.3.5 Model Sensitivity

When conducting a field test it is often difficult to obtain accurate measurements. Therefore, a brief discussion is provided here to show the impact of the sensitivity the falling head model equations can have on the resulting hydraulic conductivity. In order to conduct a sensitivity analysis, we are mostly concerned with the time measurements. The impact of small changes in time measurements can be determined by artificially adding or subtracting small time changes to actual field data.

The original data was collected on Loop 360 and had the following measurements: middle time t_m = 3.89 sec, final time t_f = 11.12 sec, and hydraulic conductivity K = 1.44 in/s (3.66 cm/s). The sensitivity analysis based on the time measurement is conducted by adding or subtracting a small value from the actual data and then determining the resulting hydraulic conductivity. Figure 6-7 shows the results of this analysis. The x-axis represents the change in time measurement and the y-axis represents the resulting change in hydraulic conductivity. Therefore, for a zero change in time, we see a zero change in hydraulic conductivity. The blue line represents changes to the t_m value. We can see that for small increases in t_m, the hydraulic conductivity increases significantly. For example, if t_m = 4.09 sec (as opposed to the actual 3.89 sec), the resulting hydraulic conductivity is roughly 2.75 in/s (7.0 cm/s) larger. This is nearly three times the original estimated hydraulic conductivity and shows that small errors in the middle time measurement can have a large impact on the resulting hydraulic conductivity. For decreases in t_m, the hydraulic conductivity will decrease, but to a lesser extent.

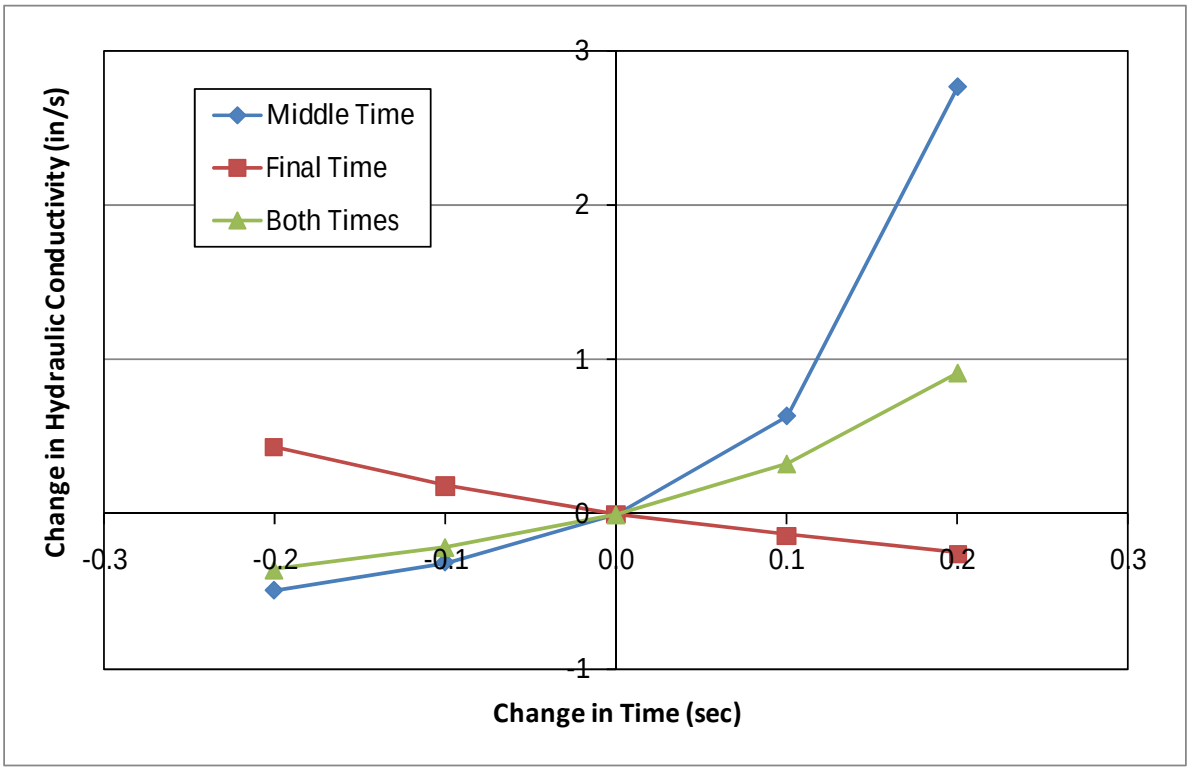

Figure 6-7 Sensitivity of Time Measurements on Hydraulic Conductivity

Similarly, we investigate changes to the final time shown as the red line in Figure 6-7. The opposite trend is seen in changes to t_f, i.e. increases in t_f cause a decrease in K and vice

versa. As expected, if we change both t_m and t_f by the same amount, we will obtain a change in hydraulic conductivity somewhere between the two individual time measurement changes. This is shown by the green line in Figure 6-7. Therefore, small changes in the time measurements can drastically impact the resulting hydraulic conductivity measurements. This analysis helps to give an idea of the reliability of the in-situ hydraulic conductivity measurements as well as the possible errors associated with the measurements. However, the resulting hydraulic conductivity measurements will be the same order of magnitude regardless of small changes in the time measurements.

6.4 Proposed Field Test Procedure

Use this test procedure for existing PFC pavements to determine the in-situ hydraulic conductivity. The following materials are needed to complete the test:

- *Proposed field test apparatus*: used to channel water into the PFC surface and create radial flow without surface runoff; the standpipe should be graduated in divisions of 0.01 ft (0.12 in.) (see Figure 6-2).
- *Stopwatch*: used to record the time for water to drain in divisions of 0.01 seconds; must have a split function to record an intermediate time during the test.
- *Vacuum grease*: used to seal the PFC surface under the base plate of the test apparatus; Dow Corning silicon high vacuum grease works well, and typically 7 to 8 ounces (one and a half tubes) is sufficient to cover the base plate surface.
- *Water*: roughly 12 gallons of water is sufficient to conduct one falling head test.

The test procedure for the proposed field test is a falling head permeability test, similar to the current TxDOT procedure. The following steps represent the test procedure:

1) Select an area of the existing PFC surface to test. Remove any debris on the surface and choose a sufficiently flat area so that the base plate of the test apparatus can sit flat on the roadway surface and create a good seal with the PFC.
2) Place roughly 7 to 8 ounces of vacuum grease on the underneath side of the base plate. Spread the vacuum grease by hand to create a uniform distribution.
3) Place the test apparatus onto the PFC pavement surface. Use enough force (typically standing on the base plate is sufficient) to create a watertight seal between the base plate and the pavement surface such that the vacuum grease enters the surface voids of the PFC.
4) Flush an initial volume of water though the test apparatus to saturate the pore space. Typically about 5 gallons of water is necessary for sufficient saturation.
5) Fill the test apparatus with water to the top of the standpipe.
6) Start the timing device when the water level reaches the marking of 1.2 ft on the standpipe. This corresponds to a water depth of 15.9 in. above the PFC surface.

7) Use the split function on the timing device when the water level reaches the marking of 0.6 ft on the standpipe. This corresponds to a water depth of 8.7 in. above the PFC surface.
8) Stop the timing device when the water level reaches the marking of 0.0 ft on the standpipe. This corresponds to a water level of 1.5 in. above the PFC surface.
9) Record the three time-depth measurements.
10) Repeat steps 5 through 9 until a total of three falling head tests are completed. Average the three time measurements to get the average time-depth measurement necessary to calculate the hydraulic conductivity.

The above proposed field test procedure results in three time-depth measurements that are averaged from three falling head tests. With these three time-depth measurements, the modified Forchheimer coefficients α and β can be experimentally determined. The hydraulic conductivity can then be calculated for the PFC layer at the testing location. The water depths suggested above (15.9 in., 8.7 in., and 1.5 in.) are somewhat arbitrary. Three other water depths could be used, as long as they are the same for each falling head test that will be averaged. In addition, an initial water depth greater than one foot is ideal for the test, and the intermediate water depth should be roughly half of the initial depth. The final water depth should be much closer to the PFC surface without actually reaching the pavement surface.

6.4.1 Example Calculation to Determine Hydraulic Conductivity

An example is provided here to show how to convert the three time-depth measurements into the estimated in-situ hydraulic conductivity. Use of the Solver function in MS Excel is necessary to complete the calculations. The test analyzed in the model sensitivity section will be used here. This test was conducted on the shoulder of Loop 360 on June 29, 2008. The dimensions of the test apparatus and PFC thickness are necessary in estimating the hydraulic conductivity. The PFC thickness is estimated from the average thickness of 12 core samples that were extracted near the time of the field test. These dimensions are as follows: R_s = 2.0 in., R_c = 9.0 in., and b_c = 1.627 in. The resulting shape factor for these dimensions is F = 0.66. The three depth measurements are: $h_s(t_0)$ = 15.9 in., $h_s(t_m)$ = 8.7 in., and $h_s(t_f)$ = 1.5 in. The three corresponding averaged time measurements with plus/minus one standard deviation are: t_0 = 0.0 sec, t_m = 3.89±0.14 sec, and t_f = 11.12±0.22 sec.

The first step is to obtain initial estimates for α and β using Equations (6.5) and (6.6), respectively. The initial estimates are made using the initial time-depth and final time-depth pairs. The initial estimates for the data presented above are α = 0.3749 s/in^2 and β = 0.0257 s^2/in^5. These values will be used to solve for the modeled times using Equation (6.4). The modeled time for t_m using the initial estimates for α and β is t_m = 5.84 sec. Similarly, the modeled time for t_f using the initial estimates for α and β is t_f = 18.11 sec.

Clearly these values do not match the collected data provided above. Therefore, we need to change α and β such that the modeled times match the measured times. This is accomplished using the Solver function in MS Excel. In order to obtain similar model times and measured times, we must minimize the error between the two. The error can be represented as the squared difference between the modeled time and measured time. This is represented as follows:

$$E = (t_{m,d} - t_{m,m})^2 + (t_{f,d} - t_{f,m})^2 \quad (6.8)$$

In Equation (6.8), E is the error that must be minimized, $t_{m,d}$ and $t_{f,d}$ are the middle and final times for the collected data, and $t_{m,m}$ and $t_{f,m}$ are the middle and final times using the model equations. The initial error is E = 52.62 sec^2. The Solver function in MS Excel can be used to minimize E by changing α and β. The result of using the Solver gives $E = 7.77\times10^{-9}$ sec^2, which corresponds to α = 0.1315 s/in^2 and β = 0.0166 s^2/in^5. We have now obtained the two modified Forchheimer coefficients for the PFC overlay.

The in-situ hydraulic conductivity can now be estimated using Equation (6.7). For this test, the result is K = 1.44 in/s. This provides the best estimate of hydraulic conductivity for the falling head data. However, due to the uncertainty in the time measurements, there is uncertainty in the estimate for hydraulic conductivity. This completes the calculations necessary for determining the hydraulic conductivity from the three time-depth measurements.

6.4.2 Hydraulic Conductivity Field Results

Both the current TxDOT field test and the proposed field test were performed on three roadways around Austin: Loop 360 near Bull Creek, FM 1431 near Hur Industrial Blvd, and RR 620 near Cornerwood Dr. At each of the three sites, both the proposed method and current TxDOT method were conducted. In addition, multiple proposed field tests were conducted on the shoulder of Loop 360 in order to better define the test procedure as well as investigate the issues described above.

Table 6.1 gives the results of the current TxDOT field test for each of the three roadways. All the tests on Loop 360 achieved the TxDOT guideline of less than 20 seconds drainage time. However, both FM 1431 and RR 620 were much higher than this guideline suggesting that the pore space in the PFC overlay had become clogged and no longer provides proper conveyance of water.

Table 6.1: Current TxDOT Field Test Results

Date	Road	Time (sec)
6-29-08	Loop 360	17.84
6-29-08	Loop 360	19.81
2-2-09	Loop 360	14.28
2-2-09	Loop 360	16.45
2-2-09	FM 1431	112.61
2-2-09	RR 620	69.73

Table 6.2 gives the results of the proposed field test for each of the three roadways. Of the eight tests conducted on Loop 360, very similar results were obtained, with the exception of the tests conducted in November 2008. The tests in November 2008 appear to have hydraulic conductivity significantly higher than the others. However, these tests were performed after a series of constant head tests. Therefore, there is a possibility that the large flow rates and large volume of water flowing through the PFC during the constant head tests might have flushed out some sediment in the pore space which would effectively increase the hydraulic conductivity. FM 1431 and RR 620 both have smaller hydraulic conductivity values, which correspond to the same trends seen in the TxDOT test.

Table 6.2: Proposed Method Field Test Results

Date	Road	t_m (sec)	t_f (sec)	K (in/s)
6-29-08	Loop 360	3.89	11.12	1.44
6-29-08	Loop 360	4.28	12.36	1.16
9-25-08	Loop 360	4.07	11.75	1.24
9-25-08	Loop 360	4.17	11.90	1.36
11-9-08	Loop 360	3.88	10.63	3.17
11-23-08	Loop 360	3.27	9.05	2.95
2-2-09	Loop 360	4.46	12.88	1.12
2-2-09	Loop 360	4.30	12.17	1.49
2-2-09	FM 1431	17.35	52.16	0.24
2-2-09	RR 620	9.17	25.86	0.88

6.5 Conclusions

The current TxDOT field test for determining the permeability of a PFC overlay is an empirical test that is not sufficient to provide an estimate of the in-situ hydraulic conductivity. It does, however, have a benefit in providing a guideline for evaluating the degree of compaction of the PFC overlay during the construction process. Due to the lack of ability to estimate the in-situ hydraulic conductivity, a new field test protocol has been developed. The proposed test procedure has a theoretic basis which allows for the ability to estimate the in-situ hydraulic conductivity. The test procedure, example calculations, and collected data have been provided in this report.

There are several assumptions that are necessary in developing the theoretical basis for the proposed field test protocol. When possible, these assumptions have been investigated and confirmed in order to determine whether they are being achieved in the field. A sensitivity analysis on the time measurements is provided. Certain small changes in the time measurements can result in large changes to the calculated hydraulic conductivity. Therefore, the resulting estimate for hydraulic conductivity has an uncertainty associated with it.

Chapter 7. Whole Life Cost Comparison

7.1 Introduction

Within the recharge zone for the Edwards Aquifer, the Texas Commission on Environmental Quality (TCEQ) requires 80% removal of Total Suspended Solids (TSS) from runoff of impermeable surfaces. This research indicates that PFC achieves this removal of suspended solids. The objective of this chapter is to understand the economic feasibility of PFC, as compared with sand filters, and vegetated filter strips, to meet the TCEQ requirements for TSS removal in the Edwards zone.

Sand filters have been widely used in the Edwards zone to achieve the required removal. In addition to construction costs, sand filters require annual maintenance and occupy valuable land. For highway projects, university research indicates that vegetative buffers can also remove 80% of TSS. Vegetative buffers require more land than sand filters, but no maintenance. By containing the treatment within the pavement itself, PFC eliminates the need for land dedicated to stormwater treatment. This analysis computes the net present value of incremental costs associated with three treatment alternatives:

- Vegetated filter strips,
- Austin style sand filters, and
- Permeable Friction Course (PFC).

The incremental cost of each alternative will differ for each project. The purpose of this analysis is not to provide an opinion of probable construction cost, but rather to identify projects in which PFC may provide cost effective treatment of runoff. To this end, an economic model was developed to calculate the cost for each treatment alternative based on variable project parameters. The cost for each alternative considers the project parameters, TCEQ design requirements, and estimated construction costs.

7.2 Economic Model Development

This section describes the development of an economic model that compares vegetated filter strips, sand filters, and PFC for treating stormwater from highways. The model is implemented in an Excel spreadsheet. Like the spreadsheet, this section has a section for project parameters that apply to all three treatment alternatives and a section for each alternative. The model computes the net present value cost for each treatment option.

7.2.1 Project Parameters

For this model, the project parameters are:

- Roadway length
- Paved width
- Right of way width
- Analysis period in years

- Cost of capital
- Inflation rate
- Unit cost for land

These parameters are common to all treatment options. This model assumes that the roadway is straight, so the effect of curves is neglected. The relationship between the geometric parameters is shown in Figure 7-1. The model assumes that the road is centered in the right of way so the buffer width can be calculated. The model also assumes that the entire roadway length drains to a single sand filter. Projects with multiple sand filters should use a spreadsheet for the drainage area of each filter.

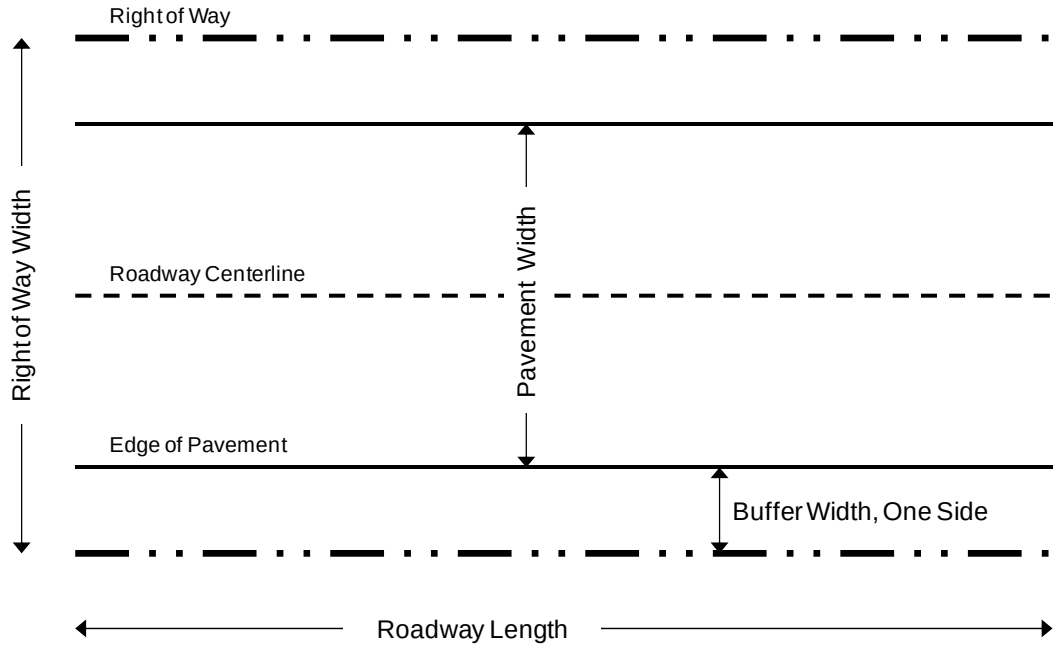

Figure 7-1: Sketch of Geometric Parameters

7.2.2 Vegetated Filter Strip

Vegetated filter strips are frequently used for stormwater treatment when abundant land is available. TCEQ rules require a buffer width of 15 feet for each side of the road (TCEQ 2005, pg 3-55). Where such a buffer is available and the slope and cover requirements are met, the TCEQ rules are satisfied and no further treatment is required. For the purposes of this evaluation, the incremental cost of a vegetated filter strip is the cost of acquiring sufficient right of way.

7.2.3 Sand Filters

Sand filters are the traditional way to meet TCEQ requirements within the Edwards zone. The total cost of a sand filter consists of construction costs, land costs, and maintenance costs. Developing a cost model for sand filters that varies with the roadway parameters was the most complicated part of this economic model. A separate tab of the model spreadsheet was created to design a generic sand filter according to TCEQ requirements. This design is used to estimate

material quantities which are applied to unit prices to estimate the construction cost. Unit prices for sand filter construction were derived from the RS Means Manual. Additional land required for the sand filter is priced using the cost specified as a project parameter. Maintenance costs were obtained from literature values. The following sections provide additional detail for each cost component.

7.2.3.1 Construction Costs

Very little data is available relating the size of a sand filter to its construction cost. To overcome this difficulty, a worksheet was developed to design a sand filter based on TCEQ requirements and some rudimentary design assumptions. The filter gets bigger or smaller based on the characteristics of the drainage area. The design is used to derive construction quantities.

The design assumes that the entire paved area—and no other area—drains to the sand filter. The worksheet carries out the design calculations described in TCEQ Manual RG-348 Technical Guidance on Best Management Practices for a full sedimentation system. The calculations essentially consist of finding the required water quality volume from the drainage area characteristics and tabulated BMP efficiency. The design volume and required filtration area are computed from the water quality volume.

Once the filter volume and area have been established, excavation volumes are calculated for a rectangular filter layout with trapezoidal cross section (Figure 7-2). This design assumes that the sand filter is an earthen structure. The size of the basin liner is also computed from this layout. Within the sand filter design worksheet, the ratio between the width and length of the basin and the side slope may be specified by the user. The default aspect ratio is 2:3 (W:L) and the default side slope is 3:1 (H:V).

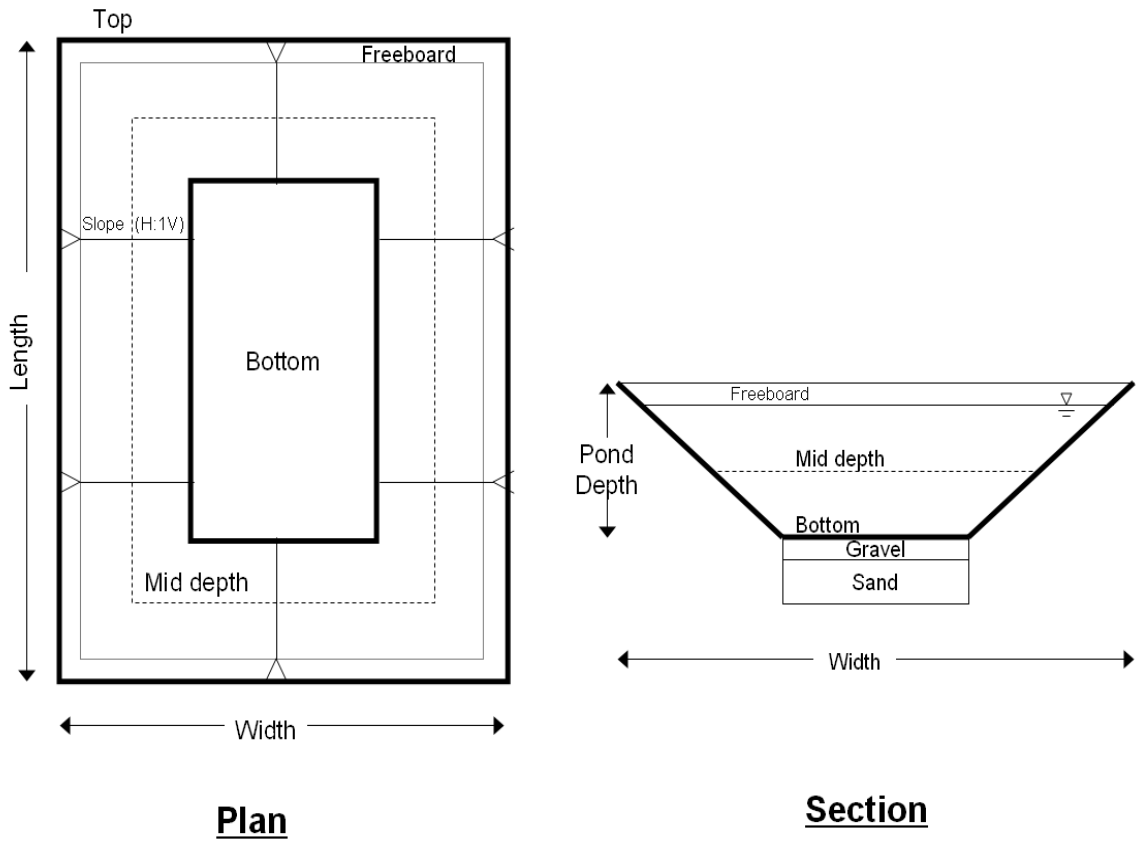

Figure 7-2: Rectangular layout of sand filter with trapezoidal cross section

The underdrain system is designed from the filter layout. The underdrain system uses a main collector pipe that runs the length of the filter, with lateral pipes spanning the filter width. The required length of pipe and number of fittings is estimated from the filter design.

An inlet structure for the sand filter is sized using the rational method for peak discharge. The generic inlet structure is shown in Figure 7-3. The structure is assumed to be made of cast in place concrete, the quantity of which is estimated from the sketch. The inlet structure also includes a concrete pipe of the same length as the roadway to convey runoff from curb inlets to the sand filter. The inlet pipe has a minimum diameter of 24-inches.

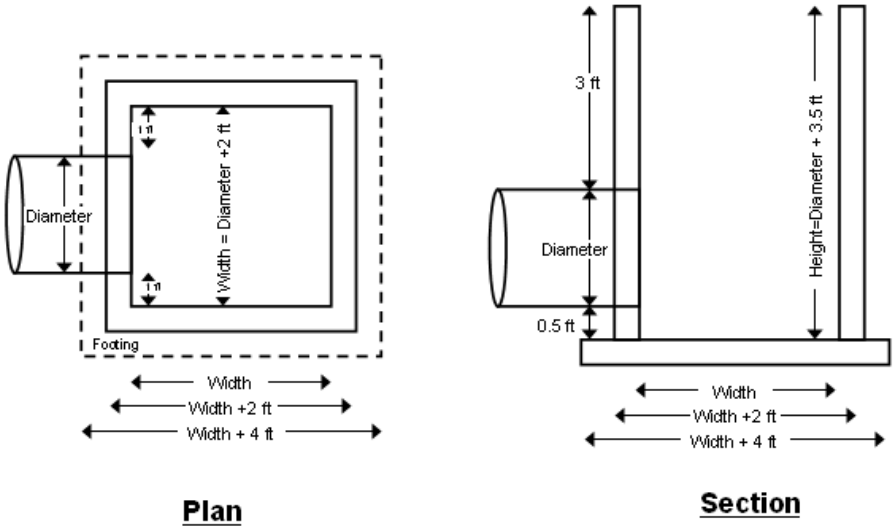

Figure 7-3: Sand filter inlet structure

The sand filter outlet structure was taken to be a culvert pipe with concrete headwall and wing walls as shown in Figure 7-4. The quantities of cast in place concrete are estimated from the sketch.

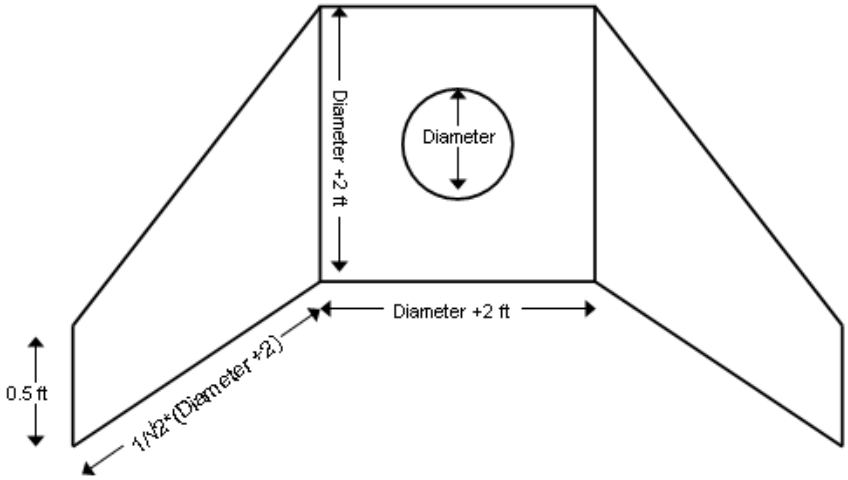

Figure 7-4: Sand filter outlet headwall with 45 degree wingwalls

The construction quantities for the sand filter components are combined into a table along with the unit price for each item. Unit prices are based on RSMeans Heavy Construction Cost Data, 19th edition. This edition lists costs for the year 2005. All costs were converted to 2008 dollars using the Engineering News Record construction cost index. The construction cost also includes 15% for engineering design of the filter.

7.2.3.2 Land Cost

The land cost for a sand filter is calculated using the unit price for land ($/AC) and the area required by the filter design. The filter is assumed to be completely outside the right of way.

The area required for the sand filter is estimated assuming the layout shown in Figure 7-2—a staging area is added if required by TCEQ rules.

7.2.3.3 Maintenance Cost

Sand filters require annual maintenance to control vegetation and periodic maintenance to replace the sand in the filter. The annual maintenance cost is based using the number of man-hours required and a fully burdened labor rate. The model defaults are 28 man hours per year (Barrett, 2003) at a fully burdened labor rate of $55/hr. These defaults may be changed by the user. Sand replacement is assumed to cost three times that of installation, and occur at 5 year intervals.

7.2.4 Permeable Friction Course

The cost of using PFC on a roadway consists of the initial installation and periodic replacements of the overlay. The incremental cost of PFC installation is the difference between installing a PFC and installing a final course of hot mix asphalt (HMA). Both of these paving materials are purchased by the ton, but have different densities, and are placed at different thicknesses. For each pavement, the spreadsheet computes the installation cost per unit area ($/SY) from the bid price per ton, density, and thickness. The incremental cost of installing PFC is the difference between the PFC installation cost and the HMA installation cost.

PFC replacement requires milling up the old layer before installing the replacement layer. The replacement cost is the milling cost plus the incremental installation cost. This replacement cost assumes that the road would require resurfacing with HMA at the same frequency that PFC replacements are needed. The replacement interval for PFC is also a model input. The total cost for PFC is the present value of the replacements that occur during the analysis period plus the installation cost.

7.3 Sample Calculation

In order to illustrate the use of the spreadsheet model for PFC cost comparison, this section presents an example calculation. The example considered here is a roadway having a width of 64 feet in a right of way that is 80 feet wide. The financial parameters for this example include: an analysis period of 50 years, cost of capital of 5%, inflation rate of 2%, and land cost of $500,000 per acre. The project parameters portion of the spreadsheet is shown in Figure 7-5. Some quantities such as the buffer width and right of way area are computed from the input parameters for reference. The real discount rate is computed from the cost of capital and inflation rate and is used for all subsequent time value of money calculations.

	A	B	C	D	E
1		PFC Whole Life Cost Comparison			
2		Description	Unit	Quantity	Notes
3	Project Parameters				
4		Roadway length	FT	2,500	
5		Paved Width	FT	64	
6		Total ROW width	FT	80	
7		Buffer width (one side)	FT	8	if > 15 use Vegetated Filter Strip
8					
9		Paved Area	SF	160,000	
10			AC	3.7	A_D
11		Total Area	SF	200,000	
12			AC	4.6	
13					
14		Analysis Period	yrs	50	
15		Cost of Capital	%	5%	i
16		Inflation Rate	%	2%	f
17		Real Discount Rate	%	2.94%	i' = (i-f) / (1+f); Newnan et al. 2000
18					
19		Land Unit Cost	$/AC	$500,000	
20					

Figure 7-5: Project parameters portion of spreadsheet, input cells are shaded blue

In this scenario, a vegetated filter strip requires an additional 7 feet of right of way for each side of the roadway. From the roadway length and land cost specified as project parameters, the incremental cost of using a vegetated filter strip for stormwater treatment is $401,745 (Figure 7-6).

	A	B	C	D	E
1		PFC Whole Life Cost Comparison			
2		Description	Unit	Quantity	Notes
21	Vegetated Filter Strip Option				
22		Extra width needed (one side)	FT	7	
23		Extra ROW area needed (both sides)	AC	0.8035	
24		Cost of additional ROW to reach 15'	$	**$401,744.72**	

Figure 7-6: Vegetated filter strip portion of spreadsheet

The sand filter for this example is sized according to TCEQ requirements. The paved area of this roadway is 3.7 acres. A sand filter located in Travis County that treats this runoff has a water quality volume of 20,000 cubic feet and an estimated construction cost of $204,652 (Figure 7.7).

The largest component of the sand filter construction is the cost of the piping to move water from the curb inlets to the sand filter.

	A	B	C	D	E
106					
107				Unit	Extended
108		Description	Qty	Cost [a]	Cost
109		Excavation and Hauling (CY)	1277	27.00	34479.00
110		Impermeable Liner (SF)	3066	1.00	3066.00
111		Underdrain Pipes (LF)	203	10.00	2030.00
112		Sand Fill (CY)	51	25.00	1283.33
113		Gravel Fill (CY)	17	25.00	427.78
114		Inlet structure concrete (CY)	6.4	450.00	2900.00
115		Inlet structure culvert pipe (LF) [b]	2500.0	53.00	132500.00
116		Outlet Structure concrete (CY)	0.43	450.00	192.56
117		Outlet structure culvert pipe (LF)	68	16.00	1080.00
118		Construction Cost:			177958.67
119		Engineering Fee	1	15%	26693.80
120		Total:			204652.47
121	Notes:				
122	a Unit costs based on RSMeans Heavy Construction Cost Data, 19th ed (2005$ inflated to 2008$ using ENR index)				
123	b Length of inlet pipe is equal to length of roadway				

Figure 7-7: Itemized cost estimate for construction of the sand filter

The construction cost is combined with maintenance costs, and land cost to develop a total cost for the sand filter option. In this example the total sand filter cost was $356,259 and was comprised of 27% land cost, 57% construction cost, and 16% maintenance cost. The detailed cost calculations for the sand filter are shown in Figure 7-8.

	A	B	C	D	E
1		PFC Whole Life Cost Comparison			
2		**Description**	**Unit**	**Quantity**	**Notes**
26	Sand Filter Option				
27	*Construction*				
28		Construction Cost	$	204,652	See Sand Filter Tab
29	*Land*				
30		Land Required	AC	0.18710	See Sand Filter Tab
31		Land Unit Cost	$/AC	$500,000	Project parameter
32		Land Cost	$	$93,549	
33	*Maintenance*				
34		Annual Maintenance Requirement	h/yr	28	
35		Labor Cost	$/hr	55	
36		Annual Maintenance Cost	$	1540	
37		PV of Annual Maintenance Cost		$40,070	
38					
39		Sand Replacement Cost	$	3850	3x sand installation
40		Sand Replacement Interval	years	5	
41		Number of replacements		9	
42		Effective Interest Rate for replacement interval	%	0.156	
43		Present Value of Replacements		$17,987	
44					
45		PV of Maintenance Costs (annual+sand)		$58,057	
46	*Total*				
47		Total Cost (Const.+Maint.+Land)		**$356,259**	
48					

Figure 7-8: Sand filter portion of spreadsheet, input cells shaded blue

The final section of the cost comparison spreadsheet develops the incremental cost of using PFC for stormwater treatment. Using bid prices of $80/ton for HMA and $100/ton for PFC (Lantrip, 2009a) and other parameters shown in Figure 7-9, the incremental cost of a PFC installation is $2.73/SY. At this price, the capital cost of the installation is $48,444. The replacement cost—including $2/SY for milling up the old PFC (Lantrip, 2009b)—is $84,000. The present value of four replacements during the 50 year analysis period is $171,456. This value reflects an inflation rate of 2% and a capital cost of 5% as shown in Figure 7-5. Summing the installation and present value of replacement costs gives an incremental cost of $219,901 or $12.37/SY for the PFC option.

	A	B	C	D	E
1		PFC Whole Life Cost Comparison			
2		**Description**	**Unit**	**Quantity**	**Notes**
49	PFC Option				
50	*Installation*				
51		*Conventional Asphalt*			
52		Bid Price for Item 0340 - HMA	$/ton	80	
53			$/lb	0.0400	
54		HMA Density	lb/SY/in	110	
55		HMA Thickness	in	1	
56		Installation Unit Cost	$/SY	4.4	
57					
58		*Permeable Friction Course*			
59		Bid Price for Item 0342 - PFC	$/ton	100	
60			$/lb	0.0500	
61		PFC Density	lb/SY/in	95	
62		PFC Thickness	in	1.5	
63		Installation Unit Cost	$/SY	7.125	
64					
65		Incremental Installation Cost	$/SY	2.725	
66			$/sf	0.303	
67		Capital Cost of Installation	$	48,444	
68	*Replacement*				
69		*Milling Cost*	$/SY	2	
70		Replacement Unit Cost (includes milling)	$/SY	4.73	
71			$/sf	0.525	
72		Replacement Cost	$	84,000	
73		Replacement Interval	years	10	
74		Number of replacements		4	
75		Effective Interest Rate for the replacement interva	%	0.336	
76		Present Value of Replacements		$171,456	
77	*Total*				
78		PV of PFC (install +PV of replace)		**$219,901**	

Figure 7-9: PFC portion of spreadsheet, input cells shaded blue

To summarize, this sample calculation has considered stormwater treatment options for a roadway that is 64 feet wide and 2500 feet long. The most economical option was installing a PFC overlay, with a present value cost of $219,901. The next best option was a sand filter at $356,259. The cost of obtaining additional right of way for a vegetated filter strip was $401,745. These results will change according to the project parameters. The variation of BMP costs with certain parameters is discussed in the next section.

7.4 Discussion

The example calculation of Section 7.3 showed how to apply the economic model to a specific roadway segment. This section describes how changes in certain project parameters influence the model results. In particular, the effect of land cost and roadway length are examined.

7.4.1 Land Cost

The cost of each BMP behaves differently with respect to land cost. A PFC installation costs the same regardless of land costs because PFC does not require any additional right of way. In contrast, a vegetated filter strip is perfectly sensitive to land cost because land is the only cost for a vegetated filter strip considered in this model. A sand filter—with construction, maintenance, and land costs—is more sensitive than PFC; but less so than a vegetated filter strip.

The cost of each BMP at various land costs for the sample roadway of Section 7.3 is shown in Figure 7-10. Although this figure applies to a specific case, some generalizations can be made:

- When land costs are low, vegetated filter strips are the most economical alternative.
- As land costs rise, a vegetated filter strip quickly becomes the least economical option.
- At high land costs, PFC is the most economical alternative.
- It is possible that the construction and maintenance costs of a sand filter exceed the incremental cost of a PFC installation.

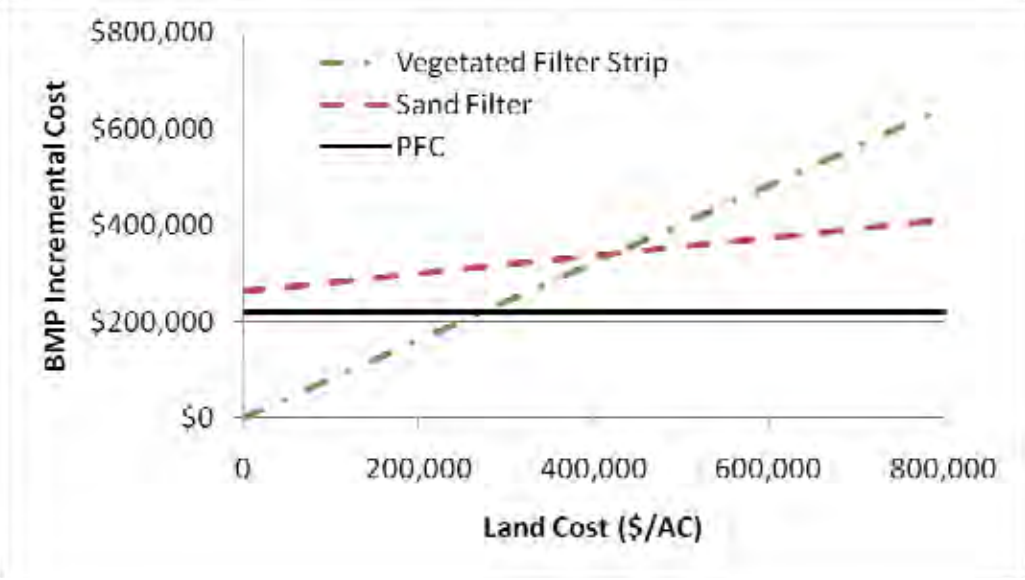

Figure 7-10: Variation of BMP cost with land cost for a roadway having a length of 2500 ft, paved width of 64 ft, and right of way width of 80 ft

In areas where filter strips are infeasible, the decision between a sand filter and a PFC will depend on the relative costs of the BMPs. For the roadway details considered in Figure 7-10,

PFC is less expensive than a sand filter at any land cost, but this result may change as the drainage area of the sand filter changes. This variation is examined in the next section.

7.4.2 Roadway Length

In addition to land price, the most economical choice of BMP may also depend on the roadway length. Due to the way in which this economic model prices BMPs, sand filters are the only BMP whose unit price varies with the roadway length. In the case of a sand filter, the road length is directly proportional to the drainage area of the filter, so variations with road length are more fundamentally variations with drainage area.

The construction cost of a sand filter varies only slightly with paved area, averaging $11.50/SY of paving for the range shown in Figure 7-11. This cost is nearly as much as the incremental cost of a PFC installation ($12.37/SY). The maintenance and land unit costs for a sand filter are higher for smaller drainage areas, and decline as the drainage area increases. The combined effect of all the cost components is shown in the total cost for a sand filter which ranges from $26.27/SY for a 1000 ft section to $18.10 for a 5000 ft section, both of 64 ft roadway. Sand filter costs do vary with the length of roadway, but this variation is not enough to make sand filters more economical than PFC at current prices.

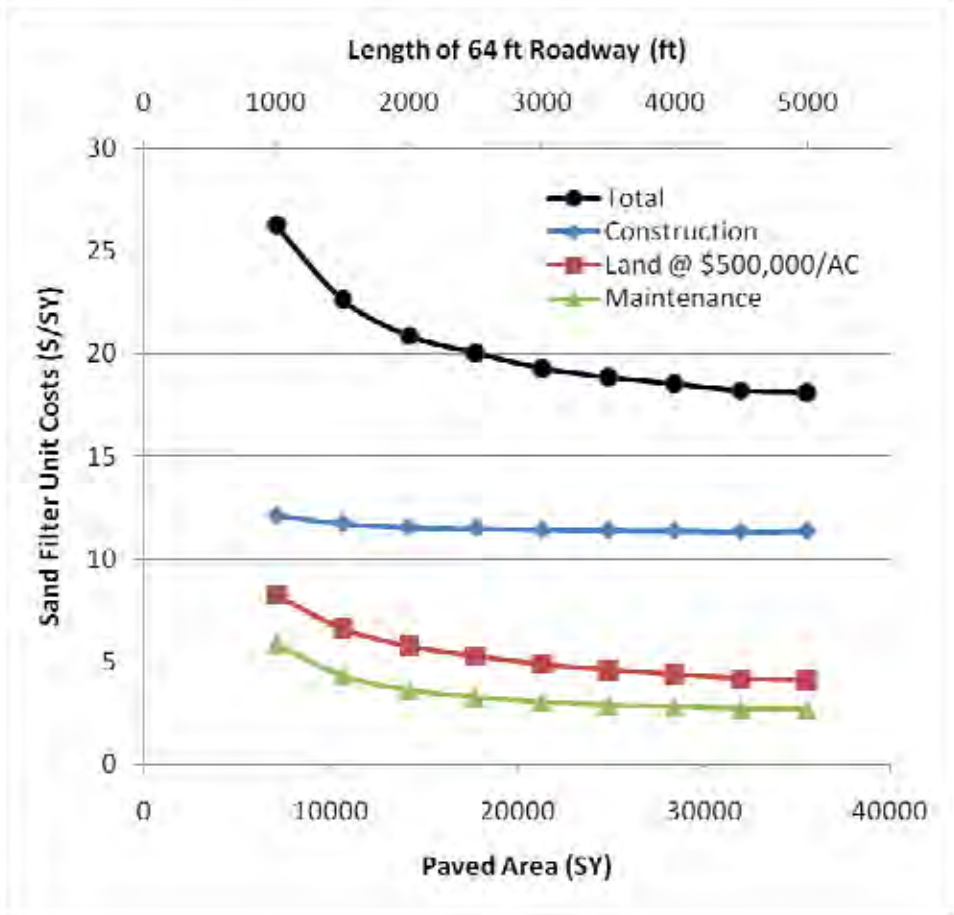

Figure 7-11: Sand filter unit costs as a function of paved area

7.5 Summary and Conclusions

A detailed cost model was developed to compare vegetated filter strips, sand filters, and PFC. The only cost associated with vegetated filter strips was the purchase of additional right of way. Sand filters had three cost components: construction, land, and maintenance. Construction costs were developed from material quantities based on a generic design. Land and maintenance costs were also based on this generic design. The cost of PFC is the difference between a PFC and a conventional asphalt layer, plus periodic replacements. These costs were implemented in a spreadsheet that computes the net present value of each option. This economic model can be used to evaluate options for stormwater treatment as prices change. Several scenarios were examined to understand the economics of the various options at current prices. These scenarios revealed the following conclusions:

- When land is available at low prices, vegetated filter strips are the most economical BMP.
- Current prices for construction materials favor PFC over sand filters.

Chapter 8. Conclusions

8.1 Project Summary

Permeable friction course (PFC) is a 50mm layer of porous asphalt placed on top of regular, impermeable pavement. PFC allows rainfall to drain within the porous layer rather than on top of the pavement. This increasingly popular pavement contributes to a sustainable transportation infrastructure by providing numerous benefits: mitigating hazards of wet weather driving, reducing vehicle noise, and producing cleaner runoff. This report describes a comprehensive multi-year research effort on the water quality, hydraulic, and economic aspects of PFC.

Water quality monitoring of three field sites near Austin, Texas showed a 90% reduction of total suspended solids (TSS) compared to conventional pavement. Significant reductions were also observed for total copper, total lead and total zinc, though concentrations of dissolved constituents were not significantly different. An analysis of particle size distribution showed that runoff from PFC contained fewer large particles than that from conventional pavement. Consequently, the Texas Commission on Environmental Quality has approved PFC for use as a permanent BMP for highways.

The hydraulic properties of PFC are of interest to assess the drainage capacity of the pavement and the effects of clogging. The properties investigated in this study were the porosity and the hydraulic conductivity. Porosity was measured from core samples and found to range from 0.12 to 0.23. Hydraulic conductivity was also measured from core samples and ranged from 0.1 to 3 cm/s. A new field method for measuring the in-situ hydraulic conductivity of PFC was developed and compared to the laboratory measurements.

Predictions of the water depth on PFC roads are needed to assist designers in selecting a pavement thickness and to evaluate the effects of clogging. A Permeable Friction Course Drainage Code (PerfCode) was developed to make these predictions. Measured porosities and hydraulic conductivities were used as inputs to PerfCode. Outputs were the variation of water depth through a storm and the runoff hydrograph. The modeled hydrograph compares favorably to runoff hydrographs obtained by field measurement.

The economics of using PFC as a stormwater best management practice were evaluated against the alternatives of an Austin style sand filter and a vegetated filter strip. The most sensitive variable was found to be the cost of obtaining additional right-of-way. Using construction prices from the year 2008, PFC was more economical than a sand filter and becomes more economical than a vegetated filter strip as land prices rise.

8.2 Implications for Design

The research described in this report has implications stormwater treatment, pavement design, and construction testing on highway design projects.

8.2.1 Stormwater Treatment

Water quality monitoring has shown that runoff from PFC is of sufficiently good quality that the overlay itself can be considered a stormwater best management practice (BMP). This finding means that using a PFC overlay, which likely would already be used for splash and noise reduction, satisfies stormwater treatment requirements for many projects. Using the road itself as

the BMP avoids the need to design, build, and maintain more conventional stormwater treatment facilities such as sand filters. The principle cost savings of this approach come from reduced right of way needs (no additional land is required for a sand filter) and forgone material costs, especially the cost of drainage piping to the sand filter.

8.2.2 PFC Pavement Design

This project has shown that drainage should be considered in selected the thickness of PFC layers. Current practice for establishing the thickness of a PFC layer focuses mostly on aggregate size: the layer must be somewhat thicker than the largest aggregate to obtain the desired structural properties. The aggregate size approach ignores the essential drainage functions provided by PFC. A better approach would design the PFC layer to contain a design storm event (e.g. 2-year storm), and then verify that this thickness exceeds the minimum established by aggregate size.

Designing PFC layers based on drainage considerations recognizes that wet weather safety benefits of PFC—reduced splash, spray, and hydroplaning—are directly related to the drainage function of the pavement. This project has developed tools to quantify the drainage process of PFC layers for steady state and unsteady conditions, and for simple and complex roadway geometries. These tools can be used to inform the design process.

8.2.3 Construction Testing

Designing PFC layers for drainage requires information about the hydraulic properties of the pavement. This study has developed new methods for measuring the hydraulic conductivity of PFC from core samples and in-situ. The field test method is suitable for confirming that new installations of PFC comply with design requirements and for monitoring the performance of PFC layers as they age.

References

Anderson, M.P. and Woessner, W.W. (1992), Applied Groundwater Modeling: Simulation of Flow and Advective Transport, Academic Press, San Diego.

ASCE (1992): *Design and Construction of Urban Stormwater Management Systems*, American Society of Civil Engineers, prepared by the Urban Water Resources Research Council and the Water Environment Federation, Reston, Virginia.

Barrett, Michael (2006). Stormwater Quality Benefits of a Porous Asphalt Overlay. Center for Transportation Research, Austin, Texas. Report No. FHWA/TX-07/0-4605-2.

Barrett, M.E., P. Kearfott, and J.F. Malina (2006): "Stormwater Quality Benefits of a Porous Friction Course and Its Effects on Pollutant Removal by Roadside Shoulders," *Water Environmental Research*, Vol. 78, No. 11, pg. 2177-2185.

Barrett, M.E. and C.B. Shaw (2007): "Benefits of Porous Asphalt Overlay on Storm Water Quality," *Transportation Research Record*, No. 2025, pg. 127-134.

Barrett, M.E., Klenzendorf, J.B., Eck, B. J., and Charbeneau, R.J. (2009), Water Quality and Hydraulic Properties of the Permeable Friction Course, Proceedings of the World Environmental and Water ResourcesConference 2009, Kansas City, MO, May 17-21, 2009.

Bear, J. (1972): *Dynamics of Fluids in Porous Media*, American Elsevier Publishing Company, Inc., New York.

Bear, J. (1979): *Hydraulics of Groundwater*, McGraw-Hill, New York.

Beavers, G.S., and Joseph, D.D. (1967), Boundary conditions at a naturally permeable wall. J. Fluid Mech. 30:197–207.

Bendtsen, H. and B. Andersen (2005): "Report 141: Noise Reducing Pavements—State of the Art in Denmark," Road Directorate, Danish Road Institute, Denmark Ministry of Transport.

Berbee, R., G. Rijs, R. de Brouwer, and L. van Velzen (1999): "Characterization and Treatment of Runoff from Highways in the Netherlands Paved with Impervious and Pervious Asphalt," *Water Environment Research*, Vol. 71, No. 2, pg. 183-190.

Bird, R.B. Stewart, W.E. and Lightfoot, E.N. (1960). Transport Phenomena, John Wiley and Sons, Inc., Madison, WI.

Bordier, C. and D. Zimmer (2000): "Drainage Equations and Non-Darcian Modelling in Coarse Porous Media or Geosynthetic Materials," *Journal of Hydrology*, Vol. 228, pg. 174-187.

Caltrans (2009): *Open and/or Gap Graded Asphalt Pavements Water Quality Project: Visual Inspection of Monitoring Location Pavements*, California Department of Transportation, Division of Environmental Analysis, Storm Water Program MS-27, Sacramento, CA.

Camacho-V., R.G. and M. Vasquez-C. (1992): "Comment on 'Analytical Solution Incorporating Nonlinear Radial Flow in Confined Aquifers' by Zekai Sen," *Water Resources Research*, Vol. 28, No. 12, pg. 3337-3338.

CAMPO (2009): "TxDOT 5 County AADT Counts: 1990-2005," 20 April 2009, Capital Area Metropolitan Planning Organization, Austin, Texas, <http://www.campotexas.org/programs_rd_traffic_counts.php>.

Candaele, R., Barrett, M., Charbeneau, R. (2008) *Porous Friction Course: A Laboratory Evaluation of Hydraulic Properties* CRWR Online Report 08- 6, Center for Research in Water Resources, The University of Texas at Austin, Austin, Texas. http://www.crwr.utexas.edu/online.shtml

Capital Area Metropolitan Planning Organization (CAMPO). (2007) "TxDOT 5 County AADT Counts 1990-2005. www.campotexas.org/programs_rd_traffic_counts.php

Carslaw, H.S. and J.C. Jaeger (1959): *Conduction of Heat in Solids*, Second Ed., Oxford University Press, Amen House, London.

Chai, K.C., S.A. Tan, and T.F. Fwa (2004): "Finite Element Analysis of Runoff Flow Within Porous Pavement System," *Journal of the Institution of Engineers, Singapore*, Vol. 44, Issue 2, pg. 10-28.

Charbeneau, R.J. (2000): *Groundwater Hydraulics and Pollutant Transport*, Prentice-Hall, Upper Saddle River, NJ.

Charbeneau, R.J. and M.E. Barrett (2008): "Drainage Hydraulics of Permeable Friction Courses," *Water Resources Research*, Vol. 44, W04417.

Charbeneau, R. J., Jeong, J. and Barrett, M.E. (2009). Physical Modeling of Sheet flow on Rough Impervious Surfaces, Journal of Hydraulic Engineering, Vol 135. No. 6.

Charbeneau, R.J., J.B. Klenzendorf, and M.E. Barrett (in press): "Methodology for Determining Laboratory and In-Situ Hydraulic Conductivity of Asphalt Permeable Friction Course," *Journal of Hydraulic Engineering*.

Chen, Z., S.L. Lyons, and G. Qin (2001): "Derivation of the Forchheimer Law via Homogenization," *Transport in Porous Media*, Vol. 44, pg. 325-335.

Chow, V.T., D.R. Maidment, and L.W. Mays (1988), Applied Hydrology, McGraw-Hill, New York.

Collins, R.E. (1961): *Flow of Fluids Through Porous Materials*, Reinhold, New York.

Conover, W.J. (1980): *Practical Nonparametric Statistics*, Second Ed., John Wiley & Sons, New York.

Dabaghmeshin, M. (2008), Modeling the Transport Phenomena within the Arterial Wall: Porous Media Approach. Thesis for the degree of Doctor of Science. Lappeenranta University of Technology, Lappeenranta, Finland.
Accessed Online (18 Nov 08): https://oa.doria.fi/bitstream/handle/10024/42280/isbn9789522146274.pdf?sequence=2

Daluz Vieira, J.H. (1983), Conditions Governing the Use of Approximations for the Saint-Venant Equations for Shallow Surface Water Flow. Journal of Hydrology, 60: 43-58.

Darcy, H. (1856): *The Public Fountains of the City of Dijon*, English Translation by Patricia Bobeck (2004), Kendall/Hunt Publishing Company, Dubuque, Iowa.

Eck, B.J. (2010): *Drainage Hydraulics of Porous Pavements: Coupling Surface and Subsurface Flow*, PhD Dissertation in Engineering, The University of Texas at Austin.

Eck, B.J., M.E. Barrett, and R.J. Charbeneau (in press): "Note on Modeling Surface Discharge from Permeable Friction Courses," *Water Resources Research*.

Ergun, S. (1952): "Fluid Flow Through Packed Columns," *Chemical Engineering Progress*, Vol. 48, No. 2, pg. 89-94.

Ewing, R.E., R.D. Lazarov, S.L. Lyons, D.V. Papavassiliou, J. Pasciak, and G. Qin (1999): "Numerical Well Model for Non-Darcy Flow Through Isotropic Porous Media," *Computational Geosciences*, Vol. 3, pg. 185-204.

Ferziger, J.H. and M. Peric (2002): *Computational Methods for Fluid Dynamics*, Third Ed., Springer-Verlag, Berlin.

Fetter, C.W. (1994): *Applied Hydrogeology*, Third Ed., Macmillan College Publishing Company, New York.

Field, R., H. Masters, and M. Singer (1982): "Status of Porous Pavement Research," *Water Research*, Vol. 16, No. 6, pg. 849-858.
Forchheimer, P. (1901): "Wasserbewegung dur Bodem," *Zeitschrift des Verbundes der deutschen Ingenieurs*, Vol. 45, pg. 1782-1788.
Frasier, P.M. (2009): *Stormwater Quality Benefits of Permeable Friction Course*, M.S. Thesis in Engineering, The University of Texas at Austin.
Furman, A, (2008), Modeling Coupled Surface-Subsurface Flow Processes: A Review. Vadose Zone Journal, 7:741-756.
Fwa, T.F., S.A. Tan, and C.T. Chuai (1998): "Permeability Measurement of Base Materials Using Falling-Head Test Apparatus," *Transportation Research Record*, No. 1615, pg. 94-99.
Fwa, T.F., S.A. Tan, and Y.K Guwe (1999): "Laboratory Evaluation of Clogging Potential of Porous Asphalt Mixtures," *Transportation Research Record*, No. 1681, pg. 43-49.
Fwa, T.F., S.A. Tan, and Y.K. Guwe (2001b): "Rational Basis for Evaluation and Design of Pavement Drainage Layers," *Transportation Research Record*, No. 1772, pg. 174-180.
Fwa, T.F., S.A. Tan, C.T. Chuai, and Y.K. Guwe (2001a): "Expedient Permeability Measurement for Porous Pavement Surface," *International Journal of Pavement Engineering*, Vol. 2, pg. 259-270.
Giorgi, T. (1997): "Derivation of the Forchheimer Law via Matched Asymptotic Expansions," *Transport in Porous Media*, Vol. 29, pg. 191-206.
Goggin, D.J., R.L. Thrasher, and L.W. Lake (1988): "A Theoretical and Experimental Analysis of Minipermeameter Response Including Gas Slippage and High Velocity Flow Effects," *In Situ*, Vol. 12, No. 1&2, pg. 79-116.
Google Inc. (2010). Google Earth (Version 5.1.3533.1731) [Software]. Available from http://earth.google.com/
Google Maps. (2009) Retrieved on June 3, 2009 from the Google Maps Website: http://maps.google.com/
Halek, V. and J. Svec. (1979), Groundwater Hydraulics. Elsevier, New York.
Hassan, H.F., A.A. Rawas, A.W. Hago, A. Jamrah, A. Al-Futaisi, and T. Al-Sabqi (2008): "Investigation of Permeability and Leaching of Hot Mix Asphalt Concrete Containing Oil-Contaminated Soils," *Construction and Building Materials*, Vol. 22, pg. 1239-1246.
Hassanizadeh, S.M. and W.G. Gray (1987): "High Velocity Flow in Porous Media," *Transport in Porous Media*, Vol. 2, pg. 521-531.
He, Z., Wu, W. and Wang, Sam S. Y. (2008), Coupled Finite-Volume Model for 2D Surface and 3D Subsurface Flows. Journal of Hydrologic Engineering, Vol. 13 No. 9.
Helsel, D.R. and R.M. Hirsch (2002): "Statistical Methods in Water Resources," Techniques of Water-Resources Investigations of the United States Geological Survey, Book 4, Hydrologic Analysis and Interpretation, Chapter A3.
Hwang, H.C. and R.J. Houghtalen (1996): *Fundamentals of Hydraulic Engineering Systems*, Third Ed., Prentice Hall, Upper Saddle River, NJ.
Irmay, S. (1958): "On the Theoretical Derivation of Darcy and Forchheimer Formulas," *Journal of Geophysical Research*, Vol. 39, pg. 702-707.
Irmay, S. (1967), On the Meaning of the Dupuit and Pavlovskii Approximations in Aquifer Flow, Water Resources Research Vol. 3, No. 2, pp 599-608.
Isenring, T., H. Koster and I. Scazziga (1990): "Experiences with Porous Asphalt in Switzerland," *Transportation Research Record*, No. 1265, pg. 41-53.

Izbash, S. (1931): *O Filtracii Kropnozernstom Materiale*, Leningrad, USSR.
Jackson, T.J. and R.M. Ragan (1974): "Hydrology of Porous Pavement Parking Lots," *Journal of the Hydraulic Division*, Vol. 100, HY 12, pg. 1739-1752.
Jeong, J. (2008), A Hydrodynamic Diffusion Wave Model for Stormwater Runoff on Highway Surfaces at Superelevation Transitions. Dissertation. University of Texas at Austin.
Jeong, J. and Charbeneau, R. J., (2010), Diffusion Wave Model for Simulating Stormwater Runoff on Highway Pavement Surfaces at Superelevation Transition, *Journal of Hydraulic Engineering*, (In Press).
Kadlec, H.R. and L.R. Knight (1996): *Treatment Wetlands*, CRC Press Lewis Publishers, Boca Raton, Florida.
Kanji, G.K. (2006): *100 Statistical Tests*, Third Ed., SAGE Publications Ltd, London.
Kelkar, M.G. (2000): "Estimation of Turbulence Coefficient Based on Field Observations," *SPE Reservoir Evaluation and Engineering*, Vol. 3, No. 2, pg. 160-164.
Klenzendorf, J. B. (2010), Hydraulic Conductivity Measurement of Permeable Friction Course (PFC) Experiencing Two-Dimensional Nonlinear Flow Effects. Dissertation. University of Texas at Austin.
Kollet, S. J., and Maxwell, R. M. (2006), Integrated surface-groundwater flow modeling: A free-surface overland flow boundary condition in a parallel groundwater flow model. Adv. Water Resour.,129, 945–958.
Kovacs, G. (1981): *Seepage Hydraulics*, Elsevier Scientific Publishing Company, Amsterdam.
Kreyzig, E. (1999), Advanced Engineering Mathematics, 8th Edition. John Wiley and Sons, New York.
Krishnan, J.M. and C.L. Rao (2001): "Permeability and Bleeding of Asphalt Concrete Using Mixture Theory," *International Journal of Engineering Science*, Vol. 39, pg. 611-627.
LCRA (2010): "Hydromet," 15 February 2010, Lower Colorado River Authority, Austin, Texas, <http://hydromet.lcra.org/>.
Li, D. and T.W. Engler (2001): "Literature Review on Correlations of the Non-Darcy Coefficient," *SPE 70015*, Proceedings of the SPE Permian Basin Oil and Gas Recovery Conference, Midland, Texas, USA, May 15-16.
Liang, D., Falconer, R.A., and Lin, B. (2007), Coupling surface and subsurface flows in a depth averaged flood wave model. Journal of Hydrology, 337:147-158.
Loaiciga, H.A. (2005): "Steady State Phreatic Surfaces in Sloping Aquifers," *Water Resources Research*, Vol. 41, W08402.
Ma, H. and D.W. Ruth (1993): "The Microscopic Analysis of High Forchheimer Number Flow in Porous Media," *Transport in Porous Media*, Vol. 13, pg. 139-160.
Masad, E., B. Birgisson, A. Al-Omari, and A. Cooley (2004): "Analytical Derivation of Permeability and Numerical Simulation of Fluid Flow in Hot-Mix Asphalt," *Journal of Materials in Civil Engineering*, Vol. 16, No. 5, pg. 487-496.
Masad, E., B. Muhunthan, N. Shashidhar, and T. Harman (1999): "Internal Structure Characterization of Asphalt Concrete Using Image Analysis," *Journal of Computing in Civil Engineering*, Vol. 13, No. 2, pg. 88-95.
Mathias, S.A., A.P. Butler, and H. Zhan (2008): "Approximate Solutions for Forchheimer Flow to a Well," *Journal of Hydraulic Engineering*, Vol. 134, No. 9, pg. 1318-1325.
Moutsopoulos, K.N. and V.A. Tsihrintzis (2005): "Approximate Analytical Solutions of the Forchheimer Equation," *Journal of Hydrology*, Vol. 309, pg. 93-103.

Muskat, M. (1982): *The Flow of Homogenous Fluids Through Porous Media*, International Human Resources Development Corporation, Boston, MA.
NCHRP: National Cooperative Highway Research Program (2009), Construction and Maintenance Practices for Permeable Friction Courses, Report 640, Transportation Research Board, Washington, D.C..
Pagotto, C., M. Legret, and P. le Cloirec (2000): "Comparison of the Hydraulic Behaviour and the Quality of Highway Runoff Water According to the Type of Pavement," *Water Research*, Vol. 34, No. 18, pg. 4446-4454.
Ranchet, J. (1995): "Impacts of Porous Pavements on the Hydraulic Behaviour and the Cleansing of Water" (in French), *Techniques Sciences et Methodes*, Vol. 11, pg. 869-871.
Ranieri, V. (2002): "Runoff Control in Porous Pavements," *Transportation Research Record*, No. 1789, pg. 46-55.
Ranieri, V. (2007): "The Functional Design of Porous Friction Courses," *2007 Annual Meeting of the Transportation Research Board*.
Reddy, N.B.P. and P. Rama Mohan Rao (2006): "Effect of Convergence on Nonlinear Flow in Porous Media," *Journal of Hydraulic Engineering*, Vol. 132, No. 4, pg. 420-427.
Refsgaard, J.C., and B. Storm. (1995), MIKE-SHE. p. 809–846. In V.P. Singh (ed.) Computer models of watershed hydrology. Water Resour. Publ., Highlands Ranch, CO.
Regimand, A. and L. James (2004): "Systems and Methods for Determining the Porosity and/or Effective Air Void Content of Compacted Material," U.S. Patent 6,684,684 B2, Feb. 3, 2004.
Reynolds, O. (1900): "Papers on Mechanical and Physical Subjects," Cambridge University Press.
Ruth, D. and H. Ma (1992): "On the Derivation of the Forchheimer Equation by Means of the Averaging Theorem," *Transport in Porous Media*, Vol. 7, pg. 255-264.
Sen, Z. (1987): "Non-Darcian Flow in Fractured Rocks with a Linear Flow Pattern," *Journal of Hydrology*, Vol. 92, pg. 43-57.
Sen, Z. (1988): "Analytical Solution Incorporating Nonlinear Radial Flow in Confined Aquifers," *Water Resources Research*, Vol. 24, No. 4, pg. 601-606.
Sen, Z. (1990): "Nonlinear Radial Flow in Confined Aquifers Toward Large-Diameter Wells," *Water Resources Research*, Vol. 26, No. 5, pg. 1103-1109.
Sen, Z. (1992): "Reply," *Water Resources Research*, Vol. 28, No. 12, pg. 3339-3340.
Sidiropoulou, M.G., K.N. Moutsopoulos, and V.A. Tsihrintzis (2007): "Determination of Forchheimer Equation Coefficients *a* and *b*," *Hydrological Processes*, Vol. 21, pg. 534-554.
Simpson, M.J., Clement, T.P. and Gallop, T.A. (2003), Laboratory and Numerical Investigation of Flow and Transport Near a Seepage-Face Boundary. Ground water. Vol. 41 No.5 pp690-700.
Smith, G.D. (1965): *Numerical Solution of Partial Differential Equations*, Oxford University Press, Amen House, London.
Srivastava, R. (2009): "Discussion of 'Effect of Convergence on Nonlinear Flow in Porous Media' by N. Bhanu Prakasham Reddy and P. Rama Mohan Rao," *Journal of Hydraulic Engineering*, Vol. 135, No. 6, pg. 533-535.
Stanard, C. E. (2008), Stormwater Quality Benefits of a Permeable Friction Course. Master's Thesis. Univeristy of Texas at Austin.
Available Online: http://www.crwr.utexas.edu/reports/2008/rpt08-3.shtml

Stanard, C., Barrett, M., Charbeneau, R. (2008) *Stormwater Quality Benefits of a Permeable Friction Course.* CRWR Online Report 08- 3, Center for Research in Water Resources, The University of Texas at Austin, Austin, Texas. http://www.crwr.utexas.edu/online.shtml

Stotz, G. and K. Krauth (1994): "The Pollution of Effluents from Pervious Pavements of an Experimental Highway Section: First Results," *The Science of the Total Environment*, Vol. 146-147, pg. 465-470.

Street, R.L. (1973), The Analysis and Solution of Partial Differential Equations, Brooks/Cole, Monterey, California.

Tan, S.A., T.F. Fwa, and C.T. Chuai (1997): "A New Apparatus for Measuring the Drainage Properties of Porous Asphalt Mixes," *Journal of Testing and Evaluation*, Vol. 25, No. 4, pg. 370-377.

Tan, S.A., T.F. Fwa, and C.T. Chuai (1999): "Automatic Field Permeameter for Drainage Properties of Porous Asphalt Mixes," *Journal of Testing and Evaluation*, Vol. 27, No. 1, pg. 57-62.

Tan, S.A., T.F. Fwa, and C.T. Chuai (2002): "Drainage Testing of Porous Asphalt Road Mixes," U.S. Patent 6,367,310 B1, Apr. 9, 2002.

Tan, S.A., T.F. Fwa, and C.T. Han (2003): "Clogging Evaluation of Permeable Bases," *Journal of Transportation Engineering*, Vol. 129, No. 3, pg. 309-315.

Tan, S.A., T.F. Fwa, and K.C. Chai (2004): "Drainage Considerations for Porous Asphalt Surface Course Design," *Transportation Research Record*, No. 1868, pg. 142-149.

Tan, S.A., T.F. Fwa, and Y.K. Guwe (2000): "Laboratory Measurements and Analysis of Clogging Mechanism of Porous Asphalt Mixes," *Journal of Testing and Evaluation*, Vol. 28, No. 3, pg. 207-216.

Tarefder, R.A., L. White, and M. Zaman (2005): "Neural Network Model for Asphalt Concrete Permeability," *Journal of Materials in Civil Engineering*, Vol. 17, No. 1, pg. 19-27.

Texas Department of Transportation (2004) Item 342 Permeable Friction Course (PFC) *Standard Specifications for Construction and Maintenance of Highways, Streets, Bridges*, Austin, Texas, pp. 312-328.

Thauvin, F. and K.K. Mohanty (1998): "Network Modeling of Non-Darcy Flow Through Porous Media," *Transport in Porous Media*, Vol. 31, pg. 19-37.

Theis, C.V. (1935): "The Lowering of the Piezometer Surface and the Rate and Discharge of a Well Using Groundwater Storage," *Transactions, American Geophysical Union*, Vol. 16, pg. 519-524.

Thiruvengadam, M. and G.N. Pradip Kumar (1997): "Validity of Forchheimer Equation in Radial Flow Through Coarse Granular Media," *Journal of Engineering Mechanics,* Vol. 123, No. 7, pg. 696-705.

TRB (2009): *Construction and Maintenance Practices for Permeable Friction Courses,* National Cooperative Highway Research Program Report 640, Transportation Research Board of the National Academies, Washington, D.C.

TxDOT (1993): *Special Specification 3231—Porous Friction Course*, Texas Department of Transportation, Austin, TX.

TxDOT (2004a): *Test Procedure for Permeability or Water Flow of Hot Mix Asphalt*, Texas Department of Transportation, Construction Division, Designation Tex-246-F, Austin, TX.

TxDOT (2004b): *Item 342—Permeable Friction Course (PFC)*, Texas Department of Transportation, Austin, TX.
Van Heystraeten, G. and C. Moraux (1990): "Ten Years' Experience of Porous Asphalt in Belgium," *Transportation Research Record*, No. 1265, pg. 34-40.
Venkataraman, P. and P. Rama Mohan Rao (1998): "Darcian, Transitional, and Turbulent Flow Through Porous Media," *Journal of Hydraulic Engineering*, Vol. 124, No. 8, pg. 840-846.
Venkataraman, P. and P. Rama Mohan Rao (2000): "Validation of Forchheimer's Law for Flow Through Porous Media with Converging Boundaries," *Journal of Hydraulic Engineering*, Vol. 126, No. 1, pg. 63-71.
Wang, X., F. Thauvin, K.K. Mohanty (1999): "Non-Darcy Flow Through Anisotropic Porous Media," *Chemical Engineering Science*, Vol. 54, pg. 1859-1869.'
Ward, J.C. (1964): "Turbulent Flow in Porous Media," *Journal of the Hydraulic Division*, Vol. 90, HY 5, pg. 1-12.
White, F.M. (1999), Fluid Mechanics, Fourth Edition. WCB/McGraw-Hill.
Wiles, T.J. and J.M. Sharp (2008): "The Secondary Permeability of Impervious Cover," *Environmental and Engineering Geoscience*, Vol. 14, No. 4, pg. 251-265.
Woolhiser, D.A. and Liggett, J.A. (1967), Unsteady, One-Dimensional Flow over a Plane—the Rising Hydrograph, Water Resources Research, Vol. 3 No. 3 753-771.
Wu, Y.S. (2002): "An Approximate Analytical Solution for Non-Darcy Flow Toward a Well in Fractured Media," *Water Resources Research*, Vol. 38, No. 3, 1023.
Yates, S.R., A.W. Warrick, and D.O. Lomen (1985a): "Hillside Seepage: An Analytical Solution to a Nonlinear Dupuit-Forchheimer Problem," *Water Resources Research*, Vol. 21, No. 3, pg. 331-336.
Yates, S.R., D.O. Lomen, and A.W. Warrick (1985b): "Solutions for a Dupuit Aquifer with Sloping Substratum and Areal Recharge," *Computers and Geosciences*, Vol. 11, No. 4, pg. 477-469.
Zeng, Z and Grigg, R. (2006), A Criterion for Non-Darcy Flow in Porous Media, Transport in Porous Media 63: 57-69.

Appendix A: Water Quality Monitoring Data

Date	Site	Surf-ace	Sampler	TSS (mg/L)	TKN (mg/L)	NO2/ NO3 (mg/L)	Diss. P (mg/L)	Tot. P (mg/L)	COD (mg/L)	Tot. Cu (µg/L)	Tot. Pb (µg/L)	Tot. Zn (µg/L)	Diss. Cu (µg/L)	Diss. Pb (µg/L)	Diss. Zn (µg/L)
3/1/04	1	HMA	PASSIVE	85	1.3	1.4	ND	0.08	72	23.9	6.17	207	9.88	ND	95.1
4/12/04	1	HMA	PASSIVE	44	0.703	0.26	0.03	0.08	29	16.9	7.56	101	5.24	ND	45.4
5/14/04	1	HMA	PASSIVE	130	1.05	0.13	0.08	0.17	65	28.4	15	157	2.06	ND	7.5
6/3/04	1	HMA	PASSIVE	121	1.53	0.32	0.07	0.16	84	29.7	9.93	163	9.32	ND	46.3
6/9/2004	1	HMA	PASSIVE	209	1.06	0.06	ND	0.17	70	35.3	24.2	209	3.18	ND	41
11/15/04	1	PFC	PASSIVE	9	0.863	0.728	0.04	0.029	77	11.1	1.54	58.5	8.84	ND	47.2
11/22/04	1	PFC	PASSIVE	3	0.41	0.2699	ND	ND	13	2.94	ND	26.7	2.26	ND	20.3
1/28/05	1	PFC	PASSIVE	16	0.48	0.2453	ND	0.524	22	6.13	1.14	54	2.73	ND	43.1
3/3/05	1	PFC	PASSIVE	4	0.43	0.3518	0.271	0.368	10	2.8	ND	41.1	1.94	ND	24.4
5/9/05	1	PFC	PASSIVE	6	1.02	0.3044	0.056	0.047	52	11	ND	21.9	9.33	ND	19.3
7/14/05	1	PFC	PASSIVE	10	1.42	0.4531	0.048	0.12	69	14.7	ND	37.1	11.8	ND	41.9
7/28/05	1	PFC	PASSIVE	14	0.921	1.035	ND	0.033	71	13.6	ND	35.4	10.8	ND	38.6
10/10/05	1	PFC	PASSIVE	12	1.3	0.4803	ND	ND	91	10.2	ND	23.1	8.58	ND	21.3
11/1/05	1	PFC	PASSIVE	11	1.4	0.5892	0.048	0.089	90	13.2	ND	52.9	9.5	ND	40.8
11/26/05	1	PFC	PASSIVE	12						45.7	ND	81.3	37.5	ND	61.7
1/22/06	1	PFC	AUTO	10	4.97	2.41	0.13	0.162	388	67.1	2.4	116	58.7	1	103
1/28/06	1	PFC	AUTO	12	0.897	0.51	ND	0.038	85	17.4	1.3	36.9	14	1	27.3
2/10/06	1	PFC	AUTO	16	1.54	0.62	ND	0.02	124	23.9	2.25	57.9	15.8	ND	37
2/25/06	1	PFC	AUTO	3	1.15	0.73	ND	0.02	67	14.7	ND	31.4	12.8	ND	27
3/20/06	1	PFC	AUTO	14	0.471	0.05	ND	0.028	13	3.75	ND	12.7	1.84	ND	6.16
3/28/06	1	PFC	AUTO	23	0.811	0.11	ND	0.043	36	12	ND	47.9	4.98	ND	23.2
4/30/06	1	PFC	AUTO	10	1.8	0.33	ND	0.027	34	8	ND	61.4	6.73	ND	51.4
5/5/06	1	PFC	AUTO	8	1.22	0.25	ND	0.02	30	6.58	ND	24.7	4.88	ND	19.9
5/6/06	1	PFC	AUTO	6	0.377	0.19	ND	0.02	19	4	ND	14.2	3.16	ND	10.3
5/7/06	1	PFC	AUTO	4	0.227	0.11	ND	0.02	14	2.96	ND	12.8	1.82	ND	8.17
6/17/06	1	PFC	AUTO	6	0.371	0.08	ND	0.023	16	4.49	ND	14.7	2.57	ND	13.9

Date	Site	Surf-ace	Sampler	TSS (mg/L)	TKN (mg/L)	NO2/ NO3 (mg/L)	Diss. P (mg/L)	Tot. P (mg/L)	COD (mg/L)	Tot. Cu (µg/L)	Tot. Pb (µg/L)	Tot. Zn (µg/L)	Diss. Cu (µg/L)	Diss. Pb (µg/L)	Diss. Zn (µg/L)
1/13/07	1	PFC	AUTO	11	0.163	0.08	ND	ND	30	5.89	ND	11.8	3.47	ND	9.63
1/14/07	1	PFC	AUTO	2	1.18	0.26	ND	ND	63	5.49	ND	25.8	4.4	ND	23.2
3/11/07	1	PFC	AUTO	11	0.434	0.25	ND	ND	42	11.2	1.01	27.4	8.31	ND	18.9
3/13/07	1	PFC	AUTO	4	0.261	0.05	ND	ND	32	6.6	1.17	17.8	4.46	ND	12.9
3/26/07	1	PFC	AUTO	2	5.45	0.14	ND	0.052	25	8.53	ND	20.9	7.06	ND	16.4
3/30/07	1	PFC	AUTO	8	0.692	0.1	ND	0.063	49	12.5	1.45	28.1	8.03	ND	17.9
4/25/07	1	PFC	AUTO	3	0.462	0.52	0.045	0.074	61	15.3	ND	15.9	11.5	ND	11.5
4/30/07	1	PFC	AUTO	8	0.555	0.32	ND	0.055	80	17.6	ND	22	12.5	ND	18.2
5/3/07	1	PFC	AUTO	6	0.39	0.18	ND	0.024	23	7.51	ND	8.09	5.01	ND	6.17
5/16/07	1	PFC	AUTO	2	1.29	0.72	0.03	0.069	86	17.8	ND	13.4	16.1	ND	17.2
5/24/07	1	PFC	AUTO	4	0.482	0.12	ND	ND	57	10.2	ND	24.9	8.4	ND	12.7
6/4/07	1	PFC	AUTO	8	0.479	0.21	ND	0.038	35	8.96	ND	10.5	5.95	ND	5.44
7/20/07	1	PFC	AUTO	13	0.114	0.03	ND	0.062	37	7.45	ND	18.7	4.05	ND	8.02
11/26/07	1	PFC	AUTO	3	0.586	0.43	0.046	0.064	66	14.2	ND	14.8	12.5	ND	9.72
12/12/07	1	PFC	AUTO	10	0.865	0.28	ND	ND	42	14.4	1.33	19.4	10.4	ND	8.31
3/3/08	1	PFC	AUTO	7	1.37	0.97	0.042	0.053	93	20.9	ND	21.2	17.8	ND	12
3/18/08	1	PFC	AUTO	29	0.791	0.22	ND	0.052	50	16.7	1.42	35.2	8.39	ND	6.9
4/18/08	1	PFC	AUTO	23.3	1.22	0.26	ND	0.092	72	16.1	1.32	23.1	11.8	ND	11.7
8/6/08	1	PFC	AUTO	2	1.83	0.79	0.028	0.113	166	35.4	ND	20.1	34.6	ND	13.4
10/15/08	1	PFC	AUTO	4	0.422	0.07	0.023	ND	54	10.7	ND	15.9	7.75	ND	6.91
1/6/09	1	PFC	AUTO	2.4	0.526	0.32	0.032	0.033	40	11.2	ND	9.16	8.82	ND	ND
2/9/09	1	PFC	AUTO	4.2	0.755	0.37	ND	0.148	55	13.9	ND	10.7	13.5	ND	6.27
3/13/09	1	PFC	AUTO	3.2	0.795	0.4	0.021	0.043	46	8.39	ND	10.3	8.54	ND	7.49
4/12/09	1	PFC	AUTO	8.4	1.33	0.79	0.03	0.052	85	22.3	ND	12.7	16.3	ND	7.09
6/11/09	1	PFC	AUTO	23.3	4.51	0.07	0.034	0.273	75	20.3	ND	27.8	10.3	ND	12
7/1/09	1	PFC	AUTO	8.7	0.916	0.35	ND	0.052	74	17.1	ND	12	14.1	ND	8.4
10/9/09	1	PFC	AUTO	2.8	0.463	0.265	0.026	0.049	45	11.6	ND	6.32	9.7	ND	4.94
3/11/07	2	HMA	PASSIVE	223	0.996	0.1	0.02	0.12	79	27.7	12.7	169	2.7	ND	8.53

Date	Site	Surf-ace	Sampler	TSS (mg/L)	TKN (mg/L)	NO2/ NO3 (mg/L)	Diss. P (mg/L)	Tot. P (mg/L)	COD (mg/L)	Tot. Cu (µg/L)	Tot. Pb (µg/L)	Tot. Zn (µg/L)	Diss. Cu (µg/L)	Diss. Pb (µg/L)	Diss. Zn (µg/L)
3/13/07	2	HMA	PASSIVE	172	1.21	0.17	0.02	0.113	75	49.8	9.45	135	7.95	ND	11.3
3/26/07	2	HMA	PASSIVE	286	4.52	0.06	0.02	0.337	129	42.1	14.9	215	6.63	1.09	26.2
4/24/07	2	HMA	PASSIVE	127	0.348	0.22	0.155	0.135	55	16.9	13.2	79.2	5.5	ND	16.3
4/30/07	2	HMA	PASSIVE	102	1.49	0.31	0.052	0.147	110	31.7	6.79	138	10.9	ND	28.6
5/3/07	2	HMA	PASSIVE	136	1.02	0.2	0.02	0.476	50	22.2	9.53	95.1	1.75	ND	8.67
5/16/07	2	HMA	PASSIVE	22	1	0.36	0.036	0.06	55	11.7	3.36	61.7	7.7	ND	36.5
5/24/07	2	HMA	PASSIVE	197	0.799	0.15	ND	0.106	65	28.4	13.9	133	4.48	ND	8.57
6/3/07	2	HMA	PASSIVE	83	0.414	0.2	ND	0.085	40	16.9	6.95	66	3.54	ND	4.33
7/20/07	2	HMA	PASSIVE	81	0.21	0.06	0.021	0.063	38	14.3	3.74	56.2	3.12	ND	4.08
10/22/07	2	HMA	PASSIVE	93	0.657	0.1	ND	0.097	85	43.6	10.2	175	10.7	ND	25
11/24/07	2	HMA	PASSIVE	137	0.681	0.16	0.023	0.115	122	36.4	14.8	209	7.68	ND	26.4
12/11/07	2	HMA	PASSIVE	409	1.19	0.06	ND	0.124	92	42.2	23.3	184	4.24	ND	7.06
3/11/07	2	PFC	PASSIVE	36	0.474	0.21	0.02	0.02	60	13.6	1.99	30.1	8.91	ND	14.8
3/13/07	2	PFC	PASSIVE	46	0.462	0.08	0.02	0.037	40	8.94	1.88	23.1	4.89	ND	8.48
3/26/07	2	PFC	PASSIVE	19	4.03	0.29	0.024	0.08	69	13.5	1.49	28.9	10.1	ND	19
4/24/07	2	PFC	PASSIVE	7	0.706	0.43	0.092	0.143	68	12.4	ND	14.9	10	ND	13.5
4/30/07	2	PFC	PASSIVE	10	0.761	0.21	0.039	0.075	89	19.7	ND	27.1	13.1	ND	13.8
5/3/07	2	PFC	PASSIVE	21	0.504	0.21	0.02	0.048	26	6.36	ND	15.4	3.3	ND	8.54
5/16/07	2	PFC	PASSIVE	6	1.88	0.91	ND	0.071	124	21.5	ND	15.5	19.8	ND	13.9
5/24/07	2	PFC	PASSIVE	12	0.456	0.1	ND	0.023	58	9.25	ND	16.1	7.52	ND	10.3
6/3/07	2	PFC	PASSIVE	13	0.369	0.17	ND	0.039	39	7.05	ND	12.3	4.64	ND	4.47
7/20/07	2	PFC	PASSIVE	11	0.092	ND	ND	0.03	33	4.85	ND	13.5	3.26	ND	4.88
10/22/07	2	PFC	PASSIVE	8	0.797	0.3	ND	0.045	110	25.6	2.15	33.4	18.3	ND	18.4
11/24/07	2	PFC	PASSIVE	9	0.445	0.33	0.055	0.034	62	13.4	ND	17.3	11.4	ND	10
12/11/07	2	PFC	PASSIVE	23	1.11	0.13	ND	ND	32	10.3	1.07	21.9	5.93	ND	5.95
2/9/09	3	HMA	PASSIVE	31.2	0.757	0.14	0.034	0.063	38	8.07	4.45	43.1	5.14	ND	5.76
3/12/09	3	HMA	PASSIVE	85.2	5.25	1.69	0.03	0.163	245	43.3	14	217	28.1	ND	86.4
3/26/09	3	HMA	PASSIVE	186	1.98	0.24	ND	0.215	70	25.8	23.7	161	6.99	1.1	21.8

Date	Site	Surf-ace	Sampler	TSS (mg/L)	TKN (mg/L)	NO2/ NO3 (mg/L)	Diss. P (mg/L)	Tot. P (mg/L)	COD (mg/L)	Tot. Cu (µg/L)	Tot. Pb (µg/L)	Tot. Zn (µg/L)	Diss. Cu (µg/L)	Diss. Pb (µg/L)	Diss. Zn (µg/L)
4/12/09	3	HMA	PASSIVE	146	1.62	0.3	0.037	0.177	82	20.4	25.4	176	5.42	ND	14.2
6/12/09	3	HMA	PASSIVE	574	2.91	0.17	0.022	0.532	109	24.8	29.4	185	6.03	ND	7.07
10/5/09	3	HMA	PASSIVE	385	1.7	0.023	ND	0.306	137	22.7	24.7	162	1.81	ND	4.96
10/22/09	3	HMA	PASSIVE	246	1.53	0.028	0.115	0.206	200	30.2	25	250	3.06	ND	13.9
12/2/09	3	HMA	PASSIVE	123	1.17	0.194	0.023	0.116	85	21	10	191	5.3	ND	17.3
2/9/09	3	PFC	PASSIVE	3.7	0.708	0.23	0.04	0.052	39	7.53	ND	19.4	7.25	ND	19.4
3/12/09	3	PFC	PASSIVE	5.2	0.533	0.44	ND	0.029	23	7.34	ND	34.6	4.82	ND	18.1
3/26/09	3	PFC	PASSIVE	36	0.943	0.35	ND	0.076	52	14.1	3.07	54.8	5.78	ND	12.3
4/12/09	3	PFC	PASSIVE	48	0.9	0.3	ND	0.065	41	10.7	1.67	9.14	5.44	ND	9.14
6/12/09	3	PFC	PASSIVE	9	1.65	0.36	0.03	0.1	58	14.7	ND	31	10	ND	17.9
10/5/09	3	PFC	PASSIVE	7.4	0.355	0.049	ND	0.034	38	7.42	ND	14.6	5.75	ND	6.79
10/22/09	3	PFC	PASSIVE	4.4	0.24	0.148	ND	0.021	35	6.02	ND	9.36	4.7	ND	6.49
12/2/09	3	PFC	PASSIVE	5	0.221	0.215	ND	0.033	19	5.04	ND	16.2	3.47	ND	8.51

Appendix B: Hydraulic Property Measurements

CoreID	Year	Site	Position	Radius (cm)	Thick-ness (cm)	Porosity %	Porosity Method	Hydraulic Conductivity (cm/s)	Forchheimer Coef. (s^2/cm^2)
1-A-T	2007	Loop360	TrafficLane	7.51	4.45	22.78	SUW	0.18	2.785
1-B-T	2007	Loop360	TrafficLane	7.54	3.74	21.64	SUW	2.427	0.584
1-C-T	2007	Loop360	TrafficLane	NA	NA	20.36	IA	NA	NA
2-A-T	2007	FM1431	TrafficLane	7.52	3.56	23.17	SUW	0.668	1.812
2-B-T	2007	FM1431	TrafficLane	7.52	4.08	20.51	SUW	0.308	3.034
2-C-T	2007	FM1431	TrafficLane	NA	NA	20.98	IA	NA	NA
3-A-T	2007	RR620	TrafficLane	NA	NA	20.3	IA	NA	NA
3-B-T	2007	RR620	TrafficLane	7.54	4.02	19.44	SUW	0.455	7.206
3-C-T	2007	RR620	TrafficLane	7.54	3.95	19.55	SUW	0.457	2.679
1-1-T	2008	Loop360	TrafficLane	10.92	4.66	22.97	SUW	0.801	2.216
1-1-S	2008	Loop360	Shoulder	10.96	3.99	21.68	SUW	2.328	1.213
1-2-T	2008	Loop360	TrafficLane	10.97	4.81	22.77	SUW	0.829	2.797
1-2-S	2008	Loop360	Shoulder	10.91	3.75	20.28	SUW	1.115	2
1-3-T	2008	Loop360	TrafficLane	10.95	4.08	18.54	SUW	1.389	1.529
1-3-S	2008	Loop360	Shoulder	10.92	3.5	21.52	SUW	1.82	1.118
2-1-T	2008	FM1431	TrafficLane	10.93	3.25	15.77	SUW	0.474	4.136
2-2-T	2008	FM1431	TrafficLane	10.89	3.53	16.62	SUW	0.957	2.306
2-3-T	2008	FM1431	TrafficLane	10.9	3.05	16.18	SUW	0.468	4.06
3-1-T	2008	RR620	TrafficLane	10.91	3.41	12.38	SUW	0.056	64.297
3-2-T	2008	RR620	TrafficLane	10.88	2.79	12.82	SUW	0.048	166.83
3-3-T	2008	RR620	TrafficLane	10.93	3.54	14.5	SUW	0.228	15.72
1-i-T	2009	Loop360	TrafficLane	10.92	4.24	17	SUW	1.831	1.932
1-i-S	2009	Loop360	Shoulder	10.92	3.47	20.49	SUW	2.868	0.875
1-ii-T	2009	Loop360	TrafficLane	10.92	4.34	18.14	SUW	0.555	3.567
1-ii-S	2009	Loop360	Shoulder	10.92	3.18	19.2	SUW	2.106	1.613
1-iii-T	2009	Loop360	TrafficLane	10.97	4.51	18.78	SUW	1.334	1.266
1-iii-S	2009	Loop360	Shoulder	10.92	3.27	19.74	SUW	0.954	3.096
2-i-T	2009	FM1431	TrafficLane	10.93	3.24	15.57	SUW	0.194	4.496
2-ii-T	2009	FM1431	TrafficLane	10.9	3.39	16.23	SUW	0.437	2.162
2-iii-T	2009	FM1431	TrafficLane	10.93	3.44	15.9	SUW	0.992	2.007
3-i-T	2009	RR620	TrafficLane	10.93	3.68	12.96	SUW	0.102	29.132
3-ii-T	2009	RR620	TrafficLane	10.91	3.86	13.45	SUW	0.18	12.368
3-iii-T	2009	RR620	TrafficLane	10.92	3.76	17.96	SUW	0.241	17.371
1-a-T	2010	Loop360	TrafficLane	7.616	4.709	18.25	SUW	0.359	12.721
1-a-S	2010	Loop360	Shoulder	7.603	3.825	20.96	SUW	1.327	0.795
1-b-T	2010	Loop360	TrafficLane	7.639	4.599	22.67	SUW	2.074	1.067
1-b-S	2010	Loop360	Shoulder	7.511	3.98	19.95	SUW	1.51	0.63

CoreID	Year	Site	Position	Radius (cm)	Thick-ness (cm)	Porosity %	Porosity Method	Hydraulic Conductivity (cm/s)	Forchheimer Coef. (s^2/cm^2)
1-c-T	2010	Loop360	TrafficLane	7.521	4.86	16.6	SUW	0.588	3.909
1-c-S	2010	Loop360	Shoulder	7.522	3.87	19.69	SUW	1.551	0.466
3-a-T	2010	RR620	TrafficLane	7.507	4.214	13.34	SUW	0.203	34.789
3-b-T	2010	RR620	TrafficLane	7.512	4.109	13.6	SUW	0.019	640.386
3-c-T	2010	RR620	TrafficLane	7.533	4.19	13.95	SUW	0.09	133.903